

For Reference

NOT TO BE TAKEN FROM THIS ROOM

Ex LIBRIS
UNIVERSITATIS
ALBERTAEENSIS



30-185

THE UNIVERSITY OF ALBERTA

RELEASE FORM

NAME OF AUTHOR: Wayne Elmer Faszer

TITLE OF THESIS: Study of a High Repetition Rate CO₂ TEA Laser
and Repetition Rate Induced Discharge Instabilities.

DEGREE FOR WHICH THESIS WAS PRESENTED: Ph.D.

YEAR THIS DEGREE GRANTED: 1980

Permission is hereby granted to THE UNIVERSITY OF ALBERTA LIBRARY
to reproduce single copies of this thesis and to lend or sell such
copies for private, scholarly or scientific research purposes only.

The author reserves other publication rights, and neither the
thesis nor extensive extracts from it may be printed or otherwise
reproduced without the author's written permission.

THE UNIVERSITY OF ALBERTA

STUDY OF A HIGH REPETITION RATE CO₂ TEA LASER AND REPETITION
RATE INDUCED DISCHARGE INSTABILITIES

by



Wayne Elmer Faszer

A Thesis

Submitted to the Faculty of Graduate Studies and Research
in Partial Fulfilment of the Requirements for the Degree
of Doctor of Philosophy

Department of Electrical Engineering

Edmonton, Alberta

Spring, 1980

THE UNIVERSITY OF ALBERTA
FACULTY OF GRADUATE STUDIES AND RESEARCH

The undersigned certify that they have read, and
recommend to the Faculty of Graduate Studies and Research,
for acceptance, a thesis entitled "Study of a High Repetition..
Rate CO₂ TEA Laser and Repetition Rate Induced Discharge Instabilities",
.....
.....
submitted by Wayne Elmer Faszner.....
in partial fulfilment of the requirements for the degree of

DEDICATION

To my parents for encouraging me to pursue an advanced education.

Abstract

The purpose of this project was to develop a high repetition rate CO₂ TEA laser. The laser was pumped by a Marx generator and employed spark gaps for the dual purpose of preionizing the gas discharge and switching the Marx generator. Typical operating characteristics of the laser were studied. Discharge instabilities proved to be a major problem and limited repetition rates to lower values than were initially hoped for.

The discharge instabilities were then studied in more detail for the purpose of identifying their causes. Optical measurements of discharge generated shock waves in the laser showed that they were not the cause as they had sufficient time to dissipate between pulses and so would not affect following pulses. Subsequent tests in a smaller discharge system showed that the major cause of instability in the high repetition rate system was due to not allowing sufficient convection time for discharge products to clear out of the discharge region between pulses. The repetition rate drops off with increasing energy density and Dzakowic and Wutzke have proposed a theory to explain this effect. However in this study the repetition rate fell off more quickly than their theory predicts, largely due to the system geometry. That is, when the energy density gets large enough the discharge products must clear not only the discharge electrodes but the spark gaps as well.

Gas poisoning was also observed in this study and caused arcing in the closed cycle high-repetition-rate CO₂ TEA discharge after only a few minutes.

A comparison was done between a spark pin preionized discharge configuration with solid electrodes and a dielectric discharge preionized configuration with a screen electrode. Higher repetition rates could be

attained with the solid electrode system than with the screen electrode system. This was probably due to discharge products getting trapped behind the screen and causing discharge deterioration. Both systems showed poisoning after about the same length of time.

Some preliminary work was done using a streak camera and streak photographs of repetition rate induced instabilities were obtained.

Acknowledgements

The author would like to thank Dr. J. Tulip who supervised this project, and also Dr. H.J. Seguin and Dr. P. Smy for their helpful discussions.

Thanks also goes to the technical and machine shop staff in the department who provided much help. In particular Roy Schmaus who was responsible for the circuits shown in Figures 3.7 and 4.10, and George Fij who did most of the fabrication of the flowing gas discharge system. Thanks also to Ms. Barbara J. Galliaford for typing this manuscript.

In addition the author would like to thank the University of Alberta and the National Research Council for financial support provided.

TABLE OF CONTENTS

	Page
Abstract	
Chapter 1 Introduction	
Historical Survey	1
1.1 Summary of Experiments	3
1.2 Laser System	4
1.3 Recirculating Gas System	4
1.4 Electrical Discharge System	4
1.5 Optical System	8
Chapter 2 System Design	
2.1 Flow System Design	9
2.2 Marx Generator Design	12
Chapter 3 System Testing	
3.1 Flow Testing	16
3.2 Marx Generator Testing	22
3.3 Circuit Model	29
3.4 Pulse Stretching	39
3.5 Electrodes	42
3.6 Repetition Rate	42
3.7 Optics	44
3.8 Gain Measurements	52
3.9 Shock Wave Measurements	55
3.10 Discussion and Conclusions	67
Chapter 4 Flowing Gas Discharge System Design	
Introduction	69
4.1 Recirculating Gas Loop	70

	Page
4.2 Pressure Vessel Capability	70
4.3 Flow System Design	70
4.4 Heat Exchanger Design	77
4.5 Fan Seal	80
4.6 V-belts	81
4.7 Vacuum Pump	83
4.8 Motor Speed Controller	83
4.9 Fan Speed Sensing	83
4.10 Pulse Discharge Circuitry	86
Chapter 5 Flowing Gas Discharge System Testing	
5.1 Flow System Testing	92
5.2 Gas Flow Calibration	97
5.3 System Vacuum Integrity	99
5.4 Discharge Circuit	104
Chapter 6 Flowing Gas Discharge System	
Results and Conclusions	
6.1 Definitions and Theory	108
6.2 Gas Types	117
6.3 Effect of Spark Pins on the System	118
6.4 Repetition Rate Versus Gas Flow Velocity	127
6.5 Repetition Rate Versus Energy	137
6.6 Repetition Rate Versus Inductance	140
6.7 Afterglow Clearing Time Measurements	145
6.8 Afterglow Pulse Length Versus Energy Density	156
6.9 Discharge Intensity Profiles	168
6.10 Arcing Modes	181

	Page
6.11 Gas Poisoning	192
6.12 Conclusions	192
Chapter 7 Comparison of Spark Preionized System and Dielectric Discharge Preionized System	
Introduction	194
7.1 Construction	194
7.2 Gas Flow Calibration	197
7.3 Results	200
7.4 Conclusions	215
Chapter 8 Flowing Gas Discharge System Streak Camera Observations	
Introduction	216
8.1 Apparatus	216
8.2 Results	218
8.3 Conclusions	222
Chapter 9 Conclusions and Recommendations for Further Study	
9.1 Laser System Results	225
9.2 Shock Wave Measurements	225
9.3 Flowing Gas Discharge System Measurements	226
9.4 Considerations for High Repetition Rate CO ₂ TEA Laser Design	228
9.5 Suggestions for Further Work	229
References	231
Appendix	
Listing of Computer Routines	235
Vita	250

List of Tables

Table		Page
2.1	Pressure Head Loss Estimates Throughout the Flow System	11
3.1	Velocity Measurements	17
3.2	Maximum Repetition Rates for Several Marx Generator Configurations	43
3.3	Comparison of Optical Systems for the High Repetition Rate Laser	50
3.4	Probe Beam Deflection Due to Thermal Density Gradients	62
3.5	Cathode Shock Wave Propagation Measurements	66
4.1	Pressure Head Loss Estimates for the Flowing Gas Discharge System	75
4.2	Typical Shaft Speeds for 1" Diameter Shaft	81
5.1	Calibration Curve Coefficients	99
6.1	Estimates of Flow Velocity Based on the Observation of Column Discharges in CO ₂	124
6.2	Discharge Column Spacing	126
6.3	Comparison of Observed Fractional Frequencies with those Based on $1/\tau_{\text{afterglow}}$	156
6.4	Further Analysis of Afterglow Data for 60 Torr N ₂	162
6.5	Further Analysis of Afterglow Data for 80 Torr CO ₂	163

Table		Page
6.6	Fractional Frequencies Calculated from Afterglows	166
7.1	Calibration Curve Coefficients for Dielectric Discharge Preionized System	200

List of Figures

Figure		Page
1.1	Physical Layout of CO ₂ TEA Laser System	5
1.2	Schematic of Marx Generator	6
1.3	Schematic of Marx Triggering Circuit	7
2.1	Fan Characteristic and System Pressure Head Loss	13
3.1	Gas Flow Velocity Distributions	18
3.2	Flow Map for Narrow Angled Diffuser with Electrodes in Place	20
3.3	Flow Map for Narrow Angled Diffuser with Electrodes Replaced by Flat Plates	21
3.4	Output Pulses for 10 Stage Marx	24
3.5	Commutation Delay in the Marx Generator with a Single Trigger Pin	26
3.6	Construction of Triggered Spark Pin	27
3.7	HY60 Pulse Generator used as a Trigger Unit for the Marx Generator	28
3.8	Circuit Model	30
3.9	Initial Conditions for the Circuit Model	31
3.10	Typical Waveforms for the Simple Circuit Model	37
3.11	Improved Circuit Model	38
3.12	Pulse Stretching Circuit	40
3.13	Voltage and Current Waveforms of Stretched Pulse	41

Figure		Page
3.14	Typical Marx Generator Charging Waveform	45
3.15	Optical System	46
3.16	Optical Output	48
3.17	Optical Output Pulses from the Unstable Resonator at 100 Hz Repetition Rate	51
3.18	Mirror Bellows Systems	53
3.19	Apparatus Used for Small-signal Gain Measurements	54
3.20	Gas Density Perturbations	56
3.21	Apparatus for Density Gradient Measurements	58
3.22	Cross Section of Discharge Region Showing Where Shock Wave Measurements were Made	59
3.23	Detector Voltage Without and With Gas Flow	61
3.24	Deflection of Probe Beam Due to the Thermal Density Gradient	63
3.25	Detector Voltage at Position 4 Indicating Vertical and Horizontal Components of Shock Waves	65
4.1	Flowing Gas Electrical Discharge System - Recirculating Gas Loop	71
4.2	Simplified Model of Recirculating Gas Loop	73
4.3	Fan Characteristics and System Loss Curve	76
4.4	Fan Assembly and Shaft Seal	82
4.5	Grinder Mounting and Pulley Arrangement	84
4.6	Motor Speed Controller	85

Figure		Page
4.7	Discharge System Configuration	87
4.8	High Repetition Rate Discharge Circuit	88
4.9	1802 Thyratron Grid Drive Circuit	89
4.10	Voltage Controlled Pulse Generator	90
5.1	Initial Gas Flow Velocity Distribution in the Test Section	93
5.2	Apparatus for Testing Fan Static Pressure	94
5.3	Flow Distribution in Fan Elbow	95
5.4	Gas Flow Velocity Calibration Curve for 60 Torr N ₂	100
5.5	Gas Flow Velocity Calibration Curve for 80 Torr CO ₂	101
5.6	Gas Flow Velocity Calibration Curve for 700 Torr He	102
5.7	Gas Flow Velocity Calibration Curve for the Laser Mixture	103
5.8	Typical Voltage and Current Waveforms for a 60 Torr N ₂ Discharge	107
6.1	Schematic of Discharge Region Showing Terms Used to Define τ_{conv}	108
6.2	Geometry for Derivation of Gas Expansion Clearing Ratio	110
6.3	Geometry of Cylindrical Discharge	114
6.4	Effect of Upstream and Downstream Spark Pins on Arc Free Repetition Rate for 700 Torr He	119

Figure		Page
6.5	Effect of Upstream and Downstream Spark Pins on Arc Free Repetition Rate for 60 Torr N_2	120
6.6	Effect of Upstream and Downstream Spark Pins on Arc Free Repetition Rate for a Mixture of N_2 and He	121
6.7	Effect of Upstream and Downstream Spark Pins on Arc Free Repetition Rate for 80 Torr CO_2	122
6.8	Effect of Upstream and Downstream Spark Pins on Arc Free Repetition Rate for a Mixture of CO_2 and He	123
6.9	Cross-sectional View of Constricted Discharge in N_2	125
6.10	Column Discharges in CO_2	125
6.11	Repetition Rate Versus Gas Flow Velocity for 60 Torr N_2 and 8 J/ℓ	128
6.12	Repetition Rate Versus Gas Flow Velocity for 60 Torr N_2 and 29 J/ℓ	129
6.13	Repetition Rate Versus Gas Flow Velocity for 60 Torr N_2 and 58 J/ℓ	130
6.14	Repetition Rate Versus Gas Flow Velocity for 80 Torr CO_2 and 15 J/ℓ	131
6.15	Repetition Rate Versus Gas Flow Velocity for 80 Torr CO_2 and 23 J/ℓ	132
6.16	Repetition Rate Versus Gas Flow Velocity for 80 Torr CO_2 and 35 J/ℓ	133

Figure		Page
6.17	Repetition Rate Versus Gas Flow Velocity for 700 Torr He and 11 J/ℓ	134
6.18	Repetition Rate Versus Gas Flow Velocity for 700 Torr He and 37 J/ℓ	135
6.19	Repetition Rate Versus Gas Flow Velocity for 700 Torr He and 64 J/ℓ	136
6.20	Calculating an Average Fractional Frequency from Observed Data	138
6.21	Observed Fractional Frequencies for a Uniform Glow in 700 Torr He	141
6.22	Observed Fractional Frequencies for a Uniform Glow in 60 Torr N ₂	142
6.23	Observed Fractional Frequencies for a Uniform Glow in 80 Torr CO ₂	143
6.24	Discharge Circuit for Pulse Length Experiments	144
6.25	Repetition Rate as a Function of Circuit Inductance for 60 Torr N ₂	146
6.26	Repetition Rate as a Function of Circuit Inductance for 80 Torr CO ₂	147
6.27	Repetition Rate as a Function of Circuit Inductance for 700 Torr He	148
6.28	Apparatus for Afterglow Measurements	149
6.29	Typical Afterglow Waveform in 60 Torr N ₂	151
6.30	1/τ _{afterglow} as a Function of Flow Velocity for 60 Torr N ₂ and 58 J/ℓ	153

Figure		Page
6.31	$1/\tau_{\text{afterglow}}$ as a Function of Flow Velocity for 80 Torr CO_2 and 70 J/l	154
6.32	$1/\tau_{\text{afterglow}}$ as a Function of Flow Velocity for 700 Torr He and 37 J/l	155
6.33	Afterglow Pulse	157
6.34	Afterglow Pulse Length as a Function of Energy Density for 60 Torr N_2	159
6.35	Afterglow Pulse Length as a Function of Energy Density for 80 Torr CO_2	160
6.36	Agreement Between Observed Afterglow Dia- meters and Gas Expansion Model for N_2 and CO_2	164
6.37	Arcing Occurs When the Spacing Between Afterglow Pulses Was 2 msec or Less in 60 Torr N_2	165
6.38	Comparison Between Observed Fractional Frequencies for 60 Torr N_2 and Fractional Frequencies Calculated from the Afterglow Clearing Times	167
6.39	Intensity Profile for 700 Torr He Discharge with 81.2nf Capacitor	169
6.40	Intensity Profile for 700 Torr He Discharge with 20.4nf Capacitor	170
6.41	Intensity Profile for 60 Torr N_2 Discharge with 81.2nf Capacitor	171

Figure		Page
6.42	Intensity Profile for 60 Torr N ₂ Discharge with 20.4nf Capacitor	172
6.43	Intensity Profile for 80 Torr CO ₂ Discharge with 81.2nf Capacitor	173
6.44	Intensity Profile for 80 Torr CO ₂ Discharge with 20.4nf Capacitor	174
6.45	Intensity Profile for a Repetition Rate Induced Nonuniform Discharge in 700 Torr He	176
6.46	Intensity Profile for a Repetition Rate Induced Nonuniform Discharge in 60 Torr N ₂	177
6.47	Geometry of Uniform Discharge Model used for Calculating a Model Intensity Profile	178
6.48	Model Intensity Profile for a Uniform Discharge	180
6.49	Repetition Rate Induced Arcing Modes	182
6.50	Repetition Rate Induced Instabilities as a Function of Energy Density in 700 Torr He	184
6.51	Repetition Rate Induced Instabilities as a Function of Energy Density in 60 Torr N ₂	185
6.52	Onset of Arcing Modes as a Function of Energy Density in 700 Torr He	187
6.53	Onset of Arcing Modes as a Function of Energy Density in 60 Torr N ₂	188
6.54	Onset of Arcing as a Function of Energy Density in 80 Torr CO ₂	189

Figure		Page
6.55	Onset of Arcing as a Function of Energy Density in 400 Torr of Laser Mix	190
6.56	Onset of Arcing as a Function of Energy Density in 500 Torr of Laser Mix	191
7.1	Dielectric Discharge Configuration	195
7.2	Dielectric Electrode	196
7.3	Dielectric Discharge Preionization Discharge Circuit	198
7.4	Typical Voltage and Current Waveforms for a 60 Torr N ₂ Discharge in the Dielectric Discharge Preionized System	199
7.5	Velocity Profile Between the Electrodes	201
7.6	Intensity Profile for a 60 Torr N ₂ Discharge in the Screen Electrode System	203
7.7	Intensity Profile for an 80 Torr CO ₂ Discharge in the Screen Electrode System	204
7.8	Intensity Profile for a 700 Torr He Discharge in the Screen Electrode System	205
7.9	Maximum Repetition Rate as a Function of Energy Density for 700 Torr He in the Screen Electrode System	206
7.10	Maximum Repetition Rate as a Function of Energy Density for 60 Torr N ₂ in the Screen Electrode System	207

Figure		Page
7.11	Maximum Repetition Rate as a Function of Energy Density for 80 Torr CO ₂ in the Screen Electrode System	208
7.12	Maximum Repetition Rate as a Function of Energy Density for 400 Torr of Laser Mix in the Screen Electrode System	209
7.13	Maximum Repetition Rate as a Function of Energy Density for 500 Torr of Laser Mix in the Screen Electrode System	210
7.14	Repetition Rate Versus Gas Flow Velocity for 80 Torr CO ₂ in the Screen Electrode System	211
7.15	Repetition Rate Versus Gas Flow Velocity for 60 Torr N ₂ in the Screen Electrode System	212
7.16	Repetition Rate Versus Gas Flow Velocity for 700 Torr He in the Screen Electrode System	213
7.17	Repetition Rate Versus Gas Flow Velocity for 400 Torr Laser Mix in the Screen Electrode System	214
8.1	Block Diagram of Streak Camera Experiment	217
8.2	Orientation of Streak Camera Slit with Respect to the Discharge Electrodes	219
8.3	Synchronization Between Discharge Current Pulse and Streak Camera Monitor Pulse	221
8.4	Streak Camera Pictures of a Uniform Discharge, Energy Induced Glow to Arc Transition, and a Repetition Rate Induced Glow to Arc Transition	221

Figure		Page
8.5	Examples of Energy Induced Glow to Arc Transitions	223
8.6	Uniform Glow and a Repetition Rate Induced Arc	223

CHAPTER 1

INTRODUCTION

HISTORICAL SURVEY

Laser action in a CO_2 gas discharge was first reported by C.K.N. Patel in 1964 (1,2). Average power output by the laser was about 1mW at $10.4\mu\text{m}$ and $9.4\mu\text{m}$, both continuous wave and pulsed.

The next major advances were the addition of N_2 and He to the CO_2 resulting in large increases in power output (3,4,5,6). Collisions between vibrationally excited N_2 molecules and ground state CO_2 molecules proved to be a very effective means of exciting the CO_2 molecules to the upper laser level. Helium aids the laser transition by rapidly depopulating the lower level of the transition, thereby preventing a build-up of molecules in the lower level which would act as a bottleneck to transitions from the upper level.

The use of fast flowing gas in CO_2 lasers to provide convective cooling was reported in 1969 (7,8,9). This was much more effective than the diffusion cooling relied upon in sealed and slow flow systems and resulted in an increase in output power per unit length of several orders of magnitude.

Early CO_2 lasers ran at low pressures. High pressure lasers were developed in order to provide a higher density of molecules capable of lasing and hence higher output power. In addition large volume atmospheric pressure lasers are easier to construct than large volume low pressure lasers because they do not have to be as well sealed or capable of withstanding as great pressure differences.

A CO_2 laser works best with an E/P ratio of about 10 to 50 V/(cm torr), where E is electric field and P is gas pressure. So as gas pressures rose this meant working with very high voltages for

longitudinally excited plasmas. To avoid this problem Transversely Excited Atmospheric (TEA) lasers were developed (10,11) which use large surface area electrodes placed close together to excite a large volume of plasma with much lower voltages than are needed for longitudinal excitation. Since the TEA laser electrodes are closer together, lower voltages will produce just as large fields.

Another major advancement in the construction of TEA lasers was the idea of conditioning the gas with some form of preionization in order to obtain a stable, uniform, large volume plasma more easily (12). Pre-ionization has been accomplished by a number of techniques including the use of UV (13), plasma jets (14), electron beams (15), neutrons (16), and organic gas additives (17).

Most TEA laser development to date has gone into high energy single pulse CO_2 lasers. However, a few high repetition rate systems have been built (18-22). The laser described in reference 21 is not a CO_2 laser but the authors have used high-repetition-rate CO_2 TEA laser technology, only substituting rare gases for the CO_2 laser mixture. These systems all use gas convection to clear undesirable discharge products from the discharge region between pulses. The limitation on maximum repetition rate has been due to the onset of discharge arcing, and this arcing usually occurs at lower repetition rates than would be expected from the velocity of the gas flowing between the electrodes (18,19). The best explanation of this effect offered so far is that of Dzakowic and Wutzke (18). Another problem which can occur in a closed-cycle system is degradation of discharge stability due to dissociation of the CO_2 into CO and O_2 (22). A solution to the problem of CO_2 dissociation is the use of some catalyst to recombine the CO and O_2 back into CO_2 (23).

1.1 SUMMARY OF EXPERIMENTS

In this thesis the design and testing of a high repetition rate closed cycle CO_2 TEA laser is described. Although the laser did operate at high repetition rates, discharge arcing limited it to a lower repetition rate than was initially estimated. A poisoning effect due to the dissociation of the laser gases was also a suspected source of problems. In order to understand the causes of the arcing, the discharge was studied in further experiments.

To facilitate the discharge studies a smaller more flexible discharge system was designed which modeled the essential features of the laser discharge system. Using this system a number of key parameters that could contribute to discharge arcing were studied. These parameters were gas flow velocity, pulse length, discharge energy density, system geometry and preionization technique. Discharge afterglows were monitored using a photomultiplier to observe convective clearing of the discharge products from the discharge region and to observe discharge expansion, an effect which was predicted by Dzakowic and Wutzke (18). A streak camera was also used in an attempt to monitor discharge expansion. Although the streak camera failed to show the discharge expansion it did produce some streak photographs which illustrate the various types of arcing that occur.

In studying the effects of system geometry and preionization on arcing three different techniques were compared. They were solid electrodes with spark pin preionization both upstream and downstream, solid electrodes with just downstream preionization, and a system where preionization was provided by an auxiliary discharge behind a screen electrode.

Besides the parameters studied on the small discharge system, the presence of shock waves was investigated on the laser system to see if they contributed in any way to discharge arcing.

1.2 LASER SYSTEM

This project started with the design and testing of a closed cycle high repetition rate CO_2 TEA laser. The laser had three basic subsystems: a closed cycle recirculating gas system, the electrical discharge system, and the optical system.

1.3 RECIRCULATING GAS SYSTEM

The recirculating gas system is a small scale wind tunnel which circulates the laser gas mixture through the electrical discharge region. It consists of a centrifugal blower, flow ducting, and a heat exchanger. The layout of the components is illustrated in Fig. 1.1. The blower was capable of delivering a volumetric gas flow of 1500 ℓ/sec , which corresponded to a velocity of 100 m/sec between the electrodes.

1.4 ELECTRICAL DISCHARGE SYSTEM

The electrical discharge system used to pump the laser is illustrated in Figs. 1.2 and 1.3. It is a Marx generator with its switching gaps located downstream from the discharge electrodes in the flow duct. Locating the switching gaps in the flow duct has a dual purpose - to extinguish the switching gaps between pulses using gas flow and to pre-ionize the discharge using ultraviolet light produced by the spark gaps. A time delay is needed between the spark gaps firing and the formation of the discharge in order for the preionization to take effect. This time

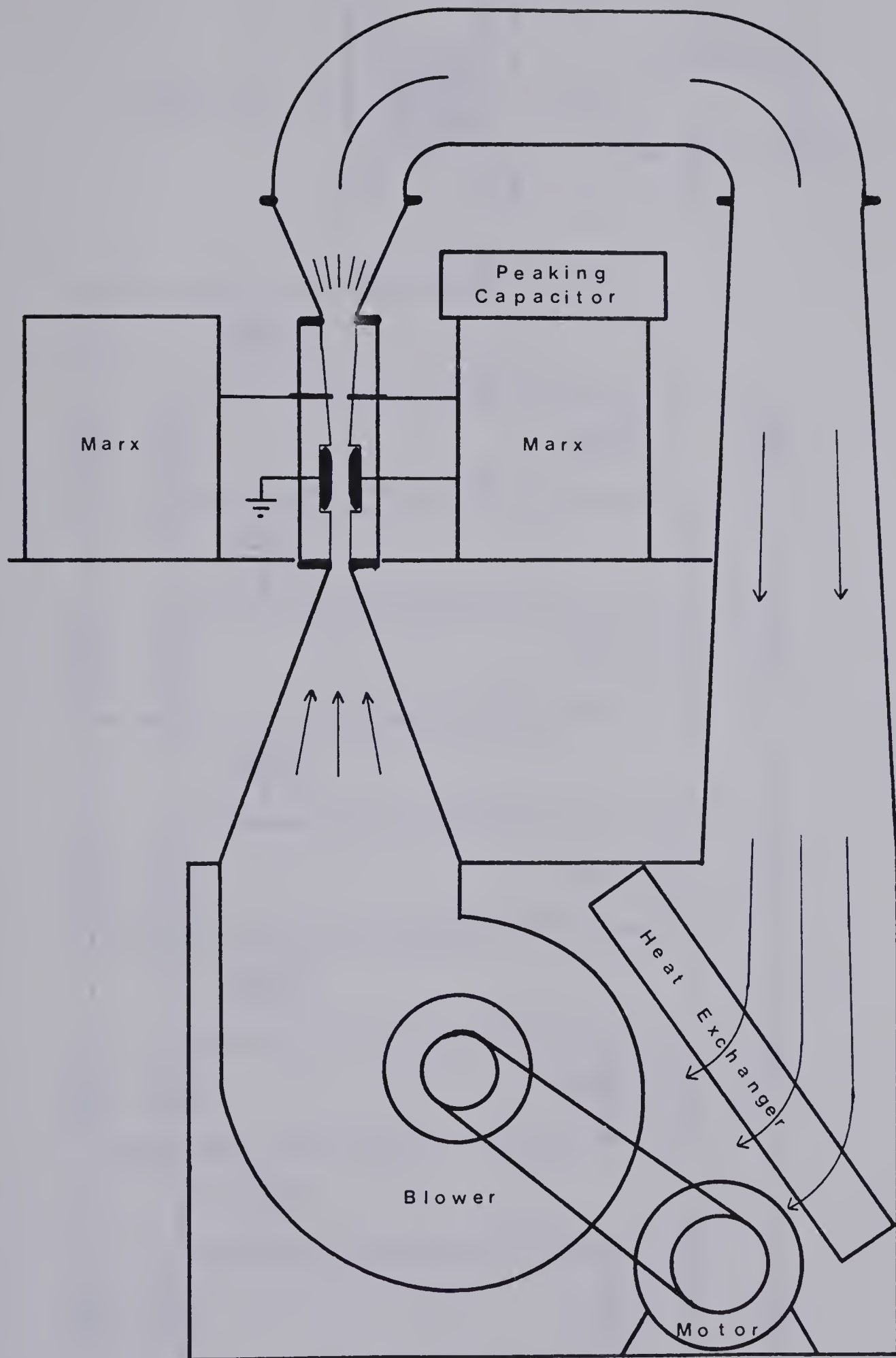


Fig. 1.1 Physical Layout of CO₂ TEA Laser System.

The system is 7 feet high, 4 feet wide and 3 feet deep.

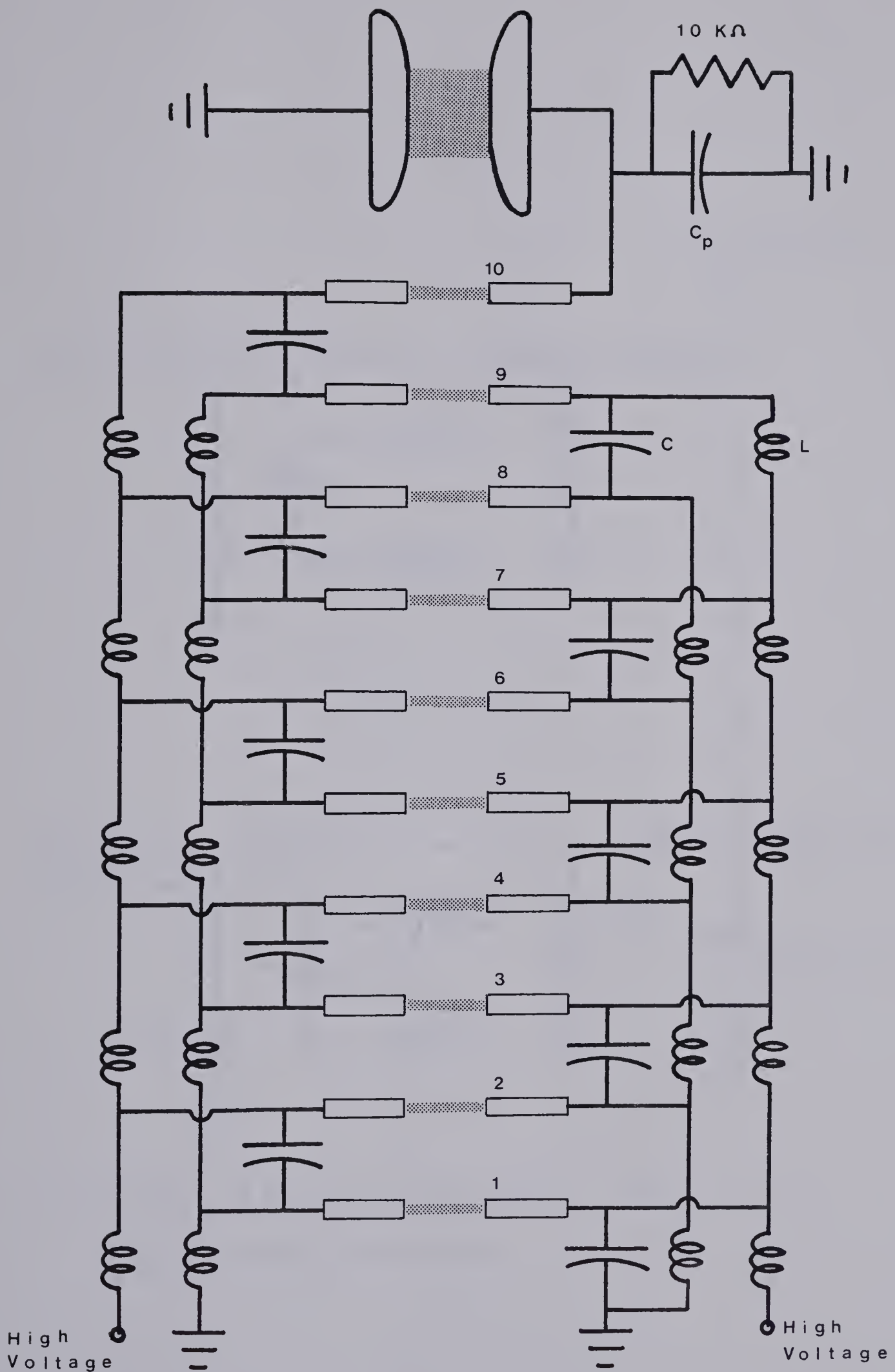


Fig. 1.2 Schematic of Marx Generator. Typical component values are $C_p = .03\mu\text{f}$, $C = .3\mu\text{f}$, and $L = 30\text{mh}$.

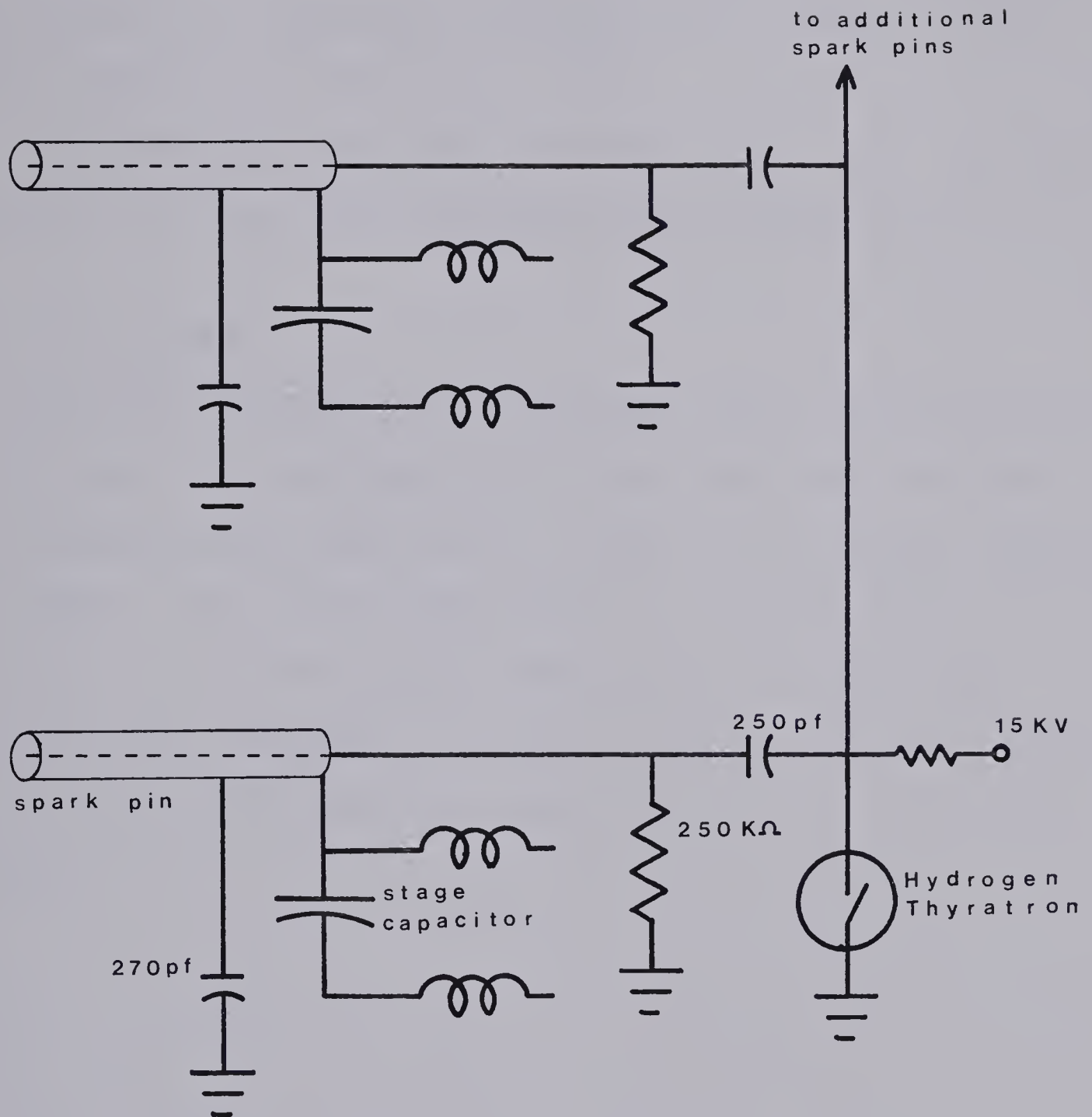


Fig. 1.3 Schematic of Marx Triggering Circuit. Pins 1, 3, 5, 7 and 9 of the Marx are triggered.

delay, and a certain amount of pulse shaping as well, is supplied by the peaking capacitor. In order for the preionization to be effective the Marx spark gaps must fire simultaneously and to accomplish this it was necessary to trigger more than one of the spark gaps. A minimum of 3 gaps have to be triggered but typically 5 are. A schematic of the trigger circuit used is shown in Fig. 1.3.

The discharge electrodes are 61 cm long and 10 cm wide. They are separated by 2.5 cm to give a discharge volume of approximately 0.37ℓ.

1.5 OPTICAL SYSTEM

Both stable and unstable resonators were tested as optical systems for the laser. Internal windows on the laser cavity were also tested but introduced too much loss into the low gain cavity, severely reducing power output. As a result it was necessary to attach the optics directly to the laser cavity with bellows. This resulted in problems with vibration being transmitted to the optics, causing unstable mode output. The unstable resonator provided a greater power output than the stable resonator.

CHAPTER 2

SYSTEM DESIGN

2.1 FLOW SYSTEM DESIGN

The laser gas was contained and circulated in a large sealed system. Although not a high vacuum system, it was reasonably airtight and could be pumped down to a pressure of 1 or 2 torr. After being pumped out the system was backfilled to the appropriate partial pressure for each gas depending on the desired laser mixture.

Gas flow through the system was driven by a centrifugal fan which was powered by a 15 HP electric motor. In order to avoid building a complicated shaft seal the motor was installed in the fan box along with the fan. A heat exchanger was also provided to remove heat introduced into the system by the discharge and fan.

A sealed recirculating system such as this is very similar to a closed cycle subsonic wind tunnel and so was designed according to principles outlined in Pope (24) and Pankhurst (25) for subsonic wind tunnels. Two other sources which proved useful were the Trane Air Conditioning Manual (26) which contained useful information on pressure measurement and fan characteristics; and the ASHRAE Handbook (27) which provided information on ducting design. Essentially the design criterion consisted of trying to offer as little resistance to gas flow in the ducting as possible, in order to achieve a high flow velocity.

In a recirculating gas system the gas flows under the influence of a pressure head developed by the system fan. Opposing the gas flow is skin friction resulting from the movement of gas through the ducting. Besides the head loss due to skin friction considerable head loss occurs due to changes in ducting cross-sectional area and changes of direction

of the duct. These losses are proportional to velocity squared and are described by eqn. 2.1.1

$$\Delta H = \frac{1}{2} c \rho u^2 \quad 2.1.1$$

ΔH is the pressure head loss, ρ is the gas density, u is the gas velocity, and c is a friction coefficient.

Initially the gas flow is converged from 37 cm. wide to 2.5 cm. wide between the electrodes. To reduce friction losses wide return passages were used. Converging the gas flow is very efficient and produces little head loss. However expanding the gas flow for the return trip is much more lossy. In order to minimize this loss diffusers are designed, where space permits, with small angles between the walls because larger angles cause flow separation which is very lossy. Such diffusers are called narrow angled diffusers and have, typically, 7° to 10° angles between the walls. Wider angled diffusers usually make use of vanes to help reduce losses and the angle between the vanes is kept around 7° to 10° . A 10° angle diffuser that expanded from 2.5 cm. to 20 cm., the width of the return passage, would be very long. In order to conserve space a wide-angle vaned diffuser was designed according to the design criterion outlined in a paper by Feil (28).

Using eqn. 2.1.1 an estimate of system performance was obtained. In this estimate only the main components contributing to system head loss were considered. They are: the throttle, or region between the electrodes, the wide angled diffuser, the two elbows, and the long narrow angled diffuser that acts as a return duct. All the estimates can be related to the velocity between the electrodes by use of the continuity

equation. This just means that the volumetric flow of gas is the same through all parts of the system, $VA = \text{constant}$. So, for instance, the cross sectional area in the elbows is 8 times that between the electrodes so the velocity in the elbows will be $1/8$ that between the electrodes. The head loss for the various parts of the system are summarized in table 2.1.

	c	v	$\frac{1}{2}\rho v^2$
high velocity region	.1	v	$.050\rho v^2$
wide angled diffuser	.35	$v/2$	$.044\rho v^2$
elbow	.3	$v/8$	$.002\rho v^2$
elbow	.3	$v/8$	$.002\rho v^2$
long diffuser	.3	$v/8$	$.002\rho v^2$
total			$0.10\rho v^2$

Table 2.1

Pressure Head Loss Estimates Throughout the
Flow System

The values of c are typical values and are obtained from references 25, 27 and 28. The values of v for the diffusers are the velocities at their inlets. It can be seen that the main sources of pressure head loss are the high velocity region between the electrodes and the wide angled diffuser because of the high gas velocities in them. Losses in the elbows and long diffuser are almost negligible. The high velocity region accounts for half the head loss by itself.

The total head loss then, as a function of velocity, is given by

$$\Delta H = 0.1\rho v^2 \quad 2.1.2$$

The cross sectional area between the electrodes is 1"x24", and using this, the head loss can be converted to a function of flow rate in CFM.

Standard air density is 0.075 lb(mass)/ft³. Using these values, and making suitable transformations to get the correct units this becomes

$$\Delta H = 4.33 \times 10^{-7} Q^2 \quad 2.1.3$$

where ΔH is pressure loss in inches of H₂O and Q is flow rate in CFM.

This is plotted, in Fig. 2.1, on the manufacturer supplied characteristics for the fan used in this system. The fan is a 13½ inch diameter centrifugal blower running at 4628 rpm. It can be seen that the system losses and fan static pressure match at a gas flow rate of 550 CFM which corresponds to a flow velocity of 160 m/sec. To achieve this velocity in air would require 20 HP but fortunately considerably less power is needed in the laser mixture because the power is proportional to the gas density. Since a typical laser mixture is mostly He (typically 80% He, 10% N₂, 10% CO₂) with an atomic weight of 2 and air is mostly N₂ with an atomic weight of 14, the laser mixture will have roughly 1/7 the density of air so will only require about 3 HP to achieve this flow velocity.

2.2 MARX GENERATOR DESIGN

This laser is essentially a double discharge design switched by spark gaps. Since the spark gaps must be blown in order to recover quickly

fan speed 4628 rpm
 gas density .075 lbs/ft³

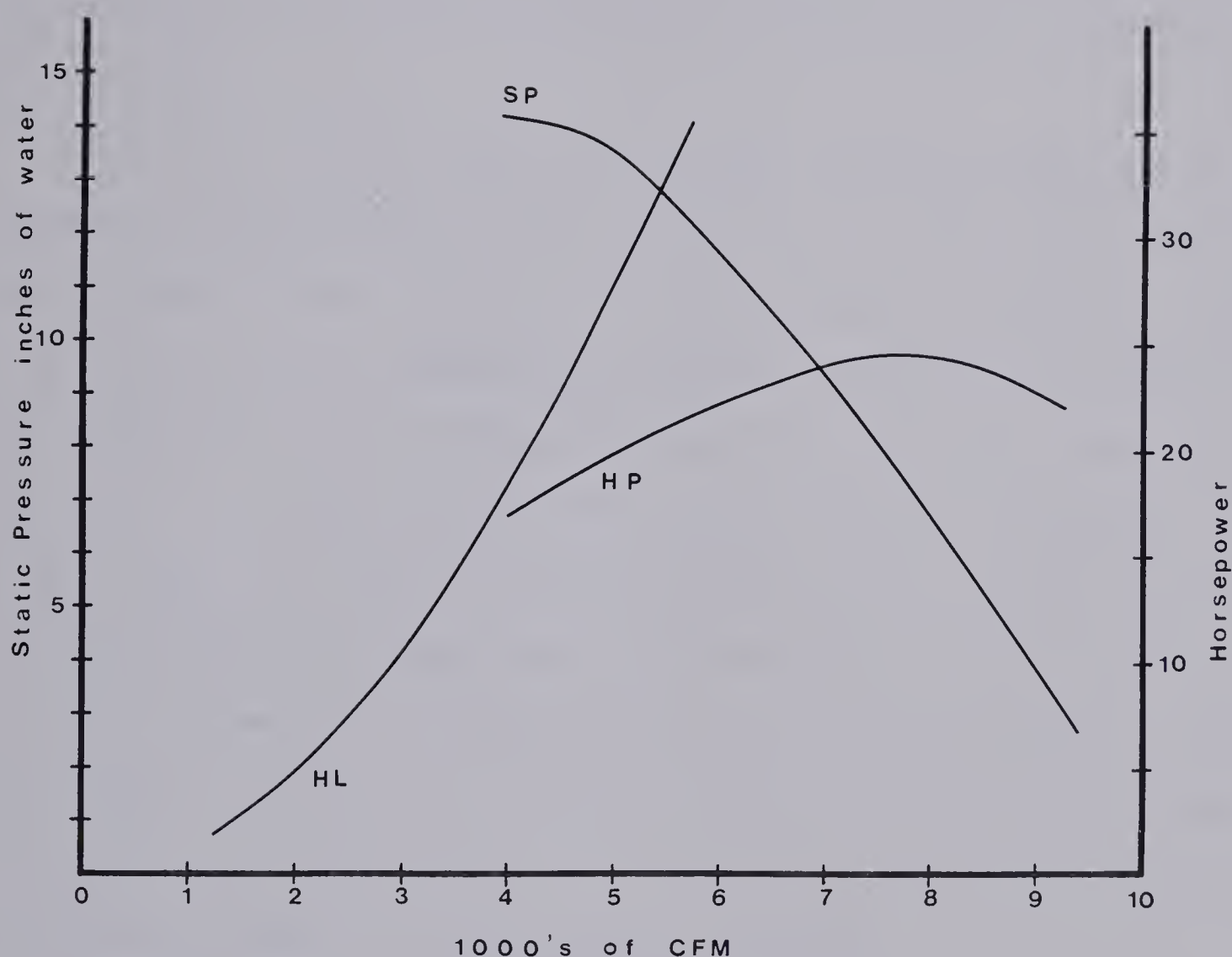


Fig. 2.1 Fan Characteristic and System Pressure Head Loss. SP is the fan static pressure curve, HL is the system head loss, and HP is the power required to drive the fan. The static pressure and system loss curves intersect at approximately 5500 CFM and 13 inches of water.

for high repetition rate operation it was decided to include them in the same flow system as the discharge electrodes which also rely on convection to remove discharge products from between them. By using a Marx generator, which is a voltage multiplying circuit, any desired pulse voltage can be achieved for optimum performance and in addition the Marx switching gaps serve as a source of ultraviolet light to preionize the discharge region. This then combines the two essential features of discharge preionization and Marx switching into one set of spark gaps, arranged along the length of the electrodes.

Design of a Marx generator is a straight forward procedure and is outlined in references 29 and 30. A schematic of the Marx used for this laser is shown in Figs. 1.2 and 1.3. A Marx generator consists of a number of capacitors which are charged up in parallel through hold-off inductors, then discharged in series through the spark gaps to provide voltage multiplication. The charging network can be either resistors or inductors but for a high repetition rate system the power loss in resistor charging would be prohibitive so inductors are used instead. For a N stage Marx the output voltage will be approximately N times the Marx charging voltage. If the hold-off inductors are too small or the time lag in the spark gaps firing is too long, enough charge can be lost through circulating currents in the Marx to reduce the output voltage appreciably.

The parameters of this Marx generator were determined largely by experimentation. However an estimate of the discharge time through the hold-off inductors was needed to determine that they would not shunt out the discharge.

The current in an LC circuit is given by

$$i_{LC} = V \sqrt{\frac{C}{L}} \sin \frac{t}{\sqrt{LC}}$$

and so has period

$$\tau = 2\pi\sqrt{LC}$$

The smallest discharge loop in this circuit would consist of two capacitors and one inductor in series. Initially C was chosen as .1 μ f and L as 30mh. This gave a discharge time of

$$\tau = 2\pi\sqrt{30 \times 10^{-3} \times \frac{0.1}{2} \times 10^{-6}} \text{ sec}$$

$$= 2.4 \times 10^{-4} \text{ sec}$$

Since the discharge pulse length is on the order of 1 μ sec this is sufficiently long that no appreciable charge is lost through the hold-off inductors during the discharge pulse.

CHAPTER 3

SYSTEM TESTING

3.1 FLOW TESTING

Flow velocity was measured using a pitot tube and a capacitance manometer. Connecting the static pressure from the tube to one port of the manometer head and the total pressure to the other port resulted in a differential measurement that gave the velocity pressure. The velocity can then be calculated from the velocity pressure using

$$\Delta P = \frac{1}{2}\rho v^2$$

or

$$v = \sqrt{\frac{2\Delta P}{\rho}} \quad 3.1.1$$

where ΔP is pressure in N/m^2 , ρ is gas density in kg/m^3 , and v is in m/sec .

Results of the velocity measurements are given in table 3.1 and are reasonably close to the original design estimates. The average gas flow velocity between the electrodes is approximately 100 m/sec . The design estimate was 160 m/sec .

Flow uniformity was examined between the electrodes, at the exit from the wide angled diffuser, and in the narrow angled diffuser connecting the two. Since these measurements were made in air, and the system drive motor is only rated for 15 HP it was necessary to slow the fan down to avoid overloading the motor. This was accomplished by exchanging the fan and motor pulleys. Although the velocity will be slower the velocity distribution should not be affected. Fig. 3.1 shows velocity distributions between the electrodes and at the exit from the wide angled

diffuser. The flow velocity between the electrodes is uniform but the

Air 730 torr

distance from endwall inches	0	2	4	6	8	10
velocity pressure torr	42	49	50	52	52	50

$$\Delta P_{av} = 50 \text{ torr}$$

$$\text{velocity} = 105 \text{ m/sec}$$

laser mix 70:70:590 torr

CO₂:N₂:He

distance from endwall inches	0	2	4	6	8	10
velocity pressure torr	17	19	19	19.5	20	20

$$\Delta P_{av} = 19.5 \text{ torr}$$

$$\text{velocity} = 107 \text{ m/sec}$$

The average values of velocity pressure were calculated without using the values at the endwall (distance = 0) because those values would be affected by the boundary layer.

Table 3.1 Velocity Measurements

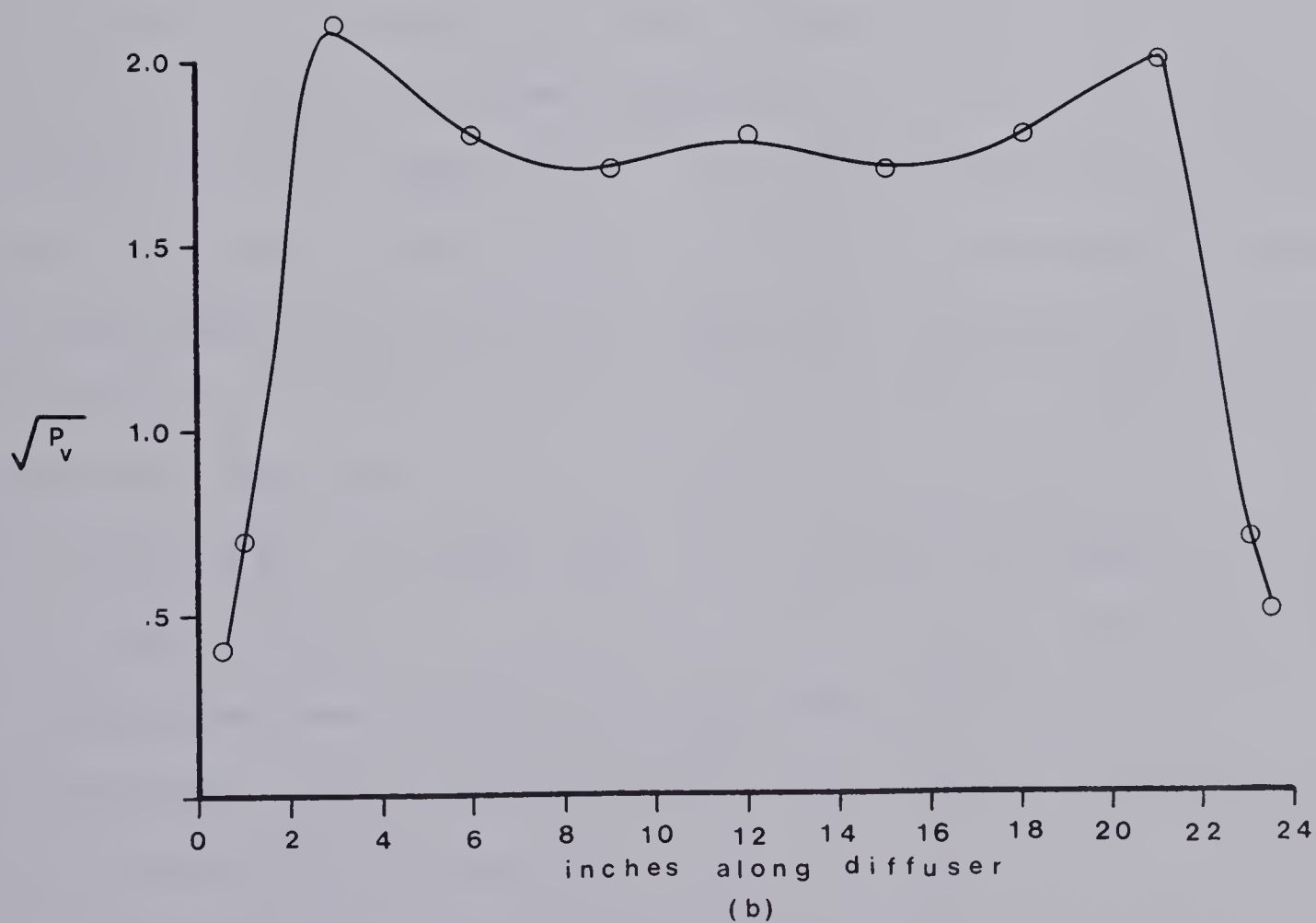
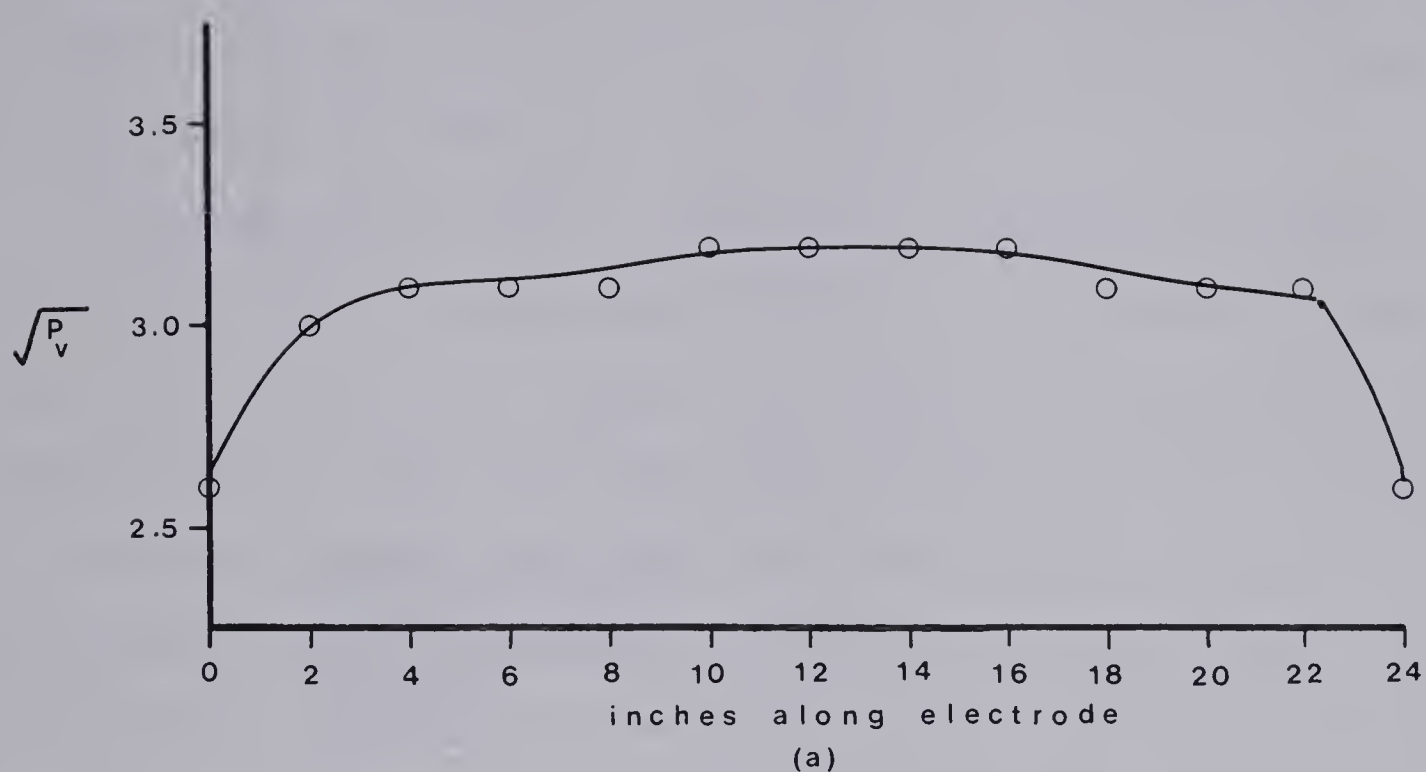


Fig. 3.1 Gas Flow Velocity Distributions (a) Between the Electrodes and (b) Leaving the Wide Angled Diffuser.

flow velocity leaving the wide angled diffuser was very nonuniform. The dead spaces near the endwalls indicate that flow separation has occurred, and this reduces the efficiency of the diffuser.

Referring back to Fig. 1.1, the wide angled diffuser is connected to the electrodes by a narrow angled diffuser that increases the channel width from 2.5 cm to 5 cm. Further tests showed that the separation was already occurring back in the narrow angled diffuser, and the gas entering the wide angled diffuser was already separated from the end walls. The wide angled diffuser only accented the effect as it slowed down the gas still further. Because the narrow angled diffuser was constructed from perspex it was transparent and a simple technique could be used to visualize the flow separation occurring in it. The method was to tape short tufts of yarn, about 5 cm long, to the walls of the diffuser. They readily showed the direction of flow and degree of turbulence in the diffuser. A resulting flow map is shown in Fig. 3.2. The electrodes were to a large extent responsible for this separation. This was demonstrated by replacing the electrodes with flat plates and taping shut the spark pin holes in the diffuser. The resulting flow map is shown in Fig. 3.3 and shows a considerable improvement over the flow with the electrodes in place. Since the electrodes are a necessary part of the system, flow separation caused by them must be tolerated. An attempt was made to reduce the separation by adding cross vanes to the narrow angled diffuser to act as flow straighteners. But since no improvement in flow velocity was observed with the vanes they were removed.

Although better diffuser design should result in reduced flow separation losses and hence a higher velocity the system is adequate for the purposes of this experiment. The flow between the electrodes meets

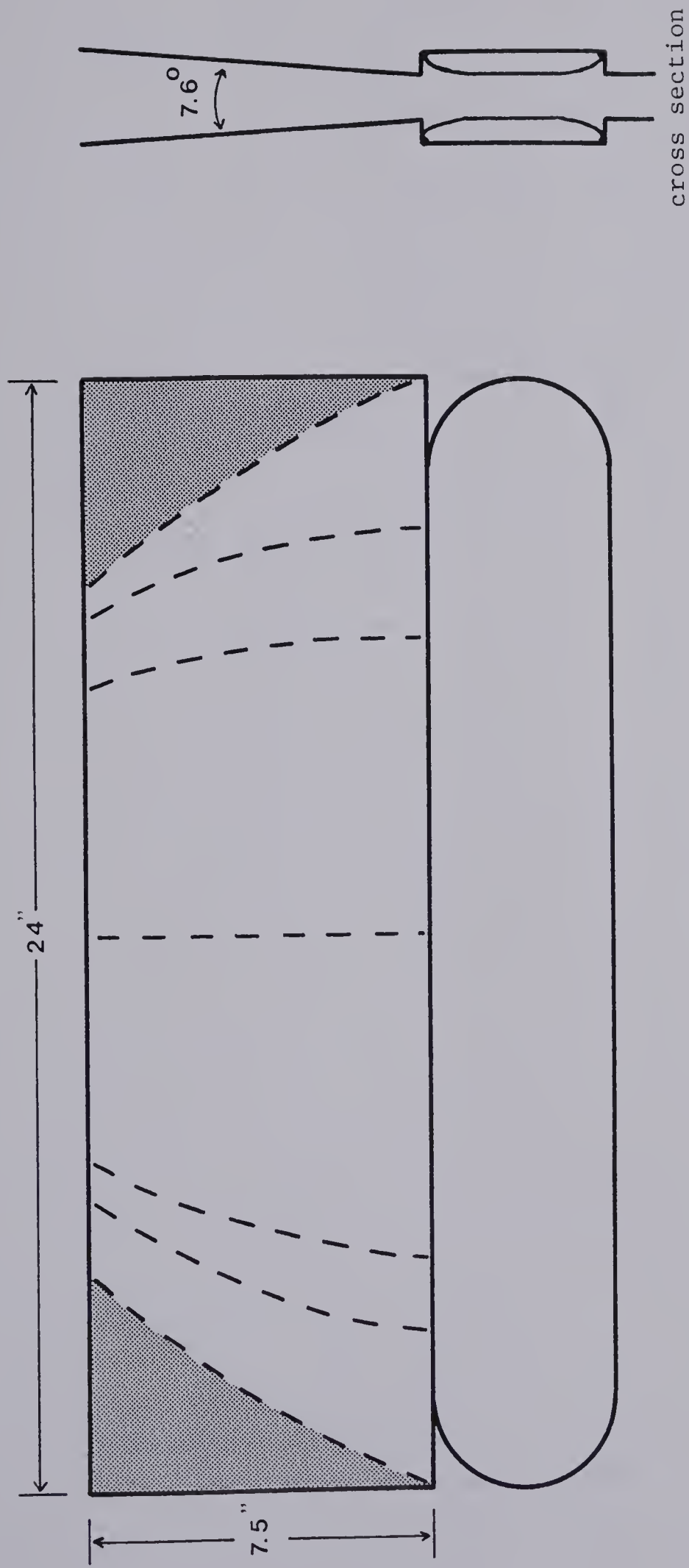


Fig. 3.2 Flow Map for Narrow Angled Diffuser With Electrodes in Place.

The dotted lines are flow lines and the shaded areas are turbulent regions.

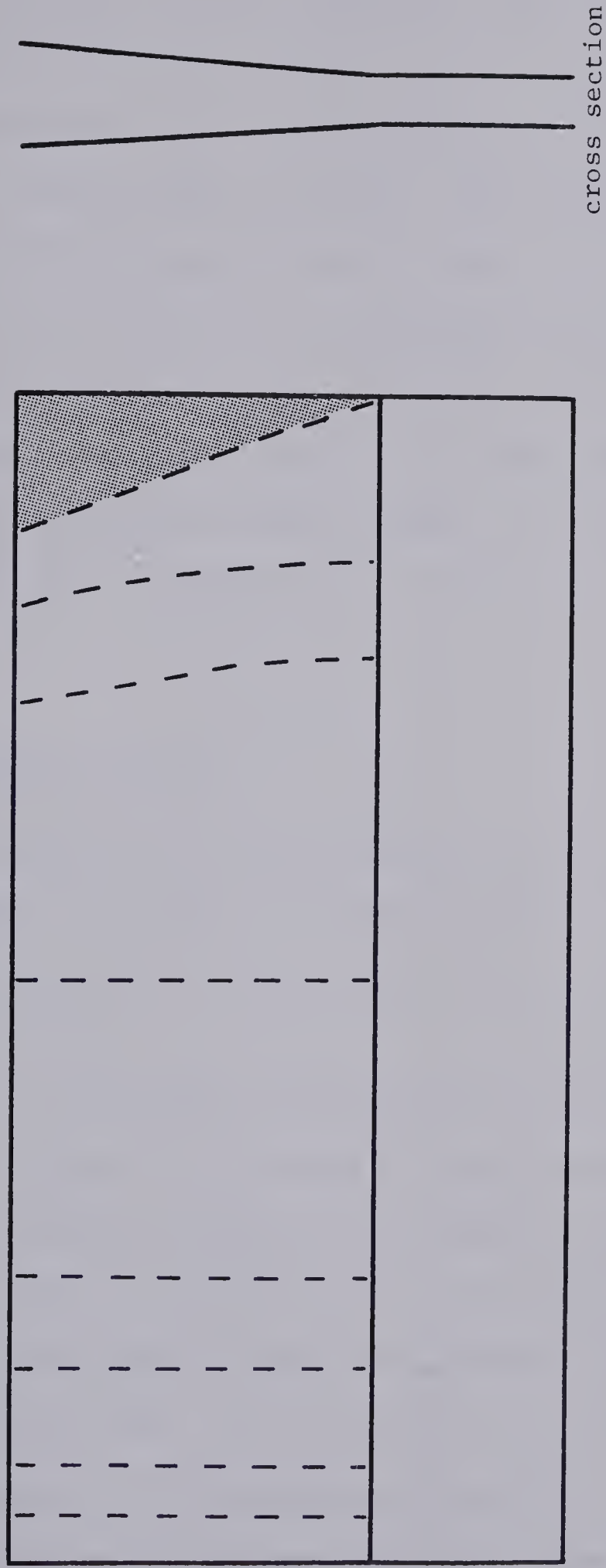


Fig. 3.3 Flow Map for Narrow Angled Diffuser with Electrodes Replaced by Flat Plates.
The dotted lines are flow lines and the shaded areas are turbulent regions.

the requirements of being uniform and fast.

Another potential problem considered to be a possibility during laser operation was the slowing down of gas flow, and hence a reduction in attainable repetition rate, due to shock waves from the discharge. To check this a run was made with a pitot tube inserted into the return duct to record velocity pressure while the laser was operating and the velocity pressure was observed on an inclined U-tube manometer. The U tube manometer was used because the capacitance manometer could not operate in the noisy electrical environment of the running laser. No change in velocity pressure was observed with a change in discharge repetition rate from 0 to 200 Hz, so flow choking due to shock waves does not occur in this system.

3.2 MARX GENERATOR TESTING

Many of the parameters of this Marx generator were determined by experimentation. They were the number of stages, triggering method, spark pin location, spark pin material, and the need for a peaking capacitor.

Originally a 6 stage Marx was designed but 5 and 10 stages were tested as well, 10 stages being chosen for the final design. The 10 stage Marx ran more stably than the 5 stage Marx of the same capacitance. This was because the spark gaps could more easily hold off the lower voltage of 4 to 6 KV needed for the 10 stage Marx than the $7\frac{1}{2}$ to 8 KV needed for the 5 stage Marx. The discharge was also more uniform for the 10 stage Marx due to the increased preionization.

Three important results were observed with respect to the Marx operation and the quality of the discharge. Firstly the Marx spark pins must be downstream from the discharge. Secondly adding a peaking

capacitor in parallel with the discharge helped stabilize it. Finally the method of triggering the Marx affected the discharge stability because it affected the Marx commutation time.

Originally the Marx was designed with its spark pins upstream from the discharge. However moving the pins downstream greatly reduced the amount of discharge arcing that occurred. This implies that discharge products from the spark gaps being swept into the main discharge region was a cause of arcing.

The addition of a peaking capacitor (C_p in Fig. 1.2) in parallel with the main discharge helped stabilize it and reduce arcing. Small peaking capacitors, typically 1000 pf to 5000 pf, were used. Originally it was assumed that the peaking capacitor introduced a time delay needed for the preionization to take effect. This explanation is not likely however, because the UV only needs on the order of 10^{-10} sec. to reach the discharge from the spark pins. A more likely explanation is that the peaking capacitor acts as a low impedance source which allows the discharge to form rapidly.

The small peaking capacitor results in a double humped current pulse (Fig. 3.4a) and in order to understand this waveform a simple circuit model, described in section 3.3, was devised. Essentially this model showed that the initial peak was due to the rapid discharge of the peaking capacitor, followed by a slower peak due to the discharge of the residual charge left in the Marx. This suggested that if all the charge could be transferred from the Marx to the peaking capacitor before breakdown occurred a much cleaner pulse would result. This was most easily done by making the trigger capacitor, C_p , equal in value to the total capacitance of the Marx with all stages in series. This resulted in a cleaner and shorter current pulse, shown in Fig. 3.4b.

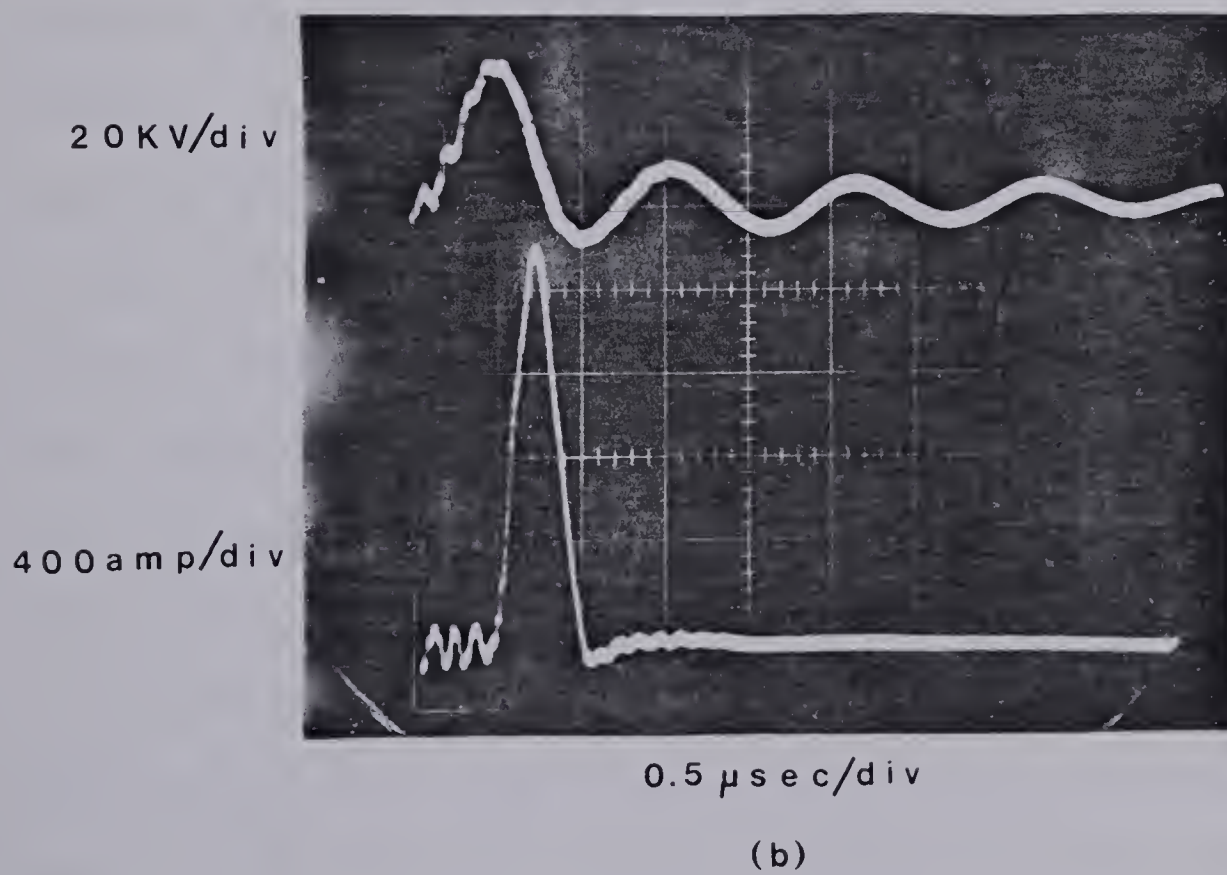
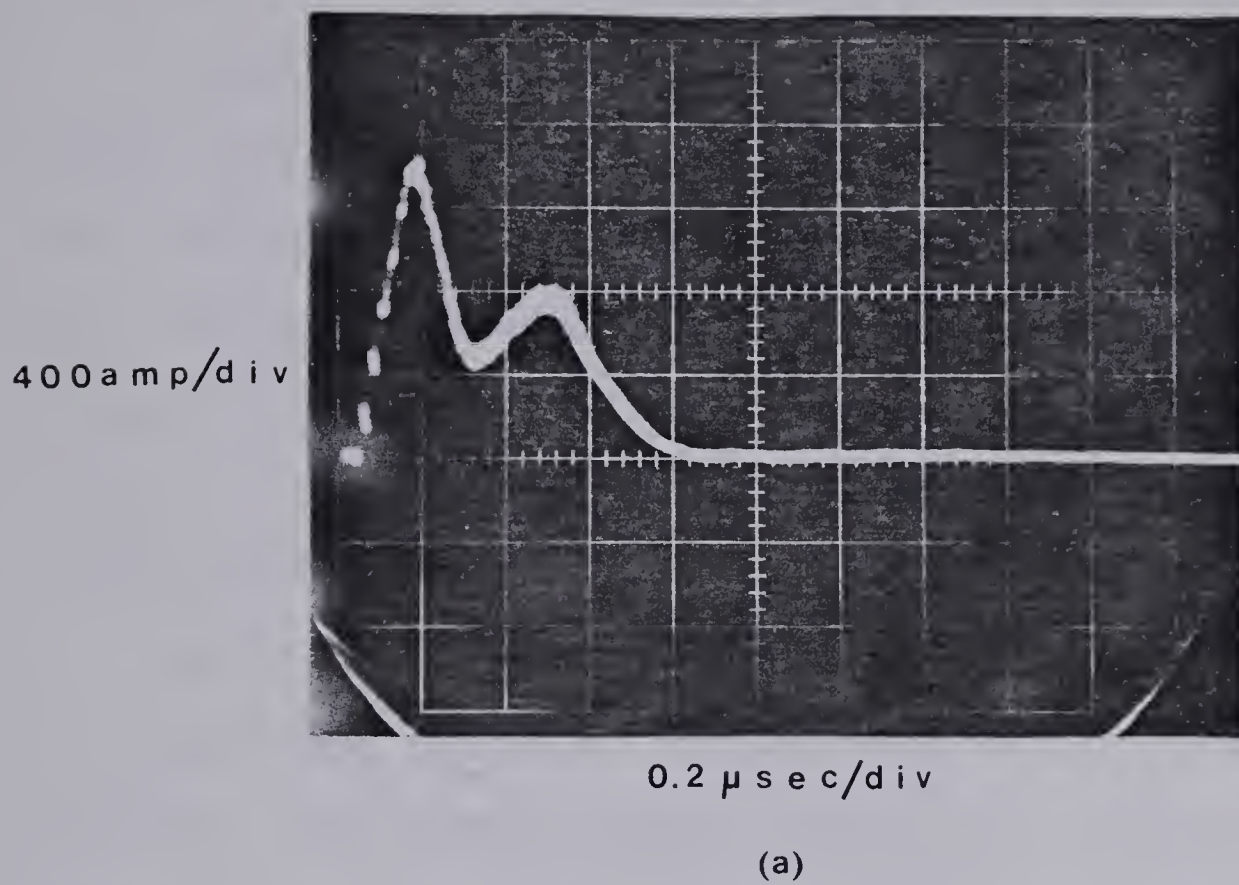


Fig. 3.4 Output Pulses for 10 Stage Marx, 0.1 μ f Per Stage, Using Two Values of C_p . In (a) $C_p = 1750$ pf and in (b) $C_p = 0.01\mu$ f.

Initially low inductance capacitors were constructed for this purpose using sheets of brass separated by glass dielectric. Although they worked well enough to demonstrate the technique they failed quickly due to the glass shattering, either from insufficient dielectric strength, or from mechanical shock caused by rapid charging and discharging. Eventually capacitors were ordered for this purpose from Condenser Products.

Finally, the method of triggering the Marx was found to be important in forming a good discharge. Initially only one gap of the Marx was triggered. The literature (29,30) indicated that this plus the UV coupling between the spark pins would be sufficient for fast switching of the Marx. However the commutation time of the Marx proved to be about 15 μ sec. (Fig. 3.5). This long time delay was detrimental to discharge formation, possibly because it gave the preionization electron density time to recombine. Triggering several Marx gaps resulted in improved discharges and a Marx switching time of less than 100 nsec. For the 10 stage Marx as many as all 10 gaps were triggered but a minimum of 3 triggered gaps was necessary for successful operation. In the final design 5 gaps were triggered. A disadvantage with triggering a number of gaps is that they cannot all be switched to ground. As a result high voltage pulses feed back into them when the Marx switches and it is difficult to build a reliable high repetition rate trigger pulser capable of surviving this. As a result pulser failures were a continual problem. Fig. 3.6 shows the construction of a trigger pin used in the Marx. A pulser unit that used an HY60 thyatron was fairly resistant to damage (Fig. 3.7).

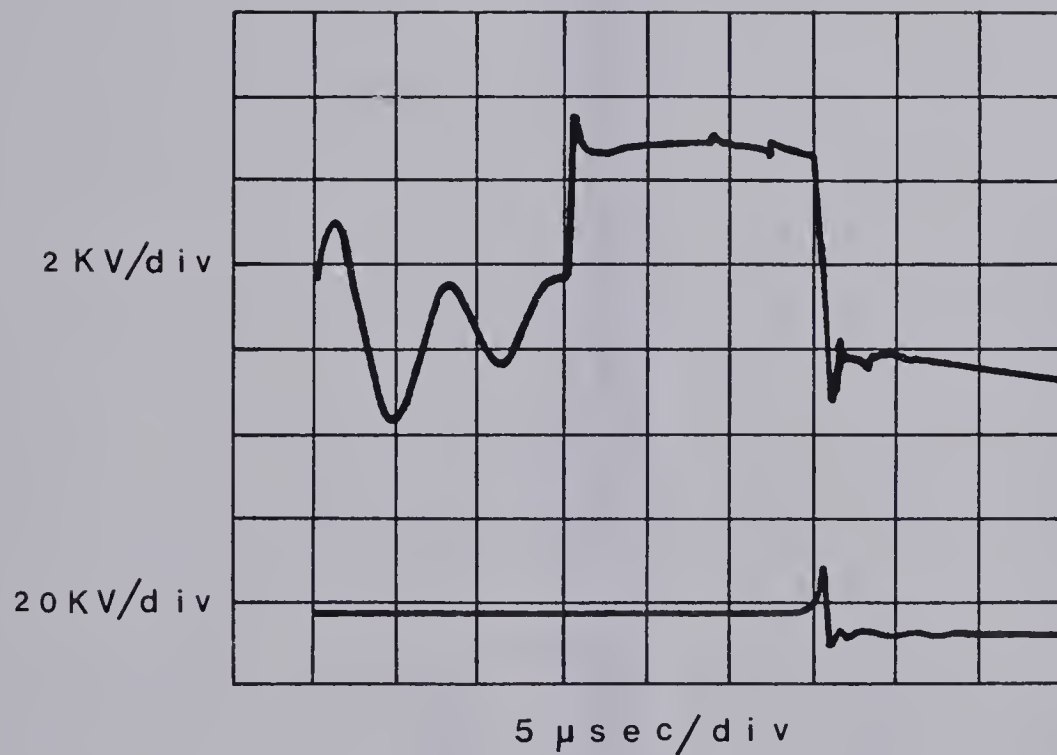


Fig. 3.5 Commutation Delay in the Marx Generator with a Single Trigger Pin.

The upper trace is the voltage at the first Marx pin and the lower trace is the Marx output voltage. These waveforms are for a six stage Marx generator. The first pin switches at the beginning of the square pulse and the output pulse occurs at the end of the square pulse approximately 15 μsec. later.

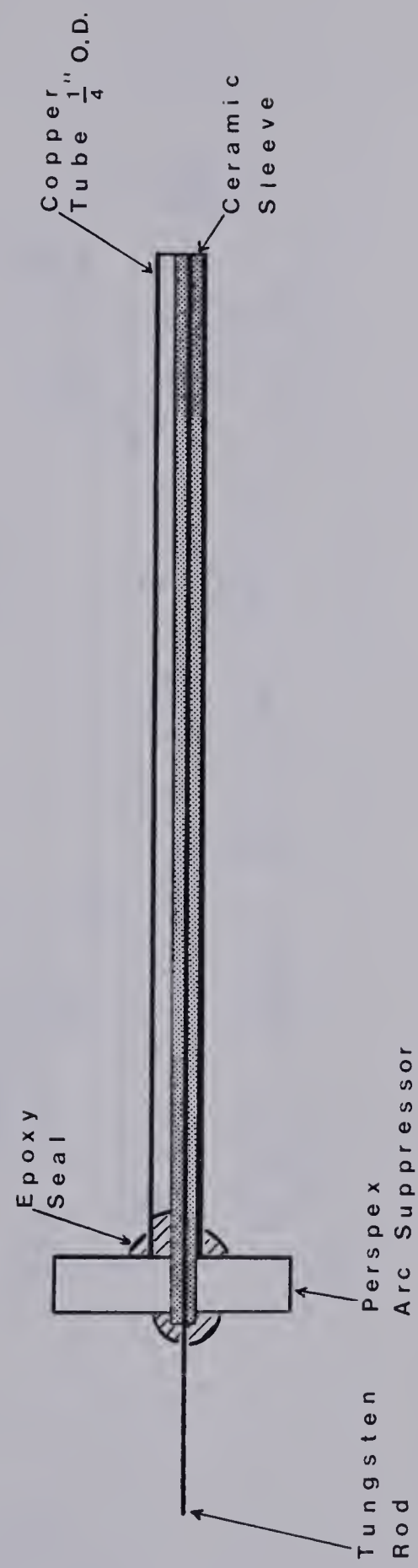


Fig. 3.6 Construction of Triggered Spark Pin.

In a triggered spark gap one of the brass Marx pins is replaced by a triggered spark pin.

For the Marx pins carbon and brass rods were both tried. The brass rods were chosen for the final design because they were more durable and caused less discharge instability than the carbon rods.

3.3 CIRCUIT MODEL

In order to understand the waveform resulting from the Marx generator and peaking capacitor combination a simple circuit model, shown in Fig. 3.8, was devised. The discharge load was represented by a switch in series with a resistor. The Marx generator was modelled by a capacitor, inductor, and switch which represented the Marx spark gaps. C_2 represents the peaking capacitor. Initially C_2 is at 0 volts and C_1 is at voltage V_o . Closing S_1 at $t=0$ is equivalent to the Marx gaps firing and C_2 then charges from C_1 .

Using Laplace transforms voltage and current waveforms can be solved for this model. The initial conditions at $t=0$ are shown in Fig. 3.9a, and the circuit equation is

$$\frac{V_o}{s} = I \left(\frac{1}{sC_1} + sL + \frac{1}{sC_2} \right)$$

or

$$I = \frac{\frac{V_o}{L}}{s^2 + \frac{1}{L} \left[\frac{C_2 + C_1}{C_1 C_2} \right]}$$

The inverse transform, from tables, is

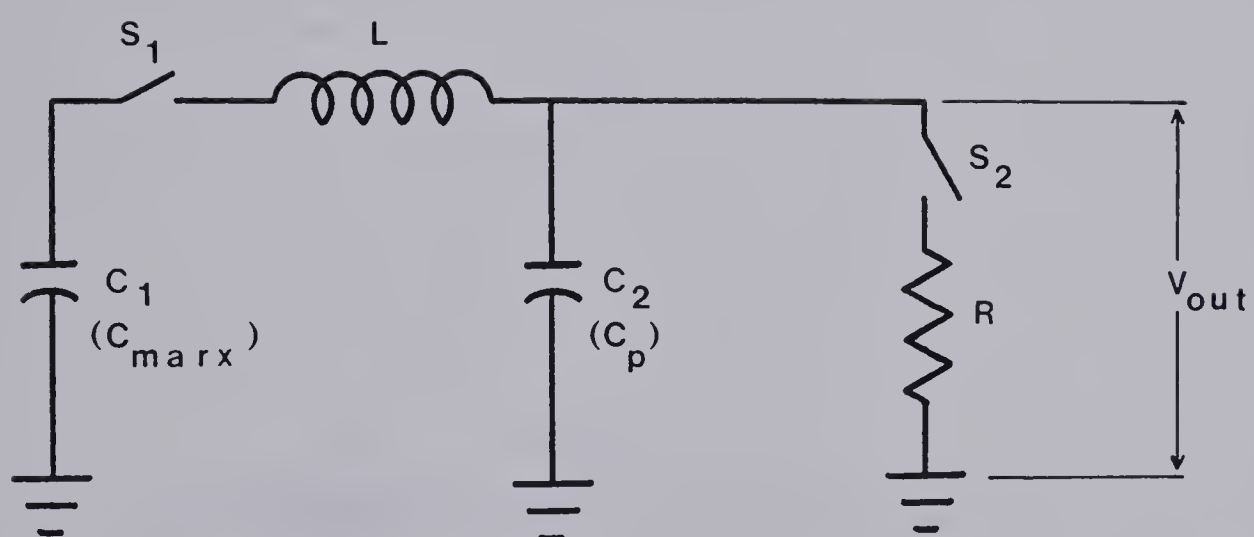
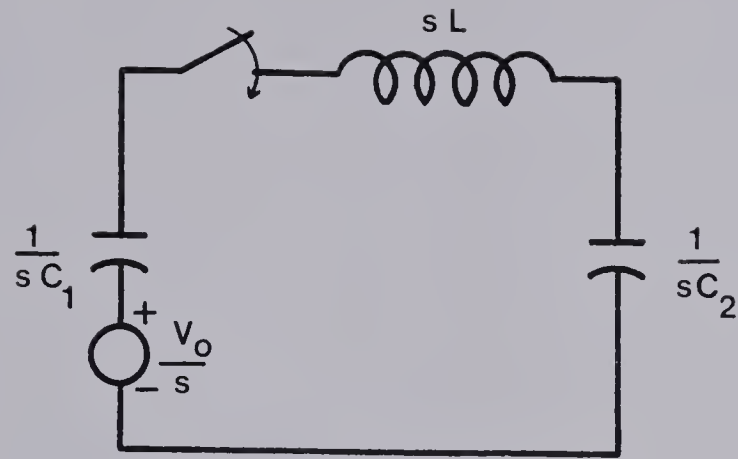
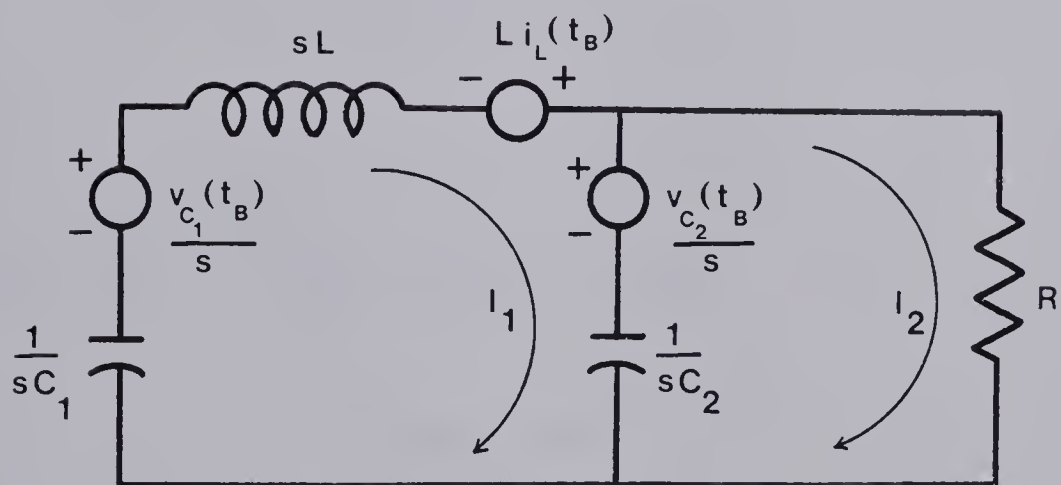


Fig. 3.8 Circuit Model.



(a)



(b)

Fig. 3.9 Initial Conditions for the Circuit Model of Fig. 3.8

at (a) $t=0$ and (b) $t=t_B$.

$$i(t) = \frac{V_o}{L\omega} \sin \omega t \quad 3.3.1$$

where

$$\omega = \sqrt{\frac{1}{L} \left(\frac{C_2 + C_1}{C_2 C_1} \right)}$$

Also

$$\begin{aligned} v_2(t) &= \frac{1}{C_2} \int_0^t i(t) dt + \cancel{v(o)}_o \\ &= \frac{1}{C_2} \int_0^t \frac{V_o}{L\omega} \sin \omega t dt \\ &= \frac{V_o C_1}{C_2 + C_1} \{1 - \cos \omega t\} \end{aligned} \quad 3.3.2$$

Similarly

$$\begin{aligned} v_1(t) &= \frac{1}{C_1} \int_0^t \frac{V_o}{L\omega} \sin \omega t dt + v(o) \\ &\quad \text{where } v(o) = -V_o \\ &= -\frac{1}{C_1} \frac{V_o}{L\omega^2} \cos \omega t \Big|_0^t - V_o \\ &= -\left\{ \frac{V_o C_1}{C_1 + C_2} + \frac{V_o C_2}{C_1 + C_2} \cos \omega t \right\} \end{aligned} \quad 3.3.3$$

The negative sign comes from the direction around the loop for which voltage drops are taken to be positive.

At the time of breakdown, t_B , switch S_2 closes. This gives a new circuit, shown in Fig. 3.9b, with the following initial conditions.

$$v_{c_2}(t_B) = \frac{V_o C_1}{C_1 + C_2} \{1 - \cos \omega t_B\}$$

$$i_L(t_B) = \frac{V_o}{L\omega} \sin \omega t_B \quad 3.3.4$$

$$v_{c_1}(t_B) = \left\{ \frac{V_o C_1}{C_1 + C_2} + \frac{V_o C_2}{C_1 + C_2} \right\} \cos \omega t_B$$

Taking t_B to be $t=0$ for the new circuit gives two loop equations.

$$\frac{I_2}{sC_2} + \frac{v_{c_1}(o)}{s} - sLI_1 + Li_L(o) - \frac{v_{c_2}(o)}{s} - \frac{I_1}{sC_2} - \frac{I_1}{sC_1} = 0$$

or

$$I_1 \left(sL + \frac{1}{s} \left[\frac{C_1 + C_2}{C_1 C_2} \right] \right) = \frac{I_2}{sC_2} + \frac{v_{c_1}(o) - v_{c_2}(o)}{s} + Li_L(o) \quad 3.3.5$$

and

$$\frac{v_{c_2}(o)}{s} - I_2 R - \frac{I_2}{sC_2} + \frac{I_1}{sC_2} = 0$$

or

$$I_1 = I_2 (sC_2 R + 1) - C_2 v_{c_2}(o) \quad 3.3.6$$

Finally, combining 3.3.5 and 3.3.6 gives

$$I_2 = \frac{\frac{C_2 v_{c_2}(0) + C_1 v_{c_1}(0)}{C_1 C_2 R L} + \frac{s i_L(0)}{C_2 R} + \frac{s^2 v_{c_2}(0)}{R}}{s^3 + \frac{s^2}{C_2 R} + \frac{s(C_1 + C_2)}{C_1 C_2 L} + \frac{1}{C_1 C_2 R L}} \quad 3.3.7$$

The solution $i_2(t)$ is the inverse transform of this expression.

Since the denominator is a cubic equation there are four possible solutions, depending on its roots. If the roots are real and unequal the solution will have the form $i(t) = Ae^{-\alpha t} + Be^{-\beta t} + Ce^{-\gamma t}$ where $-\alpha, -\beta, -\gamma$ are the roots of the equation. If the roots are real and two are equal the solution will have the form $i(t) = Ae^{-\alpha t} + (Bt + C)e^{-\beta t}$. If the roots are real and all three are equal the solution will have the form $i(t) = (At^2 + Bt + C)e^{-\alpha t}$. Finally if one root is real and two complex conjugates, the solution has the form $i(t) = Ae^{-\gamma t} + Be^{-\alpha t} \cos(\beta t - \psi)$ where the roots are $-\gamma, -\alpha - \beta j, -\alpha + \beta j$.

Of these possibilities only the last one can give a shape similar to the observed waveform. Initially then, the voltage across the electrodes rises according to eqn. 3.3.2

$$v_2(t) = \frac{V_o C_1}{C_2 + C_1} \{1 - \cos \omega t\}$$

until the breakdown voltage is reached. Note that V_b can be higher than V_o , the initial Marx voltage. If $C_2 \ll C_1$ breakdown will still occur for V_b almost as high as $2V_o$. When breakdown occurs the discharge voltage has the form

$$v(t) = Ri(t) = Ae^{-\gamma t} + Be^{-\alpha t} \cos(\beta t - \psi) \quad 3.3.8$$

So the initial spike is due to the rapid discharge of the peaking capacitor, followed by the slower discharge of the residual charge left in the Marx generator.

Eqn. 3.3.7 has the form

$$I_2 = \frac{N_2(s)}{(s+\gamma)[(s+\alpha)^2 + \beta^2]}$$

$$\text{where } N_2(s) = a_2 s^2 + a_1 s + a_0$$

and the denominator is a cubic equation with roots $-\gamma$, $-\alpha - \beta j$, $-\alpha + \beta j$. The inverse transform of this equation is (ref. 31).

$$i_2(t) = \frac{a_0 - a_1 \gamma + a_2 \gamma^2}{(\alpha - \gamma)^2 + \beta^2} e^{-\gamma t} + \frac{1}{\beta} \sqrt{\frac{(\underline{1})^2 + (\underline{2})^2}{(\alpha - \gamma)^2 + \beta^2}} e^{-\alpha t} \cos(\beta t - \psi)$$

where

$$\psi = \tan^{-1} \frac{(\underline{1})}{(\underline{2})} + \tan^{-1} \frac{\beta}{\gamma - \alpha}$$

and

$$(\underline{1}) = \text{real part of } N_2(s) \Big|_{s=-\alpha+j\beta}$$

$$(\underline{2}) = \text{imaginary part of } N_2(s) \Big|_{s=-\alpha+j\beta}$$

A small computer program was written to evaluate the roots of the denominator of 3.3.7, calculate the coefficients A, B, γ , α , β and ψ , and then to calculate the voltage across the load resistor. Typical waveforms are shown in Fig. 3.10.

Although qualitatively this model offers insight into the discharge waveform the quantitative agreement is poor. The main points of disagreement are that the model predicts an initial current spike that is much too short, and current values that are too high.

A better model is suggested in Fig. 3.11. The Laplace transform for $i_2(t)$ is

$$I_2(s) = \frac{s^2 v_{c_p}(o)}{L_p} + s \left(\frac{R_m v_{c_p}(o)}{L_m L_p} + \frac{i_m(o)}{C_p L_p} \right) + \frac{v_{c_p}(o)}{C_m L_m L_p} - \frac{v_{c_m}(o)}{C_p L_m L_p} \quad 3.3.9$$

$$s^4 + As^3 + Bs^2 + Ds + F$$

$$\text{where } A = \left(\frac{R_m}{L_m} + \frac{R}{L_p} \right)$$

$$B = \frac{RR_m}{L_p L_m} + \left[\frac{C_m + C_p}{C_m C_p} \right] \frac{1}{L_m} + \frac{1}{L_p C_p}$$

$$D = \frac{R}{L_m} \left[\frac{C_m + C_p}{C_m C_p} \right] \frac{1}{L_p} + \frac{R_m}{L_p C_p L_m}$$

$$F = \frac{1}{L_p L_m C_m C_p}$$

and $v_{c_p}(o)$, $i_m(o)$, and $v_{c_m}(o)$ are initial values when breakdown occurs.

The derivation is identical to that for the simpler model.

Since 3.3.9 has a 4th order eqn. in the denominator it can have 4 roots with imaginary components $-a + \alpha j$, $-a - \alpha j$, $-b + \beta j$, $-b - \beta j$. This would give a solution of the form

$$i_2(t) = Ae^{-at} \cos(\alpha t - \psi) + Be^{-bt} \cos(\beta t - \gamma)$$

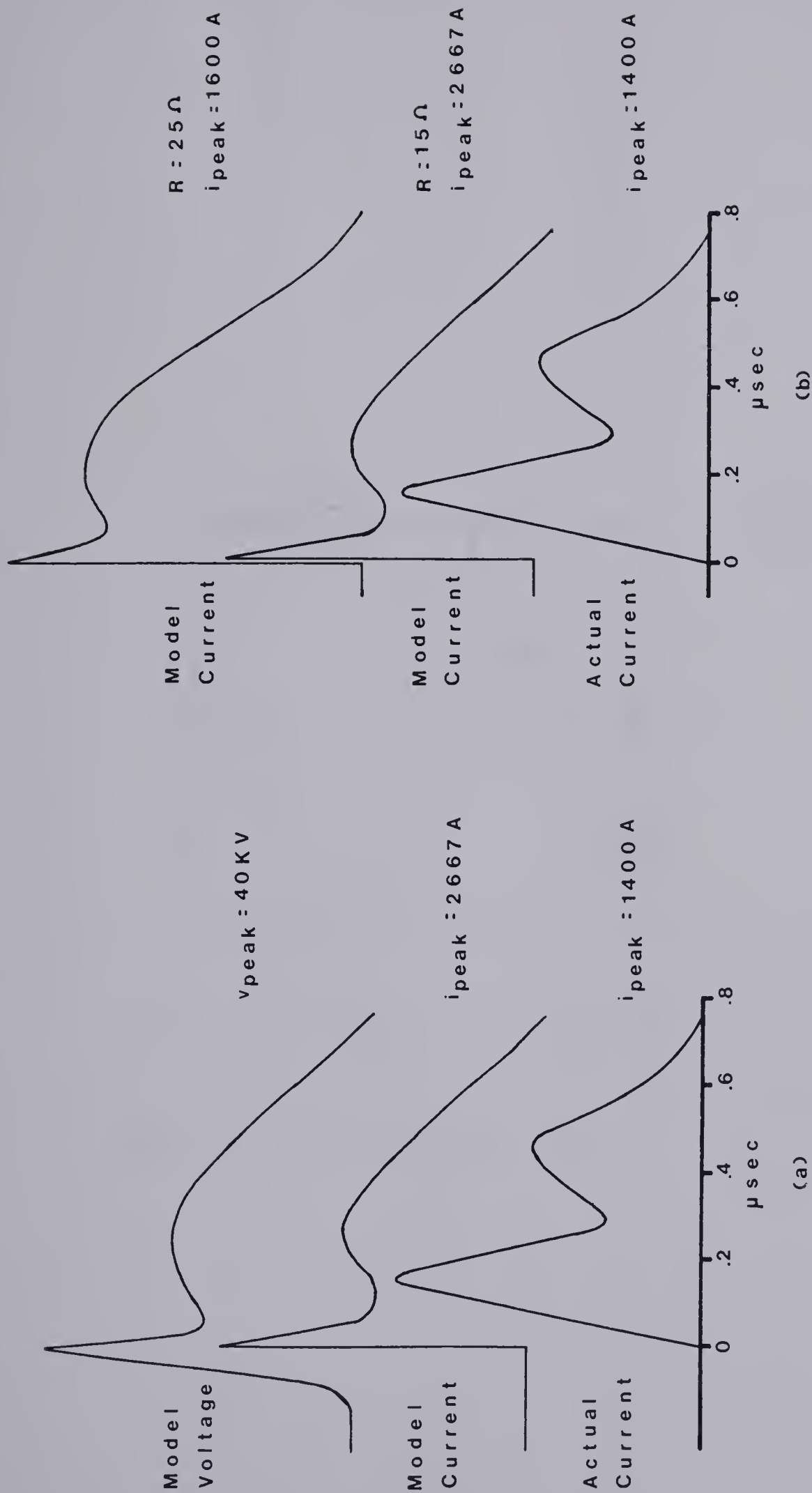
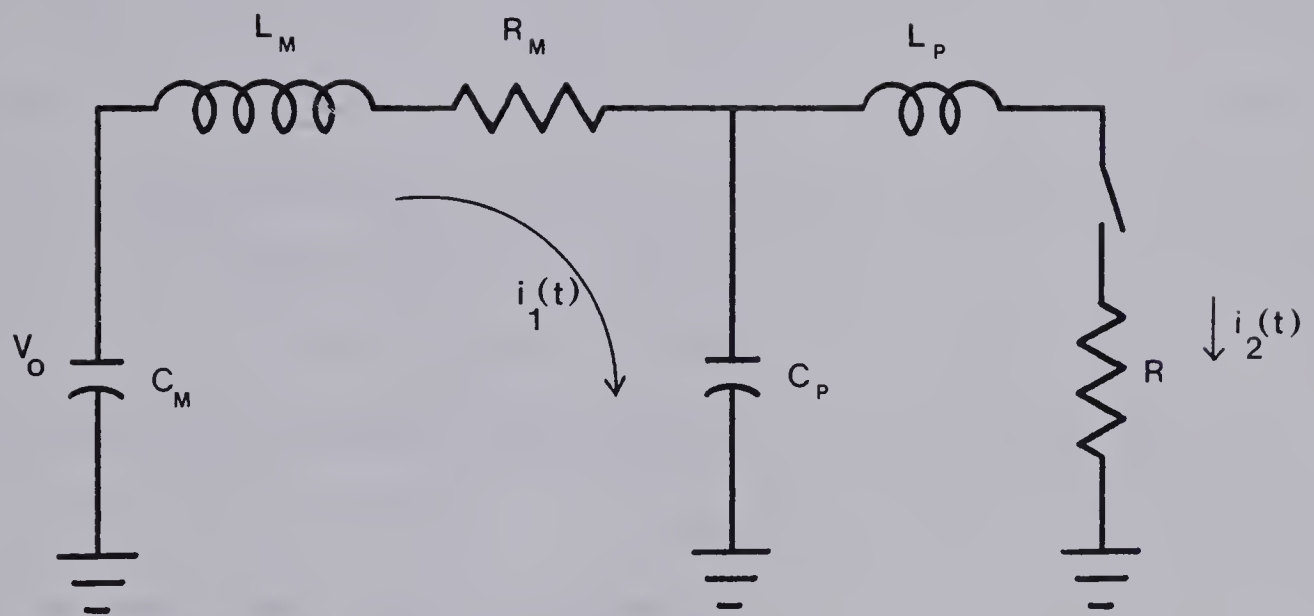


Figure 3.10 Typical Waveforms for the Simple Circuit Model. (a) Shows model voltage, model

current, and an observed current pulse. Model circuit parameters were $V_o = 60\text{KV}$, $V_B = 40\text{KV}$, $L = 6\mu\text{H}$, $C_{\text{max}} = .01\mu\text{F}$, $C_p = 1750\text{pf}$ and $R = 15\Omega$. (b) Shows the effect on the current of varying R .



$$i_2(t) = e^{-at} \cos(\alpha t - \psi) + e^{-bt} \cos(\beta t - \gamma)$$

Fig. 3.11 Improved Circuit Model.

This model is better because it would give the initial sinusoidal current rise which the other model ignores, and the inductance would widen the initial current spike.

3.4 PULSE STRETCHING

For atmospheric pressure gas discharges the Marx generator typically produced current pulse lengths of between 0.5 and 1 μsec duration. Attempts were made to increase this pulse length by adding a series inductor to the circuit (Fig. 3.12a). A small capacitor shunts the inductor to help start the discharge. For pulse lengths longer than 6 to 7 μsec in the 1:1:8 $\text{CO}_2:\text{N}_2:\text{He}$ laser mix arcing occurred. Increasing the He to 90% of the mixture permitted pulse lengths of up to 12 μsec before arcing (Fig. 3.13) but for 12 μsec pulses the discharge was nonuniform.

At reduced gas pressures the discharge is more tolerant of long pulses. At 200 torr with 90% He 18 μsec pulses produce a good discharge and up to 30 μsec pulses could be produced.

For high repetition rate operation at atmospheric pressure short pulse lengths are required for a stable discharge in this system.

Another serious problem occurred which made pulse stretching in this system somewhat impractical. With the circuit configuration in Fig. 3.12a, arcing would occur from the last Marx spark pin to the cathode, effectively bypassing the pulse stretching inductor. This problem was somewhat alleviated by distributing the inductance throughout the Marx circuit as shown in 3.12b.

However when the inductance got large the problem returned with the arcing being to some other Marx pin. This problem is serious because arcing from a Marx pin to the cathode produces a carbon track in the

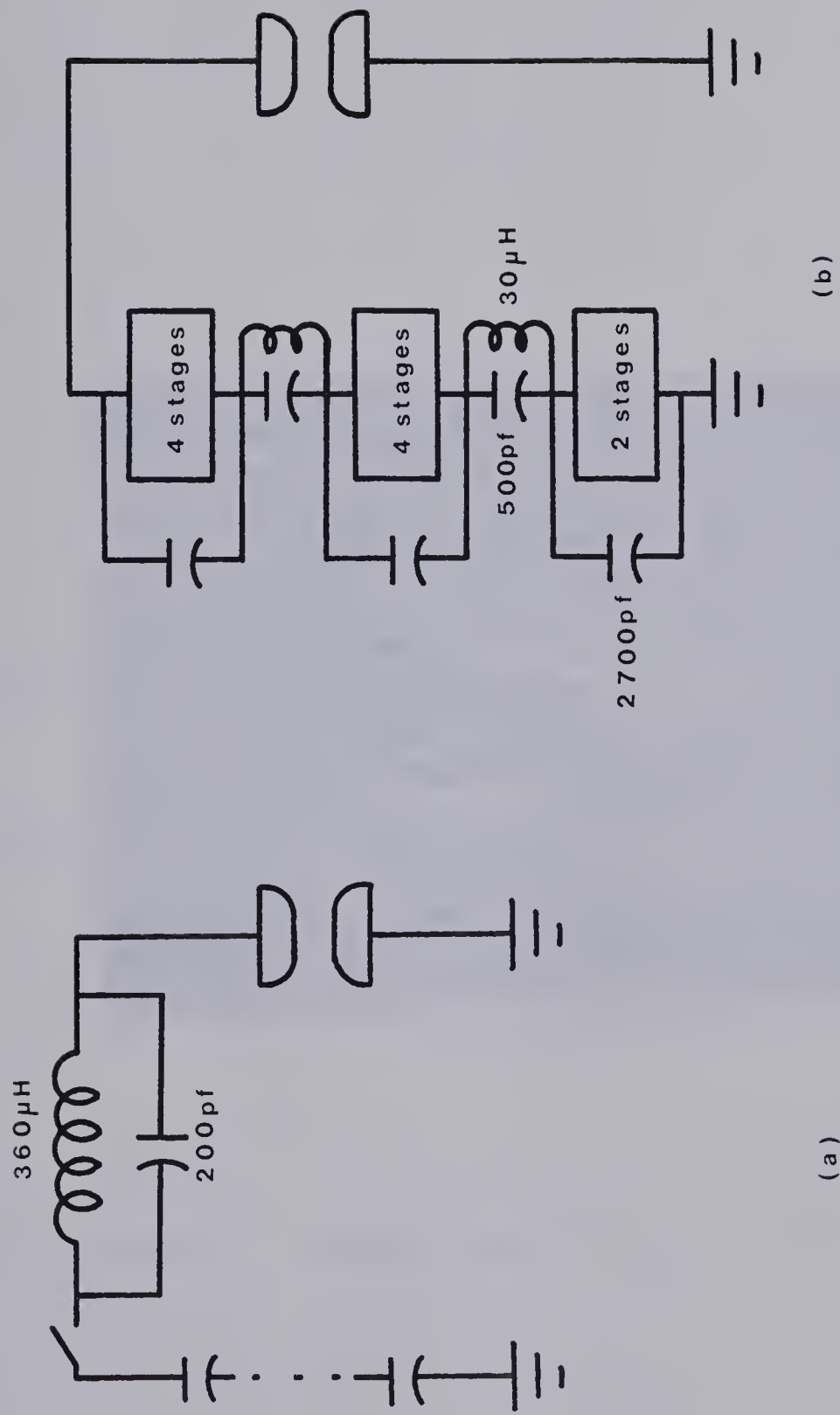


Fig. 3.12 Pulse Stretching Circuit (a) Using an Inductor, (b) With the Inductance Distributed Throughout the Marx.

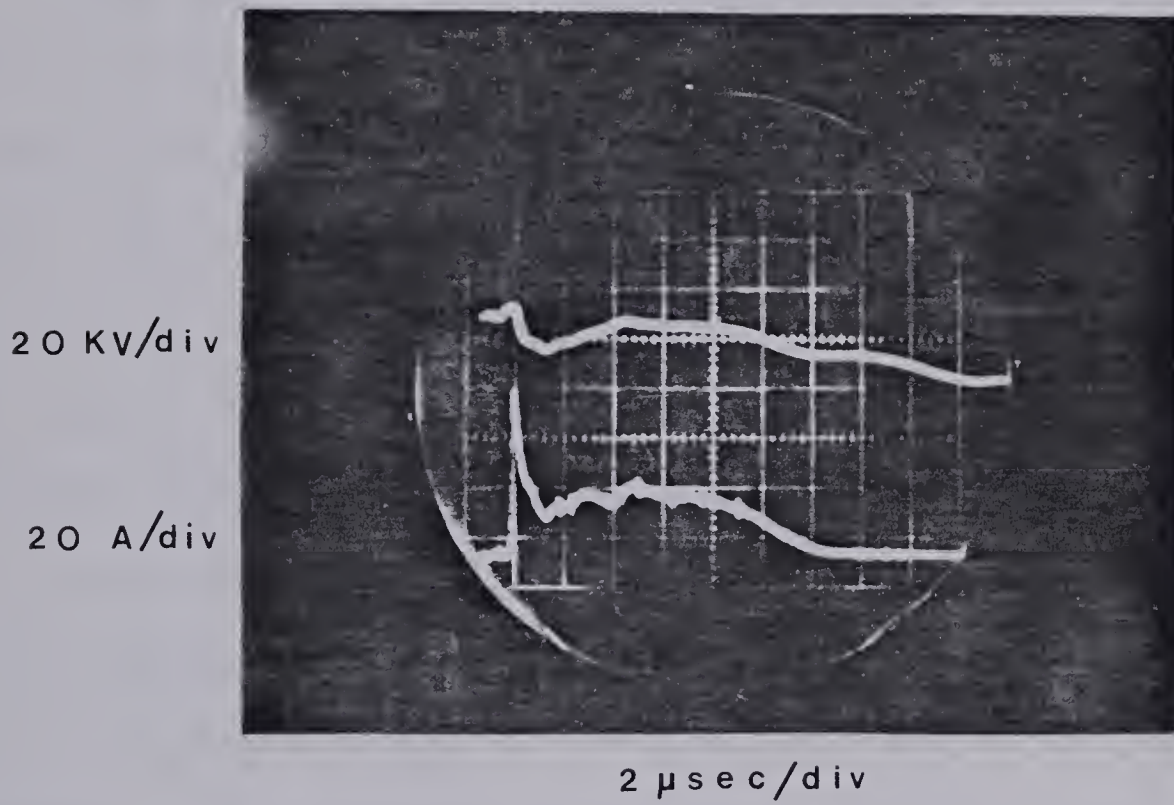


Fig. 3.13 Voltage and Current Waveforms of Stretched Pulse.

perspex insulation that acts as a short circuit and the system is disabled until the carbon track is cleaned off. The only solution to this problem is to replace the perspex with a more damage resistant material, such as ceramic, and to move the spark pins further away from the electrodes, which has the undesirable effect of reducing the intensity of the preionizing ultraviolet radiation.

3.5 ELECTRODES

Also considered with the discharge circuitry are the electrodes. Three electrode materials were tried: carbon, aluminum and copper. The carbon electrodes are very resistant to arcing damage but have two drawbacks. One is that a fine carbon dust is formed which coats the inside of the laser system (including optics). The other problem is the grainy structure of the carbon promotes the formation of many small cathode filaments which are potential arc sites. Aluminum can be polished to a very smooth surface which is less prone to arc but it is easily damaged when arcing does occur and a large arc will burn a pit into the surface. Then to eliminate the arc it is necessary to remove and repolish the electrode. Copper seems to be the best choice of the three. It can be polished to a smooth surface, is less prone to arc than carbon, and is more resistant to arcing damage than aluminum.

Copper was finally chosen as the electrode material for this system. The electrodes for this experiment were formed by plating copper over an aluminum electrode.

3.6 REPETITION RATE

One goal of this project was to see how high a repetition rate could be attained with this discharge configuration. Although repetition

rates achieved were high by ordinary TEA laser standards they were lower than expected from the clearing time of gas between the electrodes. The discharge dimension in the direction of flow is 5 cm. and the flow velocity is 100 m/sec. So this region should be swept clear in 0.5 msec. implying a maximum repetition rate of 2000 Hz. Although this was achieved in He, observed repetition rates were considerably lower in the laser mixtures. Typical maximum repetition rates are given in table 3.2. In the laser gas mixtures the maximum repetition rate was limited by discharge arcing but in He the maximum repetition rate was limited by the Marx generator spark gaps going into continuous conduction. Since the spark gaps are 5 cm. downstream from the discharge the 2000 Hz repetition rate corresponds to the time it takes ionization to blow from the discharge region to the spark pins, reducing their breakdown voltage, and causing them to go into continuous conduction.

A related problem which occurred at high repetition rates and for pulse stretching experiments was arcing from one of the electrodes to the Marx pins. This arcing took the form of surface tracking along the perspex. When it occurred the system had to be dismantled and the arc cleaned off because it would short out the circuit.

Marx Stages	Energy per Pulse J	Gas Mixture	Maximum Repetition Rate Hz
10	20	Helium 700 torr	2000
7	3	1:1:8 CO ₂ :N ₂ :He 700 torr	500
10	54	70:60:600 CO ₂ :N ₂ :He 730 torr	200

Table 3.2

It was also observed that after several minutes of running, a stable high repetition rate discharge would begin to arc sporadically. This was a good indication that gas poisoning was occurring.

In no case was it possible to reliably maintain a high repetition rate for long periods. For instance, a typical run in a 700 torr laser mix for a 10 stage Marx with .3 μf per stage was as follows. 286 pps was maintained for 40 seconds arc free after the initial fill. Then sporadic arcing began in the discharge. After 3 more minutes the run had to be terminated because an electrical feedthrough in the perspex got too hot causing the perspex to melt.

One of the factors limiting attainable repetition rate seemed to be Marx charging time, which was limited by the LC time constant of the circuit to typically 3.5 msec. for a total Marx capacitance of 3 μf . L in this case is the power supply inductance and from the time constant is calculated to be approximately 1.7 H. An attempt to pulse faster than this moves the operating region of the Marx from the plateau A to the rising voltage B on the charging waveform (Fig. 3.14). On the rising voltage portion of the waveform it is difficult to get the Marx to operate reliably.

3.7 OPTICS

Three different optical resonators were tested for this system: an unstable resonator, a stable resonator with a germanium output mirror, and a stable resonator with a hole coupled output mirror.

Originally an unstable resonator, shown in Fig. 3.15, was designed using the procedure outlined by Siegman (32). It had a cavity length of 1.2 m and an output coupling of 10%. The mirrors were gold coated beryllium copper, one being concave with a 14.4 m radius of curvature



Fig. 3.14 Typical Marx Generator Charging Waveform.

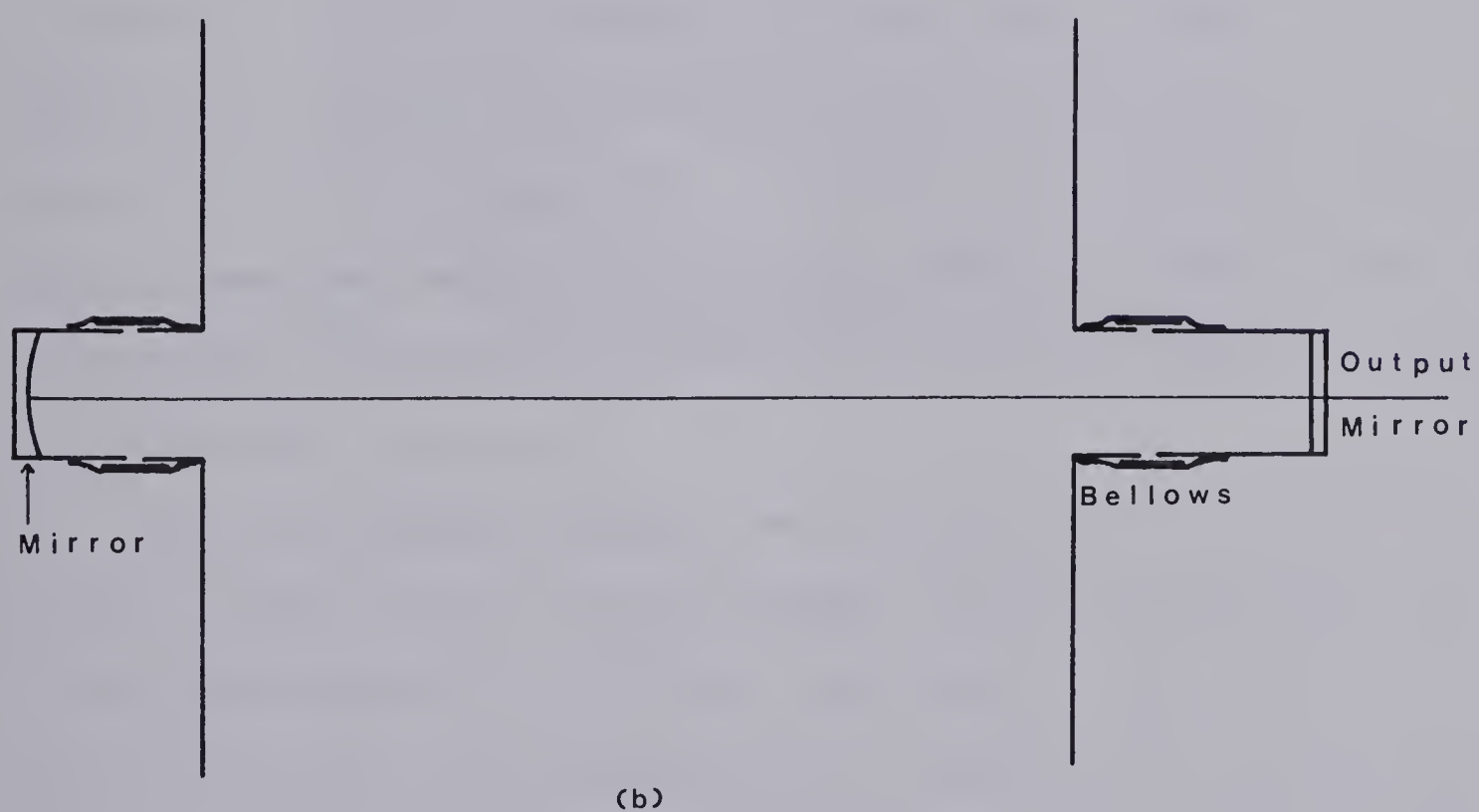
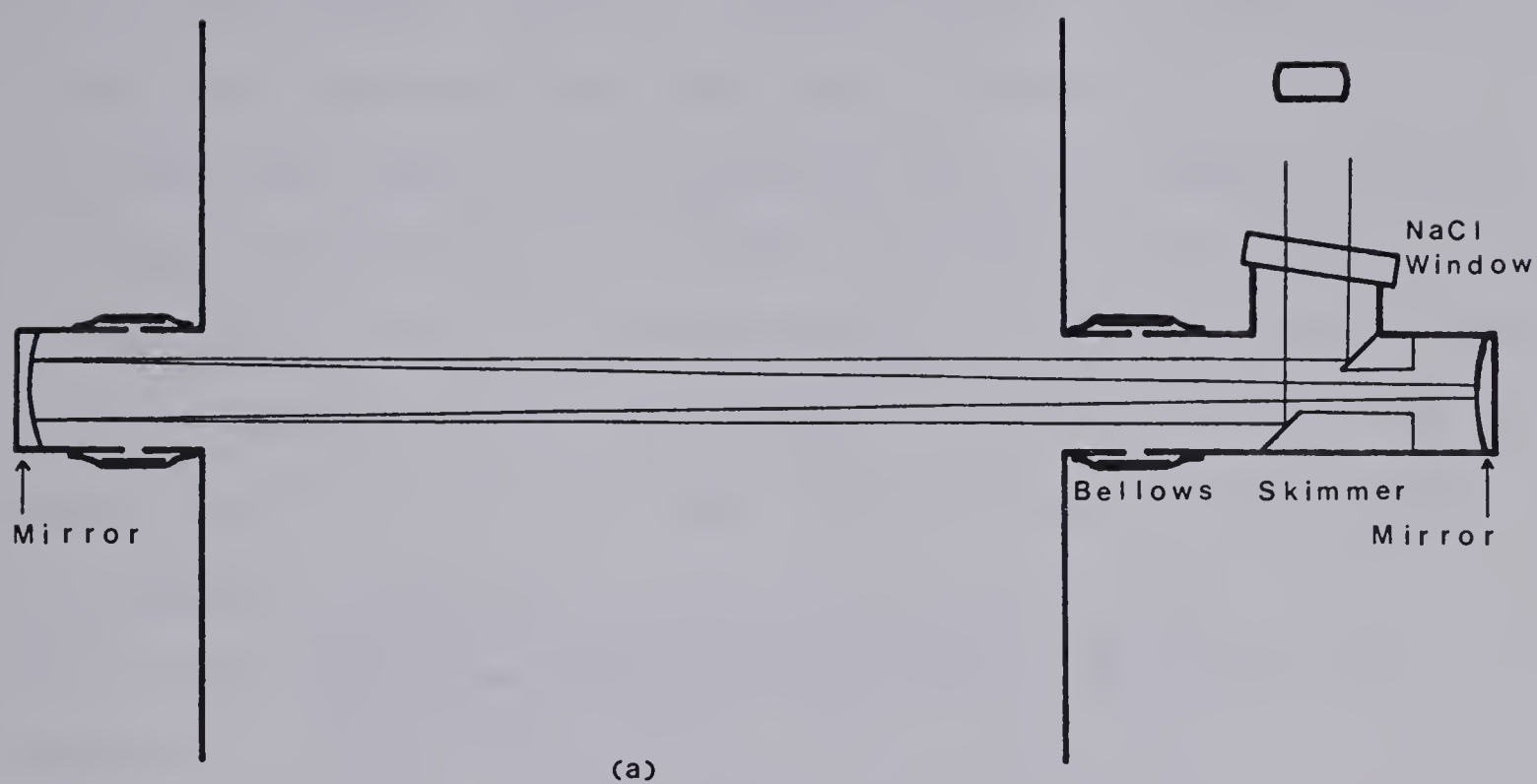


Figure 3.15 Optical System - (a) Unstable resonator and
(b) Stable resonator.

and the other convex with a 12 m radius. The output was coupled out through a salt window by means of a skimmer plate. A typical discharge current pulse and laser output pulse shape are shown in Fig. 3.16. The laser output pulse was observed using a gold doped germanium detector. Two skimmer plates were tried, one with a round hole and one with a rectangular hole. The one with the rectangular output worked much better because it used more of the cavity volume. It had an efficiency of 6% compared to 2% for the round skimmer. Efficiency is a convenient means of comparing the performance of the various optical systems. It is simply optical energy out divided by electrical energy in per pulse, converted to percent.

Bellows were used to attach the unstable resonator directly to the discharge cavity. However vibration transmitted by the bellows made it difficult to maintain alignment of the mirrors. To isolate the optics from the flow system the bellows were removed and NaCl windows were attached to the flow system. This resulted in increased output stability but the losses introduced by the windows in the laser cavity reduced output significantly, dropping the efficiency for the round skimmer from 2% to 0.8%, so bellows were reinstalled.

Since the unstable resonator was very sensitive to vibration a stable resonator was tested for comparison. The stable resonator was constructed using the 14.4 m concave mirror and a hole coupled output mirror. The hole coupled output mirror is simply a flat mirror with an array of small holes through it. The fraction of surface area occupied by the holes is equal to the fractional output coupling required. A hole coupled mirror was used because it can withstand high repetition rates without being damaged. Unfortunately the hole coupled mirror worked very

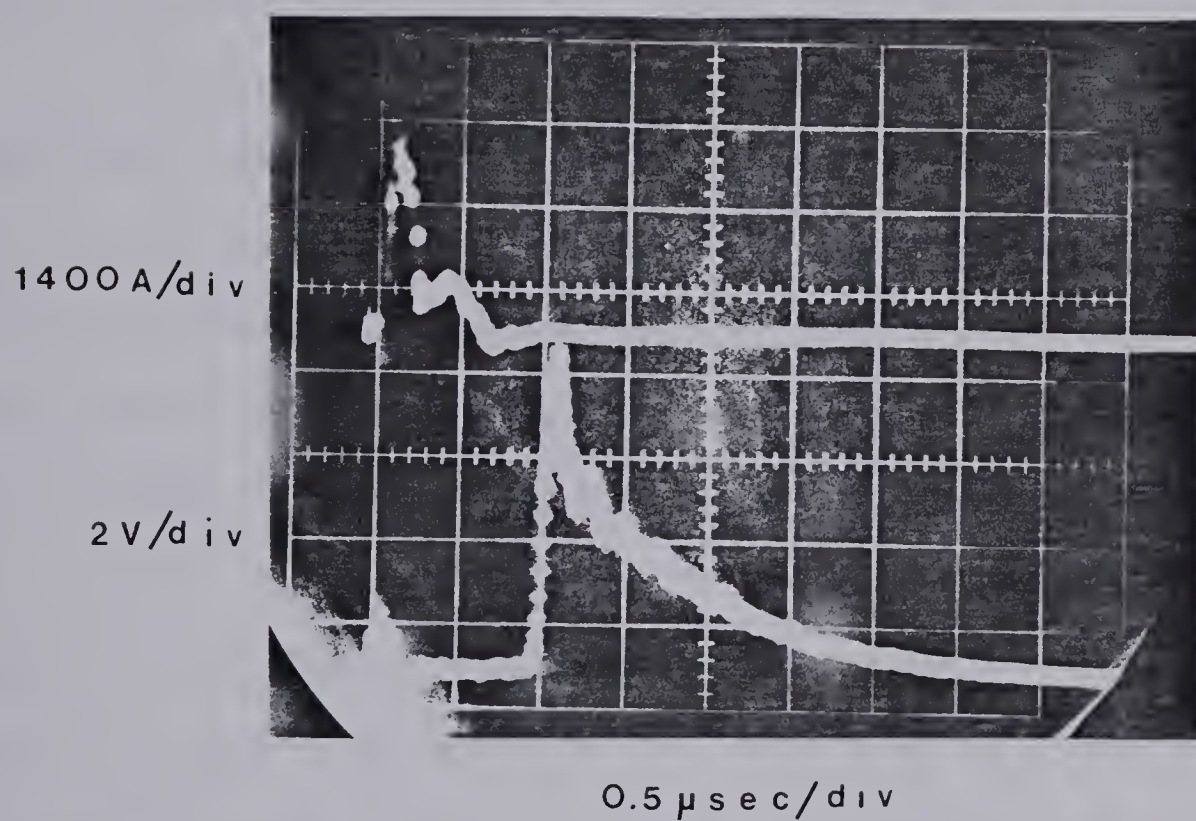


Fig. 3.16 Optical Output. The upper trace is the discharge current waveform and the lower trace is the optical output pulse shape observed with a gold doped germanium detector. The approximate energy of the optical pulse is 0.4 J.

poorly with an efficiency of typically 1% or less. For comparison, replacing the hole coupled mirror with a Germanium flat, which has 30% coupling, raised the efficiency to 3%. But the Germanium flat can be run on a single shot basis only.

The various optical systems are compared in table 3.3. The energy per pulse for the optical systems in the table was measured on a single shot basis using a Gen Tec Joule meter. The results show that the unstable resonator with the 10% output coupled square skimmer was the best system of those tested.

A gas cell beam detector described by Offenberger, Smy and Burnett (33) permitted examination of the energy output at high repetition rates. The cell is filled with a mixture of He at atmospheric pressure and a few torr of an infrared absorbing gas such as propylene. When the laser beam passes through the cell some of the energy is absorbed and produces a shock wave. The shock wave strength is sensed by a piezoelectric probe and is proportional to the energy in the laser pulse. This probe recovers in typically 4 msec compared to .3 sec for the Joulemeter. Using this probe the output of the laser could be monitored at high repetition rates. Fig. 3.17 shows a typical output from the unstable resonator at 100 Hz. The effect of the slow scale mechanical vibration can be seen quite clearly and is responsible for a variation of 100% in the output intensity of the pulses.

The first set of bellows used on this system consisted of tubes cut from rubber gloves and sliding gate valves to seal the bellows off from the system during pump-down and gas changes, because they could not withstand vacuum. Although this system worked it was unsatisfactory because the rubber failed frequently. The main cause of failure was

Type of Resonator	Input Energy J	Output Energy J	Efficiency %
unstable square skimmer 10%	16	1	6
unstable round skimmer 10%	19	.4	2
unstable round skimmer intercavity windows	19	.16	.8
stable germanium flat 30%	45	1.5	3
stable hole coupled 5%	25	.3	1
stable hole coupled 15%	54	.5	.9
stable hole coupled 20%	54	.25	.5
germanium flat low pressure discharge	13	.37	3

Table 3.3

Comparison of performance of the optical systems used on the high
repetition rate laser.

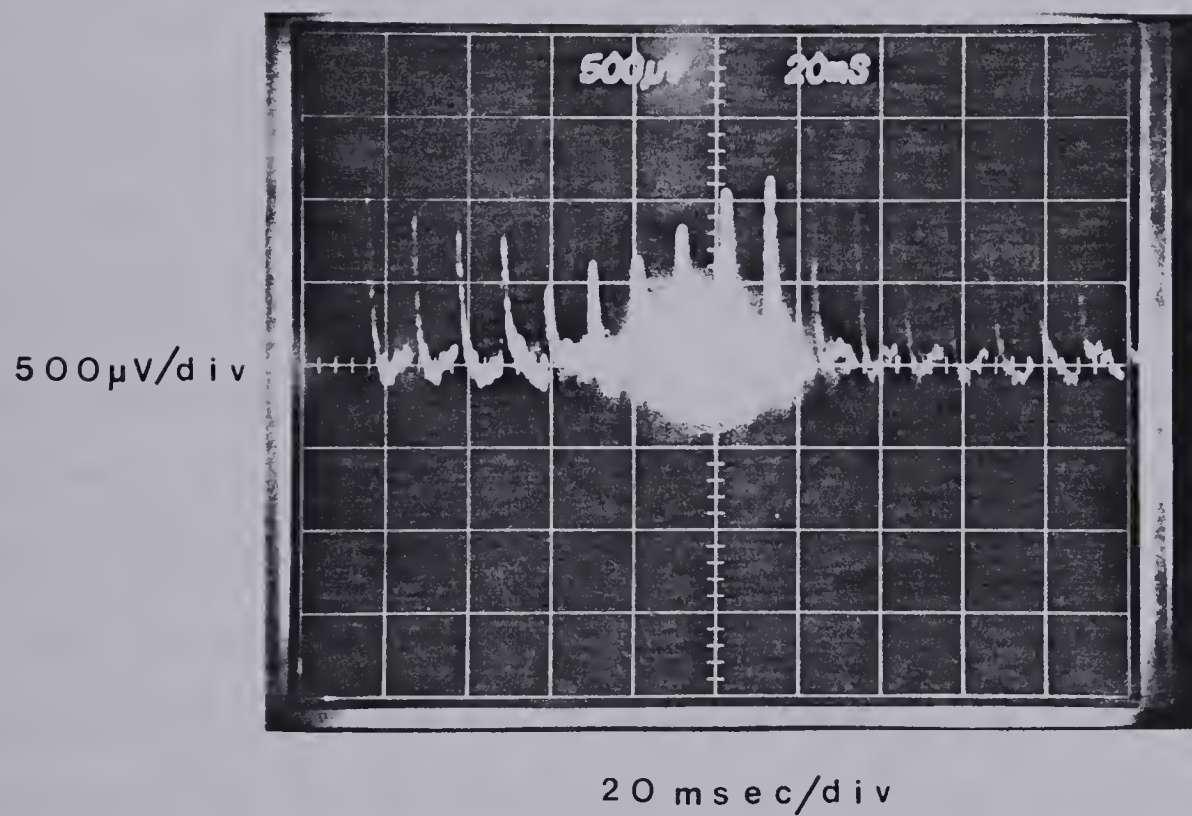


Fig. 3.17 Optical Output Pulses From the Unstable Resonator at 100Hz Repetition Rate.

deterioration of the rubber due to contact with ozone produced by the discharge. But a misaligned laser beam grazing the surface of the rubber and burning a hole was also responsible for some failures.

Because this bellows failed so frequently it was replaced by a bellows suggested by Dr. H.J.J. Seguin which proved to be much more reliable. The new bellows consisted of metal tubes joined by rubber tube. This system was better because it eliminated the problem of the rubber failing and also could withstand vacuum so the gate valves were no longer needed. Both bellows systems are shown in Fig. 3.18.

3.8 GAIN MEASUREMENTS

Small-signal gain of this laser was measured using the apparatus shown in Fig. 3.19a. The output from a small continuous wave CO₂ probe laser was chopped to produce a square wave. The resulting pulse train then made a double pass through the discharge region and was directed into a detector. A gold doped germanium detector was used with a Ge filter in front of it. The filter eliminated the light flash from the discharge, limiting the light detected to a narrow band around 10.6 μm. When the discharge fired a pulse was produced on top of the square wave due to amplification in the discharge region. The gain can be calculated from the ratio of the peak intensity of the gain pulse to the intensity of the square wave using

$$\frac{I}{I_0} = e^{\alpha \ell}$$

or

$$\alpha = \frac{\ln\left(\frac{I}{I_0}\right)}{\ell}$$

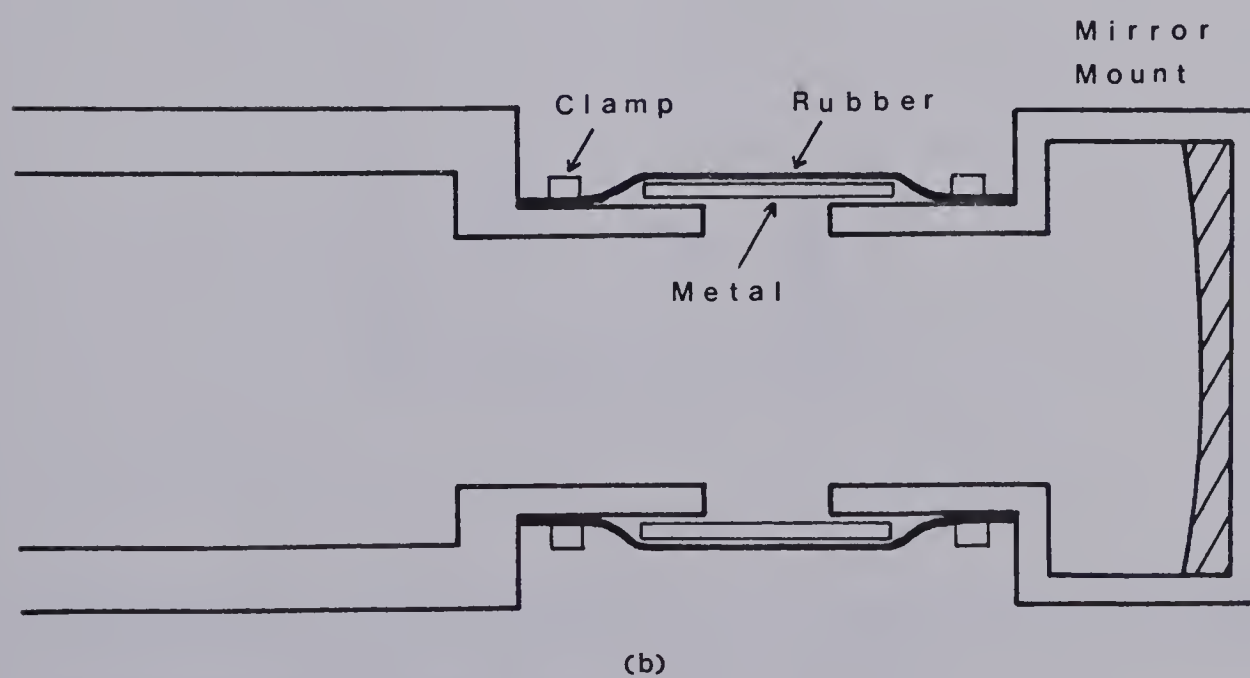
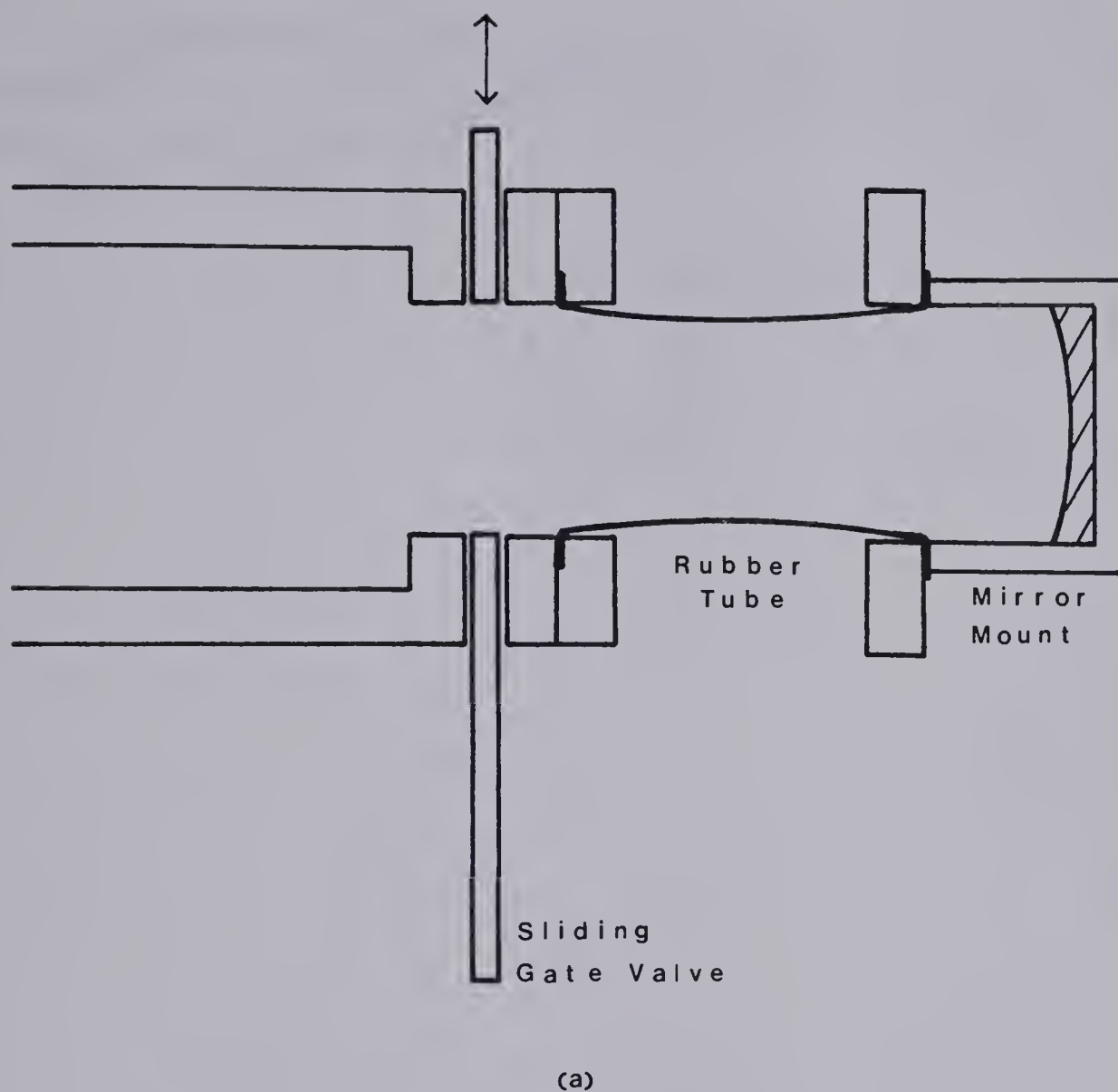
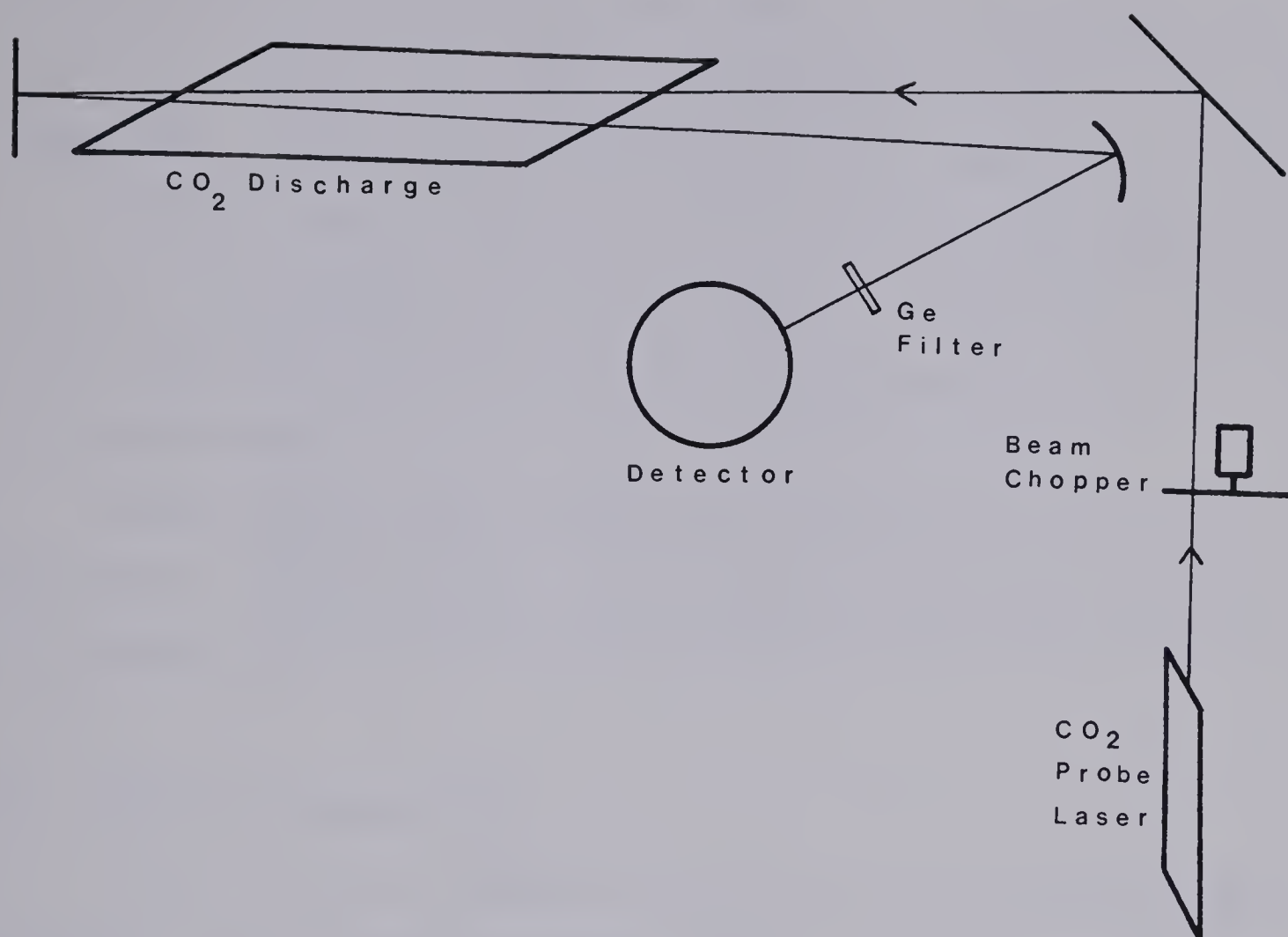
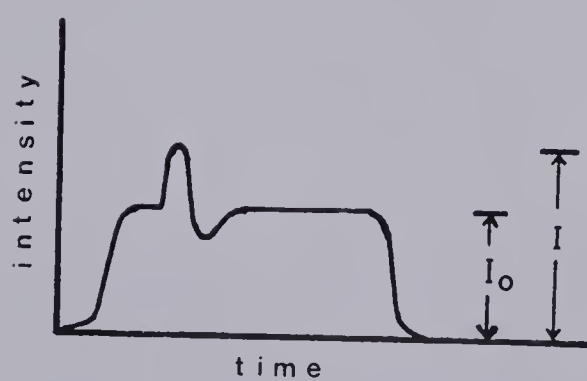


Fig. 3.18 Mirror Bellows Systems. (a) is the rubber tube bellows with a sliding gate valve and (b) is the metal tube bellows.



(a)



(b)

Fig. 3.19 (a) Shows the Apparatus used for the Small-signal Gain Measurements and (b) Shows a Typical Gain Pulse Waveform.

where I_0 is the intensity of the square wave, I is the intensity of the gain pulse, ℓ is the path length in the active medium, and α is the small signal gain. A typical small signal gain pulse is shown in Fig. 3.19b.

A double pass of the probe beam through the discharge served two purposes. It increased the size of the gain signal and made it possible to move the detector away from the laser which produced a lot of electrical noise.

Measured small signal gain was 0.5% to 0.7% per cm. Measurements were made at repetition rates of up to 200 Hz and gain was independent of repetition rate.

3.9 SHOCK WAVE MEASUREMENTS

During the gain measurements of this laser an interesting anomaly accompanied many of the gain pulses. It was a negative swing at the end of the gain pulse. The negative swing was due to discharge induced gas density gradients deflecting the probe beam so that it partially missed the detector. With the blower running the density gradients dissipated in less than 1 msec due to convection but if the blower was not running the gradients had to dissipate by diffusion and took about 300 msec to disappear (Fig. 3.20).

An experiment was devised to study these density perturbations in more detail since if they persist long enough they could degrade the optical quality, and possibly even the discharge uniformity, of subsequent pulses.

A shock wave in a gas produces an index of refraction gradient that deflects light rays passing through the gas according to (ref. 34)

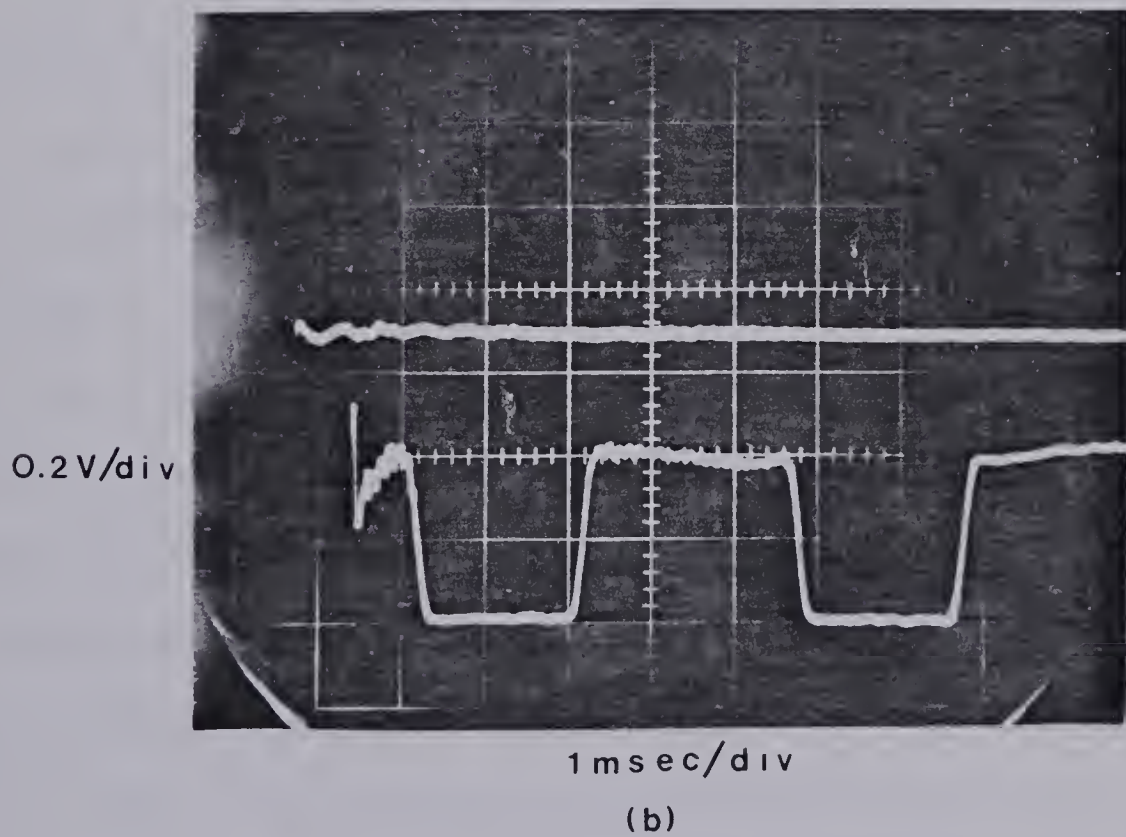
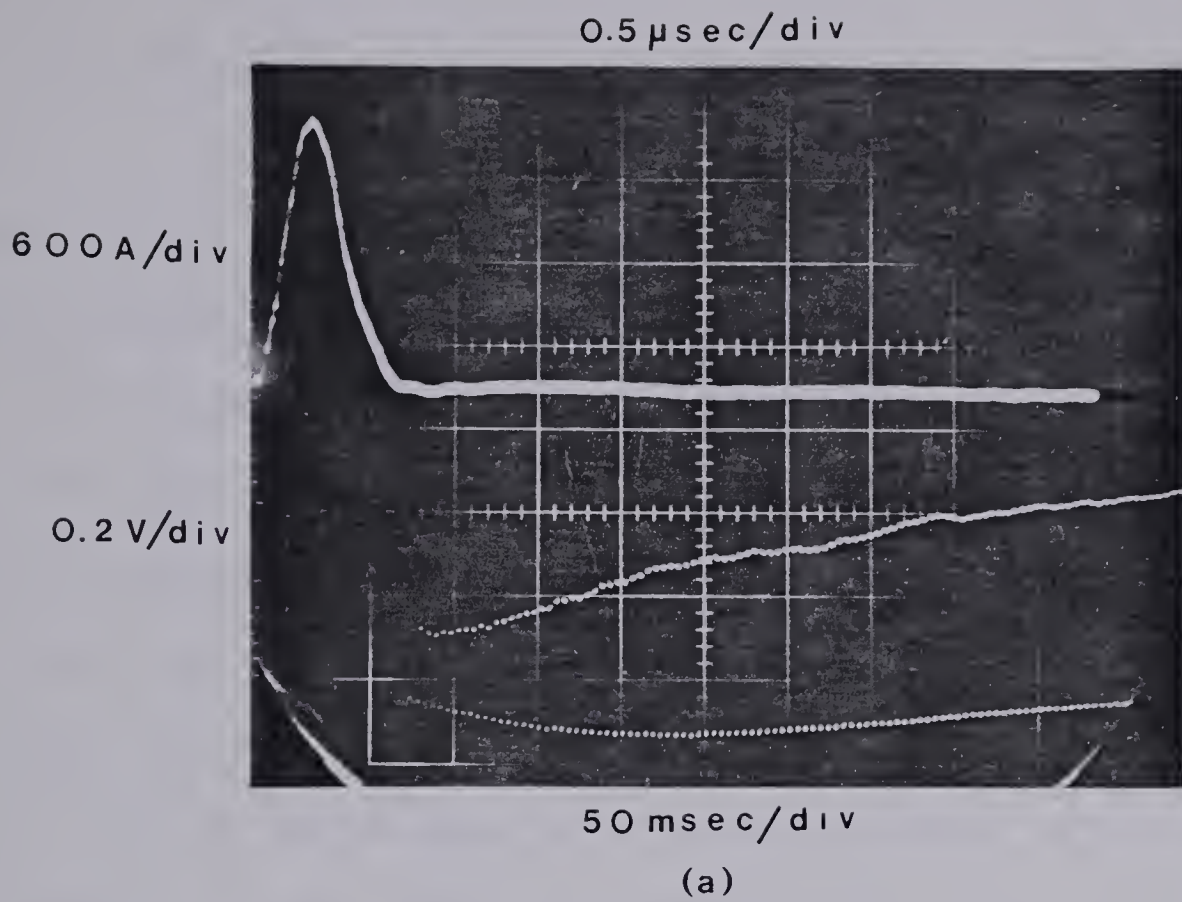


Fig. 3.20 Gas Density Perturbations (a) Without Blower Running and (b) With Blower Running. The upper trace in (a) is a discharge current waveform.

$$\theta = k t \rho_o \frac{d\eta}{dx} \quad 3.9.1$$

where k is the Gladstone Dale constant, t is the thickness (or distance through the gas the beam travels), ρ_o is the ambient gas density, η is the ratio of density at any instant to the original ambient density and θ is the angular deflection of the beam. So, as the gain measurements already indicated, passing a laser beam through the discharge region and monitoring its deflection provides a sensitive means of monitoring discharge produced density gradients. It was found that for this experiment an angular displacement of .3 mrad could easily be detected for a discharge in He gas. Using 3.9.1 this indicates that a density gradient of $1.4 \times 10^{-2}/\text{mm}$ or 1.4% per mm could be detected.

Measurements were made for a He discharge with the apparatus shown in Fig. 3.21. A He-Ne laser beam, after crossing the discharge region is directed past a knife edge, through a red filter, and then to a photovoltaic detector. The red filter blocks the broadband light flash produced by the discharge and only allows light from the He-Ne to reach the detector. The knife edge intercepts half the probe beam and a deflection of the beam toward the edge will reduce the amount of light striking the detector. Similarly a deflection away from the edge will increase the amount of light striking the detector.

Changing the orientation of the knife edge makes it possible to monitor different components of the shock wave. Fig. 3.22 is a cross sectional view of the discharge region showing the points at which shock wave measurements were made. Orienting the knife edge vertically allows monitoring of shock waves travelling in the x direction (horizontal), and orienting it horizontally allows monitoring shock waves travelling

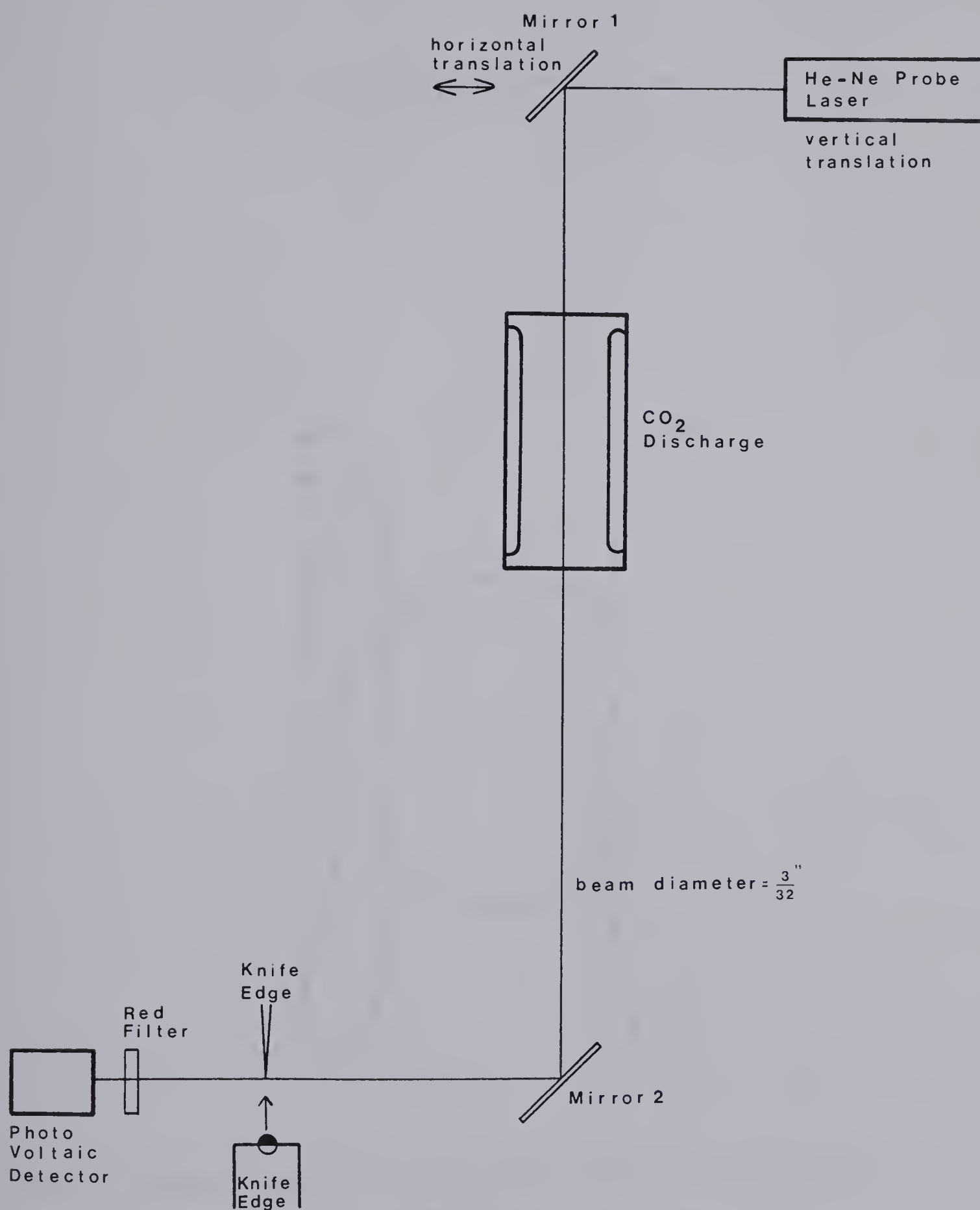


Fig. 3.21 Apparatus for Density Gradient Measurements.

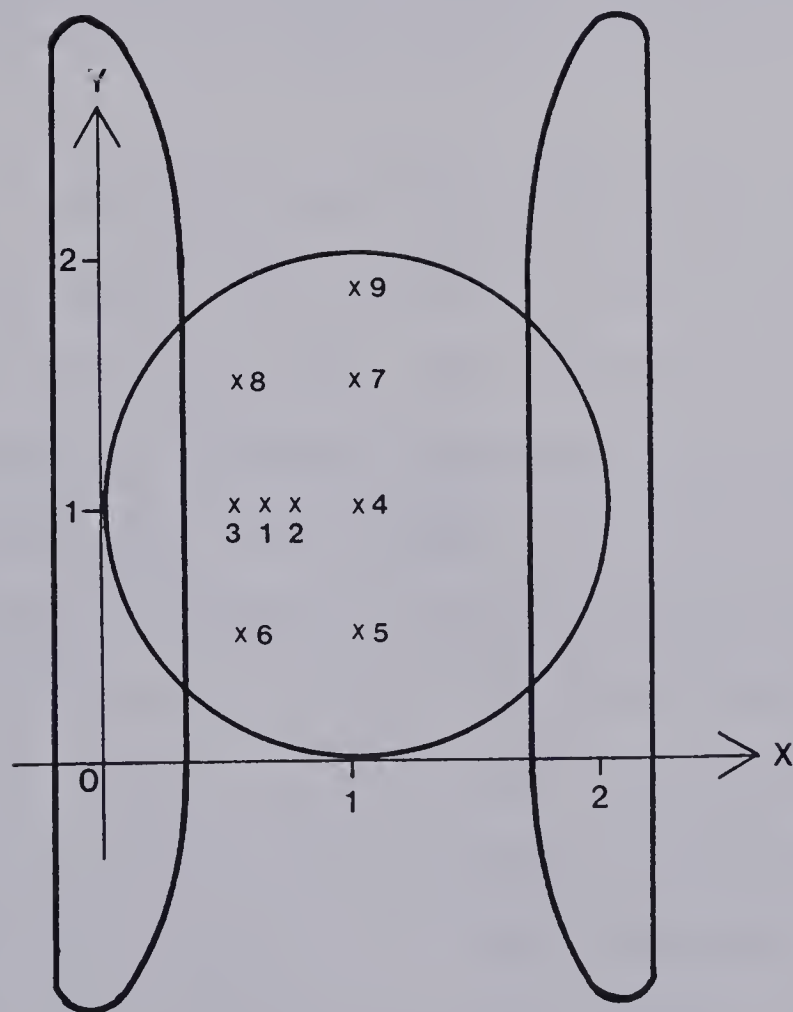


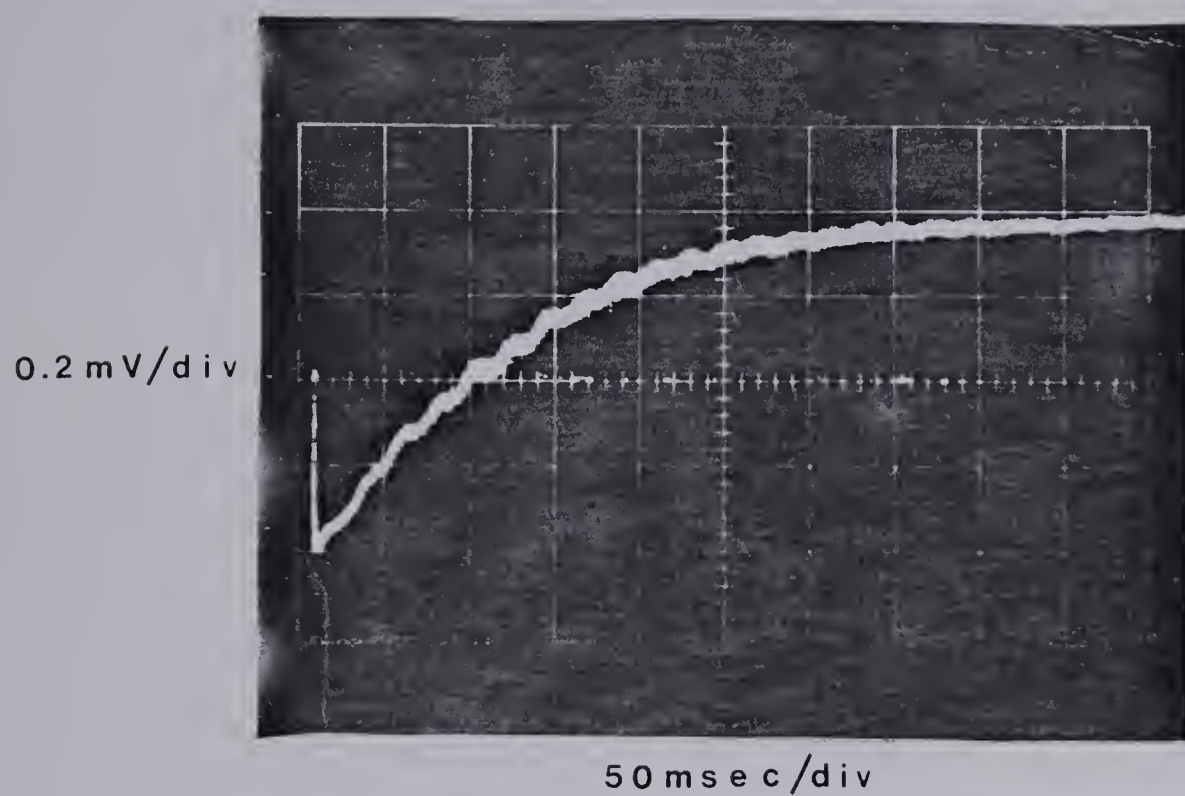
Fig. 3.22 Cross Sectional View of Discharge Region Showing Points at Which Shock Wave Measurements Were Made.

in the y direction (vertical). By moving mirror 1 in the horizontal plane and the He-Ne probe laser in the vertical plane the shock waves could be mapped at various positions in the discharge region.

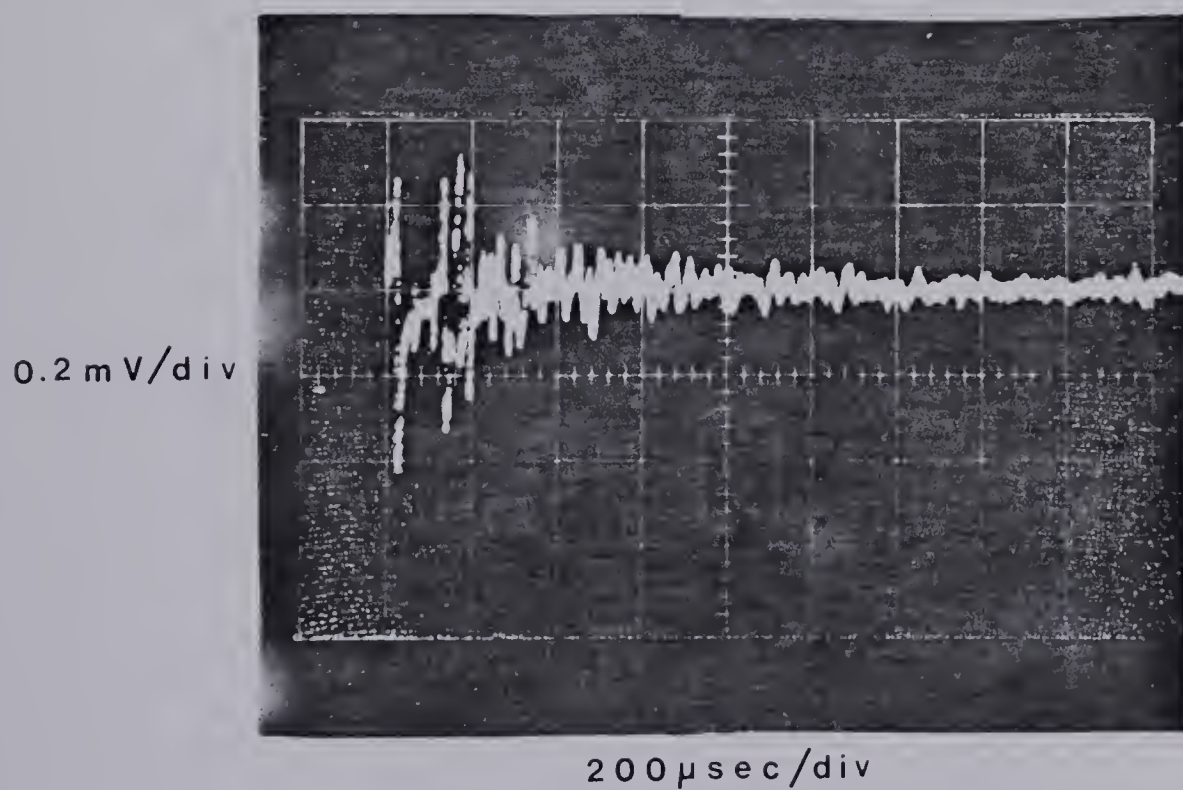
The knife edge and detector were 28 ft away from the discharge chamber. This large displacement allowed resolution of small angular deflections on the scope. A calibration figure was obtained by moving the knife edge across the beam with a micrometer. One scope division, at .2mV per division, corresponded to a deflection of .090 inches, or a sensitivity of 0.3 mrad/div. Since the beam is gaussian and has a circular cross section the actual sensitivity becomes non-linear for large deflections.

Shock waves were observed in both static and flowing gas. A large slowly varying density gradient was observed in static gas which was absent in the flowing gas (Fig. 3.23). The large scale deflection typically has a decay time constant of 150 msec, and is due to the slow diffusion of the heated gas remaining after the discharge. In contrast, with gas flow, the heated gas is quickly removed from the discharge region by convection and the thermal gradient does not appear. The fluctuations which occur in flowing gas are due to shock waves and mostly damp out within 0.5msec.

The peak values of thermal deflection are given in Table 3.4. It can be seen that the largest component of these deflections was in the vertical direction. A plot of the peak values along the central axis (points 5, 4, 7, 9) is shown in Fig. 3.24a. This suggests a density gradient and hence density distribution of the form shown in Fig. 3.24b. Since the gas heating is proportional to the current density through it, the data offers some insight into the uniformity of the discharge. It suggests that the energy was deposited with a gaussian profile rather



(a)



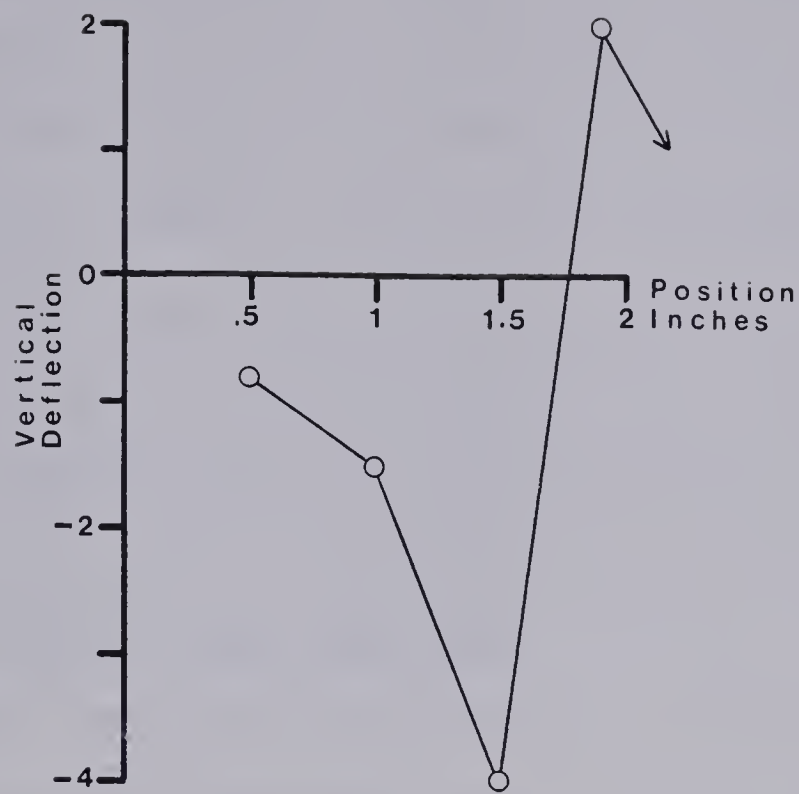
(b)

Fig. 3.23 Detector Voltage (a) Without Gas Flow and (b) With Gas Flow.

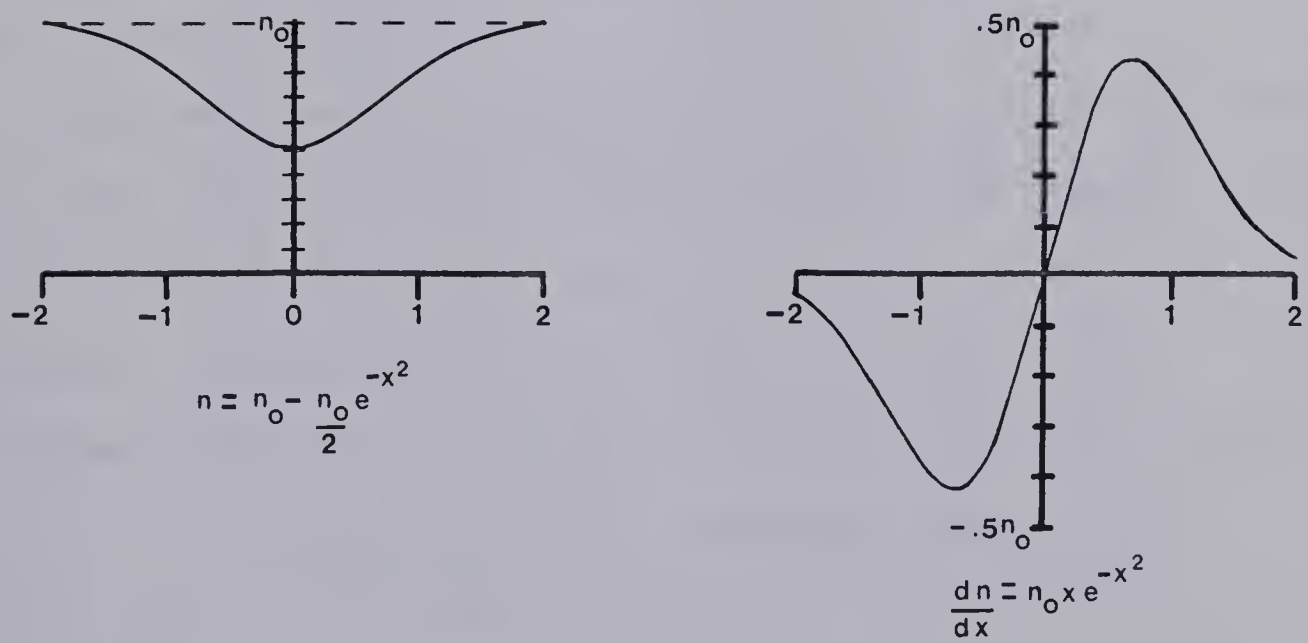
Position #	x inches	y inches	Peak Deflection	
			vertical y division	horizontal x division
1	5/8	1	-1.5	-.25
2	6/8	1	-1.0	-.2
3	4/8	1	-1.5	-.4
4	1	1	-1.5	-0
5	1	1/2	-.4	-0
6	1/2	1/2	-.1	-.4
7	1	1 1/2	-4.0	-.2
8	1/2	1 1/2	-4.8	1.2
9	1	1 7/8	+2	-.3

Table 3.4

Probe Beam Deflection Due to Thermal Density Gradients.



(a)



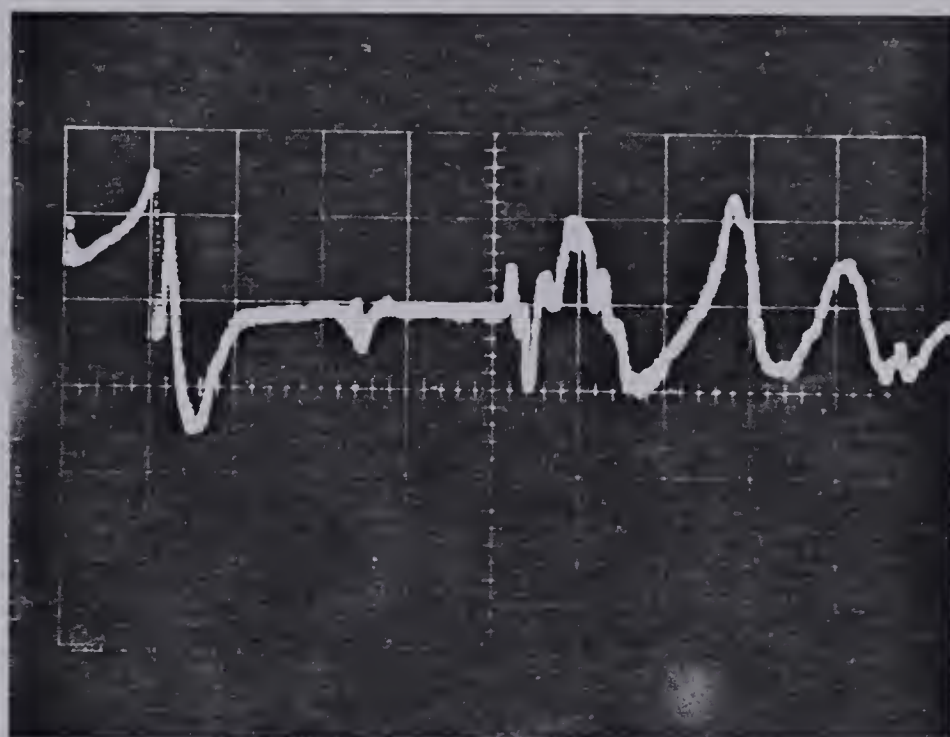
(b)

Fig. 3.24 (a) Deflection of Probe Beam Due to the Thermal Density Gradient and (b) Model Density Gradient dn/dx with Model Density Distribution n .

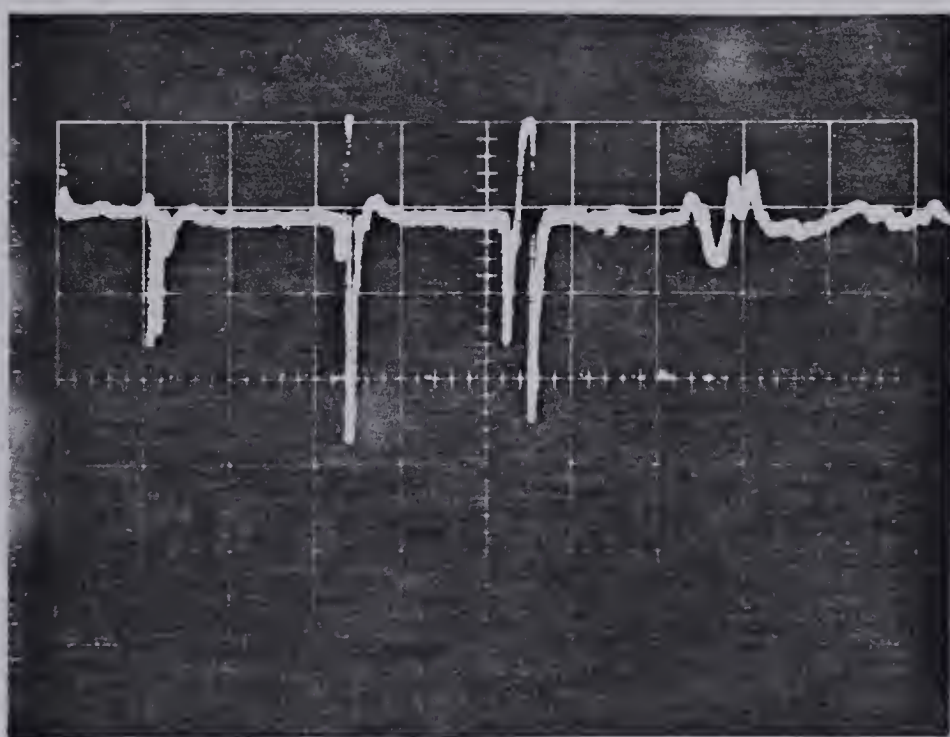
than uniformly through the discharge region. It also shows that the discharge was asymmetrical, with most of the energy being deposited near the top edge. This was verified by the visual observation that the discharge was brightest along the top edge of the electrodes. The non-uniformity is most likely due to the unsymmetrical nature of the pre-ionization, since the spark pins are on one side only, and represents a shortcoming of the integrated switching and preionization technique. Kline and Denes (35) point out the necessity of transversely uniform pre-ionization in their study of glow discharges.

Fig. 3.25 shows the vertical and horizontal components of shock waves at point 4. In the vertical direction a large refractive index gradient is followed by an oscillation. The first large peak is due to gas heating and expanding in the vertical direction. The time lag between the first pulse and the oscillations which follow is consistent with the oscillations coming from the spark pins. Typically the oscillations took $104 \mu\text{sec}$ to arrive in static gas and $112 \mu\text{sec}$ to arrive in flowing gas.

In the horizontal direction the dominant feature of the shock wave is two spikes which correspond to the time for a shock wave to travel from the measuring point to the anode and be reflected back again. The time between spikes for positions 1, 2, 3, 4 is shown in Table 3.5 and is compared with transit times calculated using $v = 9.65 \times 10^{-2} \text{ cm}/\mu\text{sec}$, the velocity of sound in He. The data is consistent with a shock wave travelling from the cathode to the anode and then being reflected but the velocity is lower than expected, having an average value of only $7.3 \times 10^{-2} \text{ cm}/\mu\text{sec}$. The likely cause of this lower velocity is N_2 leaking into the discharge system. The shock wave is produced at the cathode, due to gas heating in the cathode fall region. This result agrees with cathode shock waves

0.2 mV/div  $20 \mu \text{sec/div}$

(a)

 0.2 mV/div  $20 \mu \text{sec/div}$

(b)

Fig. 3.25 Detector Voltage at Position 4 Indicating (a) Vertical and (b) Horizontal Components of Shock Waves.

Position #	Distance from P to Anode and Back to P cm	t calc μ sec	t measured μ sec	V measured cm/ μ sec
4	3.5	36	44	7.9×10^{-2}
2	2.2	23	30	7.3×10^{-2}
1	1.6	16	20	8.0×10^{-2}
3	1.0	7.8	16	6.2×10^{-2}

Table 3.5

Cathode Shock Wave Propagation Measurements.

observed by Clark (36) in a CO_2 laser discharge using a holographic recording technique. Clarke also observed nonuniform gas heating effects due to asymmetrical preionization.

Most of the shock wave measurements are for static gas. Measurements made in flowing gas for comparison showed that gas flow had little effect on the shock waves, other than reducing their amplitude slightly and increasing the time taken for spark pin oscillations to reach the discharge region. In static gas large thermal gradients were present that took about 0.5 sec to disperse but in flowing gas they disappeared. The shock waves and spark pin oscillations had mostly dispersed within 0.5 msec of the discharge in both flowing and static gas. So shock wave induced gas density nonuniformities should not cause discharge problems in this system for repetition rates under 2 KHz.

3.10 DISCUSSION AND CONCLUSIONS

This system has shown the potential of an integrated switching and preionization technique to produce a simple high repetition rate TEA laser. Typical repetition rates of 200 Hz were achieved and the discharge in He suggests that repetition rates of 2 KHz should be possible before failure of the Marx switching sets in. Pulse stretching was attempted but was not successful and short pulses of about 1 μsec duration seem to be best. Maximum output energy per pulse was 1 J giving a typical average output power of 200 W with an electrical-to-light conversion efficiency of 6%.

Although the operation of this system was encouraging it still had a major shortcoming, the inability to run for an extended period of time. Runs were short and were usually terminated by the onset of arcing problems. Arcing could occur between the electrodes or from an electrode to the Marx spark pins. Arcing from an electrode to the Marx pins was particularly destructive because the resulting carbon track on the perspex insulation had to be cleaned off before the system could run again which meant the system had to be shut down and disassembled. Arcing between the electrodes was less destructive but still meant terminating the run to avoid damaging the electrodes.

The cause of the arcing was unclear but several possibilities were considered. One possibility, that of shock waves adversely affecting the discharge, was ruled out by the measurements in section 3.9 which showed that they did not persist long enough in this system to cause problems. Other possibilities considered were inadequate preionization, some kind of Marx generator malfunction, air leaking into the system and contaminating it, or gas poisoning due to discharge products. Some observations on this system and by other researchers suggested that gas poisoning due to dissociation of the laser gases was a possible cause. But the vacuum integrity of this system was not very good and the possibility of air leaks degrading the performance also existed. Also it was not clear whether or not the Marx generator was responsible in some way for the arcing. For instance, the preionization it provided was not entirely uniform transverse to the discharge. The remainder of this thesis deals with experiments aimed at determining the cause of arcing.

CHAPTER 4

FLOWING GAS ELECTRICAL DISCHARGE SYSTEM DESIGN

INTRODUCTION

The purpose of the flowing gas electrical discharge system is to provide a test facility to study the causes of arcing in a high repetition rate glow discharge since arcing problems had proved to be a major hinderance in the laser system. This discharge system is modelled after the one designed by Olson et al. (21) and is essentially a simpler version of theirs.

It has several improvements over the laser system, one of the most important being its smaller size. Because it is smaller only one person is needed to dissassemble it and modifications are easier to make. The vacuum integrity of the discharge system is much better than that of the laser, thereby ruling out air contamination as a source of problems. In order to model the laser system, the discharge was formed between two copper electrodes with preionization provided by brass spark pins. Rather than using a Marx generator, switching is accomplished with a thyatron pulser. This eliminated problems that might have been due to running a Marx generator in the gas flow loop and also results in cleaner voltage waveforms than were achieved with spark gap switching. It also eliminated the problem of arcing putting the switching circuit out of commission which happened frequently with the Marx.

The system consists of two main subsections. One is the discharge circuitry and the other is the recirculating gas loop which contains the electrodes, a heat exchanger, and a fan. Driving the fan with a variable speed motor allows control of the gas flow velocity in the loop.

4.1 RECIRCULATING GAS LOOP

The recirculating gas loop is shown in Fig. 4.1. It is constructed from 6 inch diameter aluminum pipe with 1/8" wall thickness. The fan housing and elbow which are 12" in diameter were constructed by rolling and welding aluminum plate. The heat exchanger is housed in a box constructed from aluminum channel. All sections are joined together using o-ring sealed flanges.

4.2 PRESSURE VESSEL CAPABILITY

The pressure that the system could be expected to withstand was estimated using a formula from the Mechanical Engineer's Reference Book (37). The collapsing pressure for a thin walled pipe is given by

$$P_{cr} = \frac{2 t^3 E}{d^3 (1-\nu^2)} \quad 4.2.1$$

where t is wall thickness, d is diameter, E is modulus of elasticity, ν is Poisson's ratio which lies between 0 and 0.5 (between .25 and .36 for metals). For aluminum alloys E is about 60,000 N/mm² so P_{cr} lies in the range 171 to 184 lb/in² for 6" diameter aluminum pipe. Since atmospheric pressure is 14.7 lb/in² the system will easily withstand being pumped out without collapsing with a wide safety margin.

4.3 FLOW SYSTEM DESIGN

In order to know what fan capacity would be needed to achieve a good gas flow velocity it was necessary to estimate the friction loss of the piping in the gas flow loop. The methods outlined in the ASHRAE handbook (27) were used and are essentially based on the formula

$$H_f = f \left(\frac{\ell}{D} \right) \left(\frac{v}{4005} \right)^2 \quad 4.3.1$$

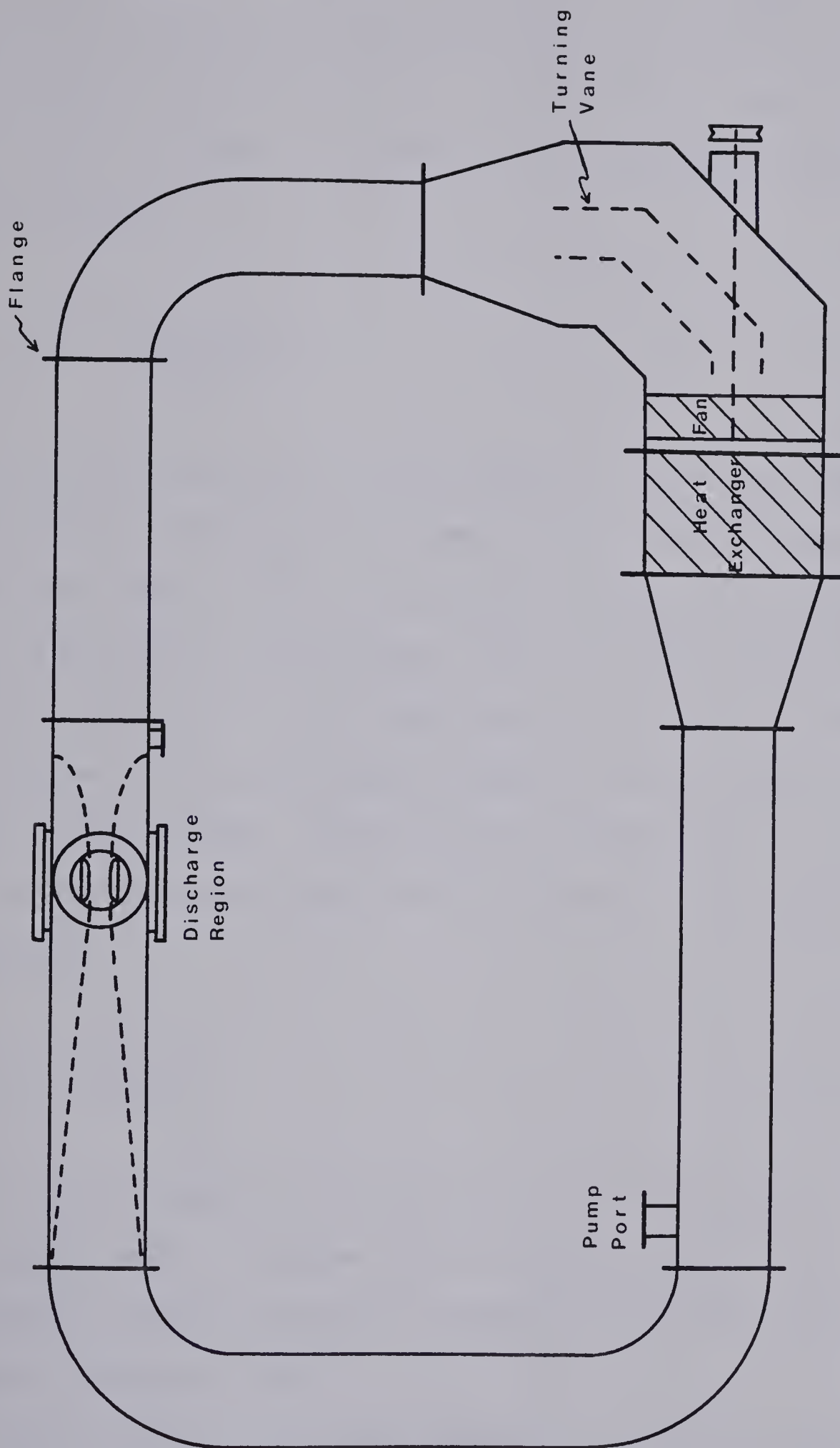


Fig. 4.1 Flowing Gas Electrical Discharge System - Recirculating Gas Loop. The recirculating gas loop is constructed from 6" diameter aluminum pipe and is approximately 7' long by 4' high.

where f is a friction coefficient ($\approx 2.5 \times 10^{-2}$), ℓ is length of the pipe in ft., D is the diameter of the pipe in ft., v is gas flow velocity in ft/min, and H_f is pressure head loss in inches of H_2O . Noncircular pipe such as the test section is converted into an equivalent circular duct using the formula

$$d_c = 1.3 \frac{(ab)^{.625}}{(a+b)^{.250}} \quad 4.3.2$$

where d_c is the equivalent circular diameter of a duct with sides of length a and b . Elbows were converted into an equivalent length of straight pipe using a chart from the ASHRAE handbook, and assuming 3 section elbows with 6 inch diameter and 1 ft turning radius led to an equivalent length of 8 ft of straight pipe for each elbow. Fortunately smooth elbows were obtained which are better than the 3 section elbows assumed in this estimate. Their effective length is only 5 feet each. The loss due to changes in area such as diffusers or converging sections is given by

$$H = C \left(\frac{v}{4005} \right)^2 \quad 4.3.3$$

where v is the velocity at the inlet to the transition section and C is a constant which is obtained from the ASHRAE handbook, C is different for different transition sections, depending on the angle between the diffuser or converger walls.

Initial pressure head loss estimates were calculated using the simplified system model shown in Fig. 4.2 The head loss due to the heat exchanger was ignored at this stage of the calculations because it was assumed to be small and there was insufficient information to estimate it.

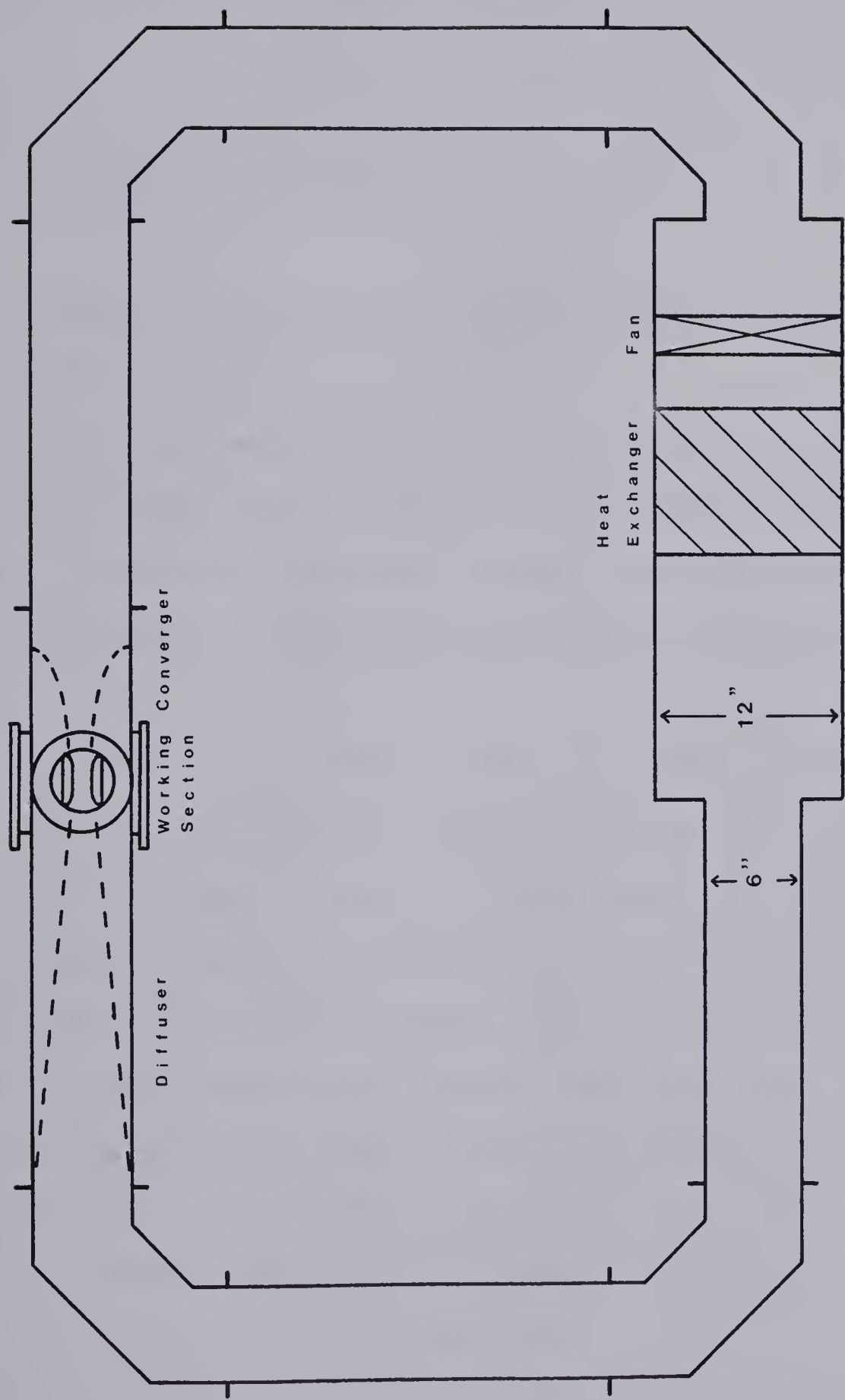


Fig. 4.2 Simplified Model of Recirculating Gas Loop Used for Calculating Design Estimates of Flow Velocity.

The continuity equation requires that volumetric flow be the same everywhere in the system so the losses in each section were converted to a function of volume flow instead of velocity by using

$$\begin{aligned} \text{CFM} &= V \times \text{cross sectional area} \\ &= V \pi \left(\frac{D}{2}\right)^2 \quad (\text{for round pipe}) \end{aligned}$$

The pressure loss through the system in inches of H_2O for various gas flow rates in CFM is shown in Table 4.1.

The cross sectional area of the working section is 1"x6" so the flow velocity between the electrodes can be calculated from the volume flow using the continuity equation. It can be seen that the diffuser is the primary source of system head loss, accounting for half the loss by itself.

To circulate the gas a fan was chosen from Sheldon's Multi-wing series. This series of fans has removable plastic blades making it possible to customize a wide variety of sizes and blade angles. They are also fairly cheap and readily available. The final choice was a 10 bladed fan with a 45° angle blade pitch and 12" diameter. From fan rating tables published by Sheldon's typical expected gas flow and power requirements for a given fan speed can be estimated. Fig. 4.3 shows the initial estimates of gas flow in CFM versus fan rpm. This however was for a 6 bladed 12 inch diameter fan with 35° blade pitch. In addition the curve for the 10 bladed 45° pitch fan is shown for comparison.

Where the family of fan characteristics intersects the system loss curve defines the gas flow delivered in the system and the amount of power needed to deliver that gas flow. Unfortunately it was necessary to extrapolate considerably beyond the values given in the rating tables

Item	Pressure loss "H ₂ O
12" dia. pipe	$7.6 \times 10^{-9} \text{ (CFM)}^2$
6" dia. pipe	$3.2 \times 10^{-6} \text{ (CFM)}^2$
1"x6" cross section working section	$2.2 \times 10^{-6} \text{ (CFM)}^2$
converger	$2.5 \times 10^{-6} \text{ (CFM)}^2$
diffuser	$9.9 \times 10^{-6} \text{ (CFM)}^2$
transition 6" to 12" pipe	$1.6 \times 10^{-6} \text{ (CFM)}^2$
transition 12" to 6" pipe	$5.2 \times 10^{-7} \text{ (CFM)}^2$
TOTAL	$2.0 \times 10^{-5} \text{ (CFM)}^2$

Table 4.1

Pressure Head Loss Estimates

Throughout the Flowing Gas Discharge System

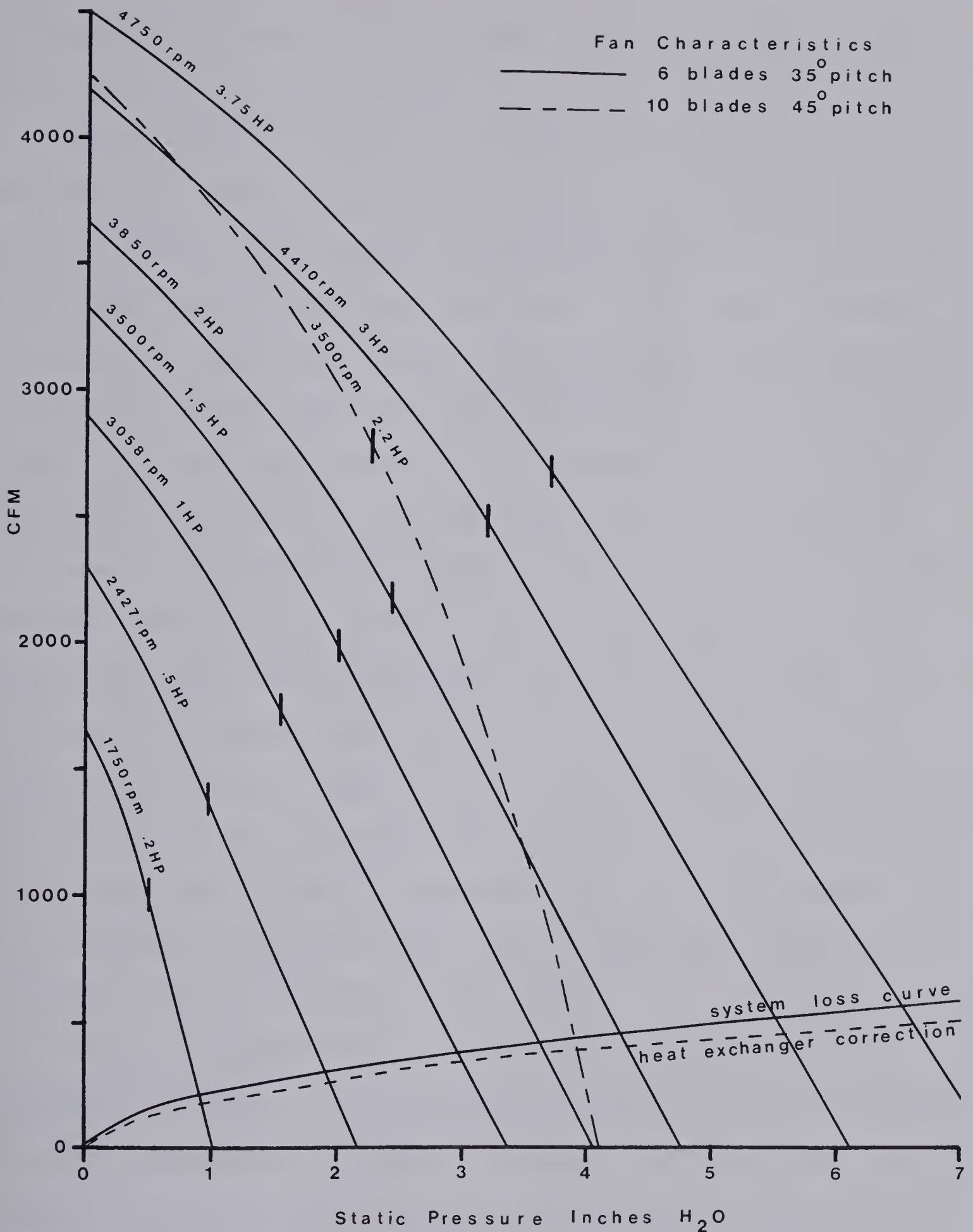


Fig. 4.3 Fan Characteristics and System Loss Curve.

The intersection of the characteristics with the loss curve determines the gas flow in the system for a given fan speed. The fan characteristics come from tables to the left of the vertical bars and are extrapolation to the right.

so the results will not be very accurate. However they will give some idea of what flow velocity to expect.

After looking for a motor to drive the fan it became apparent that the size of the motor rather than fan capacity would determine maximum gas flow velocity. For instance, to match the flow velocity of 100 m/sec of the laser system in air would require about 6 HP. Besides the fact that this power input would require a very large heat exchanger (since it would have to remove 6 HP of heat flow from the gas) such a large variable speed motor is not readily available. The simplest way to vary the gas flow was by varying the fan speed using a universal motor with a triac controller. The largest motor of this type that could be easily obtained was a 15A industrial disc grinder. This unit has a capability of only about 2 HP. Higher powered motors are available but not suitable. For instance higher powered induction motors are easily obtained but their speed cannot be varied except by going to complicated and costly techniques such as powering them from a variable frequency source. Large D.C. motors are also available but they are expensive and not as easy to obtain. In addition there is still the problem, with a larger motor, of being able to handle the heat load in the gas flow system.

Using the 2 HP grinder motor an initial estimate can be made of obtainable gas flow. A 2 HP motor should be able to deliver approximately 500 CFM of air against 5.5" H_2O static pressure. This would result in a gas flow velocity of approximately 60 m/sec between the electrodes in the test section.

4.4 HEAT EXCHANGER DESIGN

The heat exchanger was one of the more difficult parts of the system to design, mainly because of the lack of reliable specifications for the finned tubing. First an estimate of the heat load of the system is needed.

Assuming 1 KHz operation for the discharge with 1 J/pulse energy leads to a heat load from the discharge of approximately 4000 BTU/hr. In addition there is of course the heat load from the fan. For 2 HP this would be a total heat load of approximately 10,000 BTU/hr. The heat exchanger was to be constructed from Aero-fin type 140 water coils which is a finned tubing with 14 fins per inch, and was to be connected in a crossflow arrangement.

The equation which describes heat flow is

$$q = MC\Delta T$$

For N_2 gas at atmospheric pressure and an inlet temperature of $100^\circ F$

$$\Delta T = \frac{q}{MC} = \frac{10000 \text{ BTU/hr}}{2100 \text{ lb/hr} \cdot 248 \text{ BTU/lb}^\circ F} = 19.2^\circ F$$

So for a gas inlet temperature of about $100^\circ F$ the outlet temperature would be $81^\circ F$. The water supply for the heat exchanger is just tap water. The tap in our lab delivers $.23 \text{ ft}^3/\text{min}$ of water or 859 lb/hr with a temperature of $59^\circ F$. (In fact this temperature varies with the time of year.) For the water

$$\Delta T = \frac{10000 \text{ BTU/hr}}{859 \text{ lb/hr} \cdot 1 \text{ BTU/lb}^\circ F} = 11.6^\circ F$$

so for an inlet temperature of $50^\circ F$ the water will have an outlet temperature of $71^\circ F$. This gives a mean temperature difference between the

gas and water of

$$\Delta T_m = \frac{(100-59) - (81-71)}{\ln\left(\frac{100-59}{81-71}\right)} = 22^\circ\text{F}$$

The face of the heat exchanger is 12" in diameter and has eight pipes. The I.D. of the finned tubes is 9/16", and for eight pipes in the face represents an area of .014 ft². So for a water volume of .23 ft³/min the water velocity through the pipes would be .28 ft/sec. From this information and from aerofin tables a heat transfer constant can be estimated.

$$K \approx \frac{100 \text{ BTU}}{\text{hr ft}^2 \text{ } ^\circ\text{F row}}$$

This estimate is very crude because it was arrived at by extrapolating from the charts.

$$n_{\text{rows}} = \frac{q}{KA\Delta T_m} = \frac{10000 \text{ BTU/hr}}{100 \text{ BTU/hr ft}^2 \text{ } ^\circ\text{F}_{\text{row}} \times .79 \text{ ft}^2 \times 22^\circ\text{F}} = 5.8 \text{ rows}$$

where A is the face area of the heat exchanger and n is the number of rows required. So 6 rows of pipes are needed for the heat exchanger with 8 pipes in parallel in each row. At 500 CFM the face velocity of the gas would be approximately 640 ft/min and the pressure loss would be .75" H₂O. This is small compared to the other system losses but it would probably be enough to drop the actual gas flow down to about 400 CFM, or a flow velocity between the electrodes of about 50 m/sec. Referring back to Fig. 4.3 the system loss curve, corrected for heat exchanger losses is shown on the graph.

The main point of this heat exchanger design was to try and insure that there was adequate heat exchanger capacity to prevent the gas from getting unreasonably hot. The upper limit design goal was 100°F. In the laser system insufficient attention was paid to heat exchanger design and as a result the flow system got hot to the touch indicating that the heat exchanger was inadequate for the heat load.

4.5 FAN SEAL

The fan is mounted inside the flowing gas loop but to help keep the system clean the fan motor is mounted outside the loop. This necessitates bringing the driveshaft out of the vacuum system using some kind of vacuum seal. The fans of an industrial laser being developed by the laser group are powered by a Volvo hydraulic motor with the shaft sealed by a lip seal. The seal operated well and was capable of withstanding vacuum. Industry literature indicates that a lip seal should be capable of sealing against a vacuum with shaft speeds of up to 4000 rpm.

Typical values quoted for rubber are as follows. Rubber lip seals should be capable of withstanding a maximum pressure difference of 10 bar and a peripheral shaft speed of about 5 m/sec. Some literature quotes a top shaft speed for neoprene rubber lip seals as 10 m/sec with an upper temperature limit of 170°C. For a 1 inch diameter shaft this suggests a top speed of 7600 rpm.

The initial fan estimates indicated that roughly 2 HP would be needed to drive the fan at 3500 rpm in air. But considerably less power would be needed in Helium or a laser mix because of their lower density. So the maximum shaft speeds quoted here mean that it would be possible to increase the fan speed using pulleys and v-belts. Table 4.2 gives

some typical shaft speeds for a 1" diameter shaft.

Fan Speed rpm	Shaft vel. m/sec
9000	12
6000	8
4000	5.3

Table 4.2 Typical shaft speeds for 1" diameter shaft.

These speeds are all faster than are usually encountered but it would appear that the 4000 rpm and 6000 rpm values are within the capabilities of conventional lip seals. It was decided to use Volvo seals like the ones in their hydraulic motor because they have somewhat better than normal specifications. They are supposed to be good for a top speed of 10000 rpm for a 1" diameter shaft.

Fig. 4.4 shows the fan mounting and vacuum seal arrangement. Inside the system the fan shaft is supported by a self aligning bearing mounted on a support. To minimize problems of system contamination from the bearing it was packed with a low vapour pressure grease. Outside the system the shaft is supported by a bearing running in a reservoir of vacuum pump oil contained between two lip seals. Some oil leakage from the seal is inevitable but since vacuum pump oil is used, contamination would not be much worse than that due to backstreaming of oil from the vacuum pump.

4.6 V-BELTS

The fan is driven from the grinder by a V-belt. Although speeds are a bit higher than are usually encountered by V-belts, Gates has a series of polyflex belts which are capable of running this fast. A

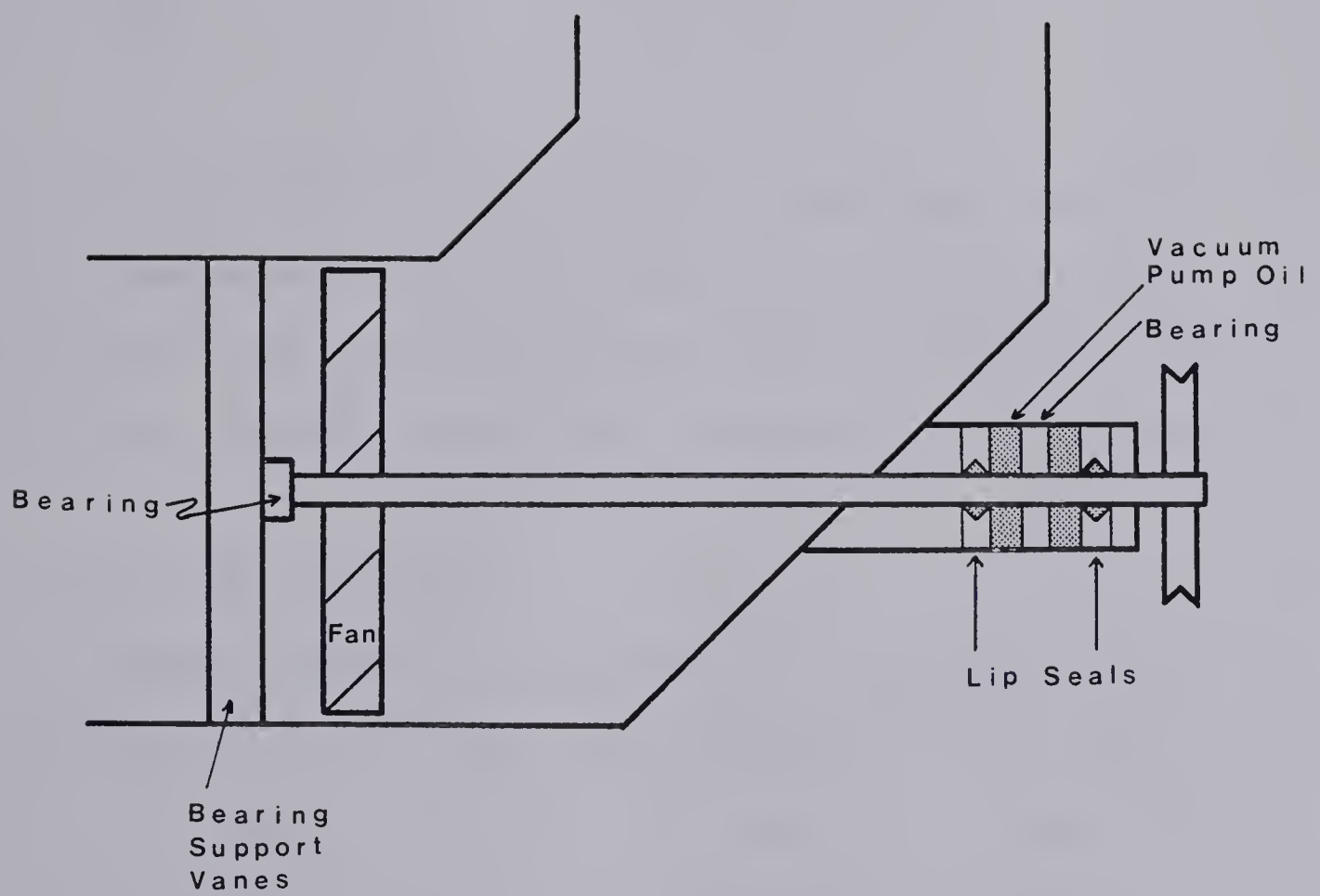


Fig. 4.4 Fan Assembly and Shaft Seal.

7M825 belt was chosen. Fig. 4.5 shows the grinder mounting and pulley arrangement.

4.7 VACUUM PUMP

Initially the volume of the vacuum system was estimated to be roughly 200 liters. A reasonable pump down time to 0.1 torr would be about 15 minutes for this volume. Using

$$T = \frac{FV}{S}$$

where F is a correction factor and for a single stage pump $F \approx 12$, a required pumping speed of $S = 160$ l/min, or better, is calculated. A Sargent-Welch model 1397 2 stage rotary pump with a pumping speed of 300 l/min was available and met this specification so it was used.

4.8 MOTOR SPEED CONTROLLER

The motor speed controller consists of a simple triac controller as diagrammed in Fig. 4.6. With this controller the fan speed could be varied between 3600 rpm, its upper limit under load, and about 1000 rpm. Although it was possible to set lower speeds they were not practical to use as they tended to drift too much.

4.9 FAN SPEED SENSING

The fan speed was sensed by painting a black strip on the fan pulley which had a shiny aluminum finish everywhere else. A phototransistor was then used to generate pulses by responding to the light reflected back from the rotating pulley. The pulses were counted by a simple

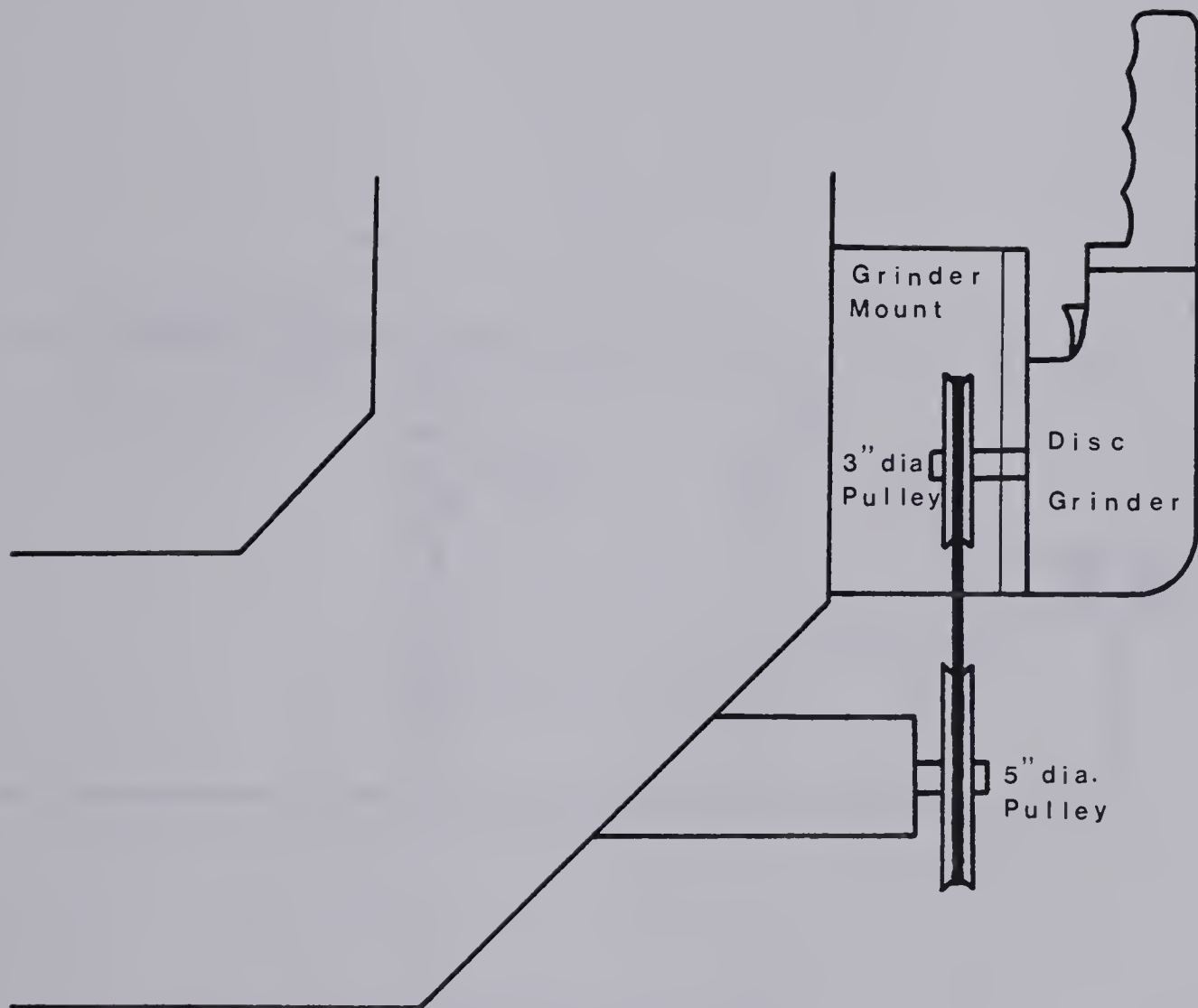


Fig. 4.5 Grinder Mounting, and Pulley Arrangement.

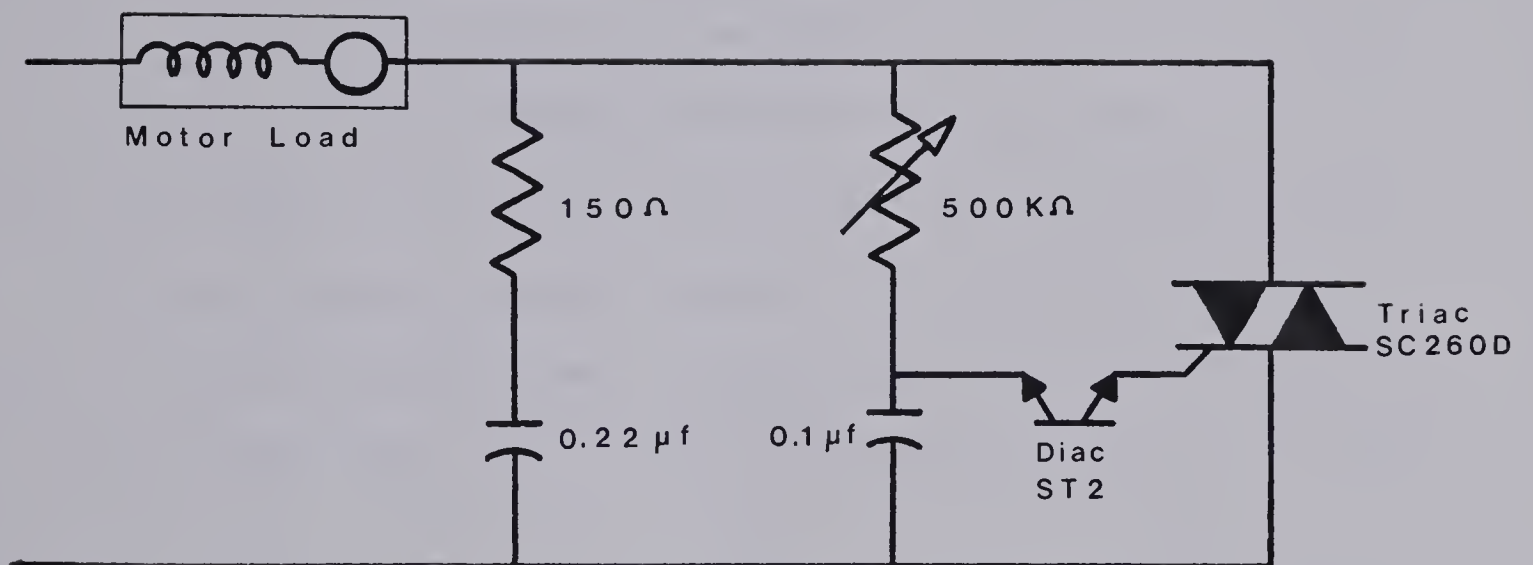


Fig. 4.6 Motor Speed Controller.

digital rpm counter and could also be monitored by the oscilloscope for a more accurate measurement.

4.10 PULSE DISCHARGE CIRCUITRY

A pulse discharge circuit was needed that would model the essential features (and hopefully essential problems) of the laser system. Therefore a spark pin preionized discharge configuration was chosen (Fig. 4.7). Spark pins were provided both upstream and downstream from the discharge electrodes. Since the energy being switched in this system was much smaller than in the laser system, and to reduce the number of vacuum feed-throughs, a thyatron was chosen for switching rather than blown spark gaps in the gas flow loop. Using the thyatron also resulted in more reliable switching and much less electrical noise than the spark gaps.

The pulse discharge circuit consists of a thyatron discharge circuit, a thyatron driver, and a voltage controlled pulse generator to vary the repetition rate. The circuits are shown in Figs. 4.8, 4.9 and 4.10.

Essentially the discharge circuit consists of a storage capacitor, the discharge electrodes, and a thyatron. The storage capacitor is charged up from a D.C. supply through the charging inductor. The thyatron acts like a switch and when it fires shorts the hot side of the capacitor to ground. Since the voltage cannot change instantly across the capacitor an inverted voltage appears across the electrodes. A discharge forms between the electrodes, completing the circuit, and the storage capacitor discharges through the discharge.

The spark pins and coupling capacitors to either side of the discharge provide preionization. As the voltage rises across the electrodes one of the spark pins will break down. It's coupling capacitor then begins

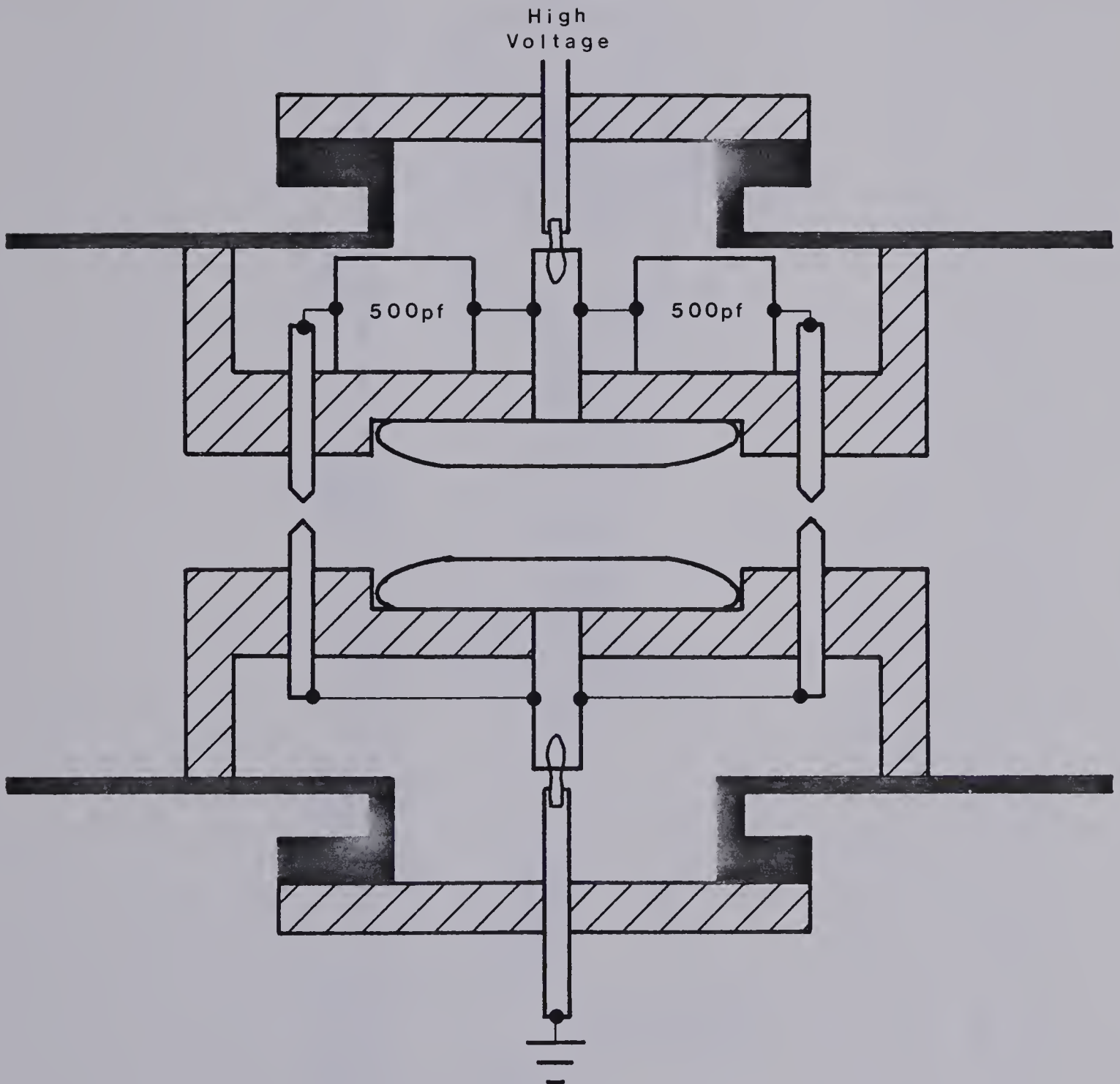


Fig. 4.7 Discharge System Configuration.

The discharge is formed between two copper Rogowski profiled electrodes with preionization provided by spark pins.

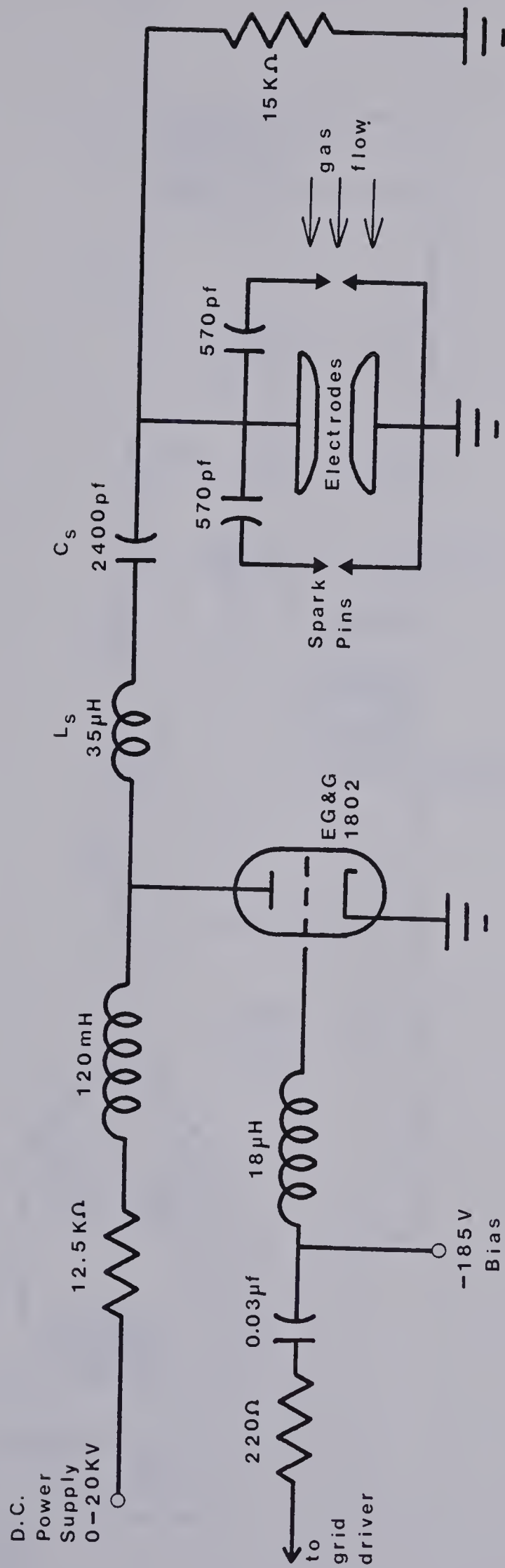


Fig. 4.8 High Repetition Rate Discharge Circuit.

The discharge pulse energy is varied by changing the storage capacitor C_s and the pulse length is controlled by the $L_s C_s$ time constant. The 15 KΩ resistor was later replaced by a 1 mH inductor (see Section 5.4)

T1:25 turns bifilar

T2:9 turns primary, 18 turns
secondary on 3" dia.
ferrite torus

VR:Varistor V480LB80B

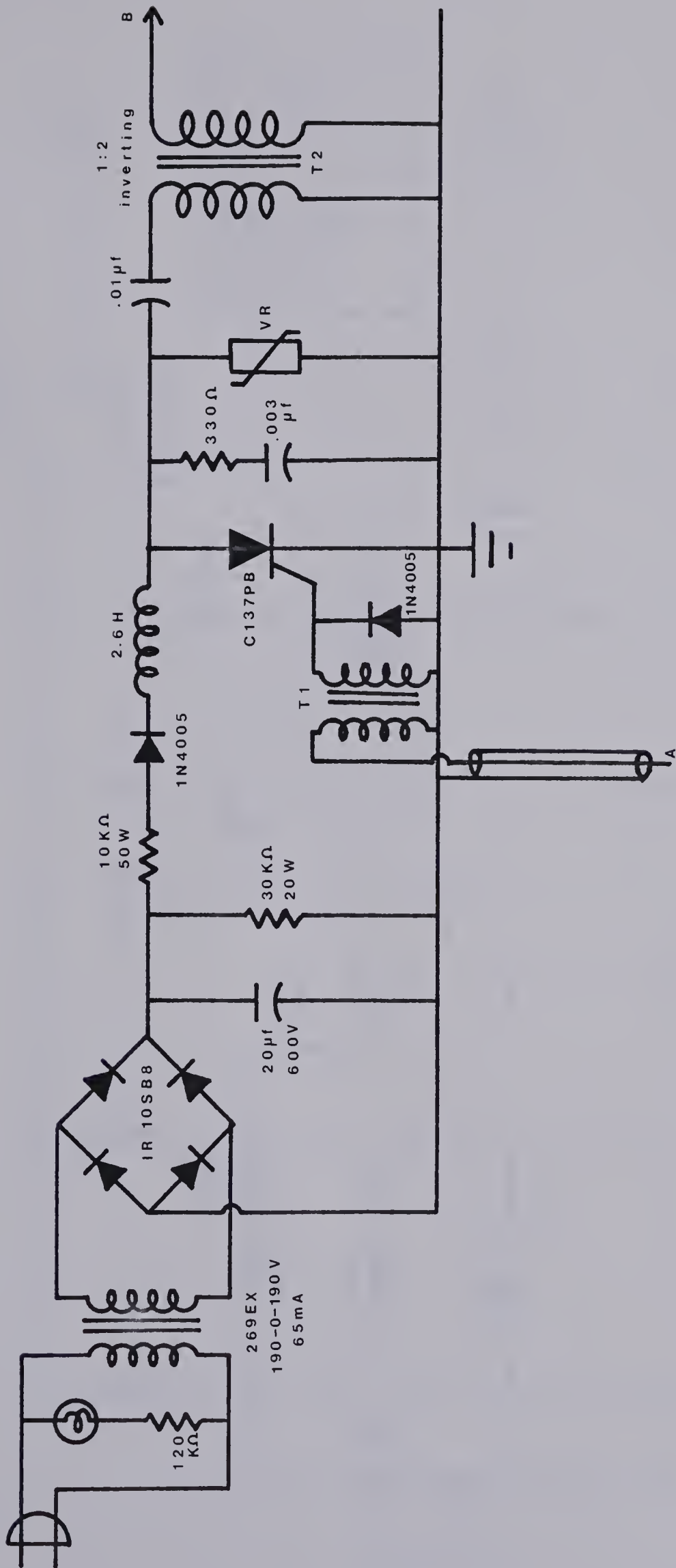


Fig. 4.9 1802 Thyatron Grid Drive Circuit.

The trigger pulse for the circuit is a 5V peak to peak pulse at A. The output pulse at B is approximately 1000 V and connects to the point marked "to grid driver" in Fig. 4.8.

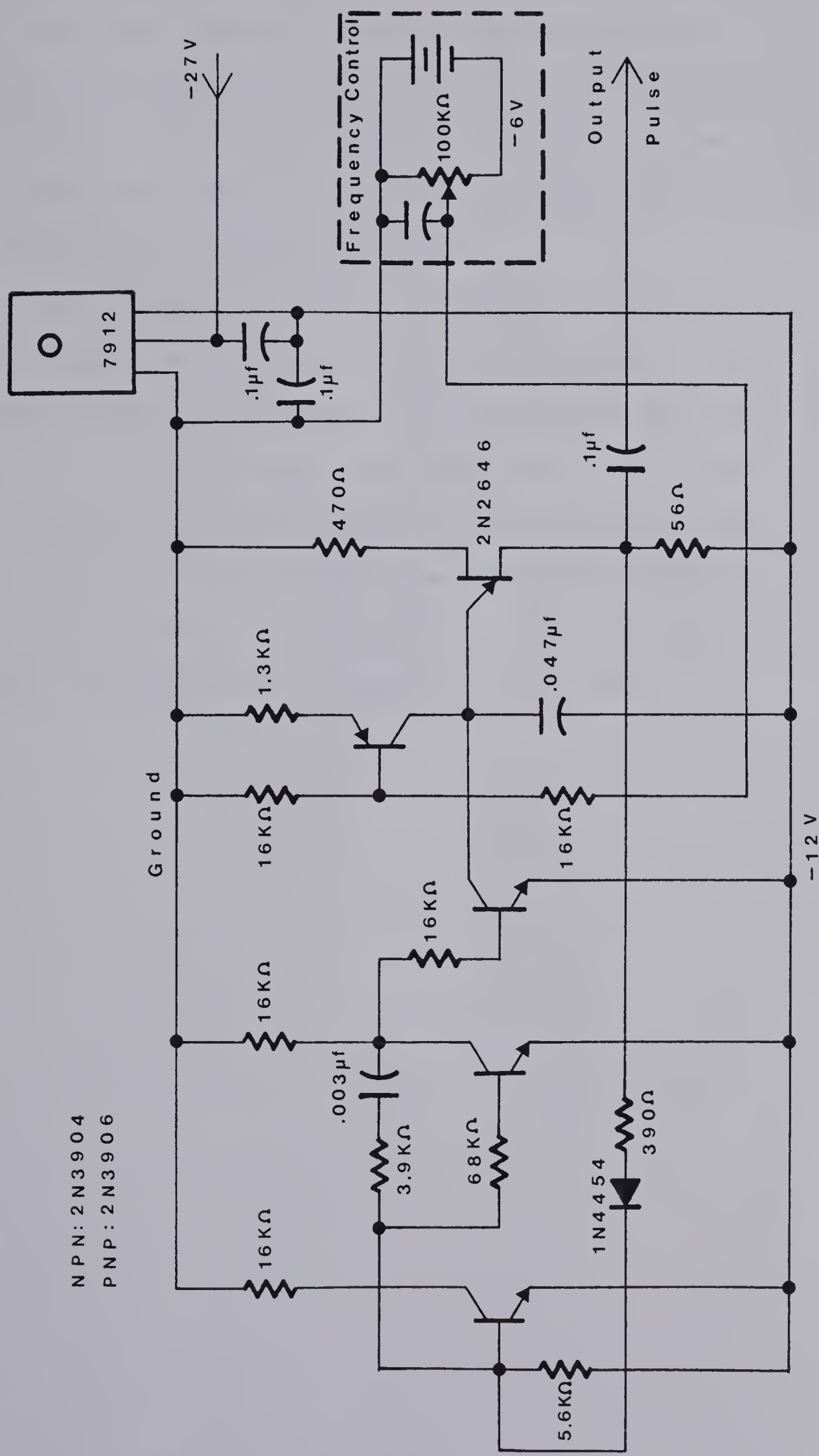


Figure 4.10 Voltage Controlled Pulse Generator. The repetition rate is controlled with the frequency control box and the 5 volt output pulse goes to point A in Figure 4.9.

to charge. When the voltage becomes high enough the other spark pin will then break down and the second triggering capacitor will charge. Finally the voltage rises again until the breakdown voltage of the main electrodes is reached. The discharge then forms between the main electrodes and drains the charge from the main storage capacitor and two coupling capacitors through this path.

The thyatron is fired by a SCR (Fig. 4.9), which in turn is controlled by the voltage controlled pulse generator (Fig. 4.10). This system is capable of switching up to 20 KV pulses and the design goal was to switch 1 J per pulse at repetition rates of up to 1 KHz. The system is capable of switching in excess of 1 KHz repetition rates and will also switch more than 1 J per pulse. The present maximum is about 10 J per pulse at 250 Hz. The repetition rate limit is due to discharge arcing rather than being due to a limitation of the pulser.

CHAPTER 5

FLOWING GAS DISCHARGE SYSTEM TESTING

5.1 FLOW SYSTEM TESTING

Initially the system was assembled and tested without turning vanes in the big elbow. The results were disappointing. The flow through the test section was very nonuniform, most of it being along the right side of the pipe with very little flow in the center and the left side of the test section (Fig. 5.1). The maximum velocity along the wall was 13.4 m/sec, as measured with a pitot tube. This was much lower than it should have been. In addition just upstream of the test section, before the gas flow began to converge, there was a great deal of swirl, with the gas flow travelling in a helical pattern down the pipe. This was easily observed by watching the action of a tuft of string held in the flow on the end of a rod.

The fan, elbow, and heat exchanger combination was tested to see what static pressure it could generate with the elbow outlet blocked off (Fig. 5.2). Since the system head loss is high and the volume flow low this will give a better estimate of expected system performance than the extrapolation done previously from the fan tables. Static pressure was measured directly in inches of H_2O using a water-filled U-tube manometer. The fan only generated a static pressure of $1\frac{1}{4}" H_2O$ which is considerably less than the $3\frac{1}{2}"$ to $4" H_2O$ that had been anticipated. In addition the gas flow out of the elbow had a lot of swirl and came out at an angle, as shown in Fig. 5.3a.

Two changes were made in a successful attempt to remedy these problems. They were the addition of two turning vanes in the large elbow and the reduction of clearance between the fan blades and the elbow wall. The

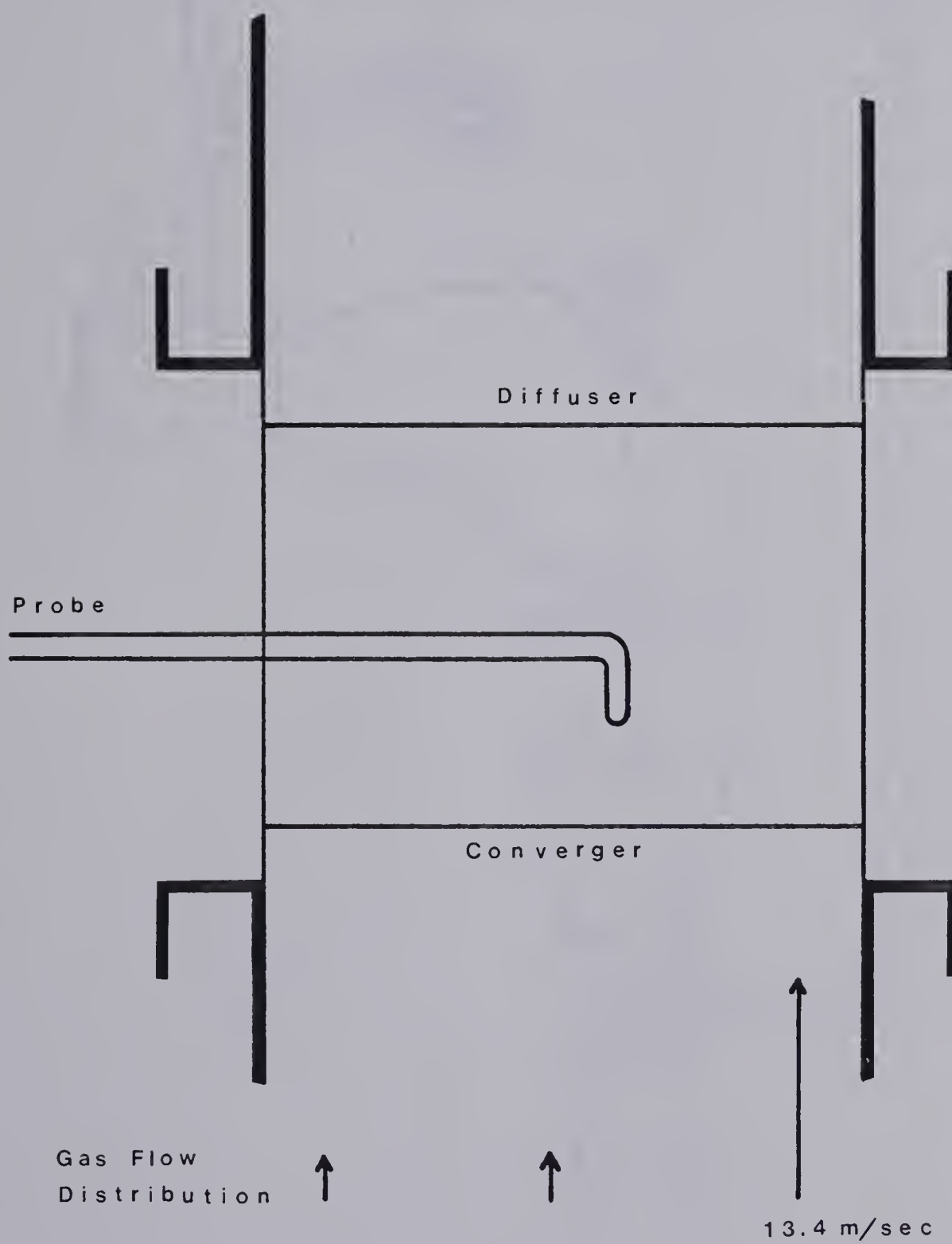


Fig. 5.1 Initial Gas Flow Velocity Distribution in the Test Section.

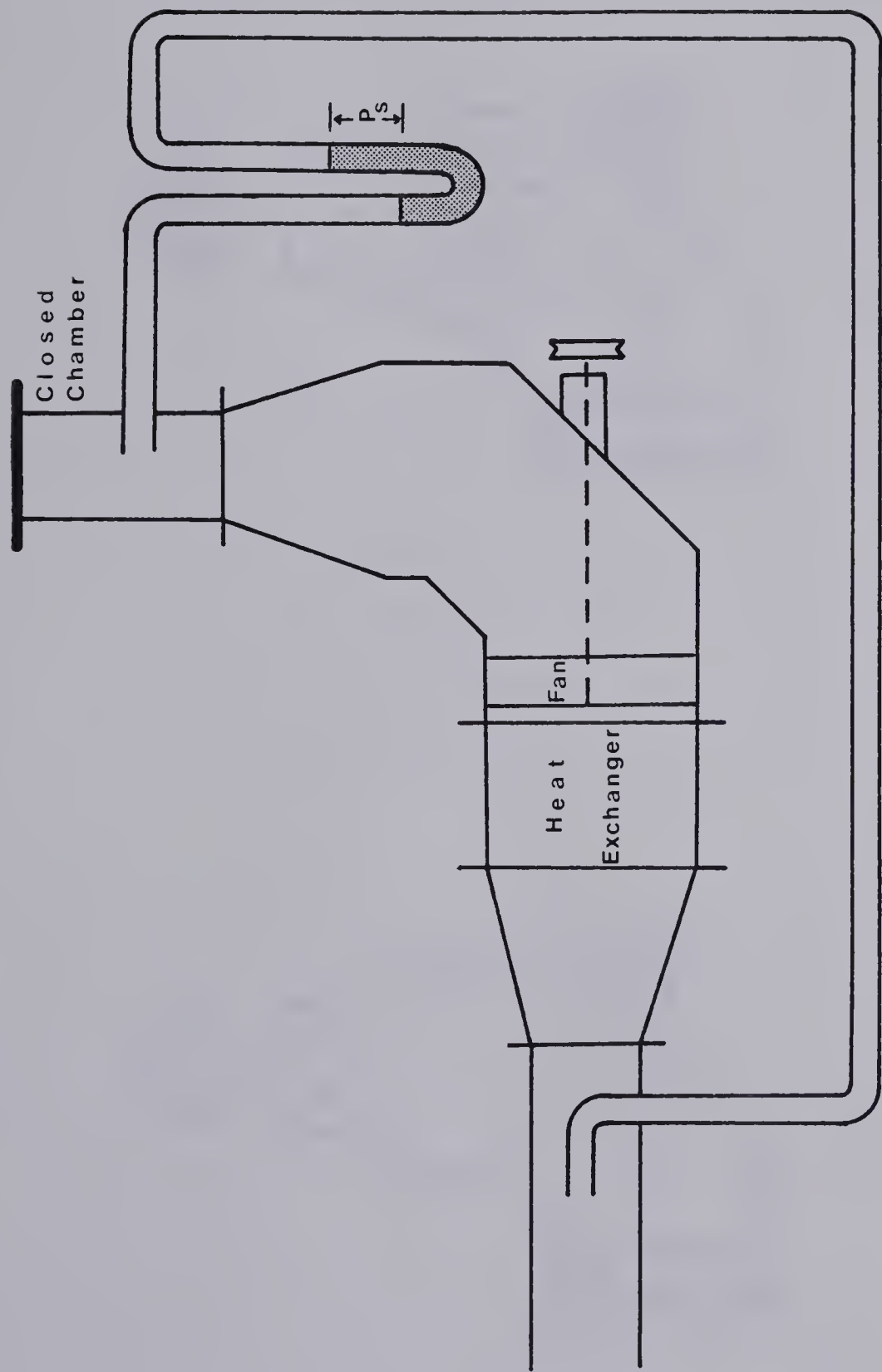


Fig. 5.2 Apparatus for Testing Fan Static Pressure.

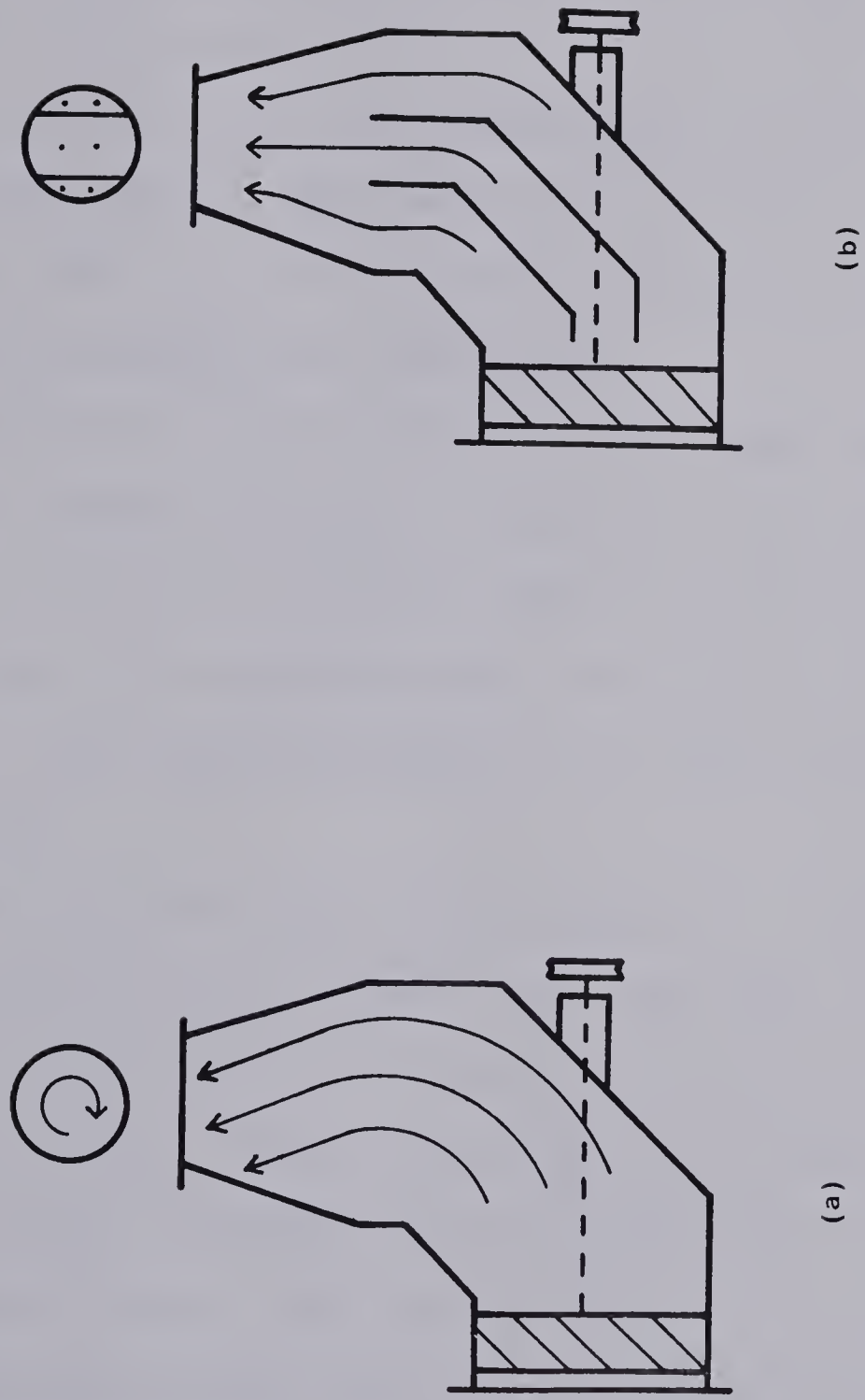


Fig. 5.3 Flow Distribution in Fan Elbow.

- a) Without Vanes and
- b) With Vanes.

addition of the turning vanes was probably the more significant change of the two. Remeasuring the static pressure generated by the fan showed that it had risen to $1 \frac{15}{16}$ " H_2O , an improvement of almost $\frac{3}{4}$ " H_2O . In both tests the fan speed was 2940 rpm and the motor drew 15.8A, which was full power. In addition the flow out of the elbow was now uniform and swirl free as shown in Fig. 5.3b.

This eliminated swirl problems downstream and the flow through the test section became uniform. The flow velocity through the test section rose to 22 m/sec which is a good improvement although it is still only half of what was estimated in the design stage.

After the system was completed and tested the losses were recalculated using the final configuration (Fig. 4.1) instead of the crude model (Fig. 4.2). For a flow rate of 225 CFM, which corresponds to 22 m/sec in the test section, the calculated system loss came to 1.18" H_2O which is a negligible change from the estimate of 1.23" H_2O calculated for the crude system model.

These results show that there are two reasons for the reduction in flow velocity from the initial estimate. The main reason is that the extrapolation of static pressure from the fan rating tables resulted in an estimate that was much too high, $3\frac{1}{2}$ " H_2O instead of the actual value of just under 2" H_2O . The other reason is that the actual system head losses were somewhat larger than estimated. This is not surprising since the tables used to obtain the friction coefficients were for galvanized air ducting and this system, which is constructed of welded aluminum pipe, has a rougher finish which would mean higher friction coefficients. The test section also would have a higher head loss than estimated since the estimate assumed that it was a smooth duct when in

fact it contained recessed wells with electrodes sitting in them.

5.2 GAS FLOW CALIBRATION

In designing flowing gas systems the fan laws are used to estimate the fan capability required to achieve a given gas flow. The laws are as follows:

$$CFM_a = CFM_b \times \left(\frac{D_a}{D_b}\right)^3 \times \left(\frac{RPM_a}{RPM_b}\right)$$

$$P_a = P_b \times \left(\frac{D_a}{D_b}\right)^2 \times \left(\frac{RPM_a}{RPM_b}\right)^2 \times \left(\frac{\delta_a}{\delta_b}\right)$$

$$HP_a = HP_b \times \left(\frac{D_a}{D_b}\right)^5 \times \left(\frac{RPM_a}{RPM_b}\right)^3 \times \left(\frac{\delta_a}{\delta_b}\right)$$

where CFM is gas flow

D is the fan diameter

RPM is fan speed

P is pressure head generated by the fan

δ is the gas density

This says that the gas flow is linearly proportional to fan speed and is independent of the gas density. The power needed to move the gas and the pressure generated do however vary with density.

Although this is adequate for system design it is true only as a first approximation. In this system the flow velocity for a given fan speed does indeed depend on the gas density and it is not linear with fan speed. Measurements indicated that although the relationship was linear for fan speeds above 1500 rpm, it was not for lower speeds. Since gas

flow velocity is monitored by measuring the fan speed it is therefore necessary to get calibration curves for the gas flow velocity as a function of fan speed.

The gas flow velocity between the electrodes was measured by using a pitot-static tube and the Baratron capacitance manometer. The fan speed is observed by a phototransistor which detects a timing mark on the fan pulley. The pulses output by the phototransistor are monitored on the scope and the time between two pulses gives the period of rotation. The fan speed in rpm can then be determined from the period, and calibration curves plotted which give gas flow velocity as a function of fan speed.

Rather than expressing the calibration curves in the form of a table it is more convenient to represent them as equations giving flow velocity as a function of fan speed. Then the calibration information can be easily used by a computer program for further data analysis. In order to generate a calibration curve it was necessary to try and fit a smooth curve to the data points but the question was which is the best curve to use. The IMSLIB library on the computer has a routine which can fit any degree of polynomial, up to degree 10, to a given set of data points. Using this subroutine polynomials of up to degree 4 were fitted to the calibration data. The program works by doing a least squares fit of a series of orthogonal polynomials to the data to generate an equation fitting the data points. To determine how good the fit is, the variance must be calculated for the data points and the predicted equation. The error sum of square is

$$\delta = \sum_{j=1}^m (y_j - y_{j_{\text{predicted}}})^2$$

and the variance is

$$\sigma_i = \frac{\delta_i^2}{m-i-1}$$

where i is the degree of polynomial and m is the number of data points. Notice that you are restricted to $i \leq m-2$. When an increase in the degree of the polynomial produces no significant change in the variance then the best fit has been achieved. Using this technique it was found that the calibration results were best described by a cubic equation. The coefficients for the equation are given in Table 5.1, and the calibration curves are plotted in Figures 5.4 to 5.7. The curve fitting program is listed in the Appendix.

$$y = A + Bx + Cx^2 + Dx^3$$

gas	A	B	C	D
60 torr N ₂	0.446222x10 ⁻¹	0.255427x10 ⁻²	0.170707x10 ⁻⁵	-0.192712x10 ⁻⁹
80 torr CO ₂	-0.106198	0.422460x10 ⁻²	0.176471x10 ⁻⁵	-0.257645x10 ⁻⁹
700 torr He	-0.174847	0.356737x10 ⁻²	0.168749x10 ⁻⁵	-0.206890x10 ⁻⁹
400-				
700 torr Mix	-0.649503x10 ⁻¹	0.456847x10 ⁻²	0.158747x10 ⁻⁵	-0.231660x10 ⁻⁹

Table 5.1 Calibration Curve Coefficients

5.3 SYSTEM VACUUM INTEGRITY

A measurements of system vacuum integrity was important because knowledge of the leak rate gives a worst case estimate of impurity levels that can be expected in the system during an experiment due to leaks.

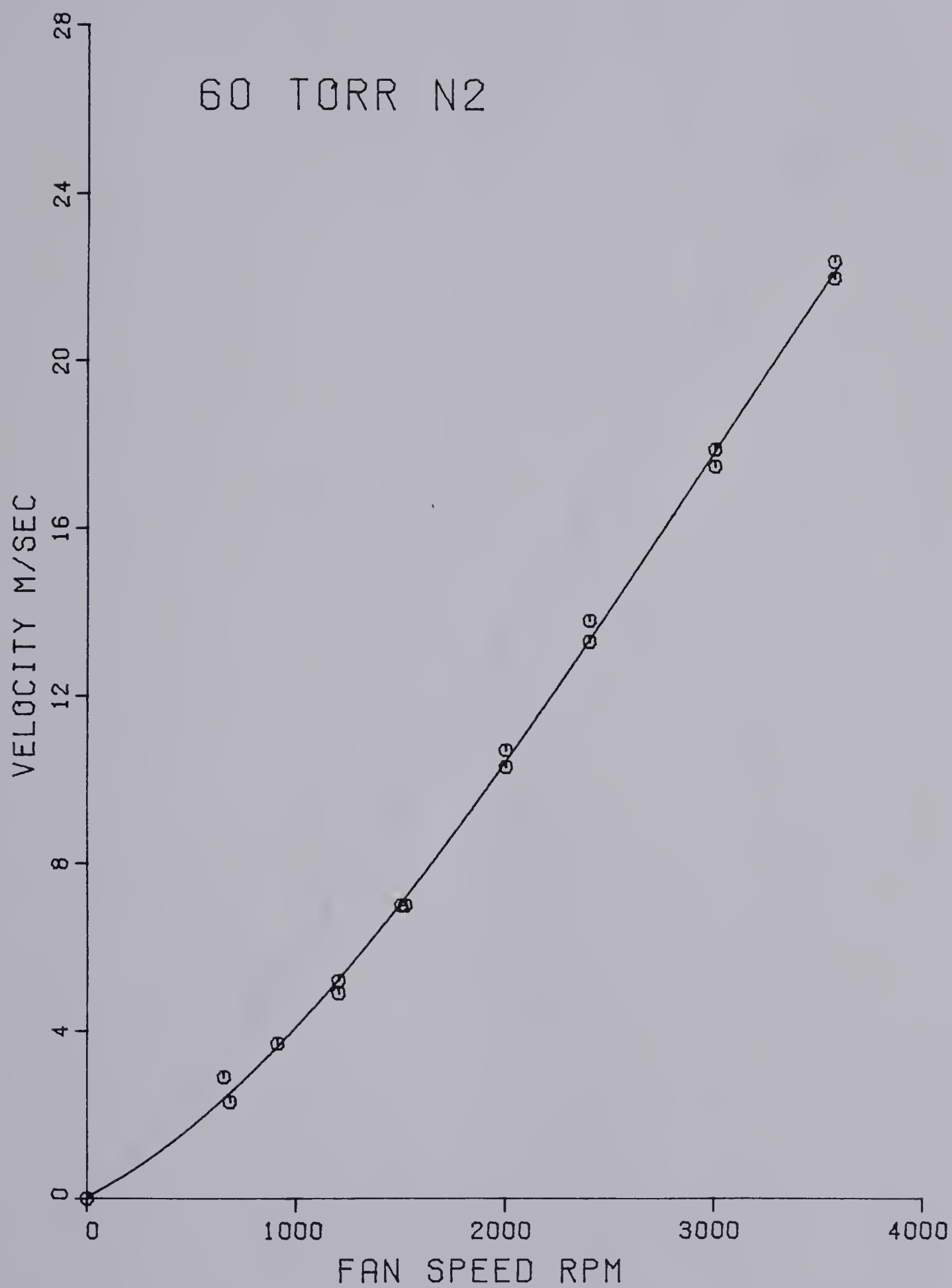


Fig. 5.4 Gas Flow Velocity Calibration Curve for 60 torr N₂.

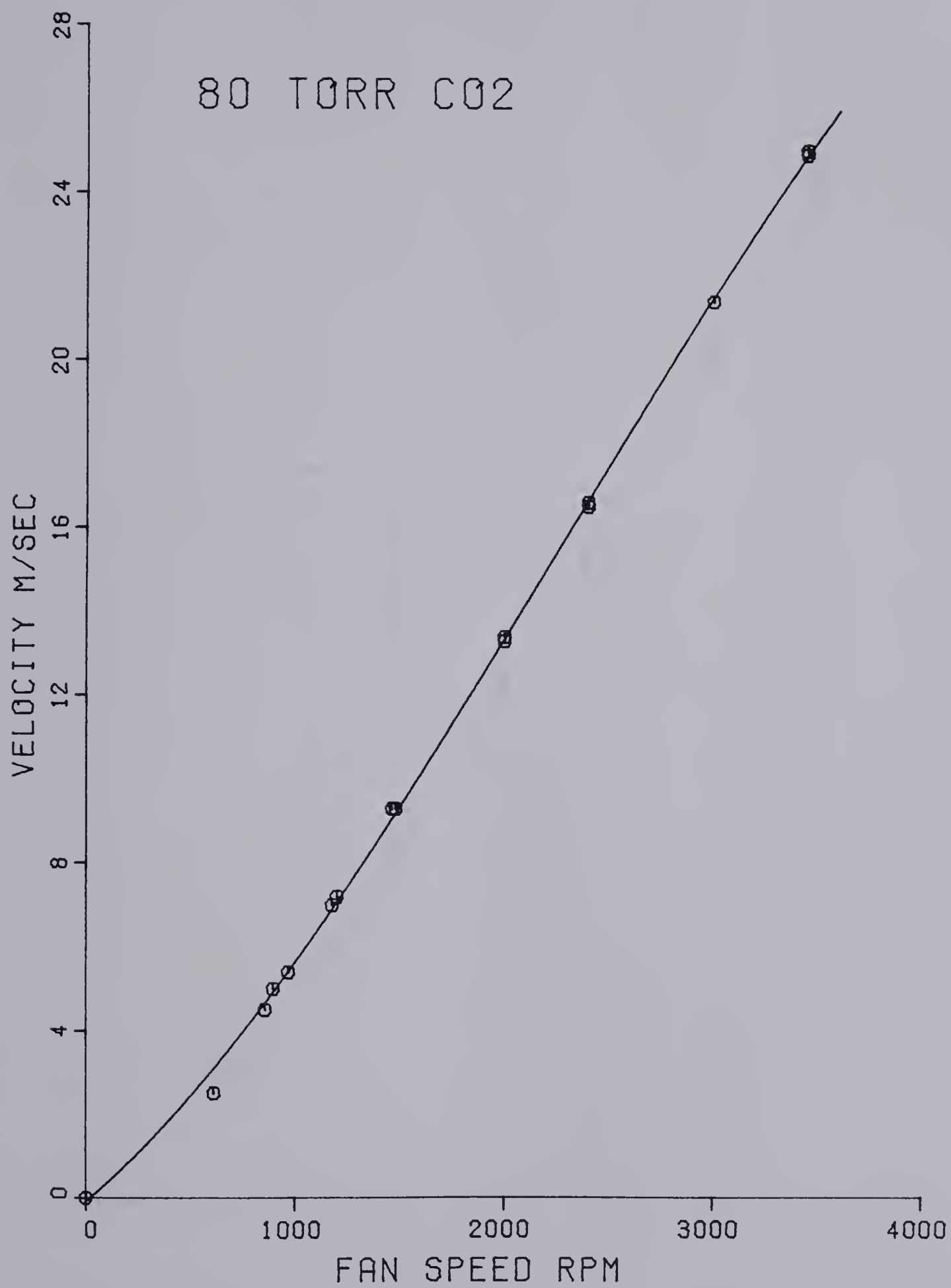


Fig. 5.5 Gas Flow Velocity Calibration Curve for 80 Torr CO₂.

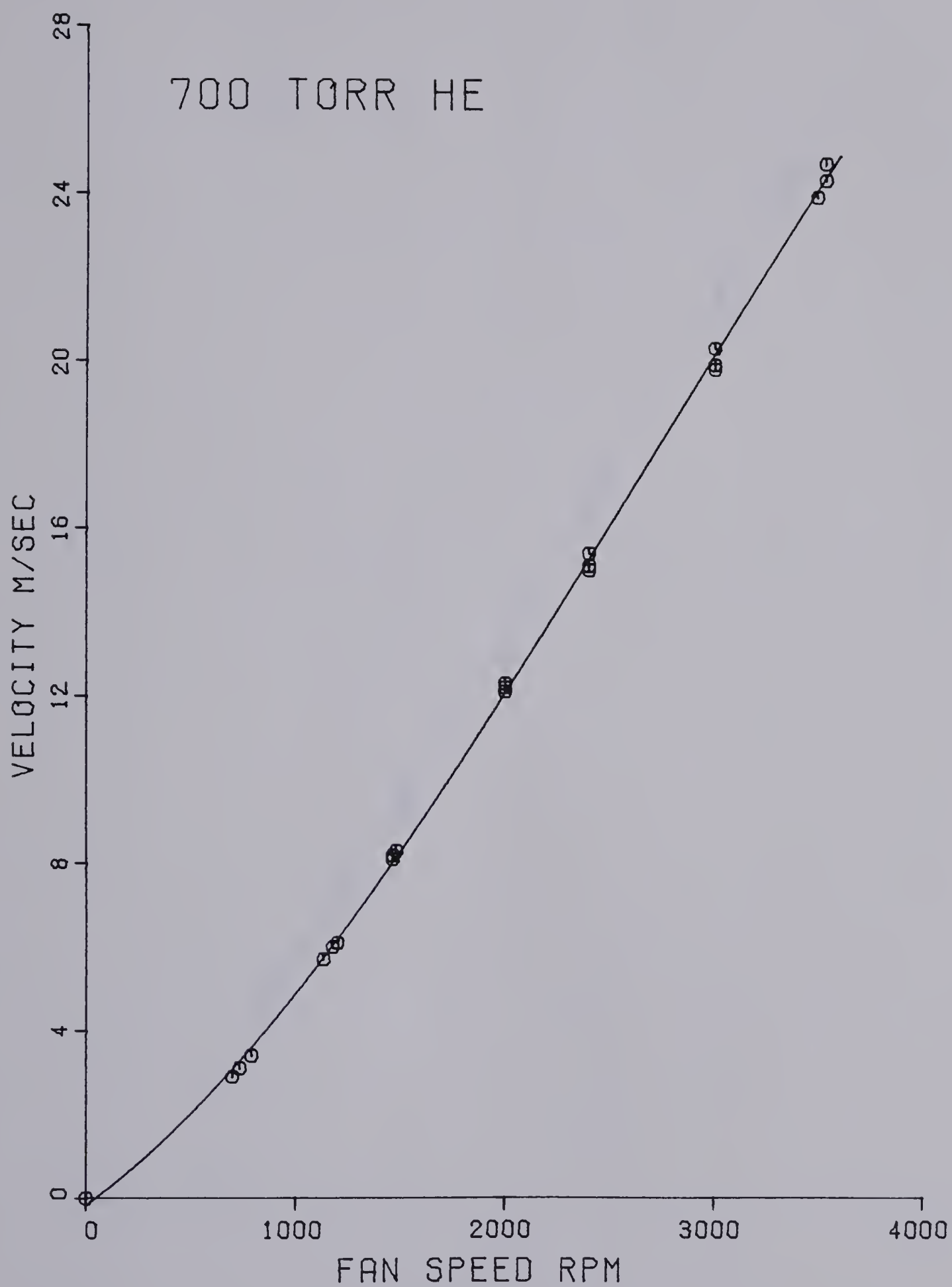


Fig. 5.6 Gas Flow Velocity Calibration Curve for 700 Torr He.

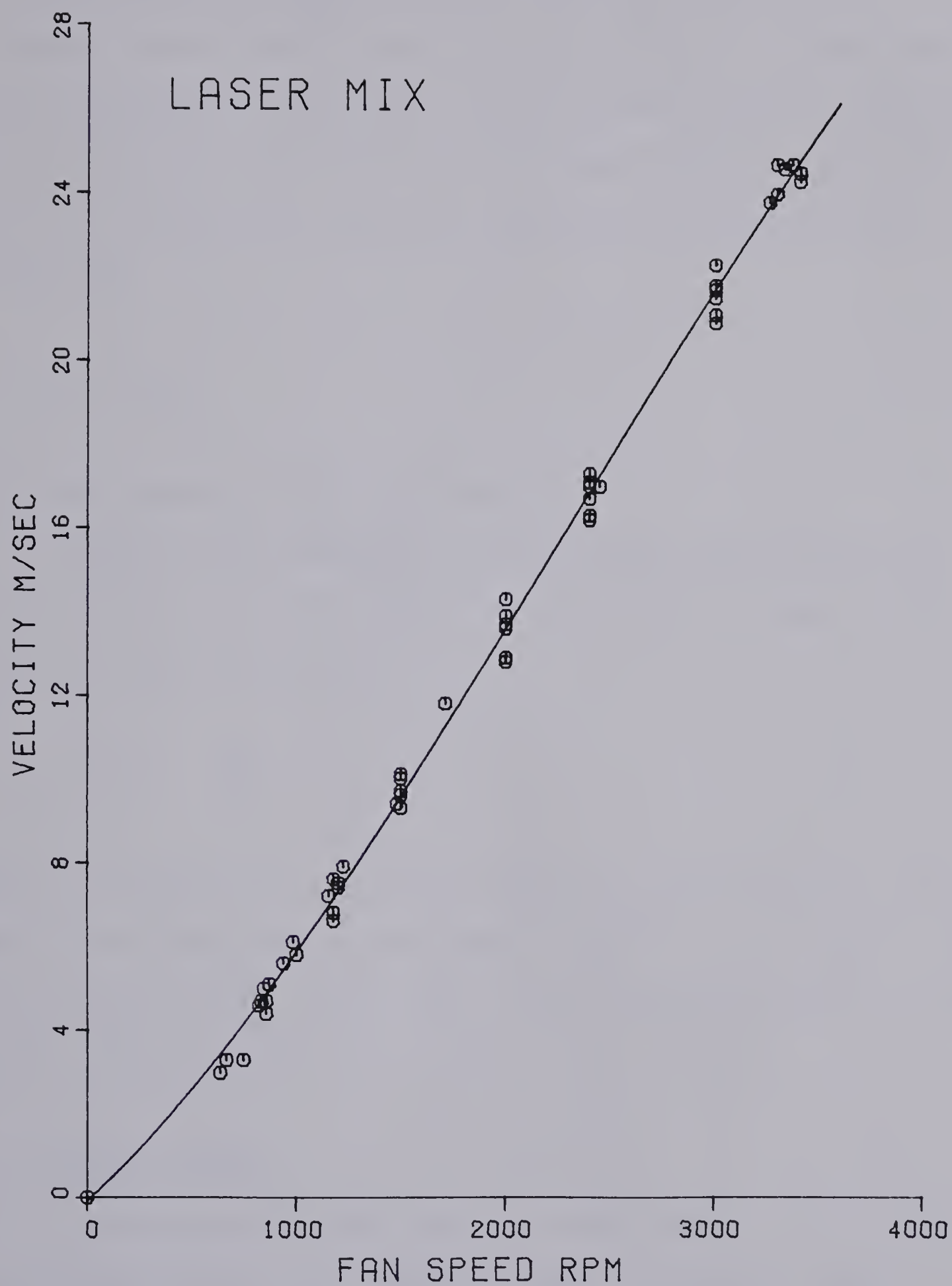


Fig. 5.7 Gas Flow Velocity Calibration Curve for a 1:1:8 $\text{CO}_2:\text{N}_2:\text{He}$ Laser Mixture in the Range from 400 to 700 Torr.

First the system volume was found. A one liter flask of air at 700 torr pressure was attached to the system with a connecting valve. Then the system was evacuated and the valve opened to allow air from the flask to expand into the system. The resulting pressure was then noted and from this information the system volume could be calculated using the gas law:

$$P_1 V_1 = P_2 V_2 .$$

The system volume was found to be 180 liters.

The leak rate is determined by pumping out the system and sealing it off, then observing the pressure rise over a period of time. It is calculated using the formula:

$$\text{leak rate} = V \frac{\Delta P}{\Delta T}$$

where V is system volume, ΔP is rise in pressure, and ΔT is time. The leak rate for this system was typically $1 \frac{\text{micron}}{\text{sec}}$ or $3.6 \frac{\text{torr}}{\text{hr}}$. This was a rise of 0.2 torr in 10.2 hours. So the system has very good vacuum integrity and contamination due to leaks is not a problem.

5.4 DISCHARGE CIRCUIT

The thyatron pulse circuit operated fairly reliably. It is capable of switching 120 nf at 10 Kv charging voltage and repetition rates of 300 pps. The limit here is due to discharge arcing rather than a limitation of circuit capability. Smaller capacitors can be switched at

higher repetition rates and 20 nf at 10 Kv charging was switched at repetition rates of up to 1 KHz without problems.

Several modifications were made to the circuit during the course of the experiments. Originally there were two preionization spark pins. The experiments demonstrated that discharge products from the upstream spark pin adversely affected the discharge uniformity so the upstream spark pin was removed from the system.

The other change involved replacing what was originally a discharge shunt resistor with a shunt inductor instead. The shunt element is needed in order for the main storage capacitor to charge up. Although the shunt resistor worked fine with He it was responsible for limiting capacitor values to 40 nf or less for N_2 and CO_2 . The problem was that the thyatron went into continuous conduction and was traced to the fact that the discharge in these gases would extinguish before the capacitor had discharged completely. When the discharge extinguished the residual voltage, typically 200 V for CO_2 , would be sufficient to force the thyatron into continuous conduction. In order to recover the thyatron needs zero or reverse voltage across it for a minimum of about 50 μ sec. This is to allow the charged gas in the tube to recombine to the point of being non-conducting. Replacing the shunt resistor by the shunt inductor allowed the residual charge to drain off the capacitor and caused the thyatron anode to ring slightly negative which helped aid its recovery.

A similar problem was encountered with the SCR in the thyatron drive circuit locking on occasionally, usually as a result of noise from high currents in the discharge circuit during arcs. This problem was traced to the voltage being reapplied to the SCR too quickly. The SCR remained reverse biased for only about 40 μ sec but it requires typically 75 μ sec to recover. Boosting the charging inductor from 7.5 mH to 2.6 H

increased the reverse bias period to over 100 μ sec which was sufficient for the SCR to recover reliably.

Typical voltage and current waveforms for the discharge are shown in Fig. 5.8. These waveforms are for a discharge in 60 torr N_2 but the waveforms in other gases were similar. The initial current spike is due to the spark pin coupling capacitor discharging while the main hump is due to the main storage capacitor discharging.

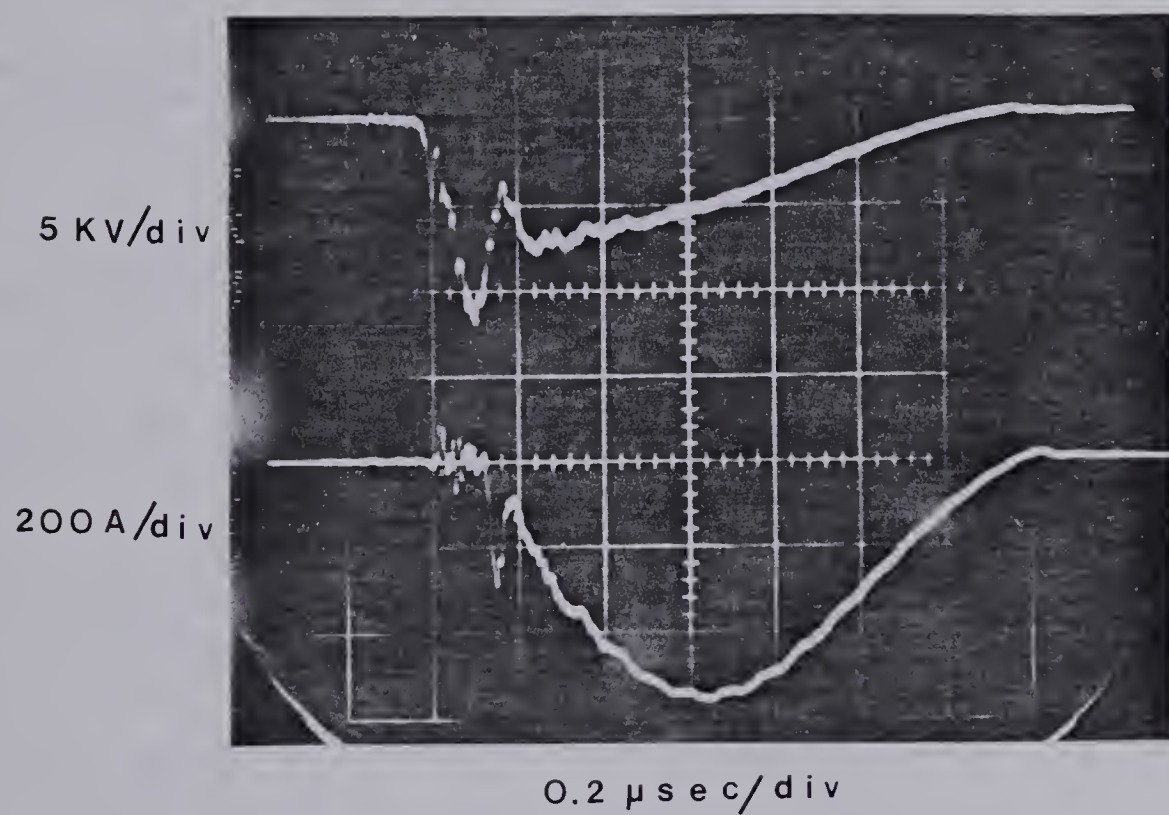


Fig. 5.8 Typical Voltage and Current Waveforms for a 60 Torr N_2 Discharge.

The discharge capacitor was 40 nf and the charging voltage was 10KV.

CHAPTER 6

RESULTS AND CONCLUSIONS

6.1 DEFINITIONS AND THEORY

In a high repetition rate pulsed glow discharge, discharge products are removed between pulses by convection. If they are not removed arcing results. The gas convection time, τ_{conv} ,

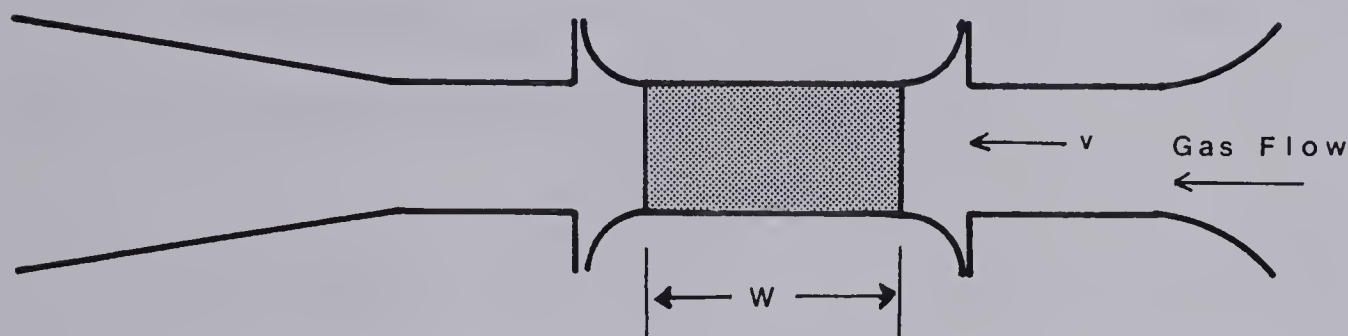


Figure 6.1 Schematic of discharge region showing terms used to define τ_{conv} .

is the time taken for the gas to traverse the discharge region

$$\tau_{\text{conv}} = \frac{W}{v}$$

and is the inverse of the ideal repetition rate, f_{ideal} . The minimum time between arc free pulses is the clearing time, τ_{clear} , and is the inverse of the maximum repetition rate. A clearing ratio is defined to compare the observed repetition rate with the gas convection time.

$$\text{CR} = \frac{\text{minimum time between arc free pulses}}{\text{time for gas to traverse gap}}$$

$$= \frac{1}{\frac{\text{PRF}}{W/v}} = \frac{v}{(\text{PRF})W}$$

6.1.1

where PRF is the maximum observed pulse frequency, or $\frac{1}{\tau_{\text{clear}}}$. The inverse of the clearing ratio is the fractional frequency

$$f_{\text{fractional}} = \frac{1}{\text{CR}} = \frac{W(\text{PRF})}{v} \quad 6.1.2$$

Usually the fractional frequency is less than one, that is, the repetition rate achieved is less than that predicted by taking the time for gas to traverse the electrodes as the interpulse period. Dzakowic and Wutzke (38) attribute the lower repetition rate to gas expansion due to heating from the energy deposited in it during the discharge. They predict that the resulting clearing ratio is given by:

$$\text{CR} = 1 + \frac{1}{2} \beta [(1 + \epsilon)^{1/\gamma} - 1] \quad 6.1.3$$

where: $\epsilon = \frac{(1-\eta)E_i}{\rho C_v T \text{ vol}}$ is the normalized energy density,

β is the ratio of upstream to interelectrode flow areas,

$\gamma = \frac{C_p}{C_v}$ is the ratio of specific heat capacities,

ρ is the density of the unheated gas,

T is the temperature of the unheated gas,

η is the electrical to optical energy conversion efficiency

so $(1-\eta)$ is the fraction of input electrical energy density, $\frac{E_i}{\text{vol}}$, that appears as heat.

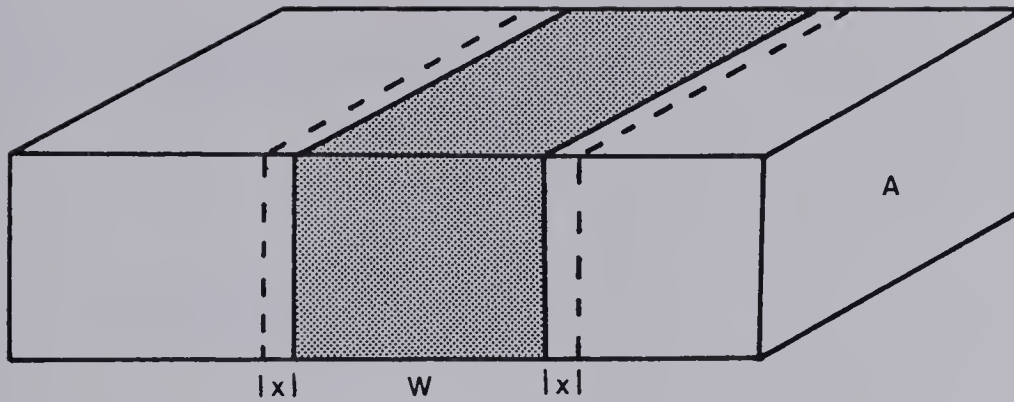


Figure 6.2 Geometry for derivation of gas expansion clearing ratio
(equation 6.1.3)

A simplified derivation will show how this expression was obtained. Consider a channel with cross sectional area, A , and a volume of gas WA in the channel. Suppose energy is suddenly deposited by a discharge in the gas along the width W . In that case the gas will heat up and the pressure in region WA will increase but the density will stay constant because the gas molecules have not yet had time to move.

$$P = \rho RT$$

so

$$\frac{P_1}{T_1} = \frac{P_2}{T_2} = \rho R$$

The energy deposited by the discharge is $\frac{3}{2} k\Delta T$ per molecule where ΔT is the change in temperature. So the total energy deposited for N molecules is:

$$\Delta E = \frac{3}{2} kN\Delta T$$

The new pressure then, is

$$P_2 = \frac{T_2}{T_1} P_1 = \frac{T + \Delta T}{T} P_1 = \left(1 + \frac{\Delta T}{T}\right) P_1$$

$$= \left(1 + \frac{\frac{\Delta E}{\frac{3}{2} kTN}}{\frac{3}{2} kTN}\right) P_1$$

The gas will then expand because the pressure in the heated gas is higher than the surrounding pressure. Assuming an adiabatic expansion:

$$P_2 V_2^\gamma = P_{\text{final}} V_{\text{final}}^\gamma$$

and let

$$\frac{\frac{\Delta E}{\frac{3}{2} kTN}}{\frac{3}{2} kTN} = \epsilon$$

then

$$V_{\text{final}}^\gamma = \frac{P_2 V_2^\gamma}{P_{\text{final}}} = \frac{(1 + \epsilon) P_1 V_2^\gamma}{P_{\text{final}}}$$

Assuming an essentially infinite duct, expansion will continue until

$P_{\text{final}} = P_1$ so:

$$V_{\text{final}}^\gamma = (1 + \epsilon) V_2^\gamma = (1 + \epsilon) V_{\text{initial}}^\gamma \quad 6.1.4$$

but

$$V_{\text{initial}} = WA$$

and

$$V_{\text{final}} = (W + 2x)A$$

so

$$W + 2x = (1 + \epsilon)^{1/\gamma} W$$

or

$$x = \frac{W}{2} [(1 + \epsilon)^{1/\gamma} - 1]$$

The clearing time will be increased from τ_{conv} by the amount of time needed to clear the gas the additional distance x past the electrodes.

$$\tau_{\text{clear}} = \frac{x + W}{v} = \frac{x}{v} + \frac{W}{v}$$

$$\text{CR} = \frac{\tau_{\text{clear}}}{\tau_{\text{conv}}} = \frac{\frac{W+x}{v}}{W/v} = \frac{W + \frac{W}{2}[(1 + \epsilon)^{1/\gamma} - 1]}{W}$$

$$= 1 + \frac{1}{2}[(1 + \epsilon)^{1/\gamma} - 1] \quad 6.1.5$$

The expression

$$\epsilon = \frac{\Delta E}{\frac{3}{2} kTN}$$

can be put in a form corresponding to 6.1.3.

$$\epsilon = \frac{\Delta E}{\frac{3}{2} kTN} = \frac{\Delta E}{\text{vol}} \frac{\text{vol}}{\frac{3}{2} kTN}$$

but

$$k = \frac{R}{N_A} = \frac{R}{N/n} = \frac{Rn}{N} = \frac{Rm}{M}$$

Where:

n is number of gram moles

N is number of molecules

m is mass of a molecule

M is molecular weight

so

$$\epsilon = \frac{\Delta E}{\text{vol}} \frac{\text{vol}}{\frac{3}{2} R \frac{m}{M} TN}$$

but $\frac{\text{vol}}{mN} = \frac{1}{\rho}$ and $c_v = \frac{3}{2} R$ for a monatomic gas

so

$$\epsilon = \frac{\Delta E}{\text{vol}} \frac{1}{\rho \frac{c_v}{M} T}$$

so 6.1.5 is essentially the same as Dzakowic and Wutzke's expression,

6.1.3, except that the $(1 - \eta)$ term has been ignored and β was set equal to 1.

A slightly different expression is applicable for the gas expansion in the flowing gas discharge system since the discharge has a cylindrical geometry (Fig. 6.3).

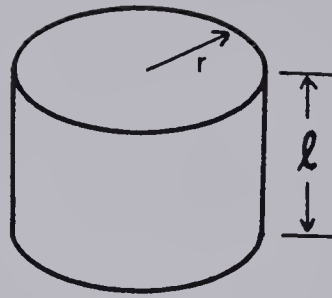


Figure 6.3 Geometry of cylindrical discharge

Going back to 6.1.4

$$V_{\text{final}} = (1 + \varepsilon)^{1/\gamma} V_{\text{initial}}$$

$$V_{\text{initial}} = \pi r_1^2 l$$

$$V_{\text{final}} = \pi r_2^2 l$$

so

$$\pi r_2^2 l = (1 + \varepsilon)^{1/\gamma} \pi r_1^2 l$$

$$r_2^2 = (1 + \varepsilon)^{1/\gamma} r_1^2$$

$$r_2 = \sqrt{(1 + \varepsilon)^{1/\gamma}} r_1 \quad 6.1.6$$

$$r_2 = r_1 + x$$

$$r_1 + x = \sqrt{(1 + \epsilon)^{1/\gamma}} r_1$$

$$x = r_1 [\sqrt{(1 + \epsilon)^{1/\gamma}} - 1]$$

so the clearing ratio is

$$CR = \frac{\frac{x + 2r_1}{v}}{\frac{2r_1}{v}} = \frac{x + 2r_1}{2r_1}$$

$$= \frac{r_1 [\sqrt{(1 + \epsilon)^{1/\gamma}} - 1] + 2r_1}{2r_1}$$

$$= 1 + \frac{1}{2} [\sqrt{(1 + \epsilon)^{1/\gamma}} - 1] \quad 6.1.7$$

If the interelectrode and upstream cross-sectional areas are different the expression for clearing time is modified.

$$\tau_{\text{clear}} = \frac{x}{v/\beta} + \frac{W}{v}$$

where β is the ratio of upstream to interelectrode areas. Then the clearing ratio becomes

$$CR = \frac{\frac{x}{v/\beta} + \frac{W}{v}}{\frac{W}{v}} = \frac{\frac{r_1 [\sqrt{(1 + \epsilon)^{1/\gamma}} - 1]}{v/\beta} + \frac{2r_1}{v}}{\frac{2r_1}{v}}$$

$$= 1 + \frac{1}{2} \beta [\sqrt{(1 + \epsilon)^{1/\gamma}} - 1] \quad 6.1.8$$

In the case of Dzakowic and Wutzke equation 6.1.3 is obtained instead of equation 6.1.5.

For small energy densities the clearing ratio should tend to 1 so the repetition rate should tend to f_{ideal} according to the above formulas. However Dzakowic and Wutzke argue that the upper limit on repetition rate is

$$f = \frac{f_{\text{ideal}}}{\sqrt{3}} \quad , \text{ or } CR = \sqrt{3} \quad .$$

This is because in the boundary layer convection effects are small and the discharge products are removed by diffusion to the electrode surfaces where recombination then occurs. The diffusion length, δ_D , is defined as the distance into the boundary layer from the electrode surface at which both diffusion time and convection time are equal. The diffusion time is given by:

$$\tau_{\text{diff}} = \frac{\delta_D^2}{\lambda \bar{c}}$$

where λ is the mean free path and \bar{c} the mean speed of the particles. Then assuming a laminar boundary layer they calculate a diffusion time of:

$$\tau_{\text{diff}} = \sqrt{3} \frac{W}{v} \quad \text{or } CR = \sqrt{3} \quad .$$

Notice that the low energy limit is independent of gas type, gas density, and energy density.

Although their data supported this low energy density repetition rate limit for energy densities less than about 30 J/l my own experiments

did not. For the flowing gas discharge system, if the energy density was low enough, several pulses per gas change could be achieved before an instability occurred. As a result $CR < 1$ and hence repetition rates $> f_{ideal}$ were observed. Olson et al (21) also report achieving clearing ratios of < 1 .

6.2 GAS TYPES

The discharge characteristics of the three CO_2 laser gases CO_2 , N_2 , and He were investigated separately and in combination. This is because theoretical calculations are easier for the individual gases than for a mixture and also to see if the repetition rate effects could be attributed to one particular gas of the three. The repetition rate effects are more likely to be common to all three gases or to be due to one gas than they are to be due to some special combination of the three.

For the individual gases 60 torr N_2 , 80 torr CO_2 and 700 torr He were chosen. The different pressures were chosen because they all had a 10 KV breakdown voltage. The three gases had very different discharge characteristics. Helium was the most stable and discharges could be easily formed. It formed the largest diameter discharge and at high repetition rates tended to form a nonuniform glow rather than a bright arc. CO_2 formed the smallest diameter discharge and, for low energy densities, the repetition rate induced arc tended to be between the electrodes rather than from the cathode to the spark pin. N_2 formed a discharge between CO_2 and He in diameter. A unique feature of N_2 was the production of long lived metastables, characterized by a long-lived orange glow, which were accompanied by high electron densities (38). This tended to promote tracking problems in N_2 , and N_2 usually arced from the cathode to the

downstream spark pin rather than between the electrodes.

6.3 EFFECT OF SPARK PINS ON THE SYSTEM

In the laser system it was observed that mounting the preionizing spark pins upstream from the discharge appeared to cause discharge arcing, presumably because of discharge products from the spark pins blowing downstream into the discharge. An experiment was done in the flowing gas discharge system to verify the effect.

Two spark pins were mounted in the system, one upstream and one downstream from the discharge. Discharges were then observed in 700 torr He, 60 torr N_2 , 80 torr CO_2 , a He- N_2 mixture, and a He- CO_2 mixture. Discharge uniformity and maximum repetition rate attainable before bright arcs occurred were compared for the system with both spark pins and with just the downstream spark pin operating. The maximum repetition rates both with and without the upstream spark pin are shown in Figures 6.4 to 6.8. As can be seen, the upstream spark pin had no detrimental effect on the He discharge but in N_2 , CO_2 , and the N_2 -He and CO_2 -He gas mixtures the maximum repetition rate was noticeably lower.

For all the runs the storage capacitor was 1960 pf and the charging voltage 10 KV. This is an energy density of about 0.1 J or an energy density of about 1.2 J/l for each pulse. Because the energy density was so low it was possible to achieve very high repetition rates. For instance, in 700 torr He for a fan speed of 3500 rpm the gas flow velocity was about 26 m/sec. For a clearing ratio of 1 the maximum repetition rate that could be achieved would be 300 to 400 Hz instead of close to 2000 Hz as was achieved. Since the energy density was so low several pulses could be produced per gas change before arcing occurred.

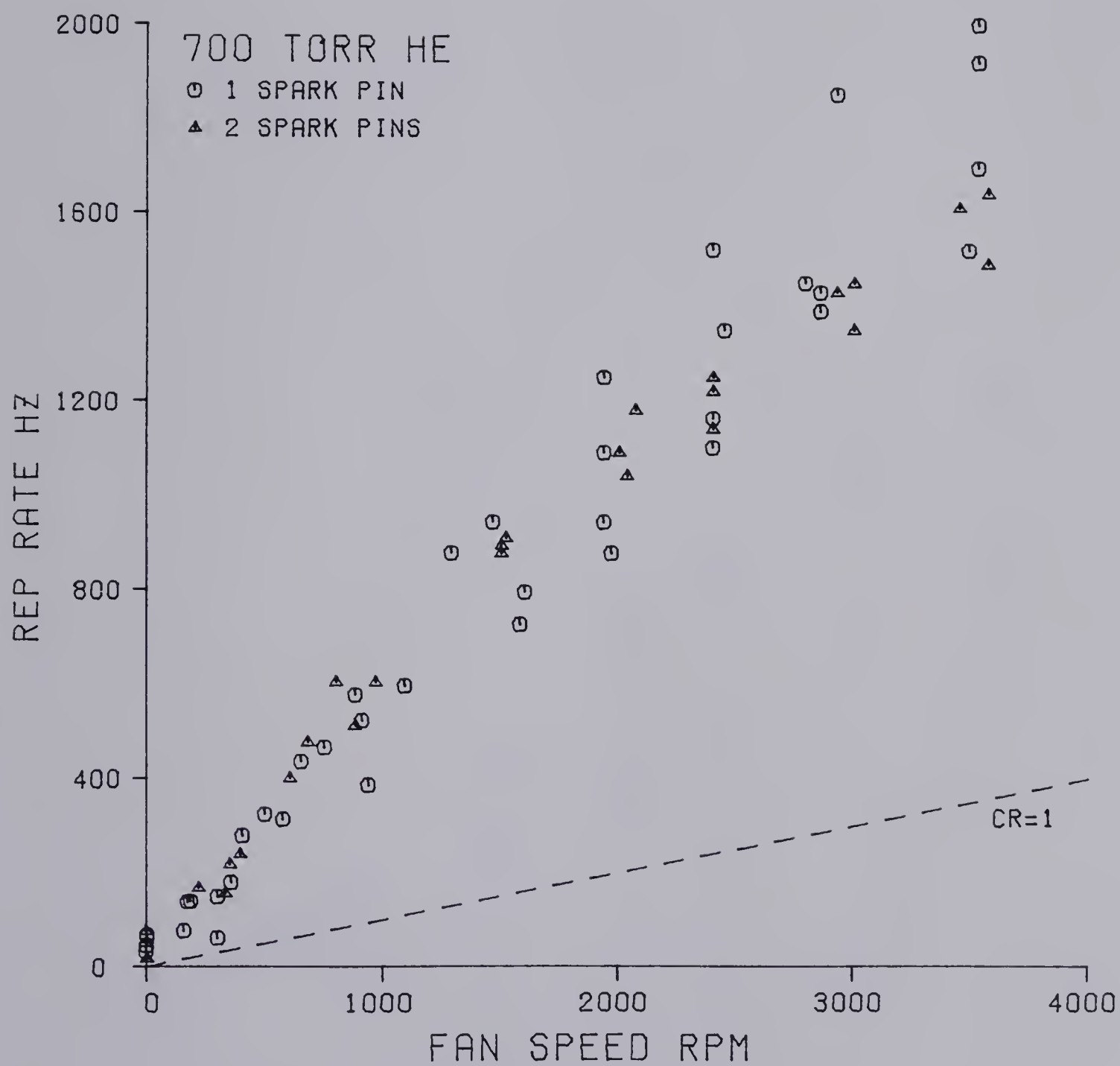


Fig. 6.4 Effect of Upstream and Downstream Spark Pins on Arc Free Repetition Rate for 700 Torr He.

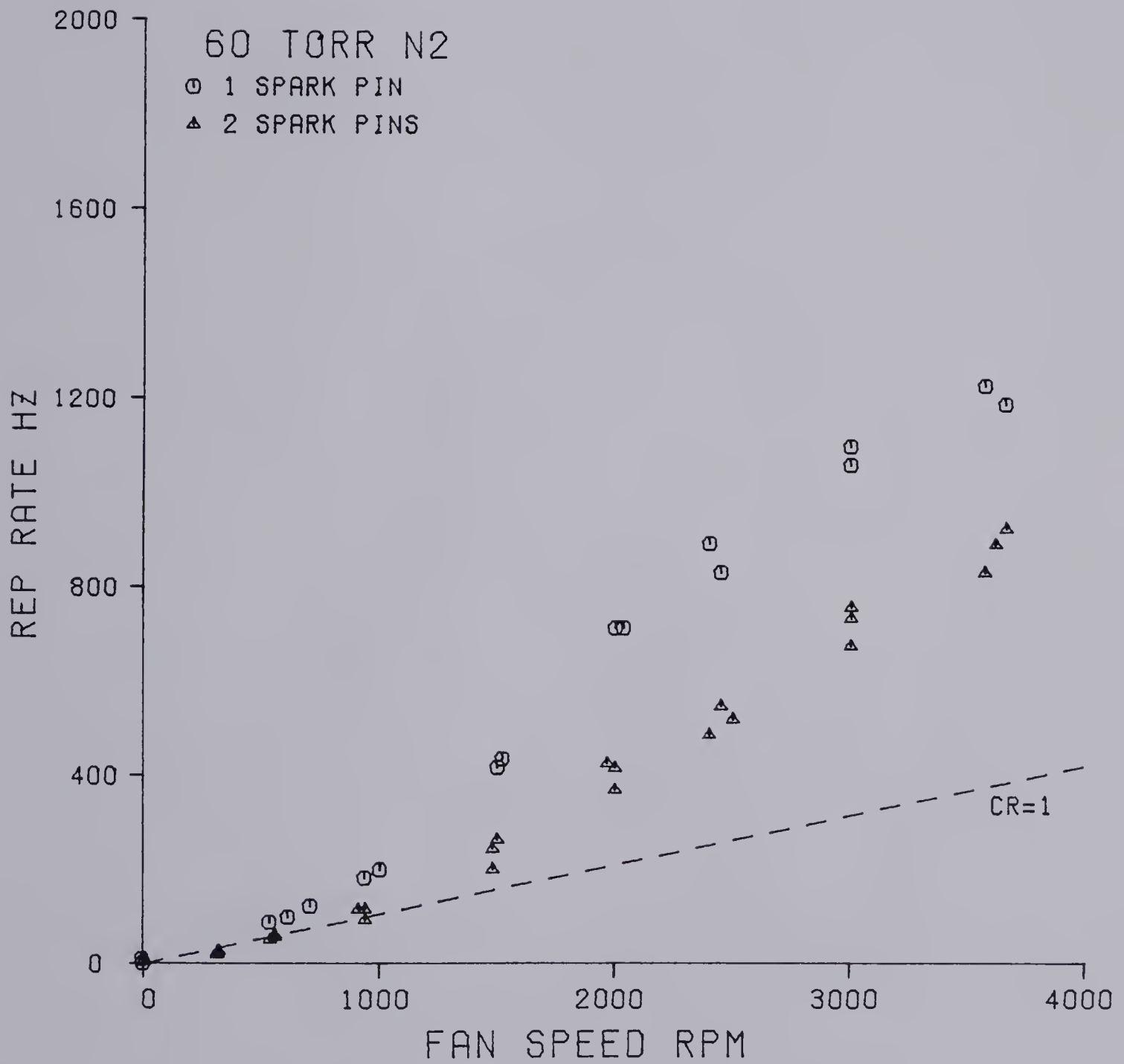


Fig. 6.5 Effect of Upstream and Downstream Spark Pins on Arc Free Repetition Rate for 60 Torr N₂.

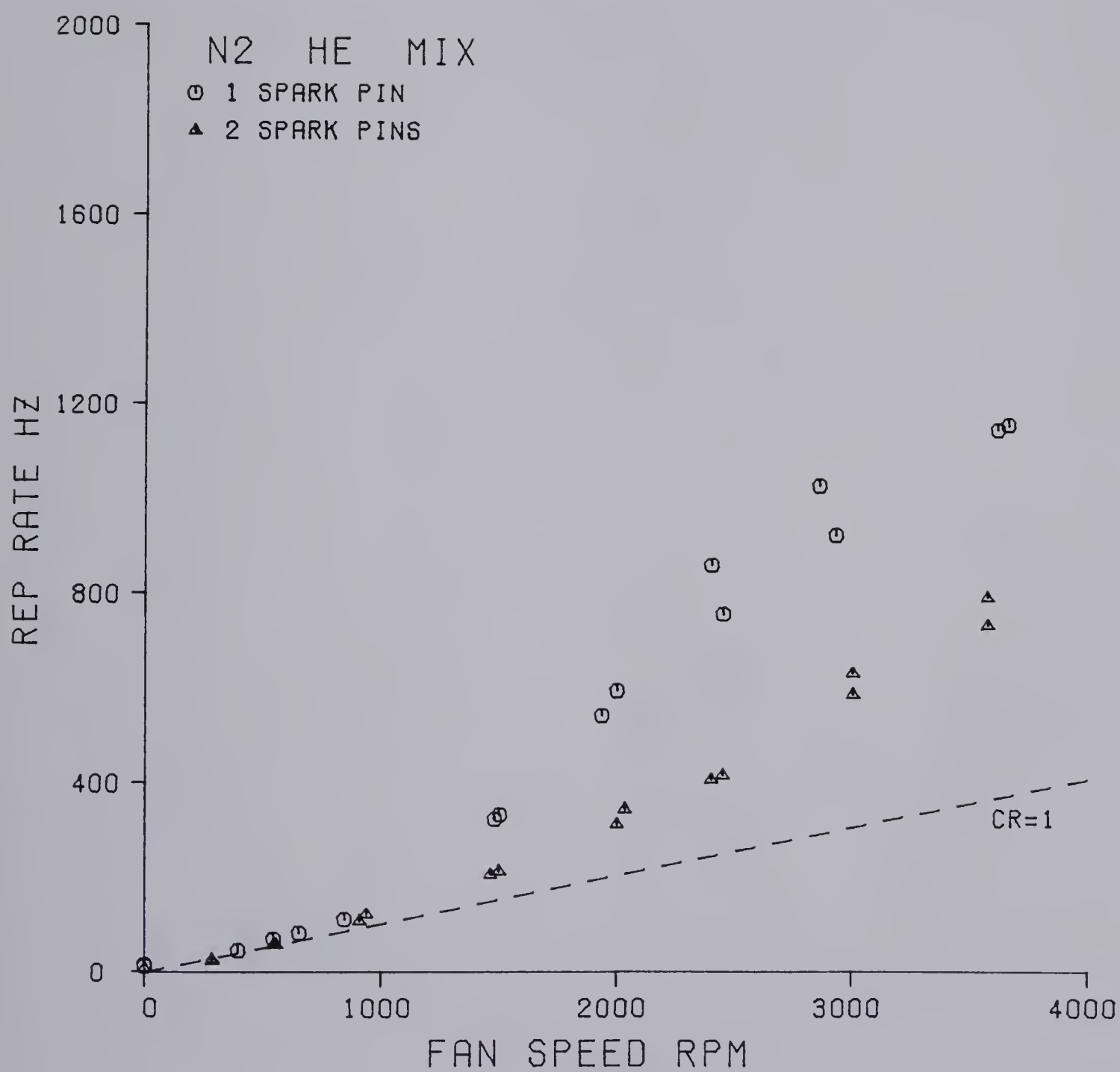


Fig. 6.6 Effect of Upstream and Downstream Spark Pins on Arc Free Repetition Rate for a Mixture of 40 Torr N_2 and 120 Torr He.

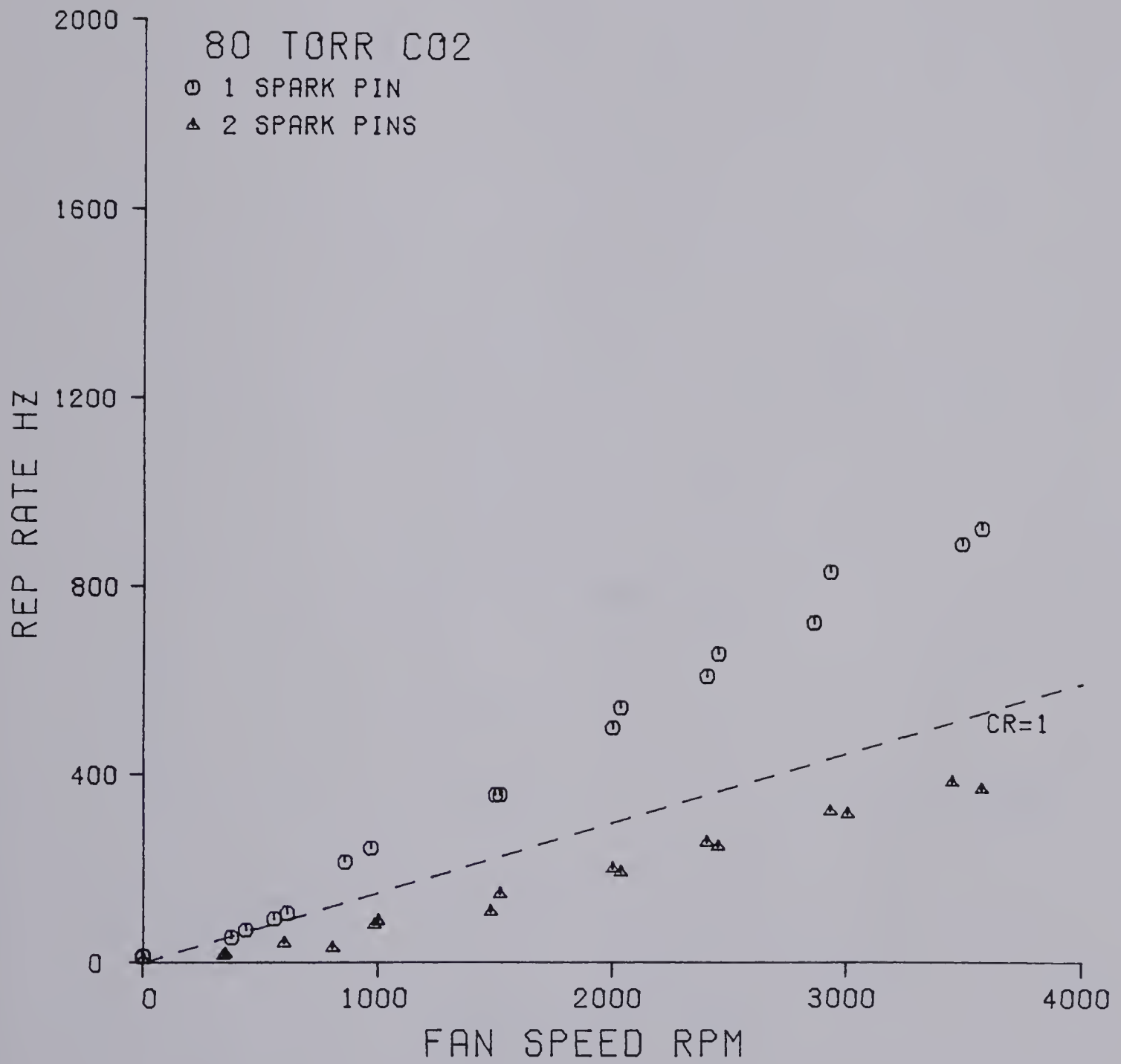


Fig. 6.7 Effect of Upstream and Downstream Spark Pins on Arc Free Repetition Rate for 80 Torr CO₂.

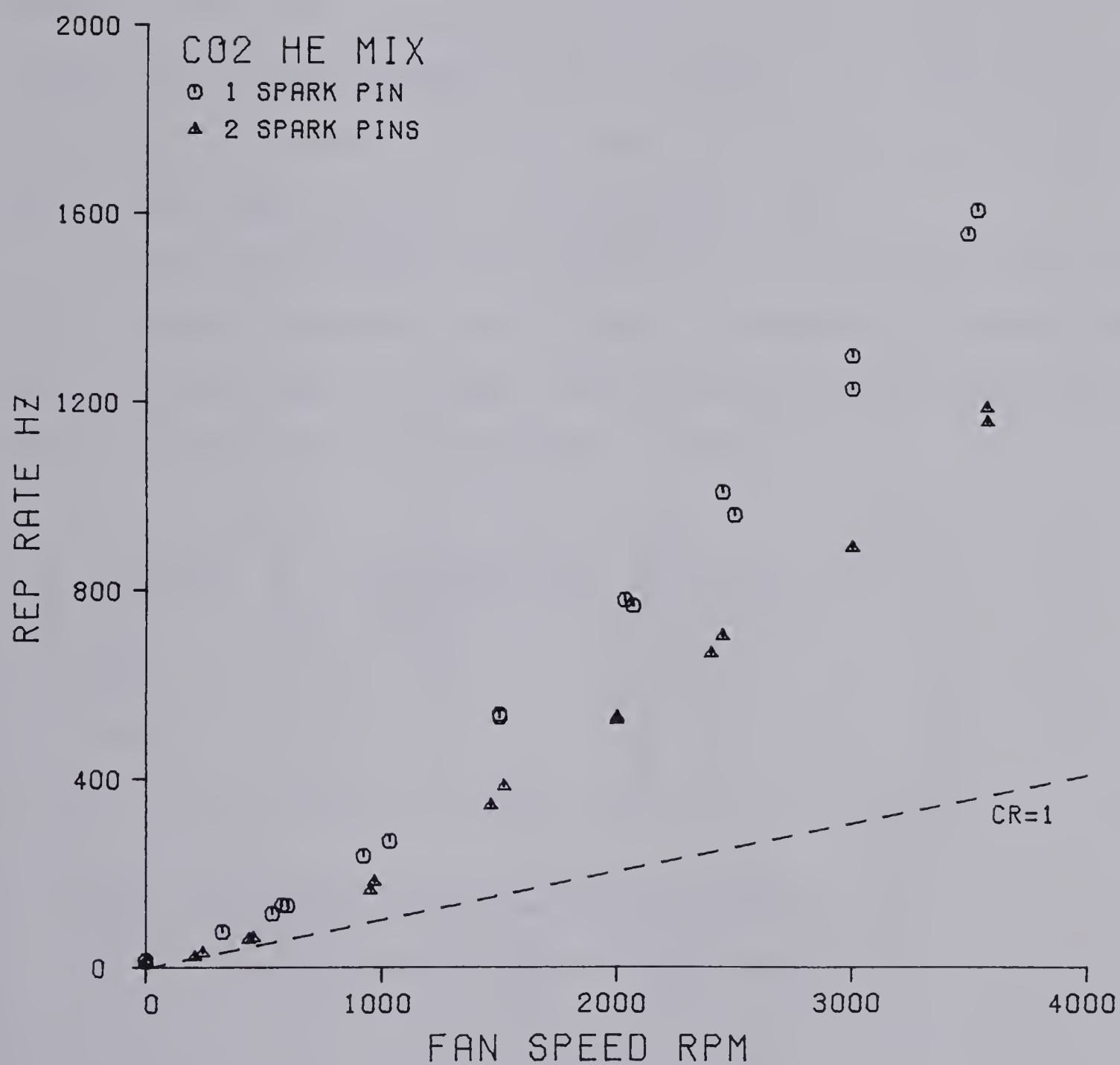


Fig. 6.8 Effect of Upstream and Downstream Spark Pins on Arc Free Repetition Rate for a Mixture of 40 Torr CO_2 and 200 Torr He.

Besides affecting the maximum repetition rate in CO_2 and N_2 , the discharge uniformity was noticeably affected whereas the uniformity of the He discharge was not. In N_2 the discharge contracted into a narrow band downstream from the spark pin rather than filling the electrode (Fig. 6.9). In CO_2 the effect was even more interesting. The discharge formed a constricted glow column approximately 1 cm in diameter and located near the upstream edge of the electrodes. For a fixed gas flow increasing the repetition rate would lead to two, then three, four and five columns spaced one behind the other (Fig. 6.10).

By observing the number and spacing of the CO_2 discharge columns for two fan speeds the gas flow velocity could be estimated and compared with the calibration values. The flow velocity estimates are shown in Table 6.1 and are based on the results displayed in Table 6.2.

fan speed rpm	calibration flow mm/msec	observed flow mm/msec
3529	26	25 ± 4
2000	13	12 ± 2

Table 6.1 Estimates of flow velocity based on the
observation of column discharges in CO_2

The discharge spacing was measured with a ruler placed against the discharge chamber window, and the results are subject to a parallax error of about $\pm 1/16''$. In addition, the spacing of the columns was not uniform but rather tended to decrease toward the downstream edge due to

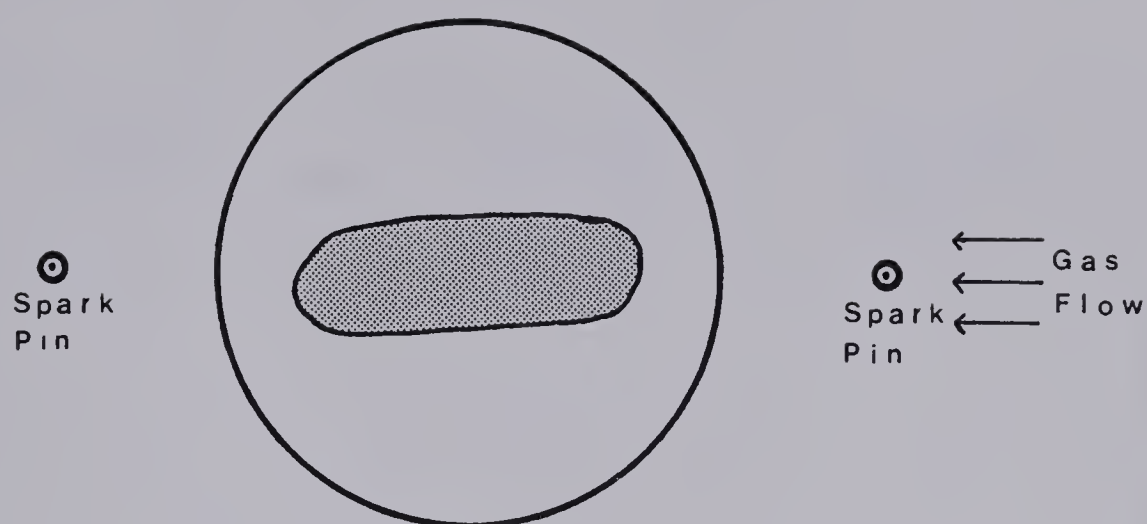


Fig. 6.9 Cross-sectional View of Constricted Discharge in N_2 .

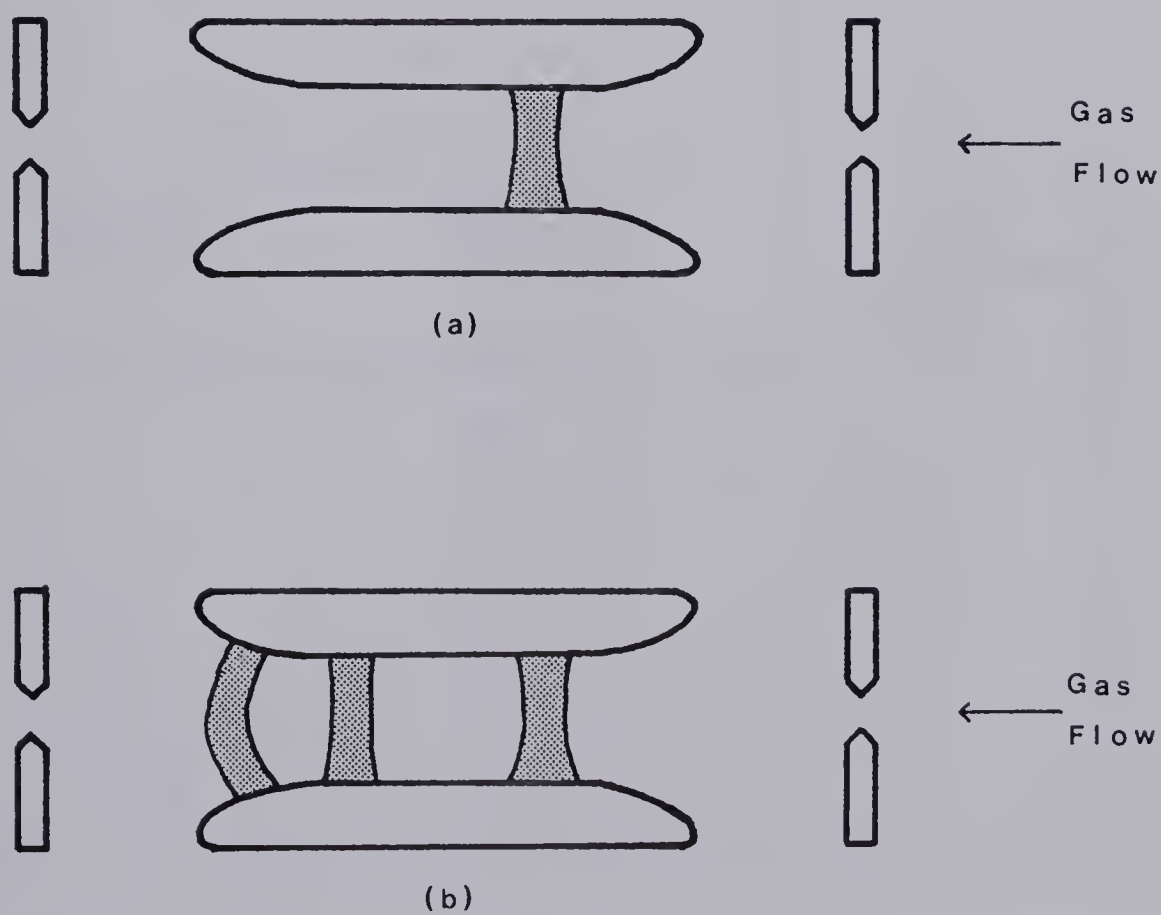


Fig. 6.10 Column Discharges in CO_2 . (a) Shows a single column and (b) shows multiple columns.

Fan speed 3529 rpm

# of glow columns	approx. spacing inches	discharge period msec	estimated flow velocity mm/msec
1		2.75	
2	2	2.25	23
3	1 1½	1.55	25
4	¼ 1 1¼	1.10	29
5	½ ¾ ¾ ¾	0.80	24

Fan speed 2000 rpm

# of glow columns	approx. spacing inches	discharge period msec	estimated flow velocity mm/msec
1		5.3	
2	2	4.5	11
3	¾ 1¼	2.9	11
4	½ 1 ⅞	2.0	13
5	¾ ½ ⅞ ⅞	1.6	14

Table 6.2 Discharge column spacing

Since the column spacing decreases downstream the flow velocity estimate uses the largest column spacing. It was obtained by taking the largest spacing and dividing it by the discharge period.

electrode curvature. But the data is adequate to show that the multiple discharge spacing corresponds to an ionized plug of gas being blown downstream. The initial plug comes from the upstream spark pin and results in a highly localized discharge. Subsequent discharges then form in this plug as it blows downstream because of its localized high pre-ionization density, resulting in the multiple glows. Since CO_2 forms multiple glow columns in the presence of an upstream spark pin instead of bright arcs the maximum repetition rate for two spark pins shown in Fig. 6.7 is the maximum repetition rate for a single glow column rather than for a bright arc.

This experiment shows that products from an upstream spark pin can be detrimental to the operation of a glow discharge. In particular CO_2 , N_2 , and mixtures containing them are affected while He is not. This could be because the detrimental products are not generated in pure He or because He is immune to their effects.

6.4 REPETITION RATE VERSUS GAS FLOW VELOCITY

Maximum repetition rate, for a uniform discharge with no arcing, increases linearly with gas flow velocity. This was verified for each of the three laser gases and for discharge energy densities ranging from 10 to 60 J/l. Typical results are shown in Figures 6.11 to 6.19. The dashed lines represent the ideal maximum repetition rate, while the circles are observed data points. The solid line is a least squares fit to the data points constrained to pass through the origin.

Although repetition rate increases linearly with gas flow, it is typically lower than the ideal repetition rate. This is in agreement with observations by other researchers (18, 19). Also, as was pointed

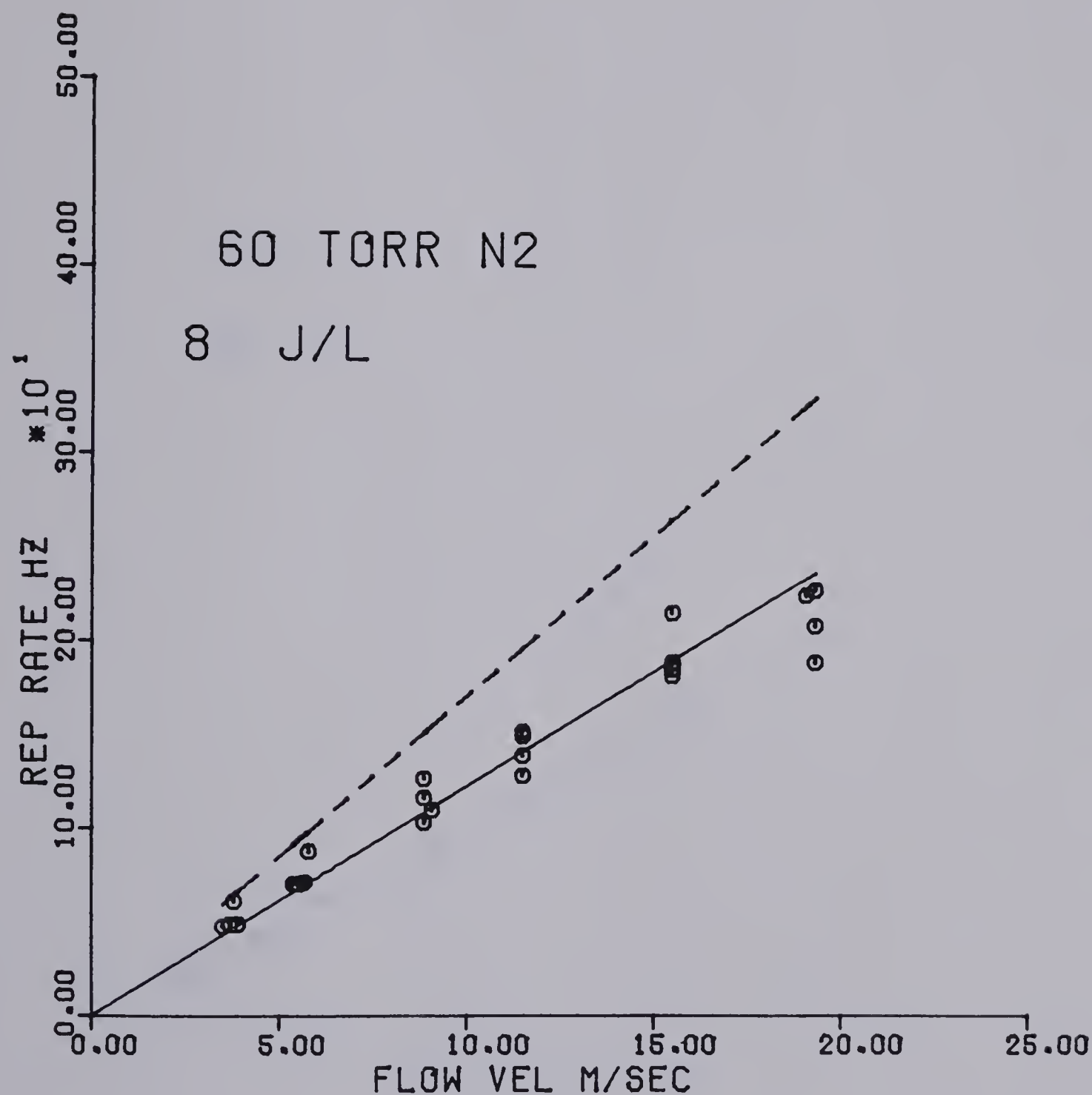


Fig. 6.11 Repetition Rate Versus Gas Flow Velocity.

Data for 60 Torr N₂ and 8 J/l Energy Density.

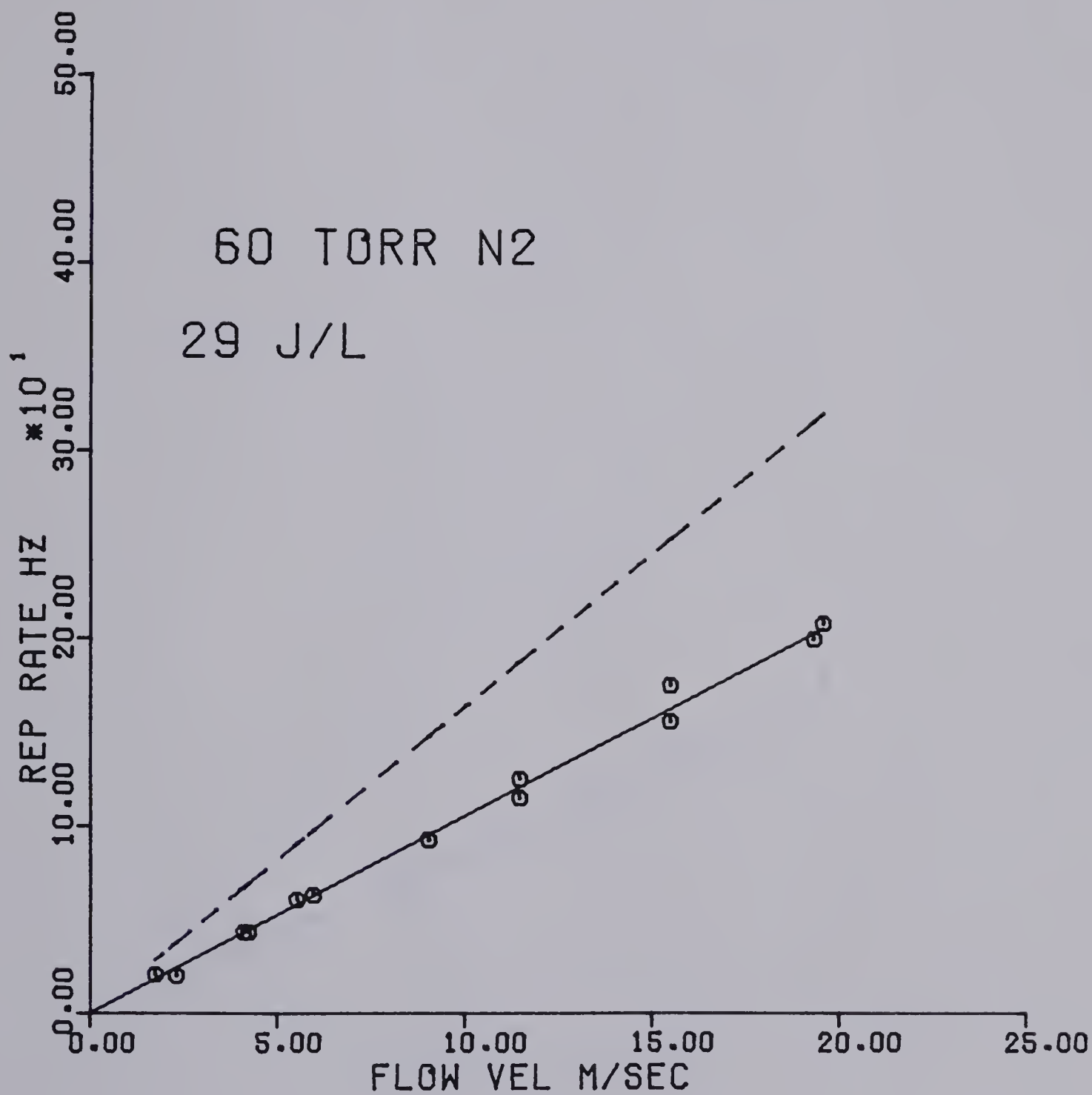


Fig. 6.12 Repetition Rate Versus Gas Flow Velocity.

Data for 60 torr N₂ and 29 J/l energy density.

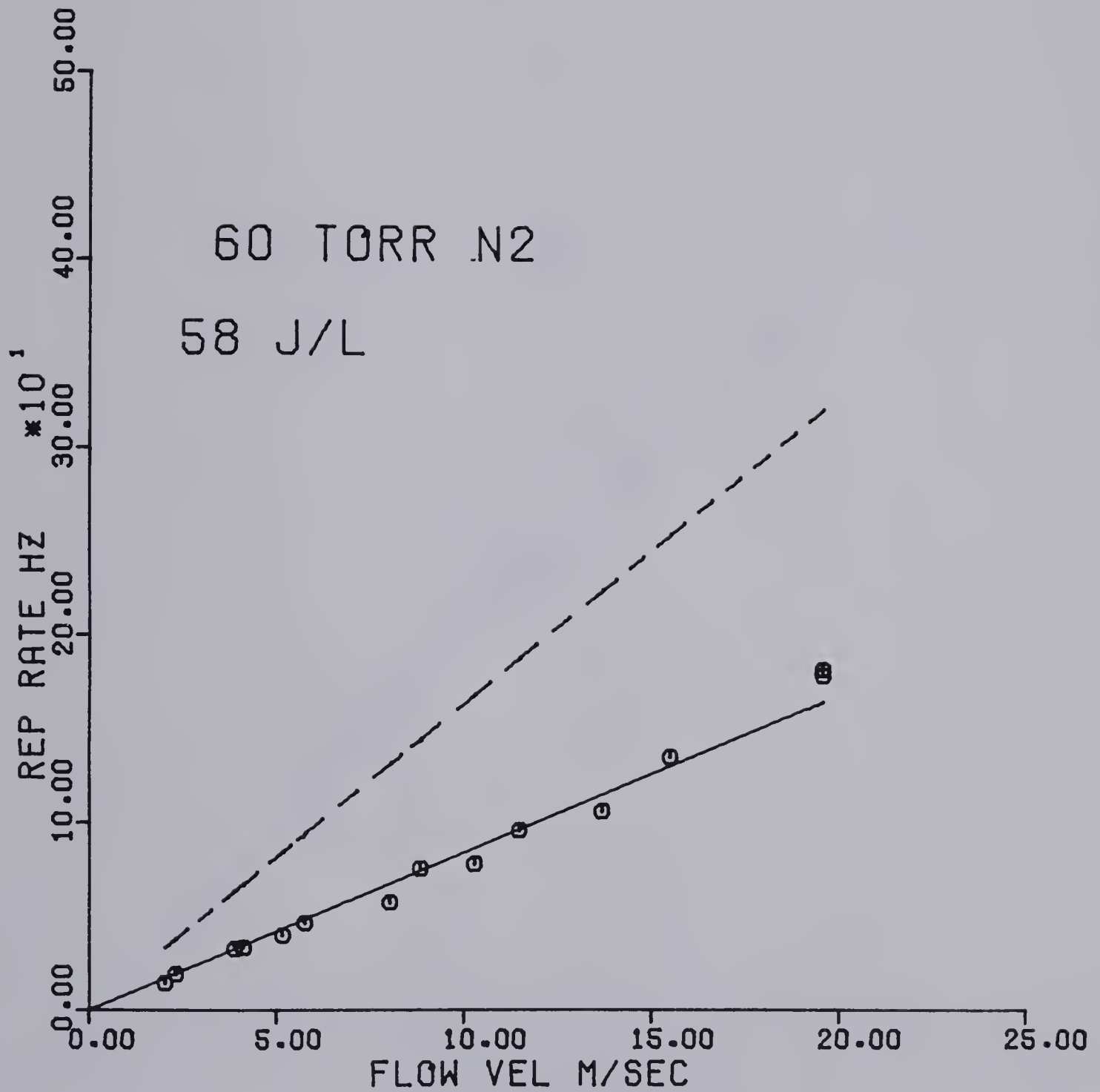


Fig. 6.13 Repetition Rate Versus Gas Flow Velocity.

Data for 60 torr N₂ and 58 J/l energy density.

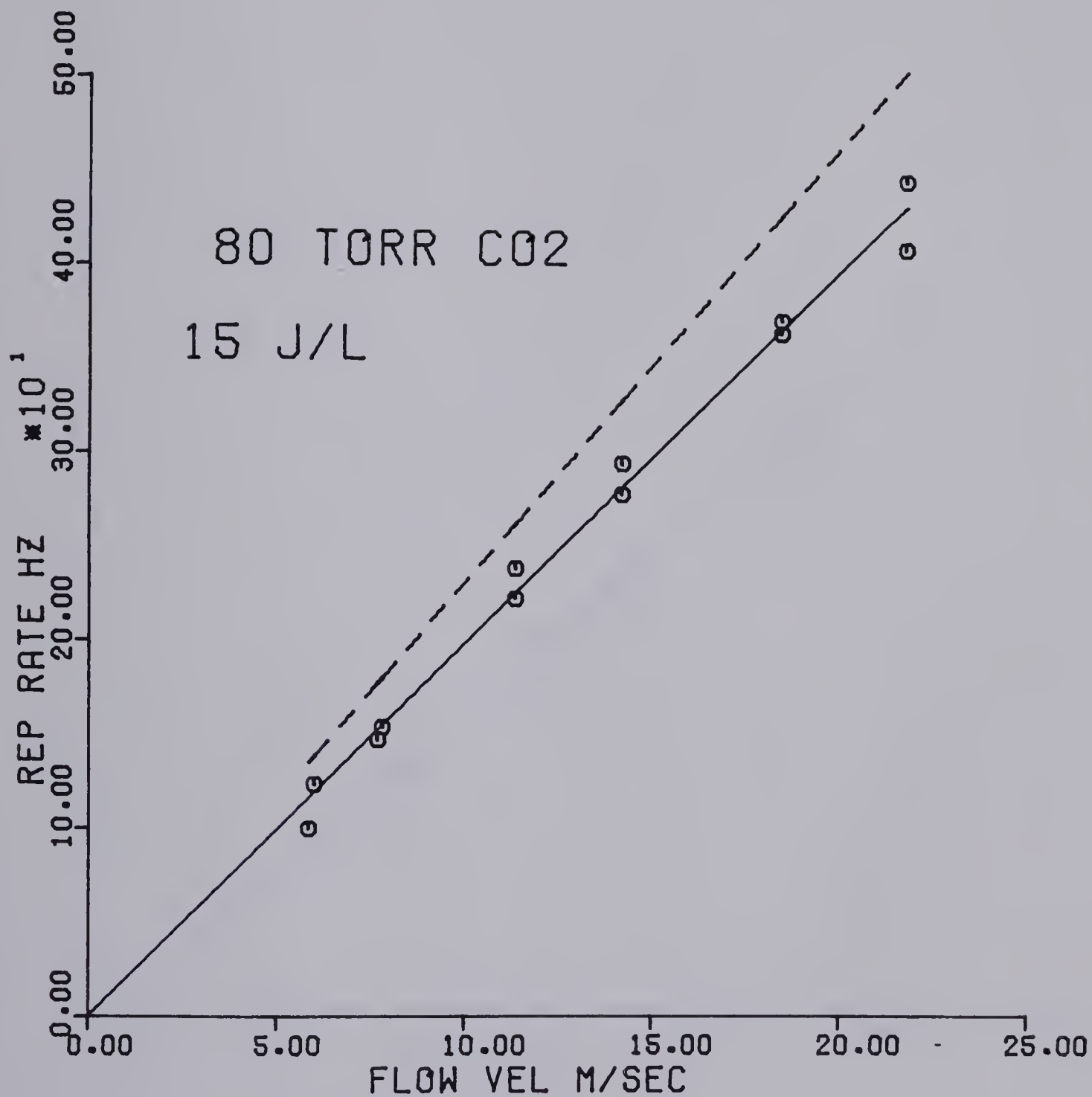


Fig. 6.14 Repetition Rate Versus Gas Flow Velocity.

Data for 80 torr CO₂ and 15 J/l energy density.

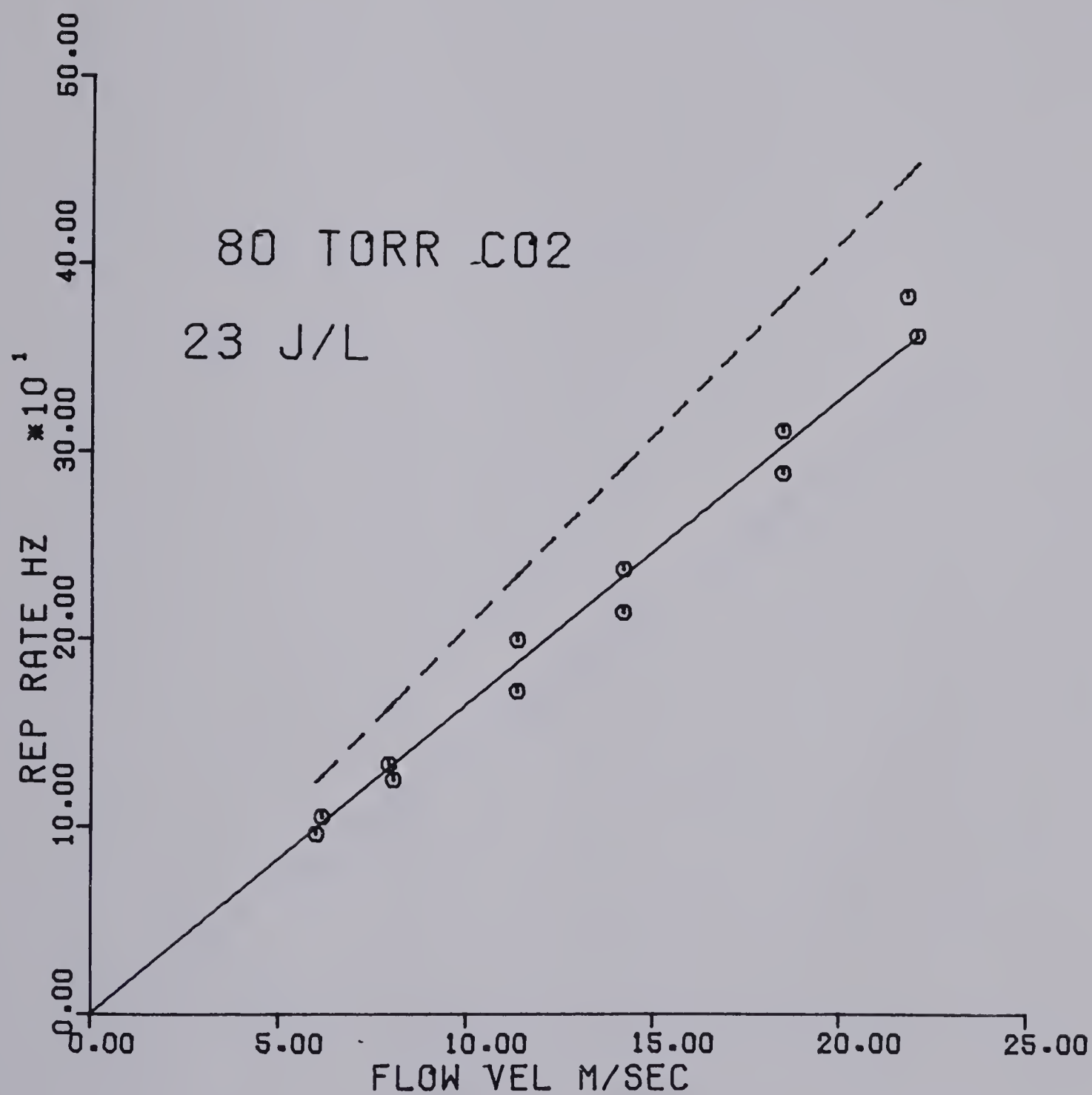


Fig. 6.15 Repetition rate versus gas flow velocity.

Data for 80 torr CO₂ and 23 J/l energy density.

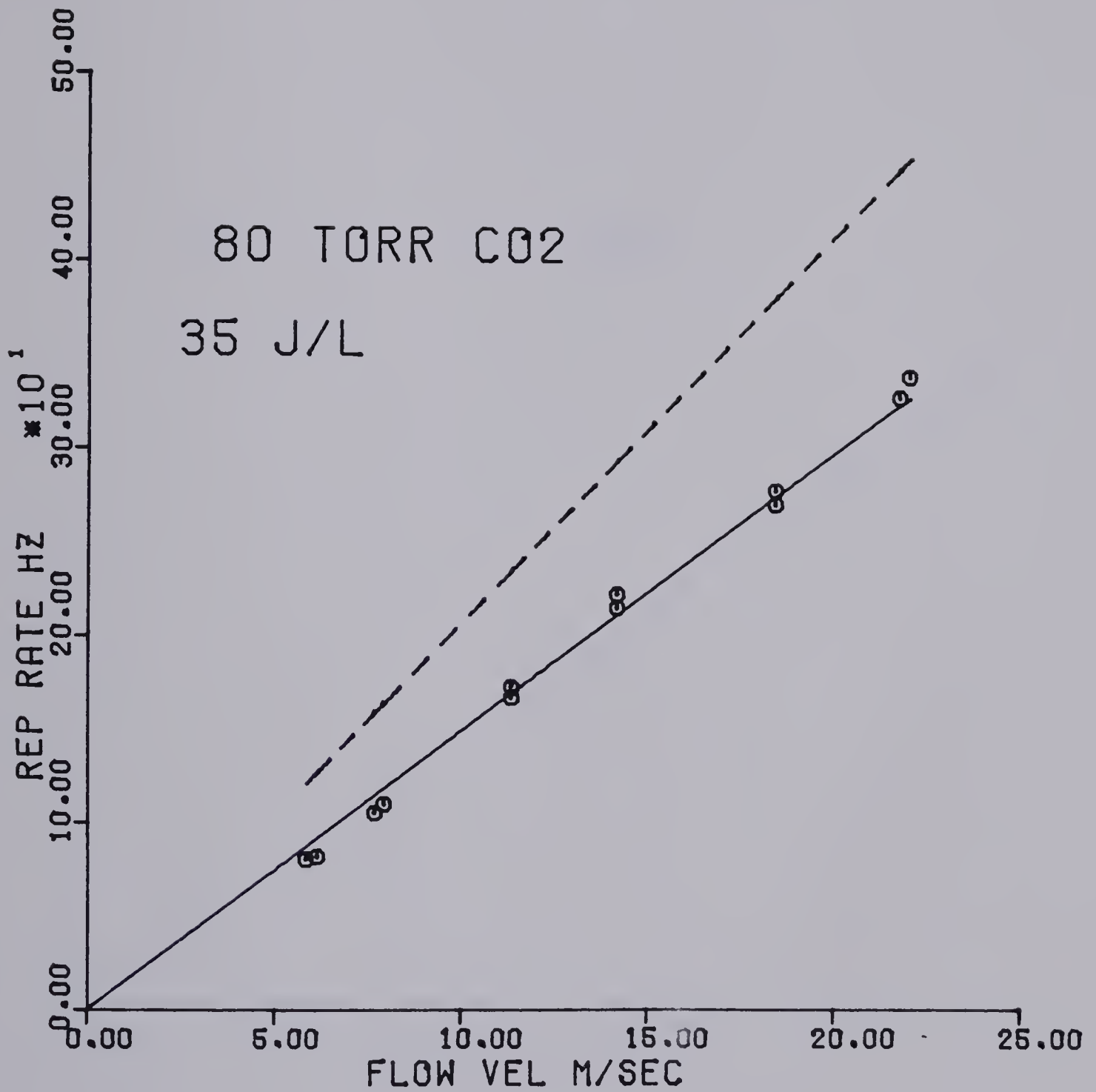


Fig. 6.16 Repetition Rate Versus Gas Flow Velocity.

Data for 80 torr CO₂ and 35 J/l energy density.

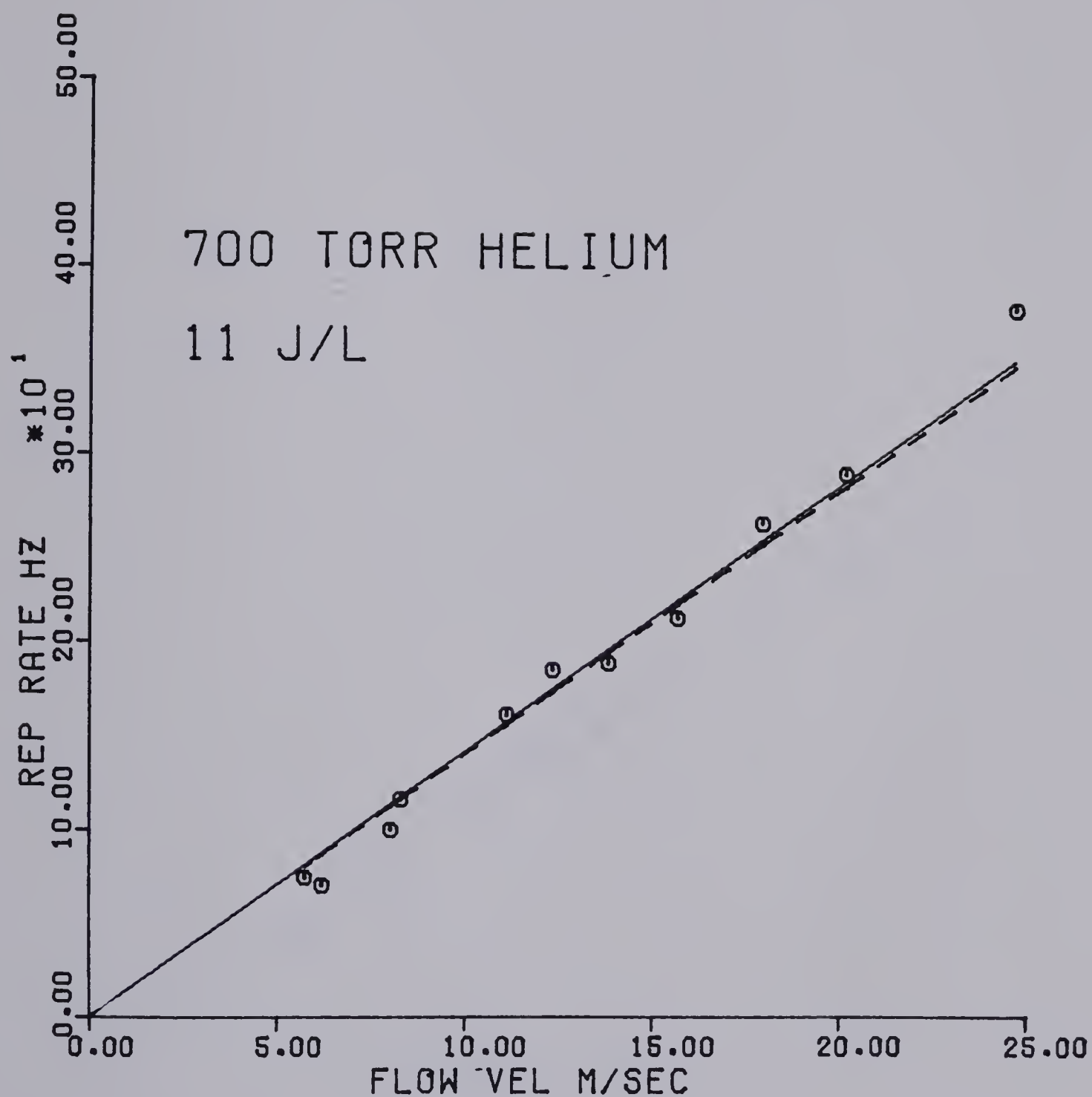


Fig. 6.17 Repetition Rate Versus Gas Flow Velocity.

Data for 700 torr He and 11 J/l energy density.

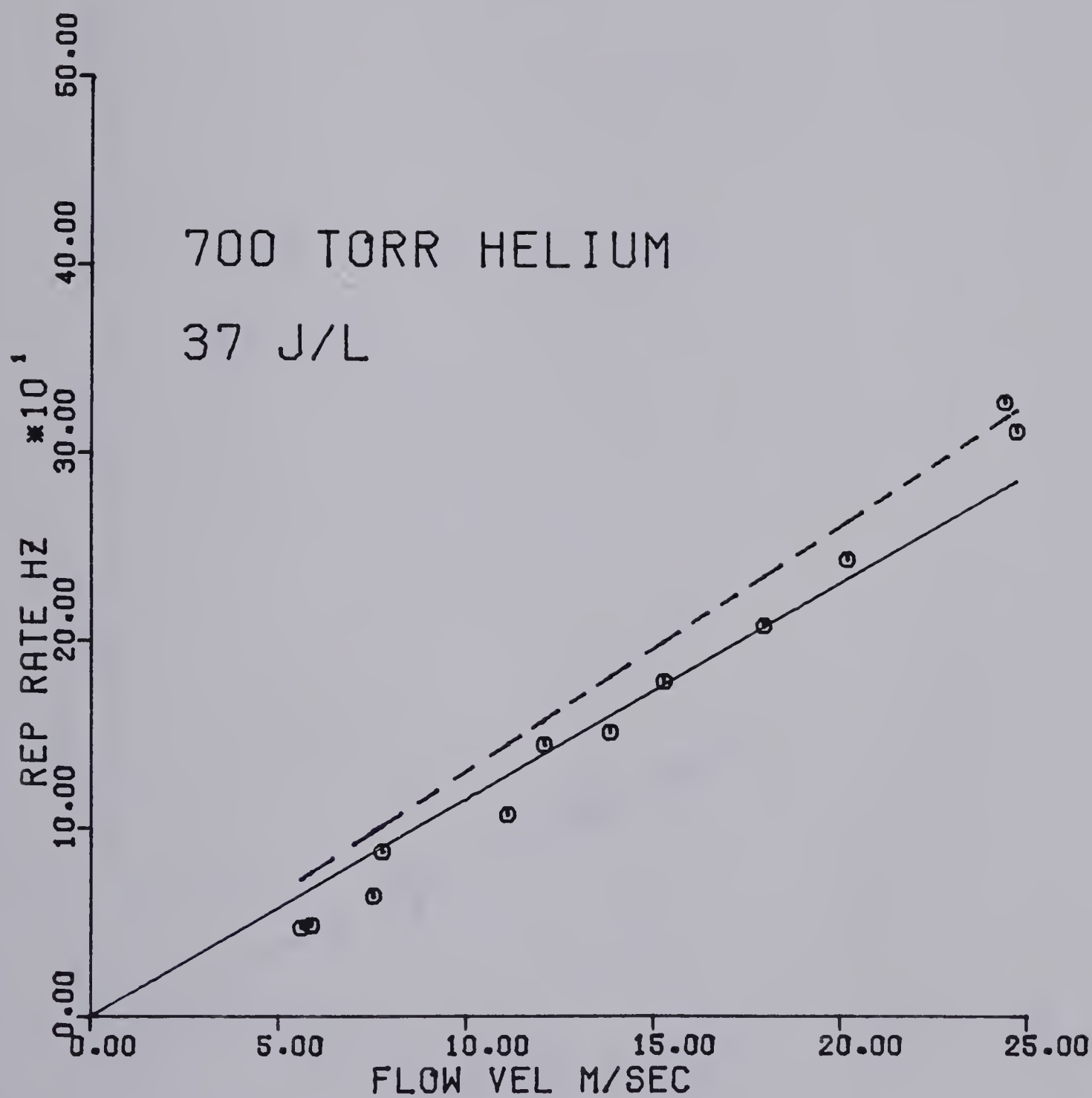


Fig. 6.18 Repetition Rate Versus Gas Flow Velocity.

Data for 700 torr He and 37 J/l energy density.

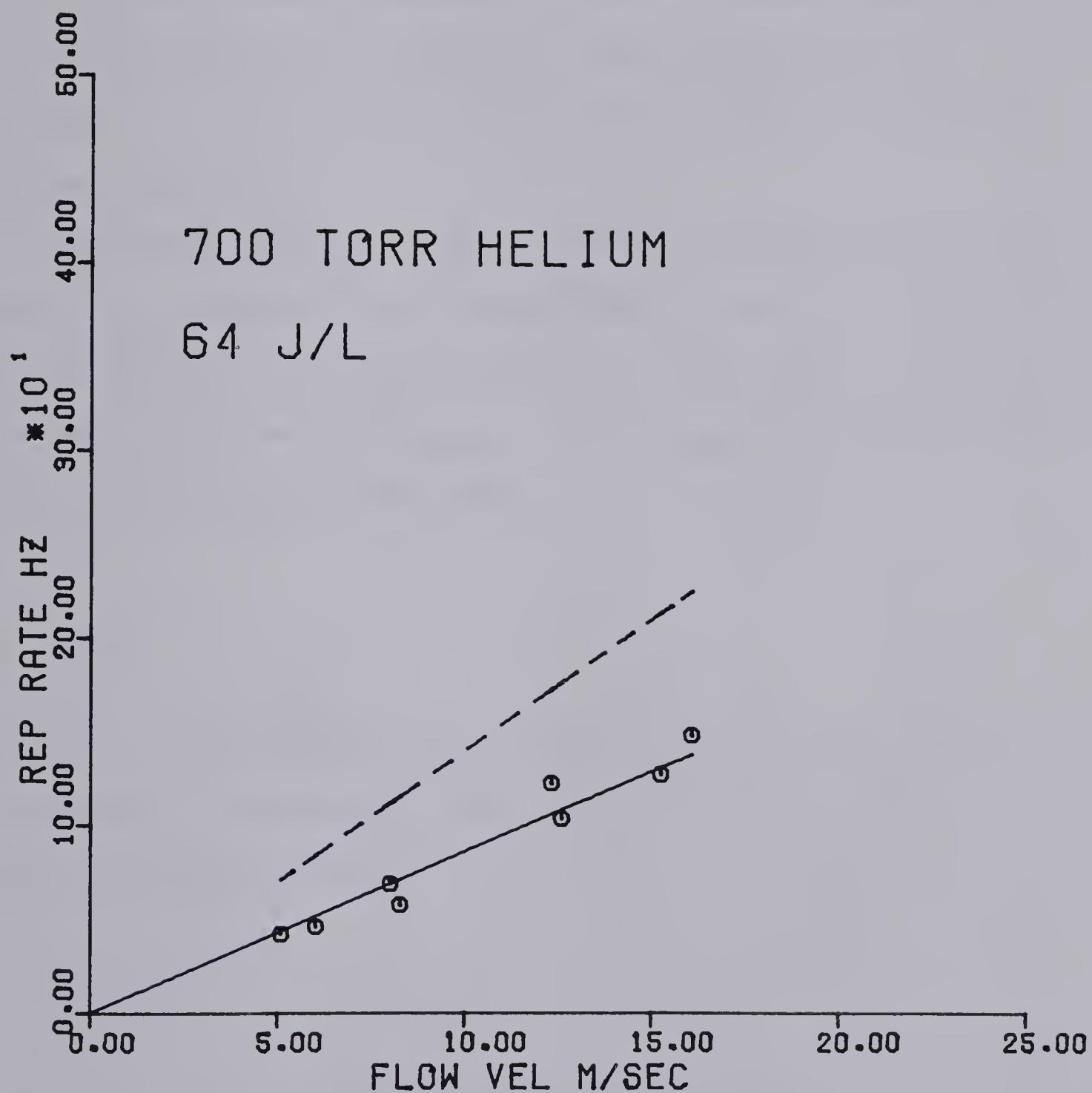


Fig. 6.19 Repetition Rate Versus Gas Flow Velocity.

Data for 700 torr He and 64 J/l energy density.

out in section 6.3, if the energy density is low enough the ideal repetition rate can be exceeded.

6.5 REPETITION RATE VERSUS ENERGY

In this section the variation of maximum obtainable repetition rate for a uniform glow is studied as a function of energy. The repetition rates are expressed as fractional frequencies for ease of comparison with theory.

The simplest estimate of maximum uniform glow repetition rate is given by f_{ideal} which can be calculated from the discharge diameter and the flow velocity. As was shown in section 6.4 the observed repetition rates are usually lower than f_{ideal} . Since f_{ideal} is a linear function of flow velocity it can be expressed as:

$$f_{\text{ideal}} = av$$

Similarly, if the observed repetition rate is also a linear function of flow velocity, as appears to be the case from the data in section 6.4, it can also be expressed as:

$$f_{\text{obs}} = bv$$

Then the fractional frequency (equation 6.1.2) would be:

$$f_{\text{fract}} = \frac{bv}{av} = \frac{b}{a} \tag{6.5.1}$$

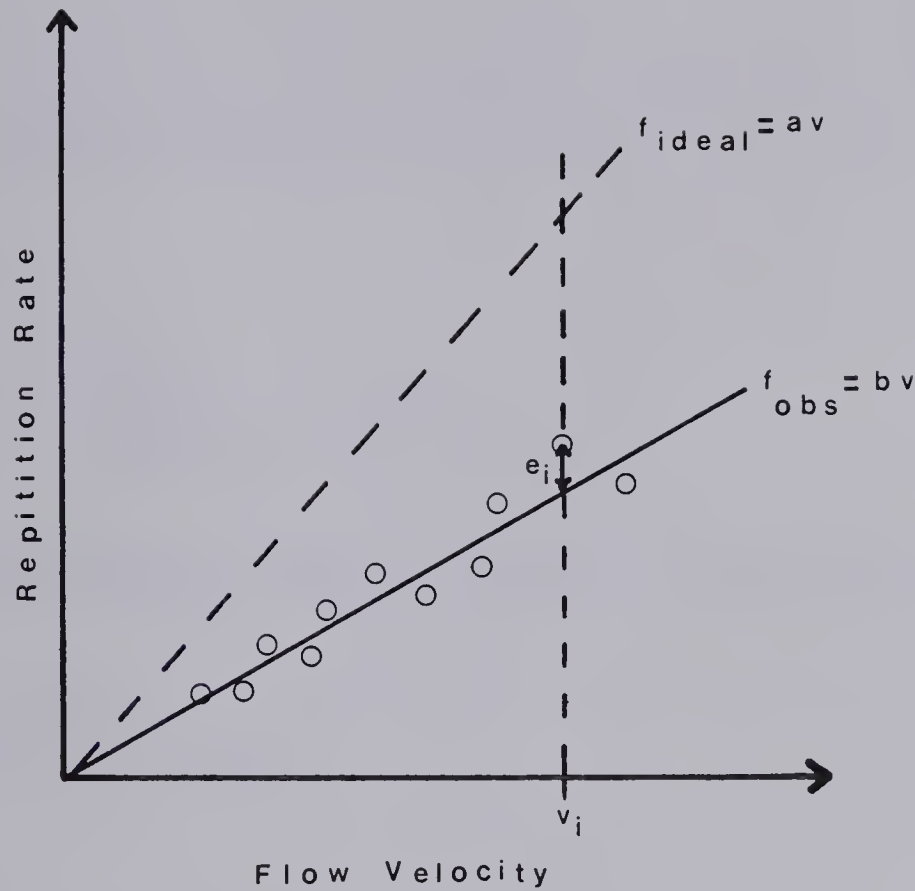


Figure 6.20 Calculating an average fractional frequency from observed data.

for any value of v . That is, the fractional frequency is equal to the ratio of the slope of the line for the observed repetition rate and the slope of the line for the ideal repetition rate.

Individual observations, however, are subject to statistical variation which introduces a random error in the value of f_{fract} calculated. But an average value of f_{fract} can be obtained. Given an observation at a particular velocity v_i the ideal repetition rate would be:

$$f_{\text{ideal}} = av_i$$

and the observed repetition rate would be:

$$f_{\text{obs}} = bv_i + e_i$$

where e_i is the error term representing the departure of the observed value from the linear equation due to random errors. The fractional frequency is:

$$f_{\text{fract}_i} = \frac{f_{\text{obs}_i}}{F_{\text{ideal}_i}} = \frac{bv_i + e_i}{av_i}$$

and, for n observations, the average value of fractional frequency is:

$$\begin{aligned} \overline{f_{\text{fract}}} &= \frac{1}{n} \sum_{i=1}^n f_{\text{fract}_i} \\ &= \frac{1}{n} \sum_{i=1}^n \frac{bv_i + e_i}{av_i} \qquad 6.5.2 \\ &= \frac{b}{a} + \frac{1}{n} \sum_{i=1}^n \frac{e_i}{av_i} \end{aligned}$$

Equation 6.5.2 describes the average fractional frequency calculated from the observed data. Although it differs from the fractional frequency for the linear model (equation 6.5.1) by the error term $\frac{1}{n} \sum_{i=1}^n \frac{e_i}{av_i}$ they are approximately equal since the random errors should tend to cancel and the error term become small. So the average fractional frequency can still be thought of as approximately equivalent to the slope of a line

fitted through the data points and constrained to pass through the origin divided by the slope of the line representing the ideal repetition rate.

For a given energy input density this gives an average fractional frequency, averaged over a range of gas flow velocities. The ideal repetition rate has a fractional frequency of 1 and the average fractional frequency shows how much the repetition rate has dropped below the ideal case for a given energy density. This provides a convenient means for comparing the theory of Dzakowic and Wutzke with the observed repetition rates.

Figures 6.21 to 6.23 show the observed fractional frequencies for a uniform glow with no arcing and the predicted fractional frequencies using Dzakowic and Wutzke's theory (equation 6.1.8). The observed fractional frequency falls off faster than predicted as energy density increases.

6.6 REPETITION RATE VERSUS INDUCTANCE

In measuring the maximum uniform glow repetition rate at various energy densities it is clear that the repetition rate decreases as energy density increases. Since the energy density was varied by increasing the size of the storage capacitor the pulse length also increased because pulse length is proportional to \sqrt{LC} . The purpose of this experiment was to see if the maximum repetition rate that could be achieved for a uniform discharge was a function of pulse length as well as energy density.

The experiment was run in 60 torr N_2 , 80 torr CO_2 , and 700 torr He. For each gas the charging voltage was kept constant at 10 KV and the storage capacitor, C, was kept constant at either 40.8 nf or 81.2 nf. The pulse length was changed by varying L, the circuit inductance (Fig. 6.24).

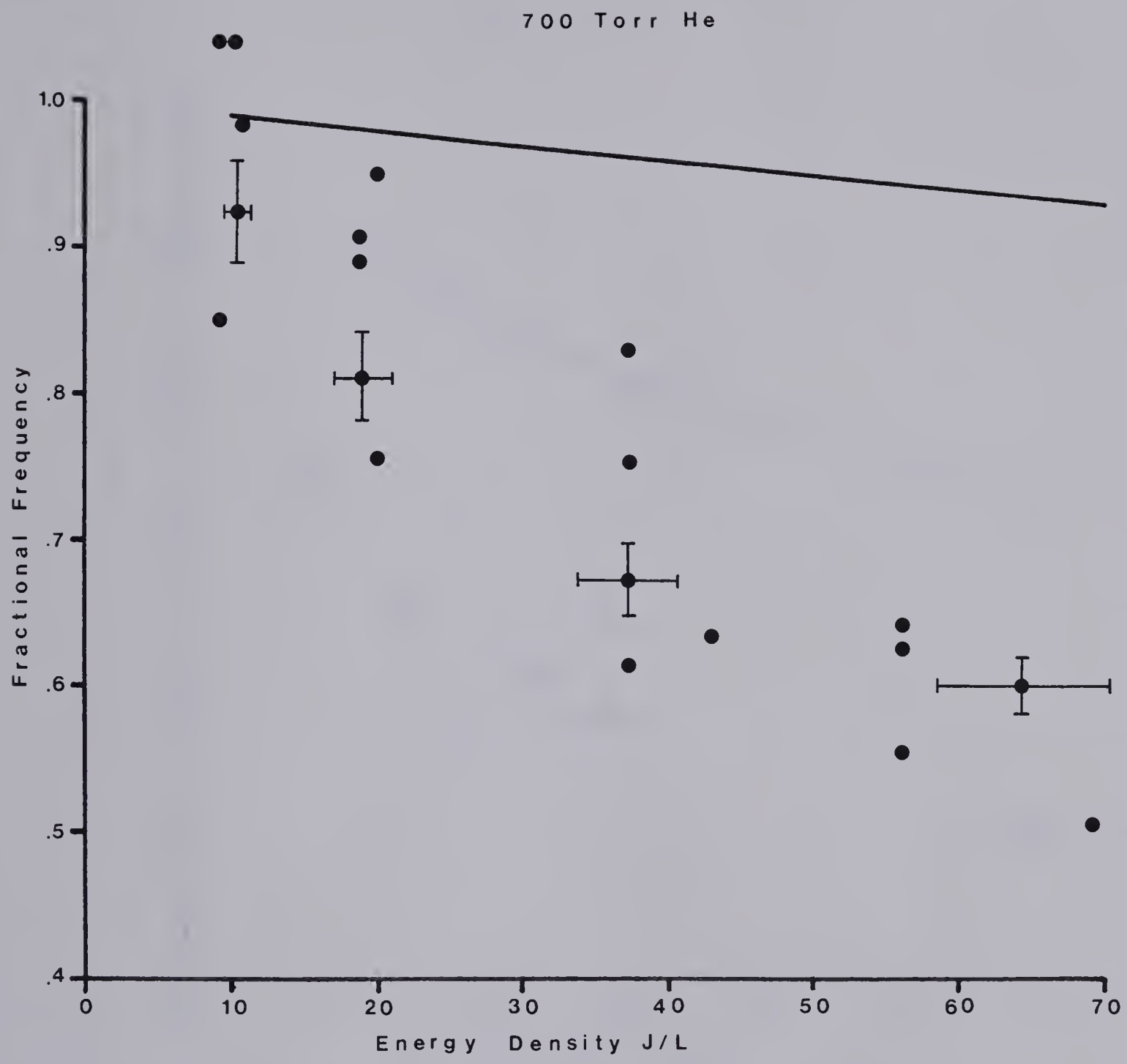


Figure 6.21 Observed Fractional Frequencies for a Uniform Glow in 700 Torr He. The solid line is the predicted fractional frequency using Dzakowic and Wutzke's theory.

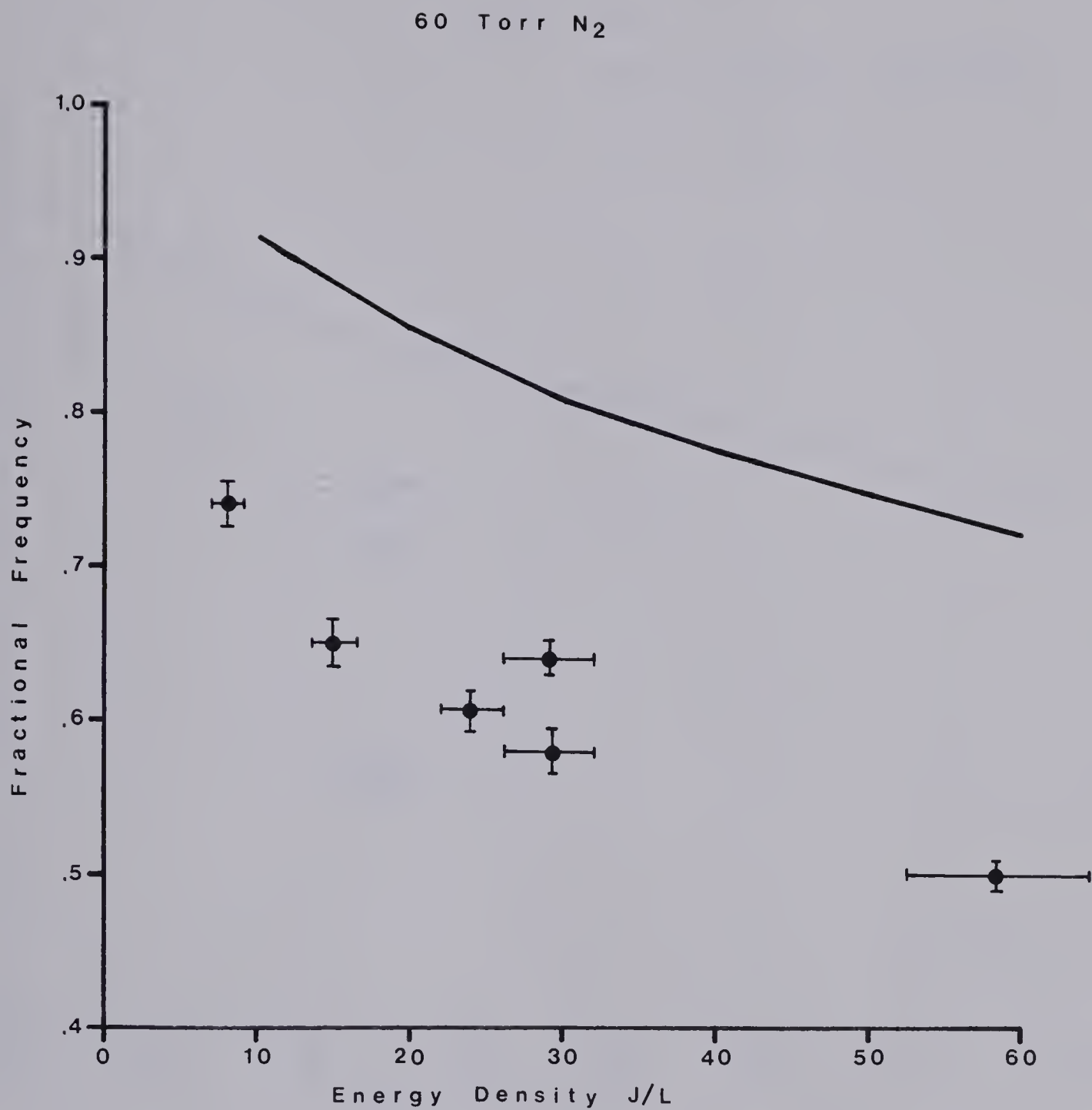


Figure 6.22 Observed Fractional Frequencies for a Uniform Glow in 60 Torr N₂. The solid line is the predicted fractional frequencies using Dzakowic and Wutzke's theory.

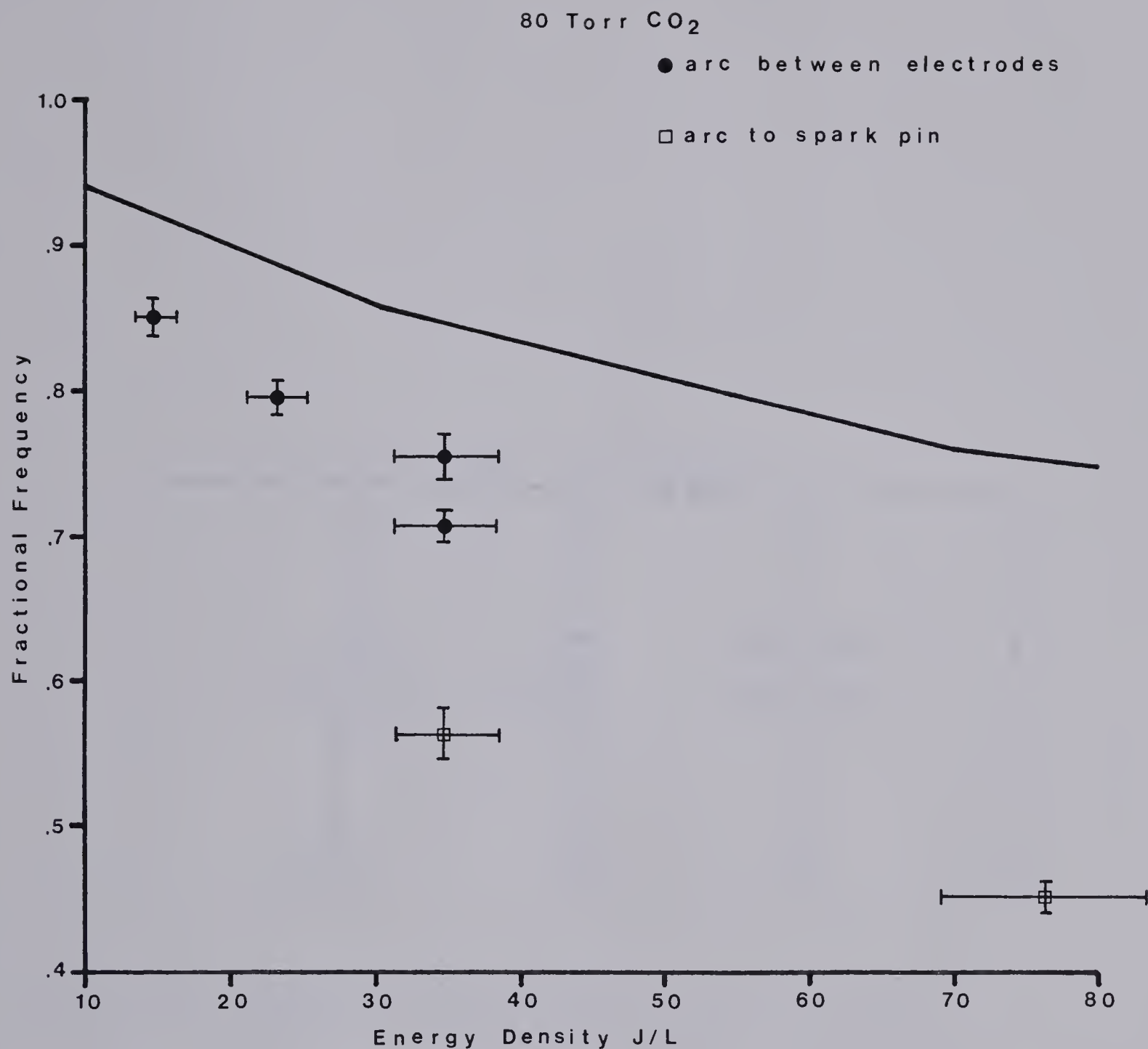


Figure 6.23 Observed Fractional Frequencies for a Uniform Glow in 80 Torr CO₂. The solid line is the predicted fractional frequency using Dzakowic and Wutzke's theory. The two sets of data points correspond to two different arcing criteria.

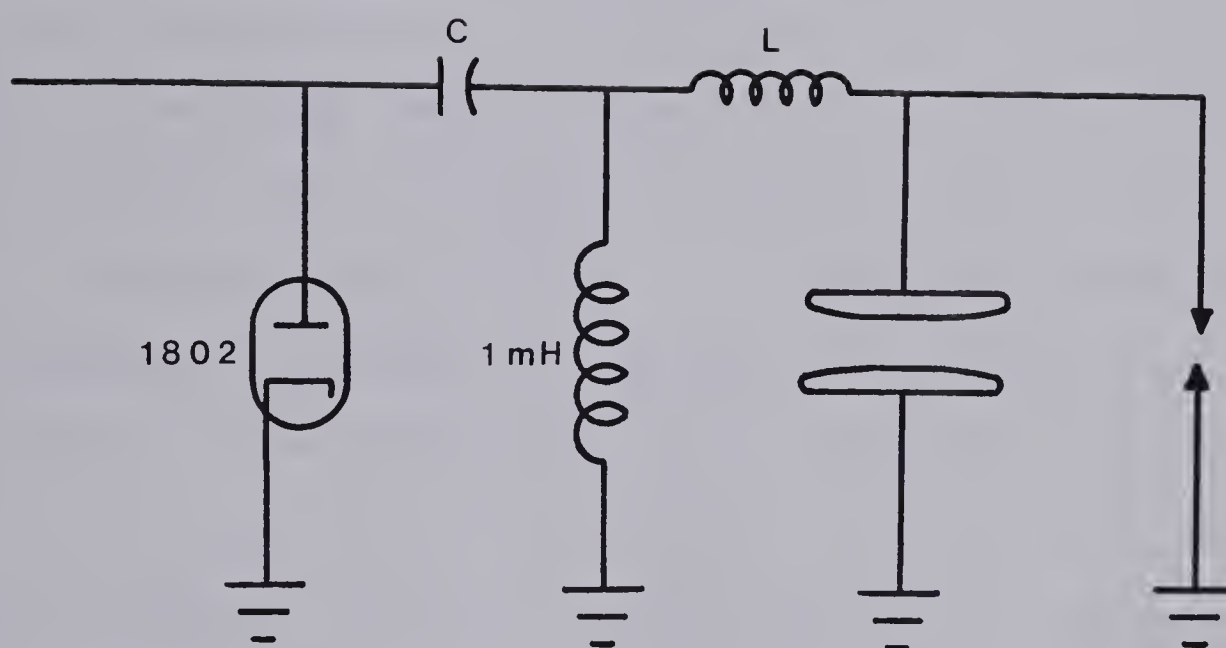


Fig. 6.24 Discharge Circuit For Pulse Length Experiments.

For a given value of C the pulse length was varied by changing L .

In this way the pulse length varied but the energy per pulse remained constant. L was varied from 2 μH , the intrinsic circuit inductance, to 101 μH producing pulse lengths that varied from 2 to 6 μsec . For each value of L maximum repetition rates for a uniform discharge were measured for seven flow velocities and an average fractional frequency calculated as outlined in section 6.5.

The results of this experiment are summarized in the plots of Figures 6.25 to 6.27. They show that the fractional frequency attainable is essentially independent of inductance, or pulse length. The two sets of fractional frequencies shown for 40.8 nf in 80 torr CO_2 require some explaining. At an energy density of about 35 J/l two types of repetition rate arcing could be seen. The lower fractional frequency of about .57 marked the transition region at which an arc between the cathode and spark pin appeared. Increasing the repetition rate further shifts the arc to between the downstream edges of the two electrodes. This transition occurred at fractional frequencies of roughly .77. Figure 6.23 also notes this phenomena. The various arcing modes are discussed in more detail in section 6.10. Figure 6.26 shows that the onset of both arcing modes is independent of pulse length.

6.7 AFTERGLOW CLEARING TIME MEASUREMENTS

Luminous afterglows were observed in N_2 , CO_2 , and He. This made it possible to use a photomultiplier tube as a diagnostic for studying the convection of discharge products away from the discharge region.

The apparatus for this study is shown in Figure 6.28. A mirror, pinhole, telescope and photomultiplier were mounted on an optical bench. The pinhole and telescope acted as a collimator to limit the photomultiplier's field of view to a very narrow beam in space. By translating



Fig. 6.25 Repetition Rate as a Function of Circuit Inductance for 60 Torr N₂. The repetition rate has been normalized by expressing it as a fractional frequency.



Fig. 6.26 Repetition Rate as a Function of Circuit Inductance for 80 Torr CO_2 . The sets of data at about .77 and .57 for 40.8 nf represent two different arcing criteria.

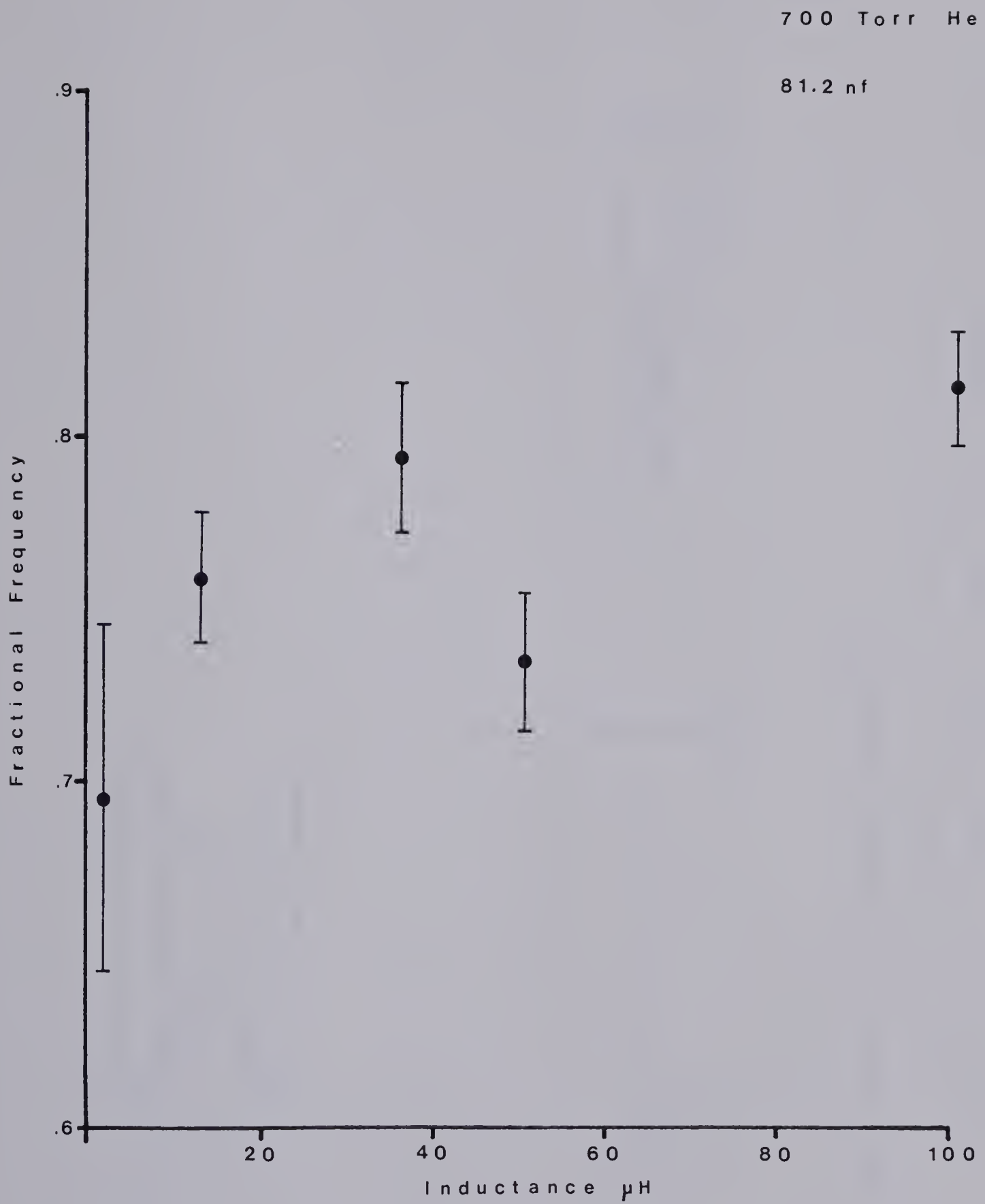


Fig. 6.27 Repetition Rate as a Function of Circuit Inductance for 700 Torr He.

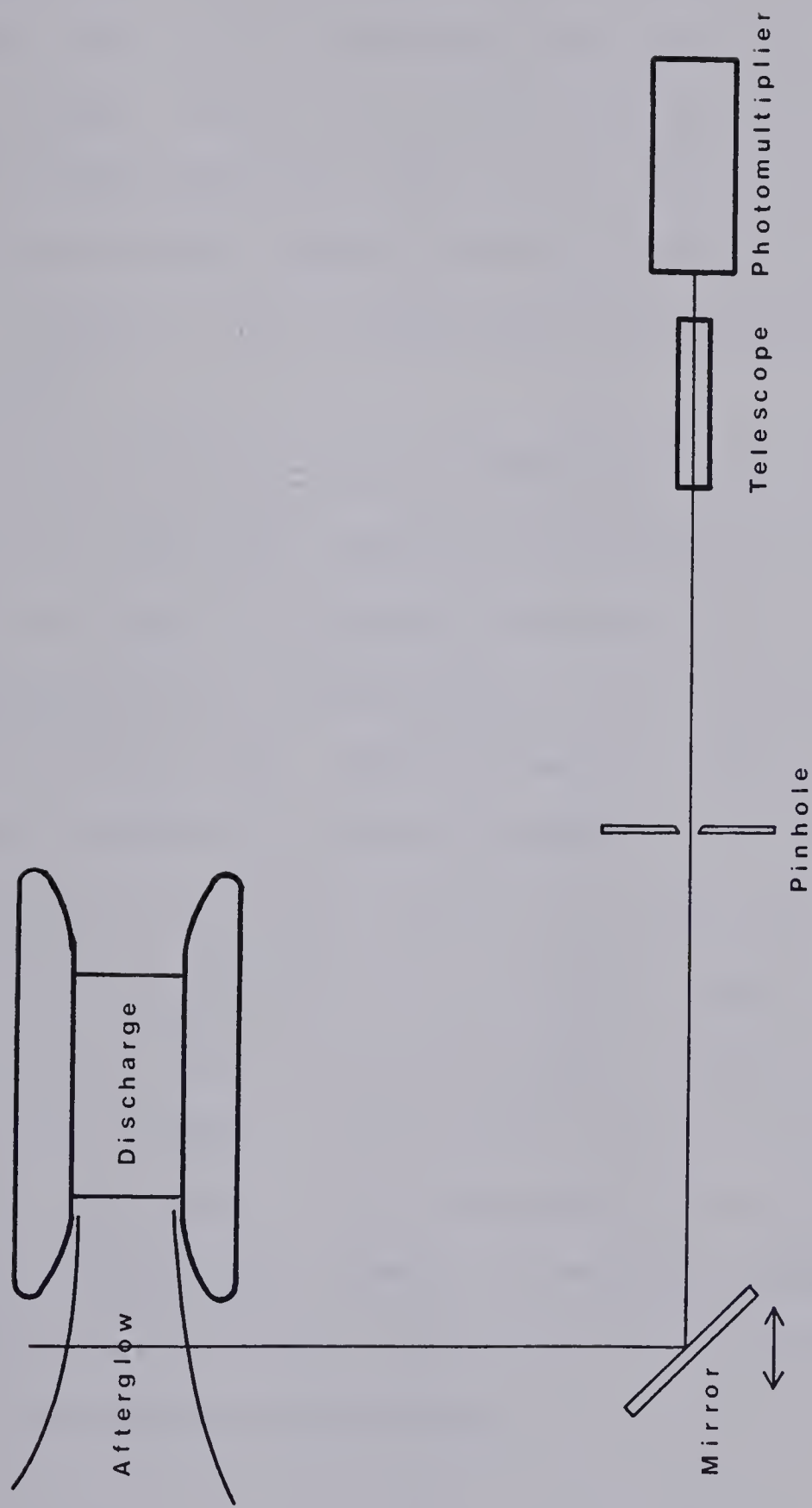


Fig. 6.28 Apparatus For Afterglow Measurements.

The pinhole and telescope act as a collimator, limiting the photomultiplier's field of view to a beam 7 mm in diameter.

the mirror along the optical bench the afterglow could be examined at various distances downstream from the discharge. The signal from the photomultiplier went to the scope through a short cable (0.5 m) and a 100 K Ω pad. The short cable and pad insured that the rc time constant was short enough to resolve the waveform and the 100 K Ω pad was the minimum value that produced a signal voltage large enough to see. A bright orange afterglow could be produced in 60 torr N₂ using an 80 nf capacitor charged to 10 Kv. Similar but fainter afterglows were produced in CO₂ and He.

A typical N₂ afterglow pulse is shown in Figure 6.29. The initial spike is due to the light flash when the discharge occurs. This discharge leaves a plug of gas in an excited metastable state. The plug of gas blowing downstream past the position probed by the photomultiplier produces the square pulse. The dip between the spike and the front edge of the pulse corresponds to the time needed for the downstream edge of the excited gas to reach this position. The back edge of the pulse corresponds to the time needed for the upstream edge of the excited gas to pass this position. So the pulse length is proportional to the diameter of the discharge, the two being related by the gas flow velocity. Ideally the pulse should be flat topped but the droop corresponds to a reduction of intensity with time as the metastable population decreases. In principle the recombination coefficient for the metastable could be estimated from the pulse decay using:

$$\frac{1}{n} = \frac{1}{n_o} + \beta t$$

but in order to do this the initial metastable density, n_o , must be known.

The CO₂ afterglow pulse is similar to the N₂ afterglow pulse except

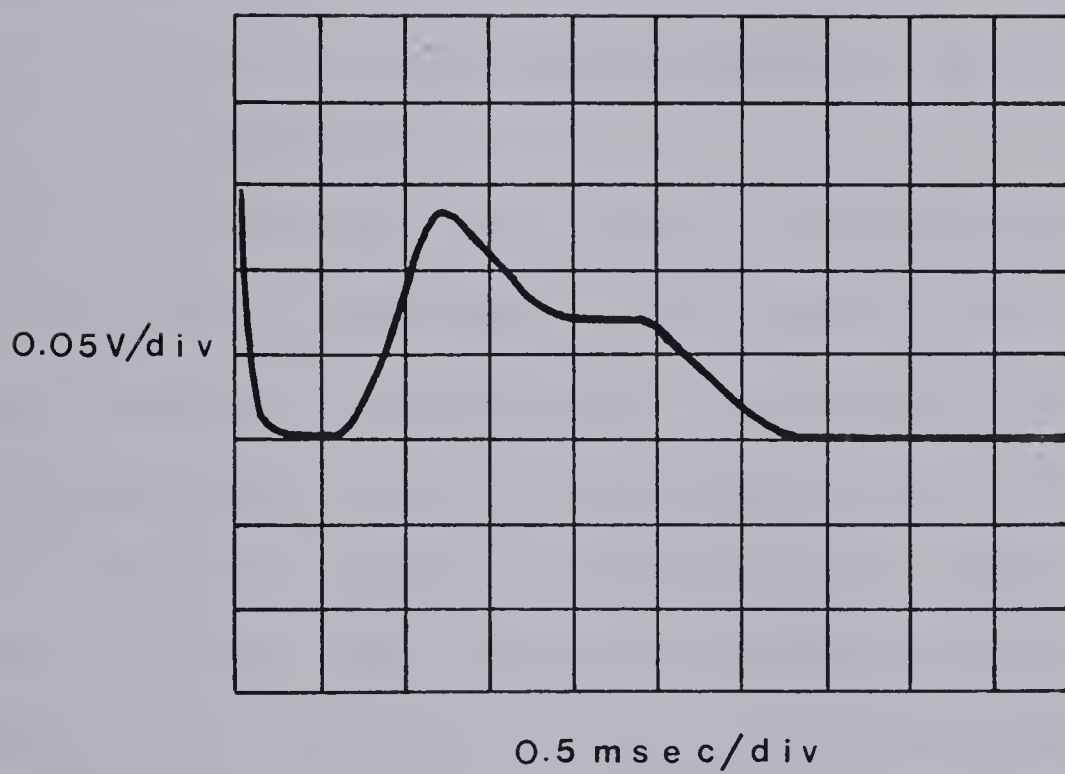


Fig. 6.29 Typical Afterglow Waveform in 60 Torr N_2 . The discharge capacitor was 81.2 nf and the charging voltage was 10 KV.

that it is lower in amplitude and has a flatter top. The intensity of the CO_2 afterglow increases after the discharge has run for a while. Since the discharge dissociates the CO_2 into CO and O_2 this suggests that the afterglow in CO_2 is associated with the presence of one of these products.

The He afterglow proved to be difficult to reproduce. Very pure He (99.999%) was used in an effort to try and improve the afterglow. But the afterglow actually got fainter with repeated fillings of the very pure gas. Adding a fraction of a torr of N_2 to the He made the afterglow come back strongly. So the afterglow observed in He was due to the presence of N_2 impurities.

Using an 81.2 nf capacitor charged to 10 Kv, afterglows were produced in the three gases. The afterglows were observed at a point $\frac{1}{4}$ " upstream from the back edge of the electrodes. The time from the beginning of the discharge spike to the end of the afterglow pulse was observed as a function of gas flow velocity. This time could be taken as a reasonable estimate of the time needed to clear the discharge products from the discharge region. The inverse of the afterglow pulse lengths are plotted as a function of gas flow velocity in Figures 6.30 to 6.32. For comparison the ideal repetition rate is shown as a dotted line.

In both N_2 and CO_2 the inverse of the time from the beginning of the spike to the end of the pulse was proportional to the gas flow velocity as expected. In He however the afterglow pulse length tended to stay quite constant indicating that recombination occurred before all the gas was convected out from between the electrodes. As was already mentioned He tends to form a nonuniform discharge rather than arcs if f_{ideal} is exceeded. If the repetition rate is increased further arcs will form in the nonuniform glow. These afterglow measurements suggest that the high

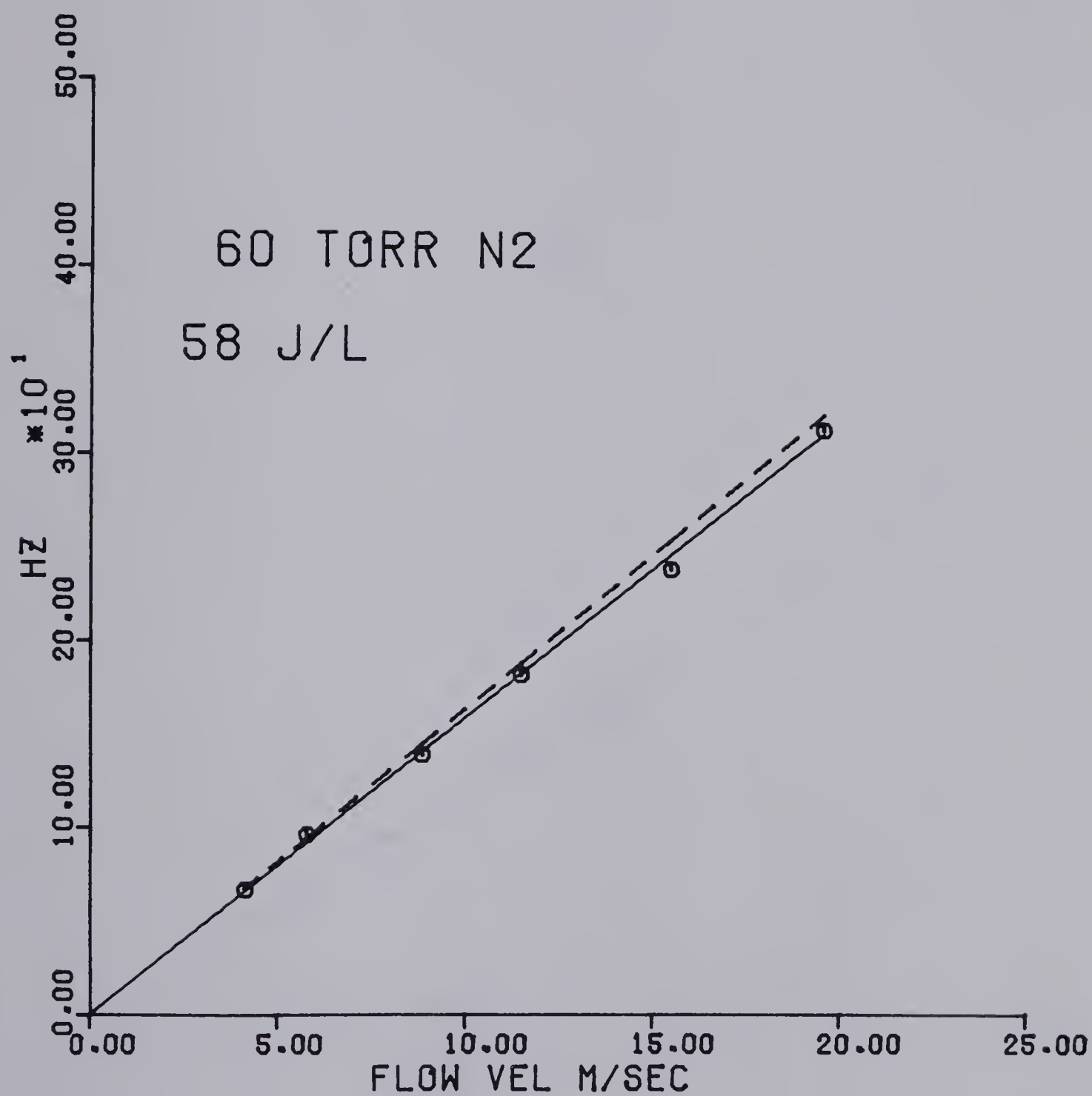


Fig. 6.30 $1/\tau_{\text{afterglow}}$ as a Function of Flow Velocity.

Data for 60 torr N₂ and 58 J/l energy density.

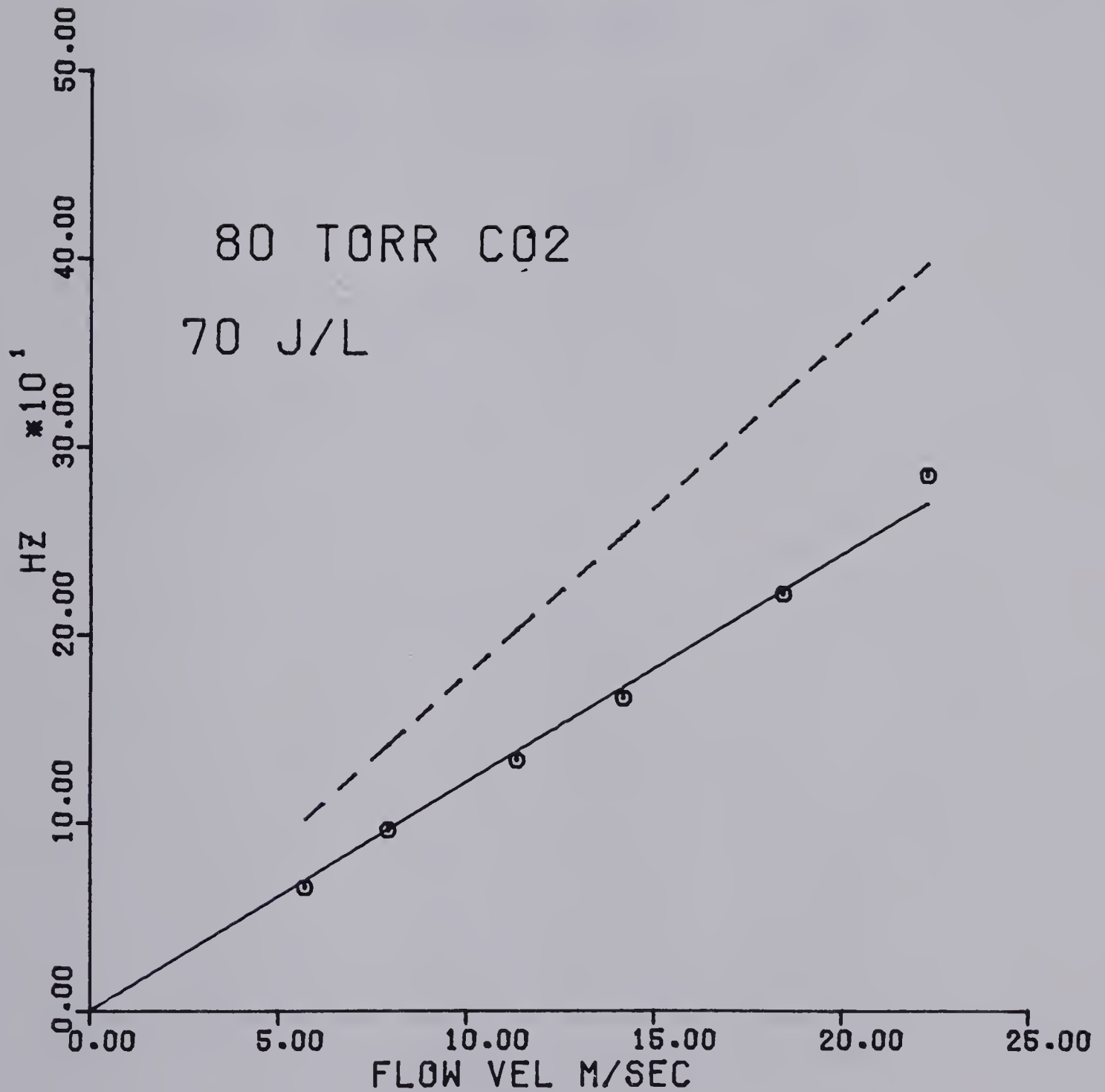


Fig. 6.31 $1/\tau_{\text{afterglow}}$ as a Function of Flow Velocity.

Data for 80 torr CO_2 and 70 J/l energy density.

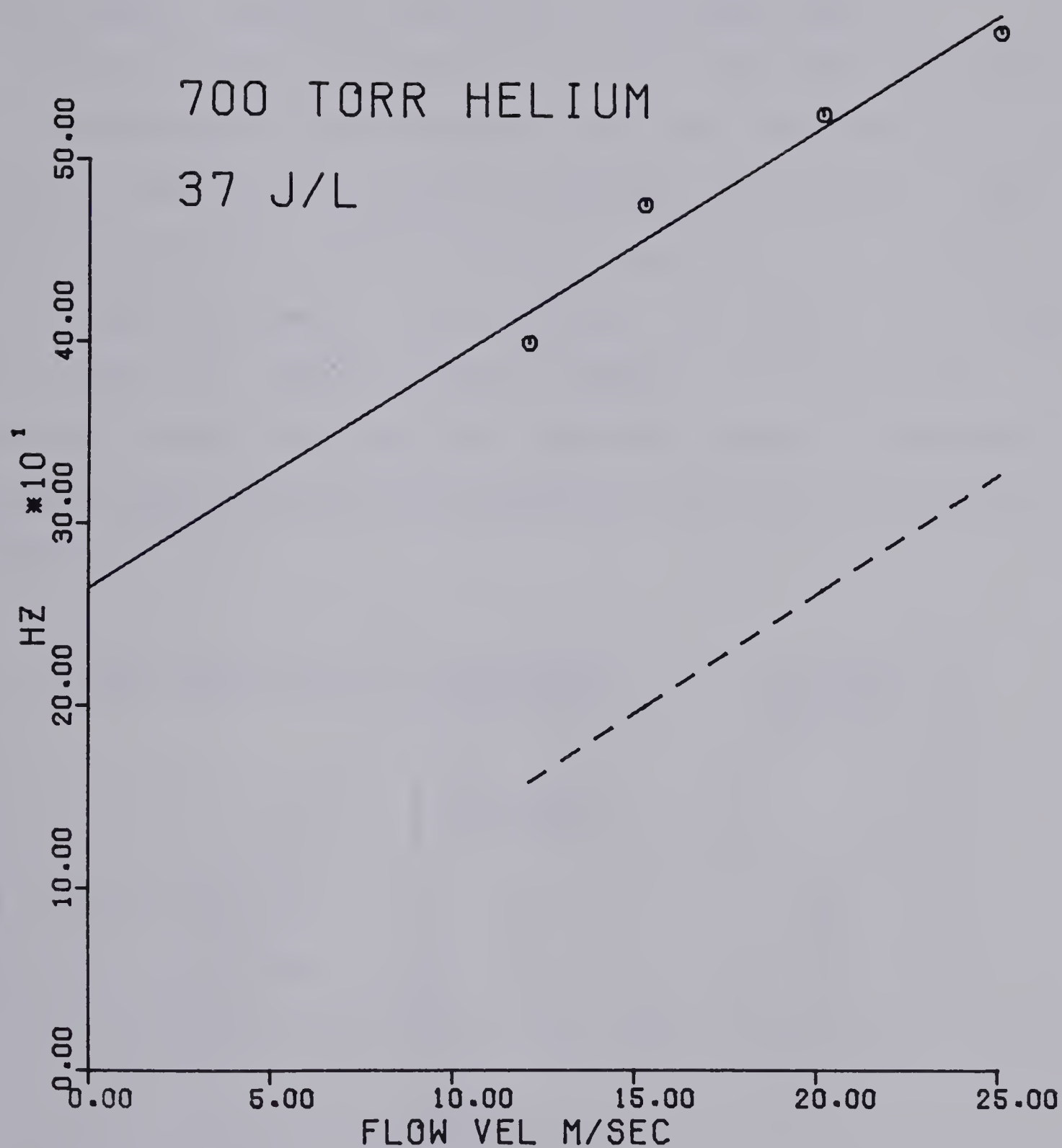


Fig. 6.32 $1/\tau_{\text{afterglow}}$ as a Function of Flow Velocity.

Data for 700 torr He and 37 J/l energy density.

repetition rates that can be achieved in pure He before arcing occurs may be due to fast recombination of left over ionization from previous discharge pulses. As a result it would not be necessary for the electrodes to be cleared by convection before the next discharge pulse.

So in N_2 and CO_2 the afterglow lifetime is longer than the convection time and observing the afterglow can give some idea of the time needed to clear discharge products from between the electrodes. In He however the afterglow lifetime is shorter than the convection time so the afterglow measurements cannot provide any useful measure of clearing time. Even in CO_2 and N_2 although qualitatively the inverse of the afterglow clearing time looks like a reasonable estimate of obtainable repetition rate the quantitative agreement is poor, as can be seen from Table 6.3.

gas and energy density	fractional frequency based on $\frac{1}{\tau_{\text{afterglow}}}$	fractional frequency observed
80 torr CO_2 70 J/l	.67	.46
60 torr N_2 58 J/l	.98	.50

Table 6.3

6.8 AFTERGLOW PULSE LENGTH VERSUS ENERGY DENSITY

The same apparatus described in section 6.7 was used for this experiment. Since maximum repetition rate decreases with increasing energy (section 6.5), and Dzakowic and Wutzke suggested that this was due

to discharge expansion, this experiment attempted to observe the expansion by monitoring the afterglow pulse length. The afterglow pulse length is $t_B - t_A$ in Fig. 6.33 and should be proportional to the diameter of the discharge products blowing downstream, the two being related by:

$$\text{diameter} = v_g (t_B - t_A)$$

where v_g is the gas flow velocity.

The gas flow velocity was kept constant at 19.7 m/sec in N_2 and 22.5 m/sec in CO_2 . The discharge diameter was measured with a travelling telescope. It was 58 mm in N_2 and varied from 46 to 58 mm in CO_2 . The discharge energy density was varied by changing the value of storage capacitor and the values t_A and t_B were measured as a function of increasing energy density.

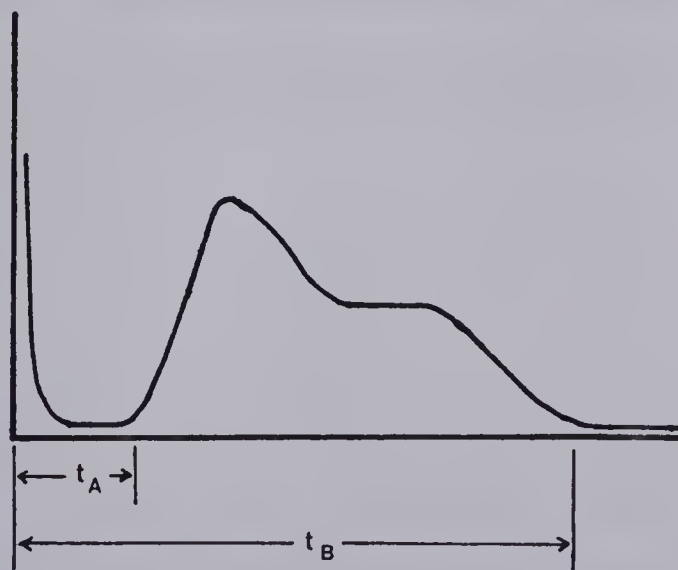


Figure 6.33 Afterglow pulse

The afterglow pulse lengths, $t_B - t_A$, are plotted as a function of energy density in Figures 6.34 and 6.35. The pulse length increases with increasing energy density. A prediction for the pulse lengths can be obtained from equation 6.1.6. It says that:

$$r_2 = \sqrt{(1+\epsilon)^{1/\gamma}} r_1$$

and so the expanded diameter is related to the initial diameter by:

$$D_2 = \sqrt{(1+\epsilon)^{1/\gamma}} D$$

where D is the initial diameter and D_2 is the final diameter. The pulse length is then given by:

$$\Delta t = t_B - t_A = \frac{\sqrt{(1+\epsilon)^{1/\gamma}} D}{v_g} \quad 6.8.1$$

Some interesting observations arise from applying equation 6.8.1 to the data. First the afterglow pulse is due to a glowing plug of gas that has a different diameter than the discharge diameter. The minimum pulse length is given by:

$$\Delta t \approx \frac{D}{v_g} \quad 6.8.2$$

since $\sqrt{(1+\epsilon)^{1/\gamma}} \rightarrow 1$ as $\epsilon \rightarrow 0$. Using the observed discharge diameter of 58 mm and velocity of 19.7 mm/msec for N_2 gives a minimum pulse length, according to equation 6.8.2, of 2.94 msec. But all the observed pulse lengths in N_2 are less than this value. Similarly in CO_2 the discharge diameters of 46 to 58 mm and flow velocity of 22.5 mm/msec give a minimum

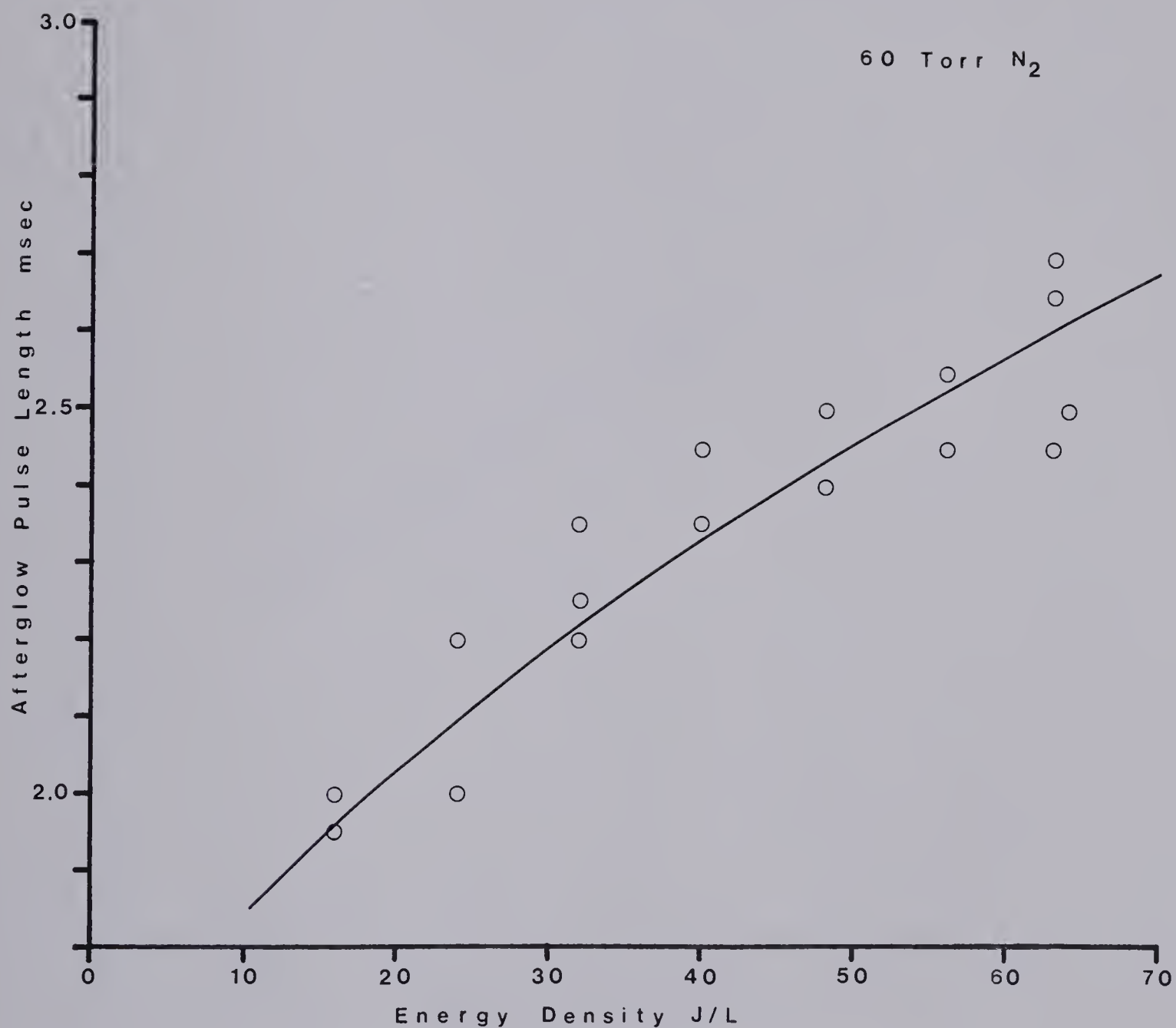


Fig. 6.34 Afterglow Pulse Length as a Function of Energy Density for 60 Torr N₂. The predicted curve is given by $\Delta t = \frac{W\sqrt{(1+\epsilon)}^{1/\gamma}}{v}$ where $W=31.7$ mm and $v=19.7$ mm/msec.

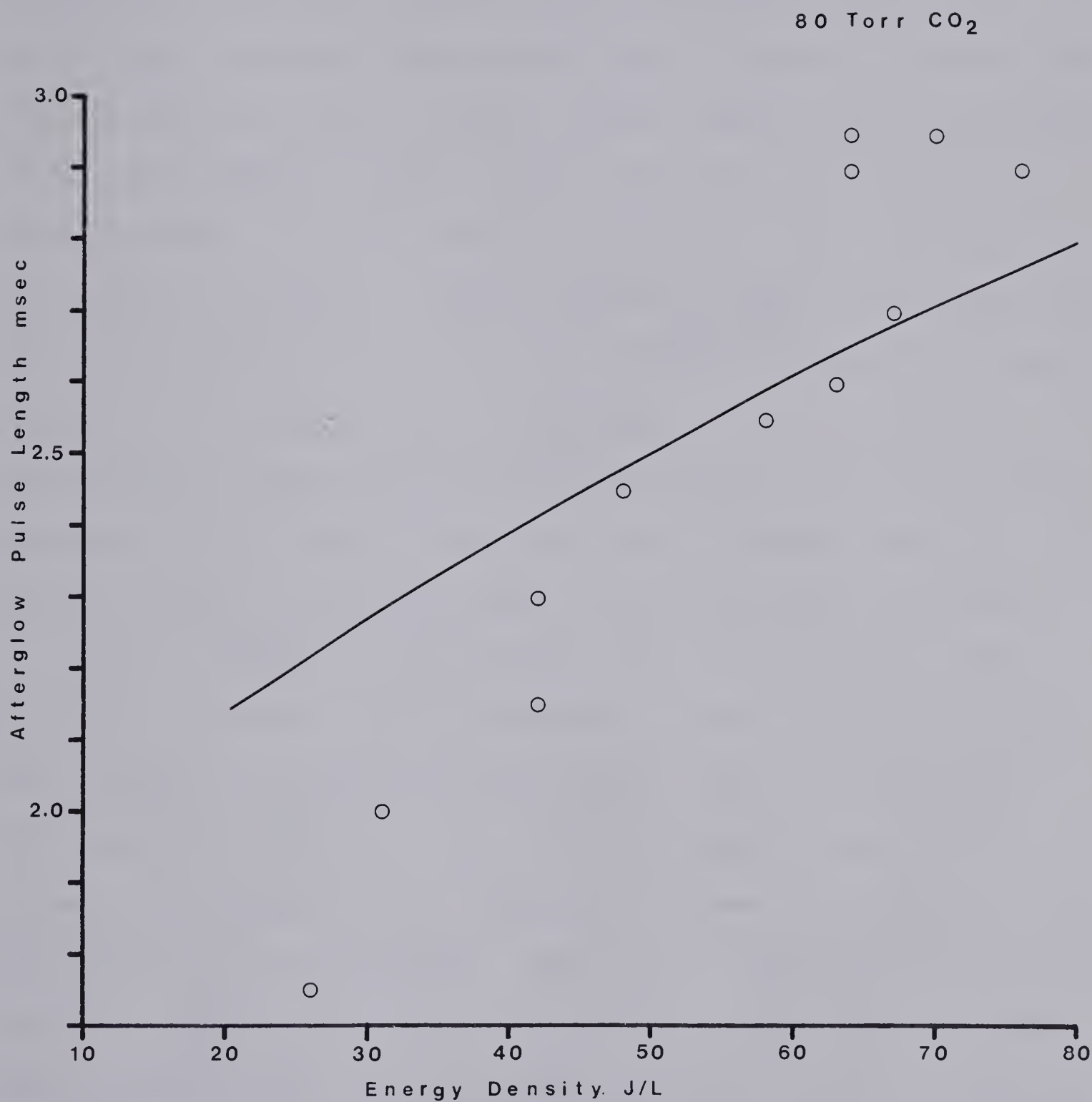


Fig. 6.35 Afterglow Pulse Length as a Function of Energy Density for 80 Torr CO₂. The predicted curve is given by $\Delta t = \frac{W\sqrt{(1+\epsilon)}^{1/\gamma}}{v}$ where $W=41.2$ mm and $v=22.5$ mm/msec.

pulse length of between 2.04 and 2.58 msec. Values both lower and higher than this range were observed. The fact that higher values were observed means that some discharge expansion must have occurred, and because lower values were observed, the initial diameter of the afterglow plug must have been smaller than the diameter observed with the telescope. These results suggest that the afterglow pulse does not represent the entire discharge volume but rather a more strongly heated inner core. From the data a diameter, W , can be estimated for this core and then its expansion predicted using the formula $\Delta t = \frac{W\sqrt{(1+\epsilon)}^{1/\gamma}}{v}$ to give the pulse length due to the expanded gas. A comparison of this model with the observed pulse lengths (Figures 6.34 and 6.35) shows that it fits the N_2 discharge well but does not seem to fit the CO_2 discharge very well. The predicted slope in CO_2 is less steep than that observed for the data.

There is, however, a complication with the data for CO_2 in that there was a large variation in the measured initial discharge diameters, and in general the initial discharge diameter tends to increase with increasing energy density. The increase in initial diameter would probably be accompanied by a corresponding increase in core diameter which could account for the discrepancy. This can be compensated for by calculating W , the afterglow diameter, from the observed pulse length, Δt , and then plotting $\frac{W}{D}$ where D is the discharge diameter. If the discrepancy is due to the increase of D with energy then $\frac{W}{D}$ should stay constant. Table 6.4 shows the result of this calculation for N_2 and Table 6.5 for CO_2 . The results are plotted in Figure 6.36. N_2 shows a constant $\frac{W}{D}$ with any variation being due to random error. Although the discrepancy between the data and the model in CO_2 seems reduced there is still an increase in core diameter with increasing energy density that the model does not

60 torr N₂ gas velocity= 19.7 m/sec D= 58.42 mm

C nf	E/vol J/l	$\sqrt{(1+\epsilon)}^{1/\gamma}$	Δt msec	$W = \frac{v\Delta t}{\sqrt{(1+\epsilon)}^{1/\gamma}}$	W/D
20.4	16	1.22	2.0	32.30	.55
30.3	24	1.30	2.2	33.34	.57
40.8	32	1.38	2.2	31.41	.54
61.2	48	1.51	2.4	31.31	.54
81.2	64	1.63	2.5	30.21	.52
20.4	16	1.22	1.95	31.49	.54
30.7	24	1.30	2.0	30.31	.52
40.8	32	1.38	2.25	32.12	.55
51.1	40	1.45	2.35	31.93	.55
61.2	48	1.51	2.4	31.31	.54
71.1	56	1.57	2.45	30.74	.53
81.2	63	1.62	2.45	29.79	.51
81.2	63	1.62	2.7	32.83	.56
81.2	63	1.62	2.65	32.23	.55
71.2	56	1.57	2.55	32.00	.55
61.2	48	1.51	2.5	32.62	.56
51.1	40	1.45	2.45	33.29	.57
40.8	32	1.38	2.35	33.55	.57
30.3	24	1.30	2.2	33.34	.57
20.4	16	1.22	2.0	32.30	.55

W/D average = .55

Table 6.4 Further analysis of afterglow data for 60 torr N₂.

80 torr CO₂ gas velocity = 22.5 m/sec

C nf	D mm	E/vol J/l	$\sqrt{(1+\epsilon)}^{1/\gamma}$	Δt msec	$\frac{W=v\Delta t}{\sqrt{(1+\epsilon)}^{1/\gamma}}$	W/D
40.8	50.80	42	1.32	2.15	36.65	.72
61.2	50.80	63	1.44	2.6	40.63	.80
81.2	53.34	76	1.51	2.9	43.21	.81
81.2	58.42	64	1.45	2.9	45.00	.77
81.2	58.42	64	1.45	2.95	45.78	.78
71.1	53.34	67	1.46	2.7	41.61	.78
61.2	53.34	58	1.41	2.55	40.69	.76
51.1	53.34	48	1.36	2.45	40.53	.76
40.8	50.80	42	1.32	2.3	39.20	.77
30.3	50.80	31	1.25	2.0	36.00	.71
20.4	45.72	26	1.21	1.75	32.54	.71
81.2	55.88	70	1.48	2.95	44.85	.80
W/D average = .76						

Table 6.5 Further analysis of afterglow data for 80 torr CO₂.

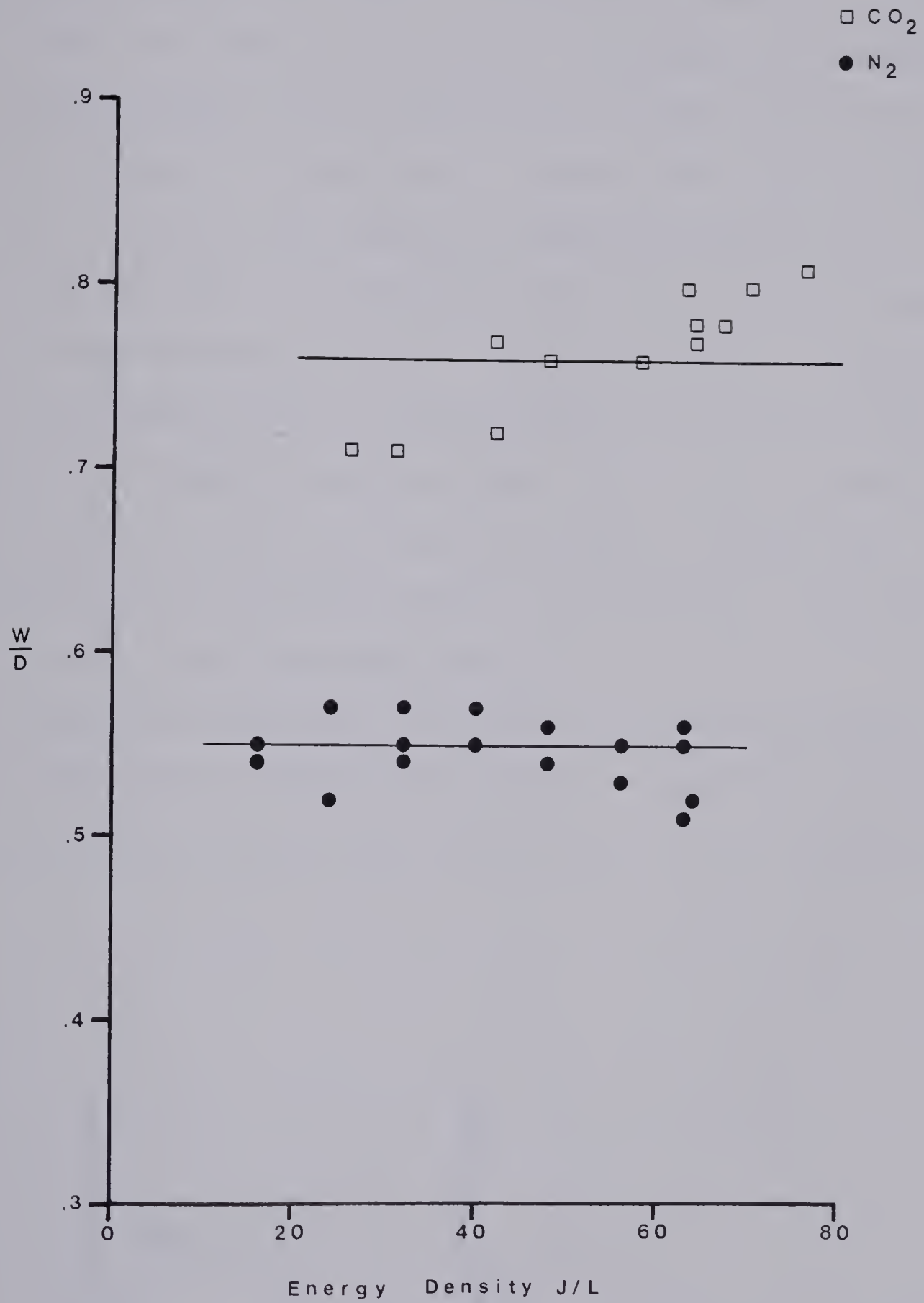


Fig. 6.36 Agreement Between Observed Afterglow Diameters and Gas Expansion Model for N_2 and CO_2 .

account for.

This experiment demonstrated the existence of long lived ionization products which blow downstream as a plug. The increase in plug diameter with increasing energy density agrees fairly well with the expansion predicted by Dzakowic and Wutzke and so supports their claim that gas expansion is an effect which lowers the achievable repetition rate. However, another effect that is probably more important becomes evident. It is a problem with system geometry. With the spark pins downstream from the discharge the plug of discharge products can bridge the gap between the electrodes and the spark pins. If its ionization density is high enough an arc will form from the cathode to the spark pin. This is the kind of arc that usually formed in N_2 and formed in the other gases as well at high enough energy densities.

An additional observation in the flowing gas discharge system supports this ionizing bridge concept. Arcing occurred when the spacing between afterglow pulses was approximately 2 msec or less in 60 torr N_2 .

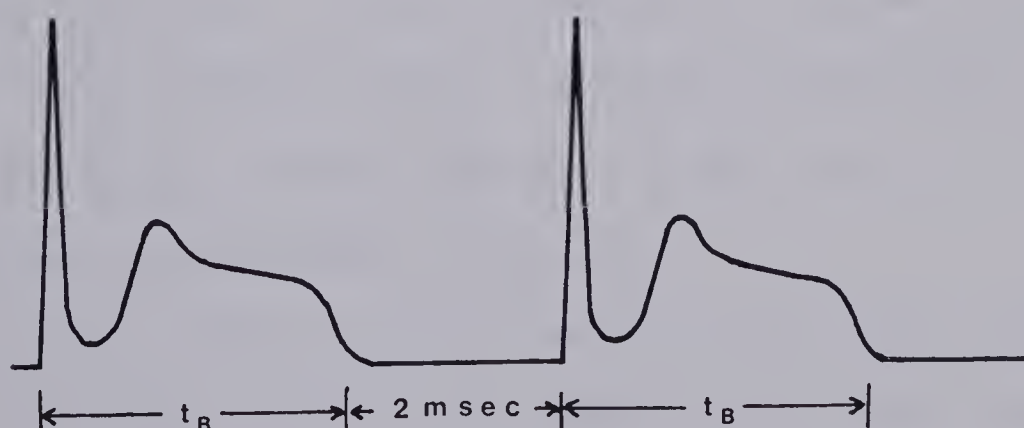


Figure 6.37 Arcing occurs when the spacing between afterglow pulses was 2 msec or less in 60 torr N_2 .

A fractional frequency can be calculated that is based on the afterglow clearing time, t_B , plus 2 msec. In 60 torr N_2 the discharge diameter is 58 mm and the gas flow velocity is 19.7 mm/msec which gives an ideal repetition rate of 339 Hz. Table 6.6 shows the fractional frequencies calculated from the afterglows.

C	$\frac{E}{Vol}$	t_B	$\frac{1}{t_B + 2msec}$	f_{fract}
nf	J/l	msec	Hz	
20.4	16	2.8	208	.61
30.3	24	2.9	204	.60
40.8	32	2.9	204	.60
61.2	48	3.1	196	.58
81.2	64	3.2	192	.57

Table 6.6 Fractional frequencies calculated from afterglows.

The fractional frequencies calculated from the afterglow clearing times are plotted in Figure 6.38 along with the fractional frequencies obtained by observing the discharge. The two agree well. Two msec corresponds to 39 mm at a flow velocity of 19.7 mm/msec and the spark pins were 38 mm downstream from the position probed by the photomultiplier. So in 60 torr N_2 the expanded discharge products must clear not only the electrodes but the spark pins as well.

The bridging effect of the discharge products also explains an arcing problem that occurred in the laser system. High repetition rate arcing would often occur from the cathode to the Marx generator spark pins and would burn a carbon track on the perspex insulation between the two. The carbon track would then have to be cleaned off before the

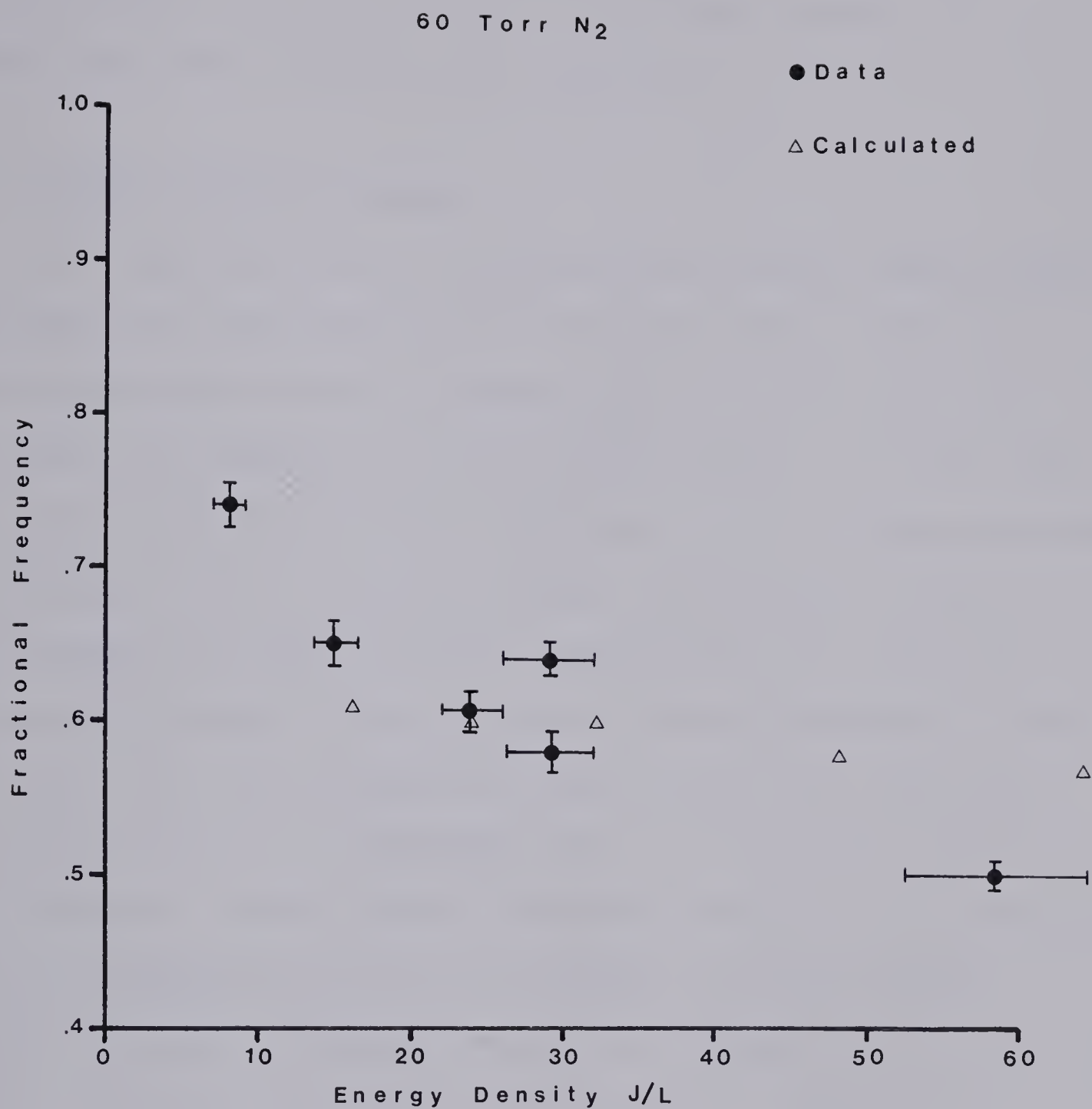


Figure 6.38 Comparison Between Observed Fractional Frequencies for 60 Torr N₂ and Fractional Frequencies Calculated From the Afterglow Clearing Times.

system could operate again. In the flowing gas discharge system the tracking problem was greatly reduced by replacing the perspex with ceramic sheet which is much more heat resistant.

6.9 DISCHARGE INTENSITY PROFILES

In the repetition rate and afterglow diameter versus energy density measurements that were discussed in sections 6.5 and 6.8, the energy density was estimated using a discharge volume obtained by observing the edges of the discharge with a travelling telescope. To verify that this gave a reasonable estimate of discharge diameter, discharge diameters were measured with the travelling telescope and intensity profiles of the discharges were measured with the photomultiplier for comparison. The apparatus used was the same as for the afterglow measurements (Figure 6.31) except that the photomultiplier was terminated with a 50Ω pad to give time resolution of the discharge pulse. By moving the plane mirror the discharge was scanned and peak intensities recorded at 5 mm intervals to develop intensity profiles of the discharge. Typical intensity profiles for uniform discharges are plotted in Figures 6.39 to 6.44. The plots are normalized to show a peak value of 1. The diameters measured with the travelling telescope and the diameters representing 10% of peak intensity on the intensity profiles agree to within 4 mm or less for discharges of typically 55 to 70 mm in diameter. So the diameter observed with the travelling telescope is a good indicator of discharge volume.

The intensity profiles could also be expanded into a diagnostic to study discharge uniformity. For example intensity profiles for discharges which became nonuniform due to excessive repetition rates are

700 TORR HE
81.2 NF

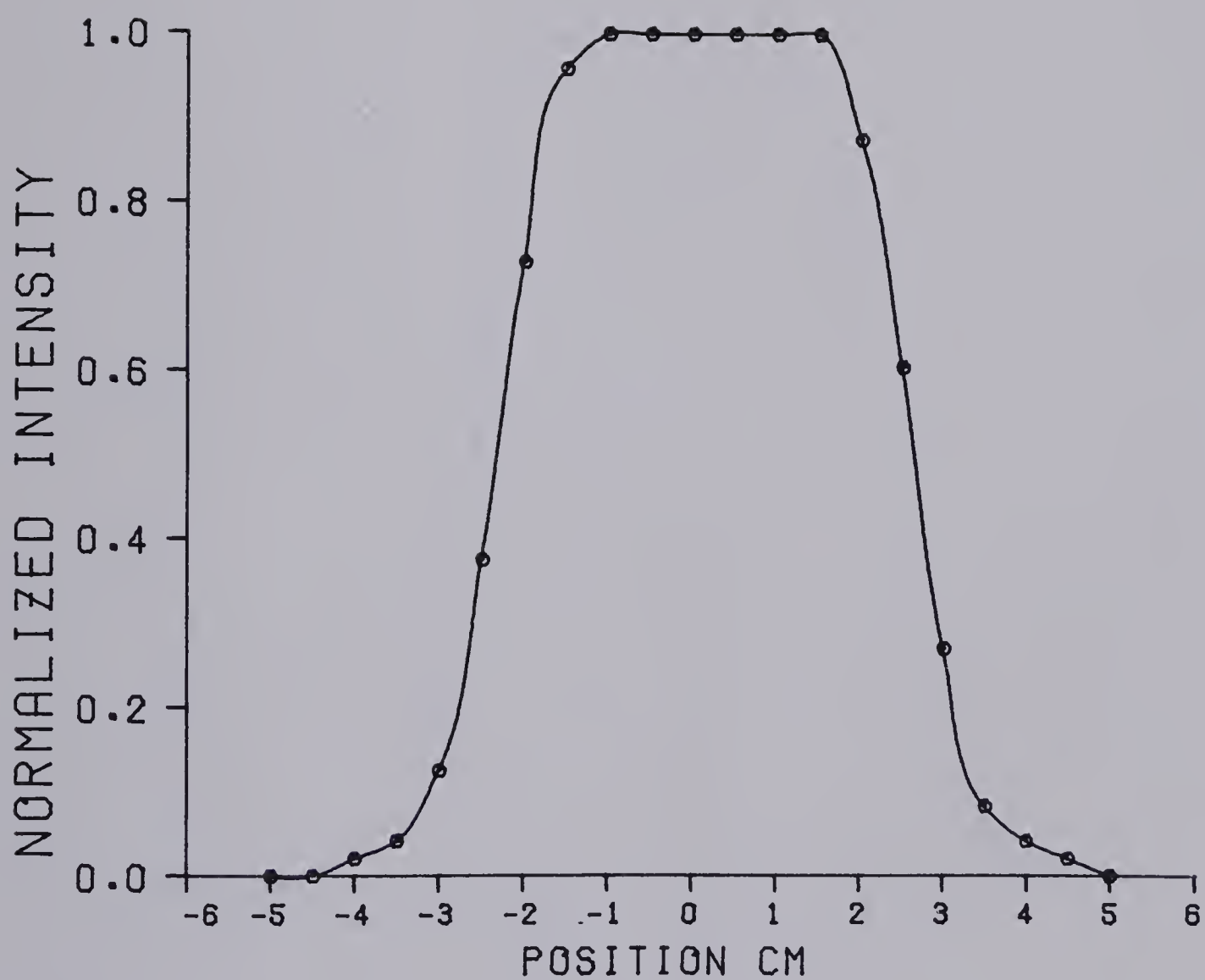


Fig. 6.39 Intensity Profile for 700 Torr He Discharge with
81.2nf Capacitor.

700 TORR HE
20.4 NF

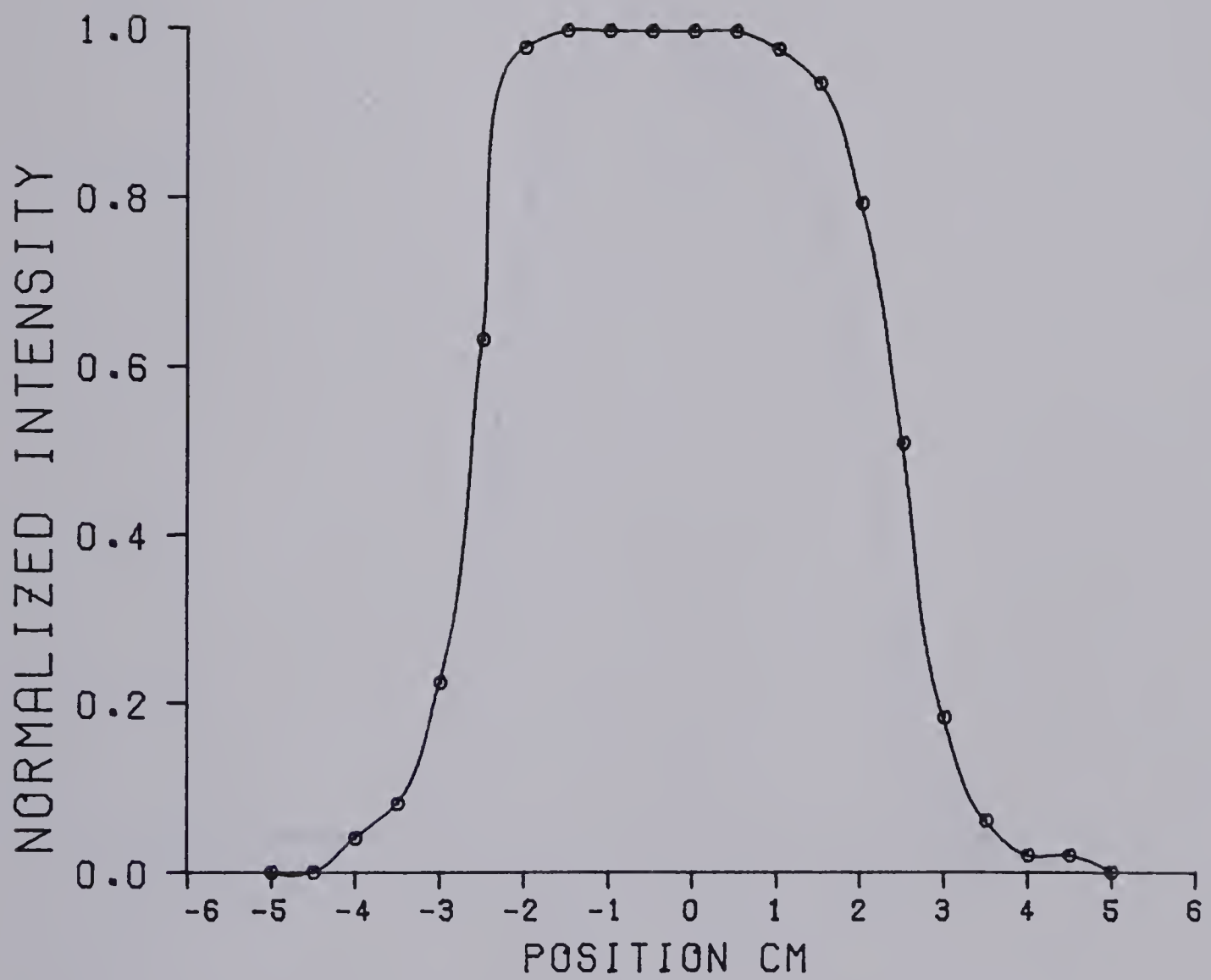


Fig. 6.40 Intensity Profile for 700 Torr He Discharge with
20.4nf Capacitor.

60 TORR N₂
81.2 NF

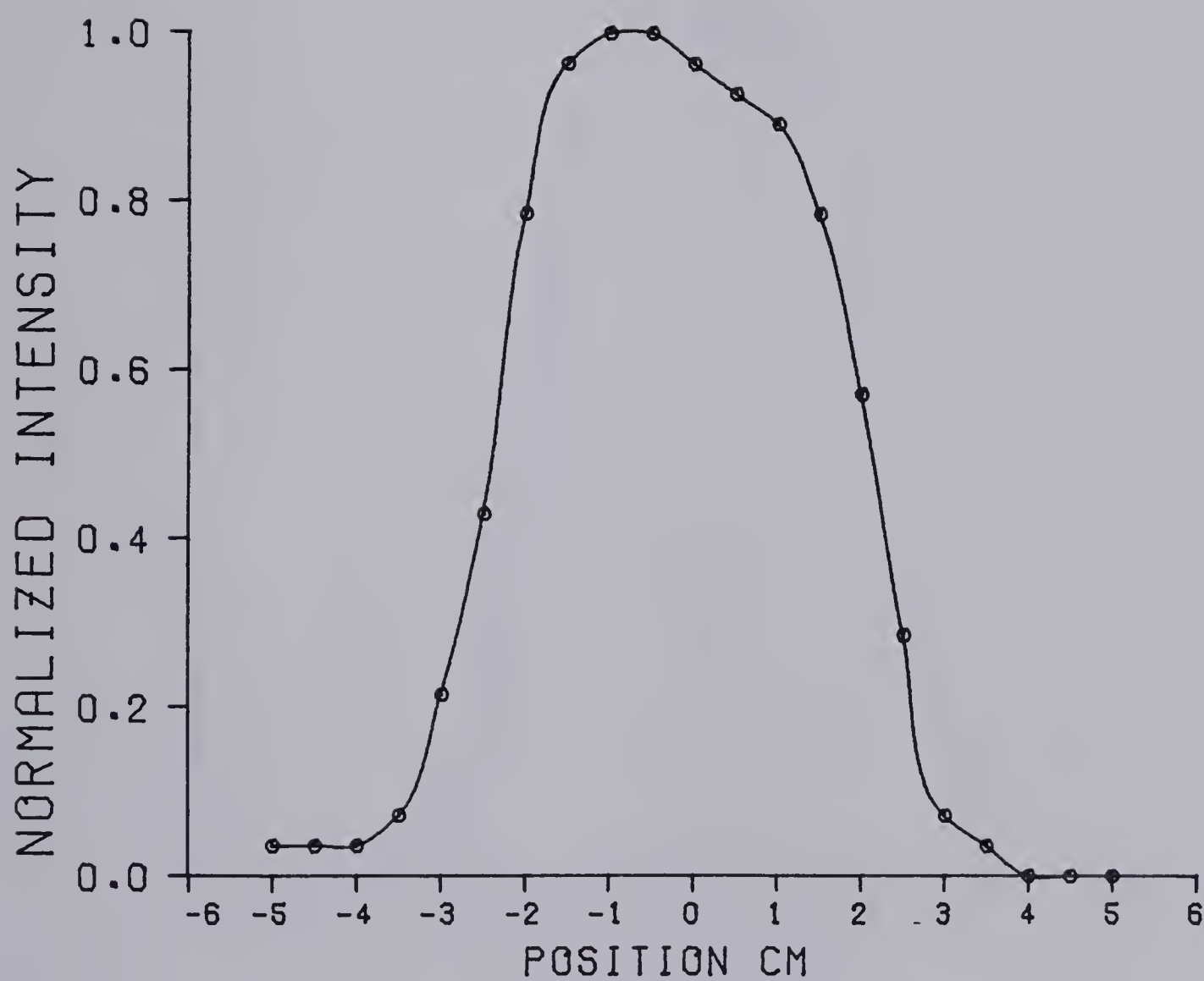


Fig. 6.41 Intensity Profile for 60 Torr N₂ Discharge with
81.2nf Capacitor.

60 TORR N2
20.4 NF

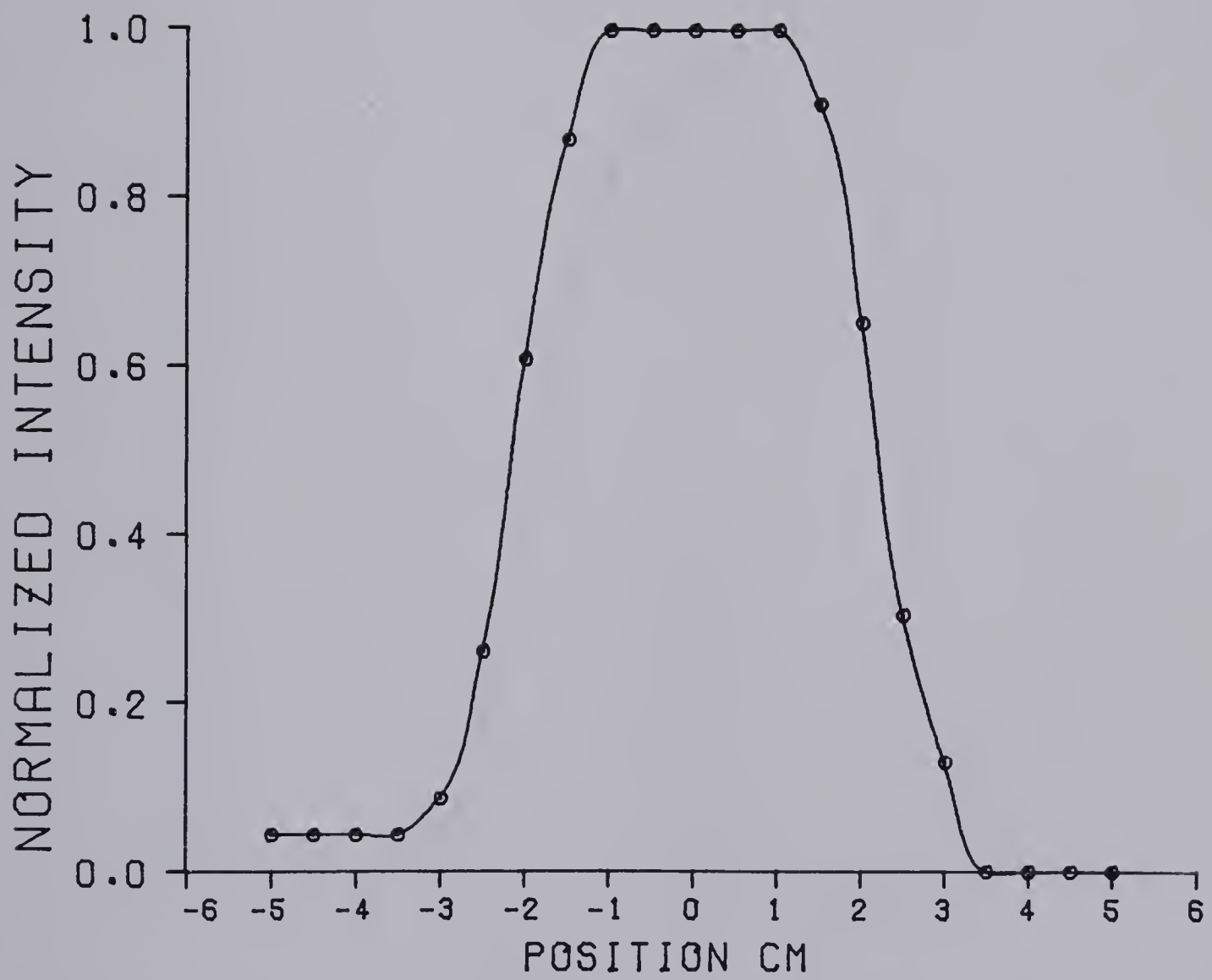


Fig. 6.42 Intensity Profile for 60 Torr N₂ Discharge with
20.4nf Capacitor.

80 TORR CO₂
81.2 NF

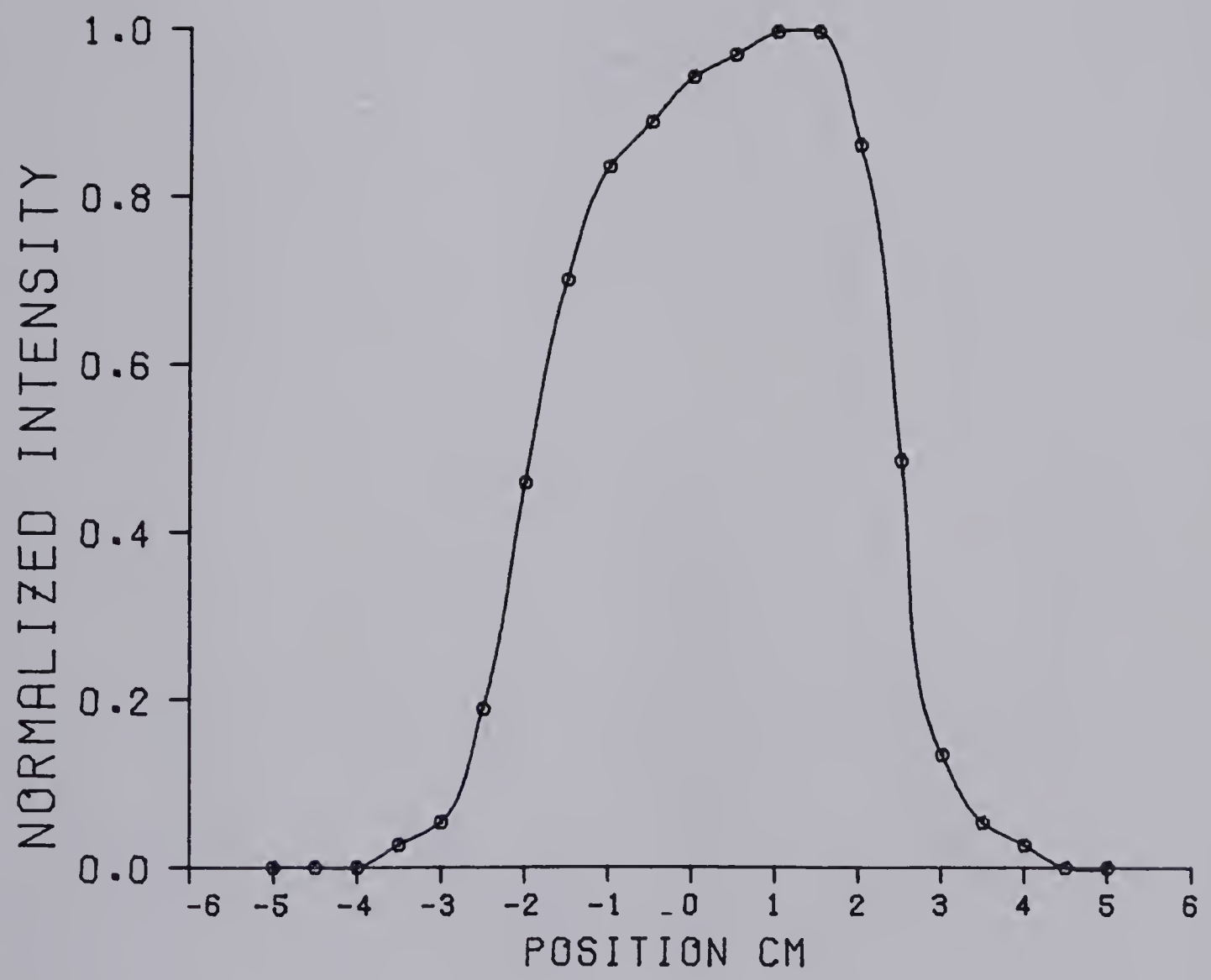


Fig. 6.43 Intensity Profile for 80 Torr CO₂ Discharge with
81.2nf Capacitor.

80 TORR CO₂
20.4 NF

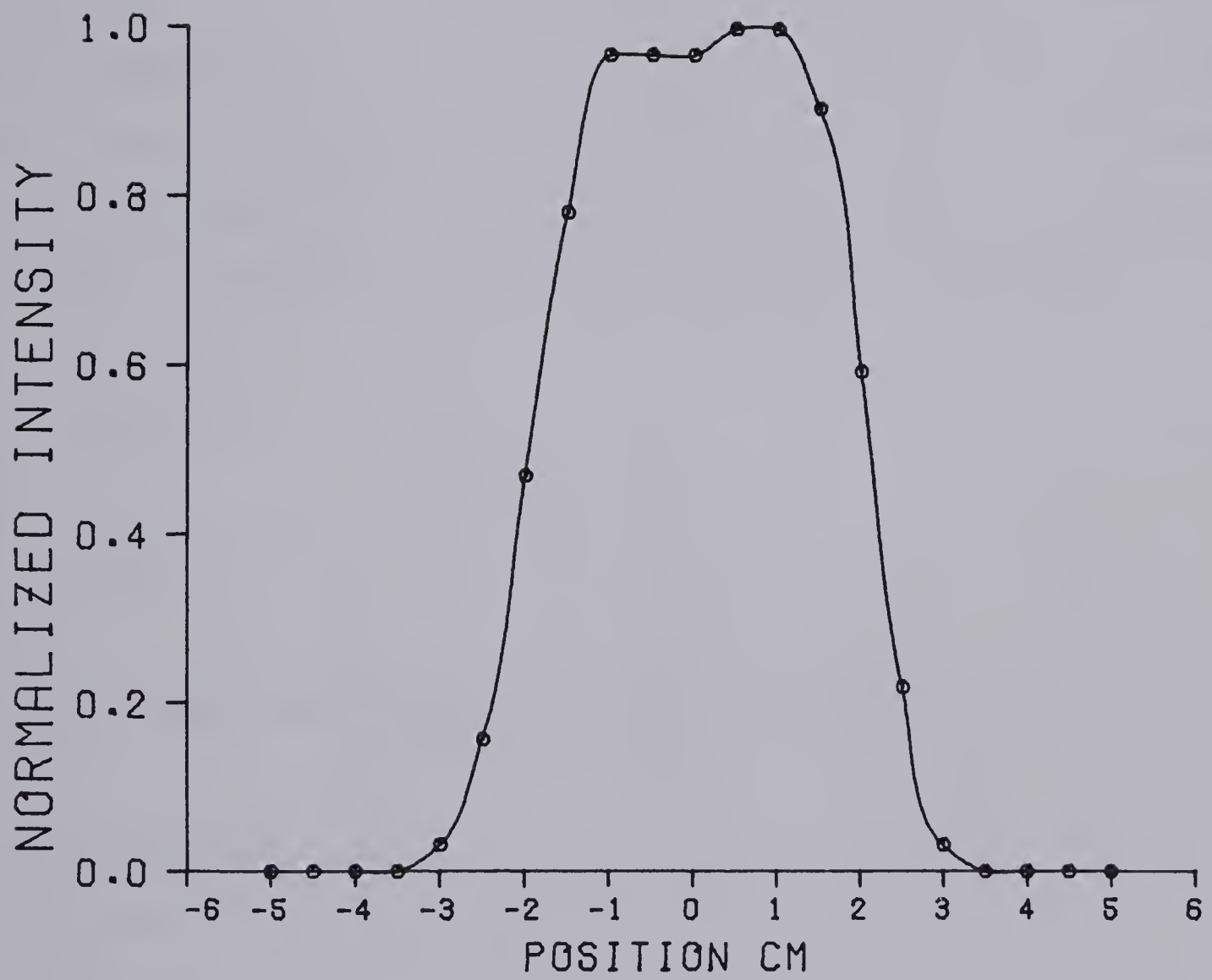


Fig. 6.44 Intensity Profile for 80 Torr CO₂ Discharge
with 20.4nf Capacitor.

shown in Figures 6.45 and 6.46. They agree with the qualitative variations visible to the eye. The He discharge was brighter on the downstream edge and the N_2 discharge on the upstream edge.

Although it is difficult to determine the light intensity distribution from an intensity profile it is easy to calculate the intensity profile from a given light intensity distribution. For comparison with the observed intensity profiles a profile is calculated for a completely uniform cylindrical discharge. Assume the discharge has a circular cross section of radius 1. If it is completely uniform, the light intensity observed will be proportional to the area probed by the photomultiplier. Take the width probed by the photomultiplier to be w . The geometry of the problem is shown in Figure 6.47. Due to symmetry the area probed in one quadrant only needs to be found. The total area will be twice this amount.

$$x^2 + y^2 = 1$$

so

$$y = \pm \sqrt{1 - x^2}$$

In the top right hand quadrant an element of area is given by:

$$dA = ydx = \sqrt{1 - x^2} dx$$

so the area is:

$$A = \int_{x - \frac{w}{2}}^{x + \frac{w}{2}} (1 - x^2)^{\frac{1}{2}} dx$$

$$= \left[\frac{x\sqrt{1 - x^2}}{2} + \frac{1}{2} \sin^{-1} x \right]_{x - \frac{w}{2}}^{x + \frac{w}{2}}$$

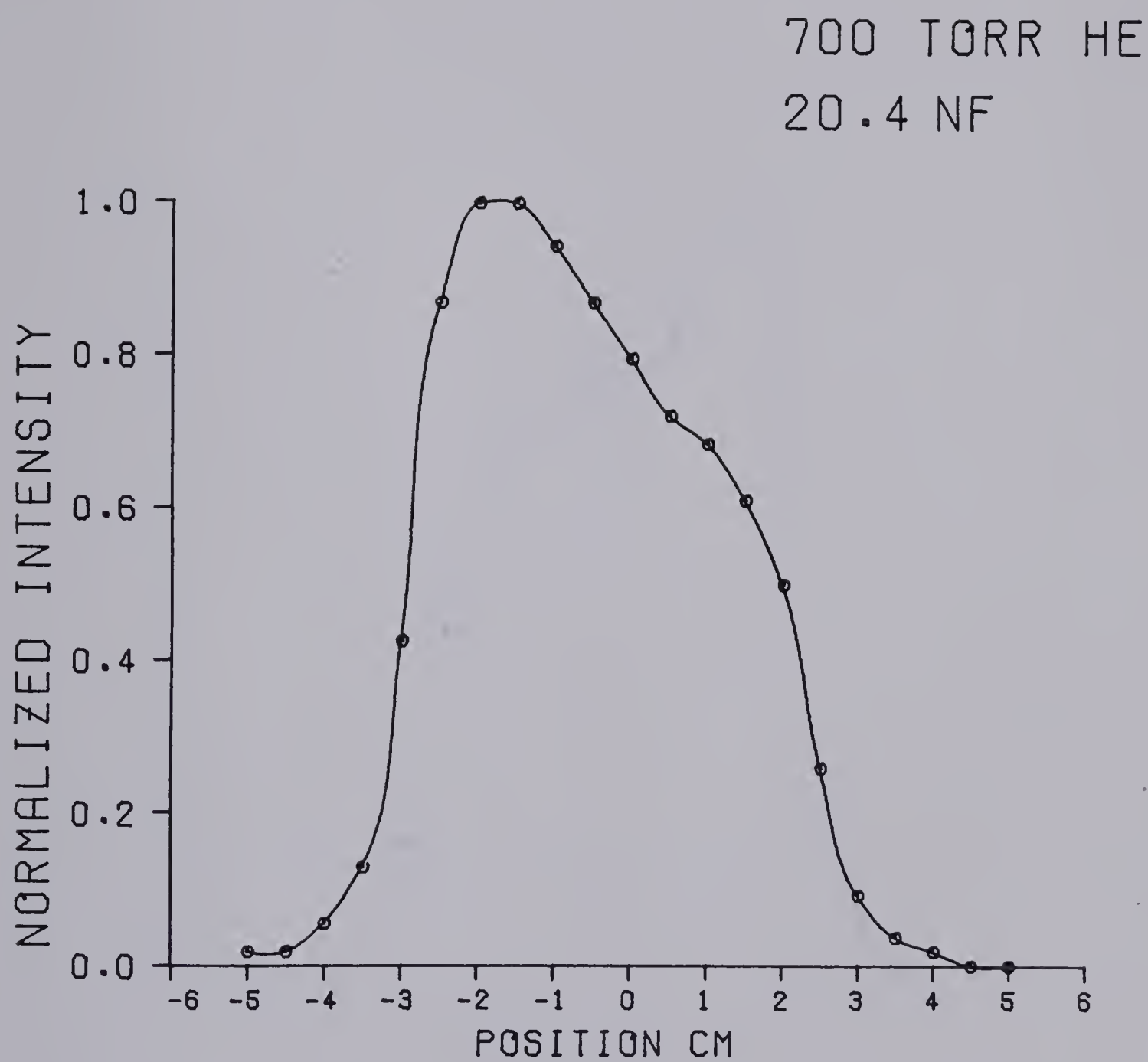


Fig. 6.45 Intensity Profile for a Repetition Rate Induced Nonuniform Discharge.

The discharge is in 700 torr He with a 20.4nf capacitor.

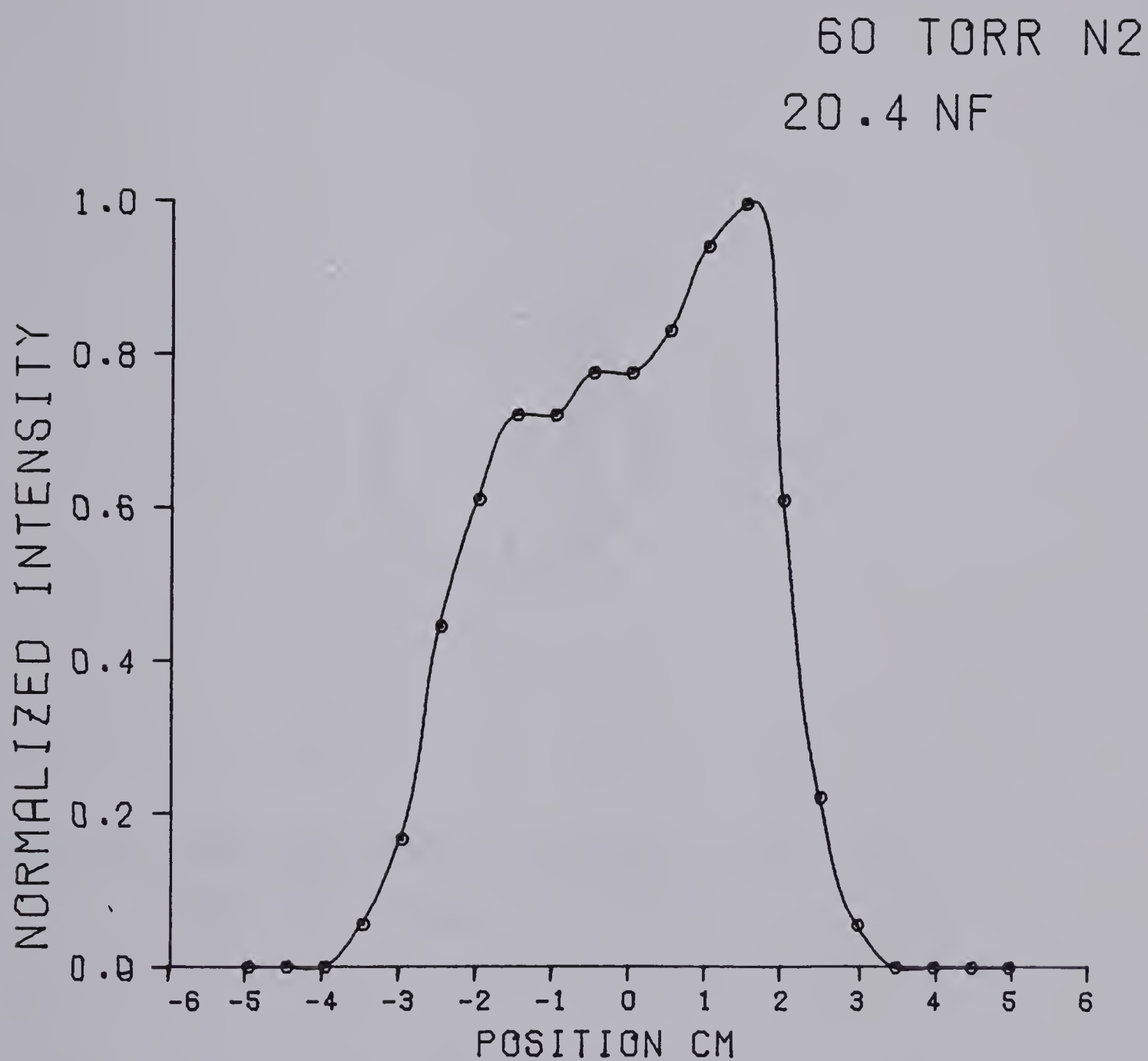


Fig. 6.46 Intensity Profile for a Repetition Rate Induced Nonuniform Discharge.

The discharge is in 60 torr N₂ with a 20.4nf capacitor.

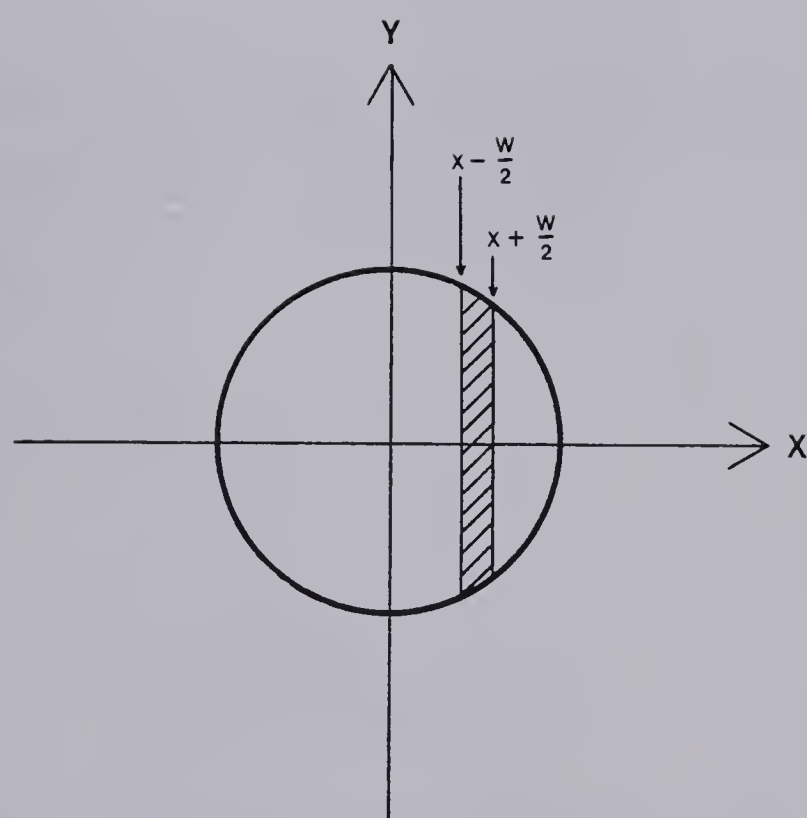


Fig. 6.47 Geometry of Uniform Discharge Model used for
Calculating a Model Intensity Profile.

From symmetry the area both above and below the x axis is double this so the total area is given by:

$$\begin{aligned} \text{Total Area} = & (x + \frac{w}{2})\sqrt{1-(x + \frac{w}{2})^2} - (x - \frac{w}{2})\sqrt{1-(x - \frac{w}{2})^2} \\ & + \sin^{-1}(x + \frac{w}{2}) - \sin^{-1}(x - \frac{w}{2}) \end{aligned} \quad 6.9.1$$

A modification of this formula is useful near the boundary $x = 1$. In this case the integration limits are changed to $x-w$ and x . Then the formula becomes:

$$\begin{aligned} A = & \int_{x-w}^x (1 - x^2)^{\frac{1}{2}} dx \\ = & \left[\frac{x\sqrt{1-x^2}}{2} + \frac{1}{2} \sin^{-1}x \right]_{x-w}^x \end{aligned}$$

Again, by symmetry the total area is double this so:

$$\begin{aligned} \text{Total Area} = & x\sqrt{1-x^2} + \sin^{-1}x - (x-w)\sqrt{1-(x-w)^2} - \sin^{-1}(x-w) \end{aligned} \quad 6.9.2$$

The total intensity is just some constant times the area so 6.9.1 and 6.9.2 can be used to plot a representative intensity profile for a uniform discharge. The discharge radius was typically 35 mm, the scan spacing was 5 mm, and the resolution (w) was 7 mm. Normalizing this the radius becomes 1, the scan spacing becomes .143 and w becomes .20. The intensity profile is shown in Figure 6.48.

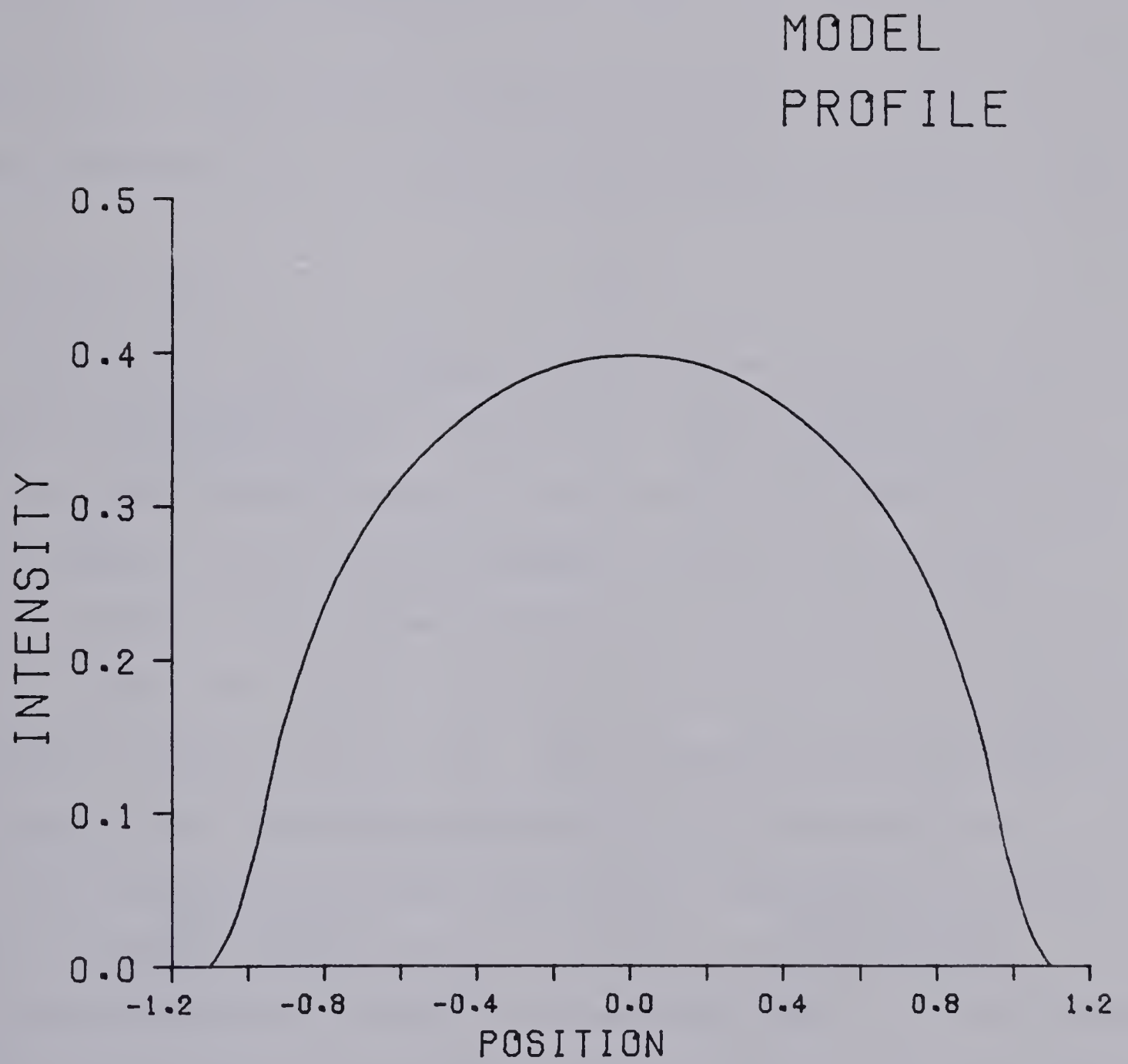


Fig. 6.48 Model Intensity Profile for a Uniform Discharge.

The procedure can be generalized to predict the intensity profile for nonuniform intensity distributions. In that case the intensity profile is given by:

$$I(x) = \int_{x - \frac{w}{2}}^{x + \frac{w}{2}} \int_{-\sqrt{1-x^2}}^{+\sqrt{1-x^2}} f(x,y) dy dx$$

where $f(x,y)$ is the intensity distribution function. In the case of a uniform discharge $f(x,y) = 1$ and the results simplify to equation 6.9.1.

6.10 ARCING MODES

Two distinct types of discharge instability were observed in the flowing gas discharge system. The first is related to energy density. When the energy density becomes too high a glow to arc transition occurs. This transition occurs for an increasing fraction of the discharge pulses as energy density rises, until at high enough energy densities it occurs all the time. At the other end of the scale, for very low energy densities it does not occur at all. This transition occurs independently of repetition rate and between the plane portion of the electrodes.

The other type of discharge instability is repetition rate induced and is related to gas flow velocity. It is due to not sufficiently clearing the discharge products from the previous pulse out of the discharge region. This instability can appear in one of three typical modes which are illustrated in Figure 6.49. They are: pulling, arcing between the electrodes on the downstream edge, and arcing from the cathode to the spark pins. Although all three repetition rate instabilities can be made to occur in each of the gases certain gases tend to favour certain instabilities. Pulling occurs in He for most energy densities and in N_2

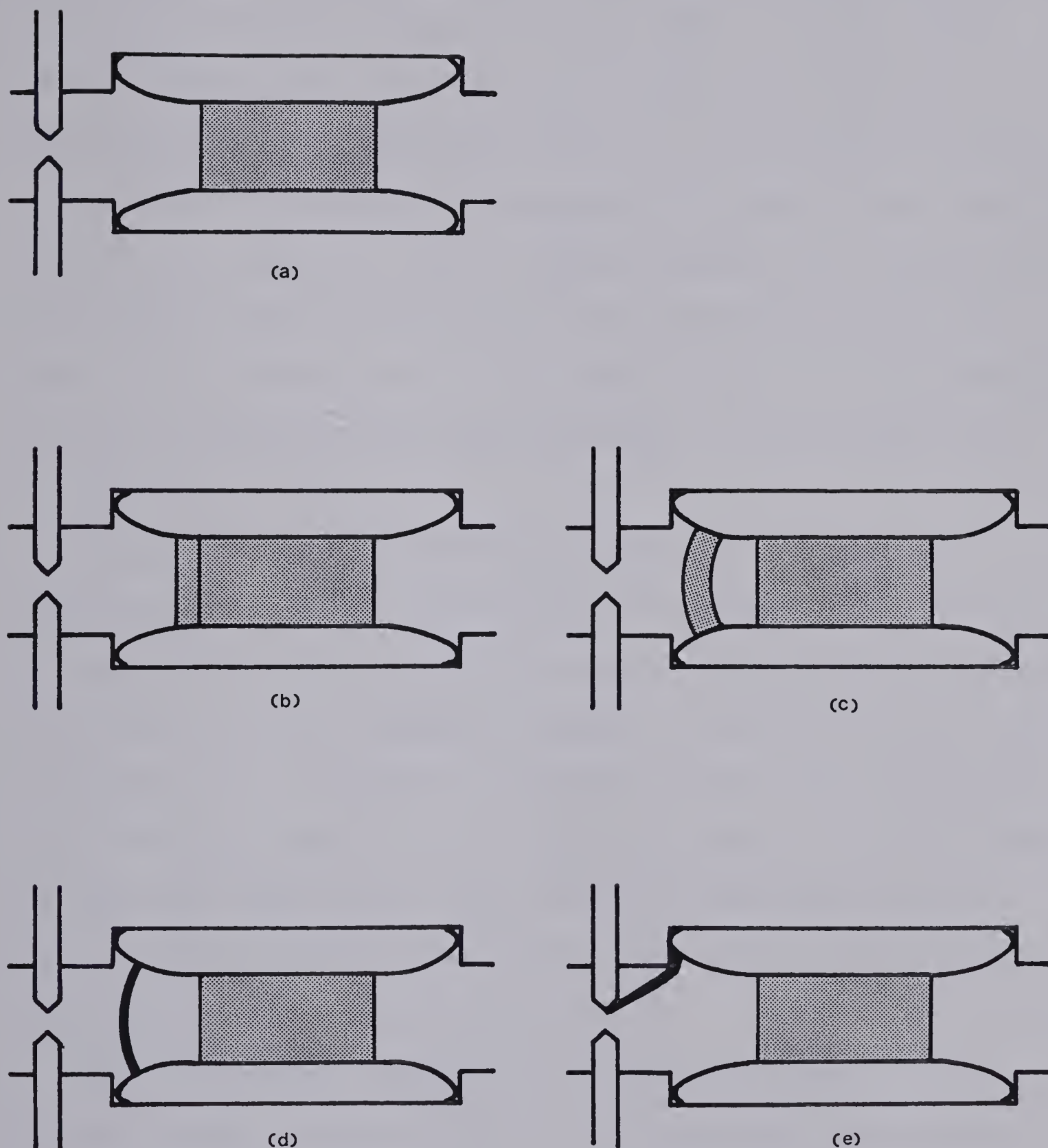


Figure 6.49 Repetition Rate Induced Arcing Modes. (a) Is a uniform discharge, (b) Shows discharge pulling, (c) Shows an auxiliary discharge (observed in CO_2), (d) Shows an arc between the electrodes, and (e) Shows an arc from the cathode to a spark pin.

at low energy densities. A variation of pulling occurs in CO_2 at low energy densities. In this variation a second smaller auxiliary discharge forms on the downstream portion of the electrodes. At higher energy densities arcing occurs and can be either between the electrodes or from the cathode to the downstream spark pin. Arcs in He and CO_2 tend to occur between the electrodes whereas arcs in N_2 tend to occur from the cathode to the spark pin. The key difference between the repetition rate induced instabilities and the energy induced instability is that the repetition rate effects occur on the downstream edge of the discharge while the energy instability occurs toward the center of the discharge where the electrodes are flat.

Figures 6.50 and 6.51 illustrate the typical repetition rate instabilities encountered, and the repetition rates at which they occur. The instability repetition rates were measured by increasing the repetition rate until a particular instability appeared to occur continuously. The lines disch, elect, and pins are estimated repetition rates based on the convection times needed for gas to clear the discharge region, electrodes, and spark pins respectively. These estimates ignore possible effects due to discharge expansion. The dominant instability is the instability that occurs at the lowest repetition rate.

In He the dominant instability is pulling and it occurs if the discharge gas has not had time to clear the electrodes between pulses. If the repetition rate is pushed higher until the gas has not yet had time to clear the discharge region arcing occurs between the electrodes. Finally if the repetition rate is pushed higher still arcing between the cathode and spark pin will occur. In 60 torr N_2 the dominant instability is pulling for energy densities less than approximately 45 J/l. If the

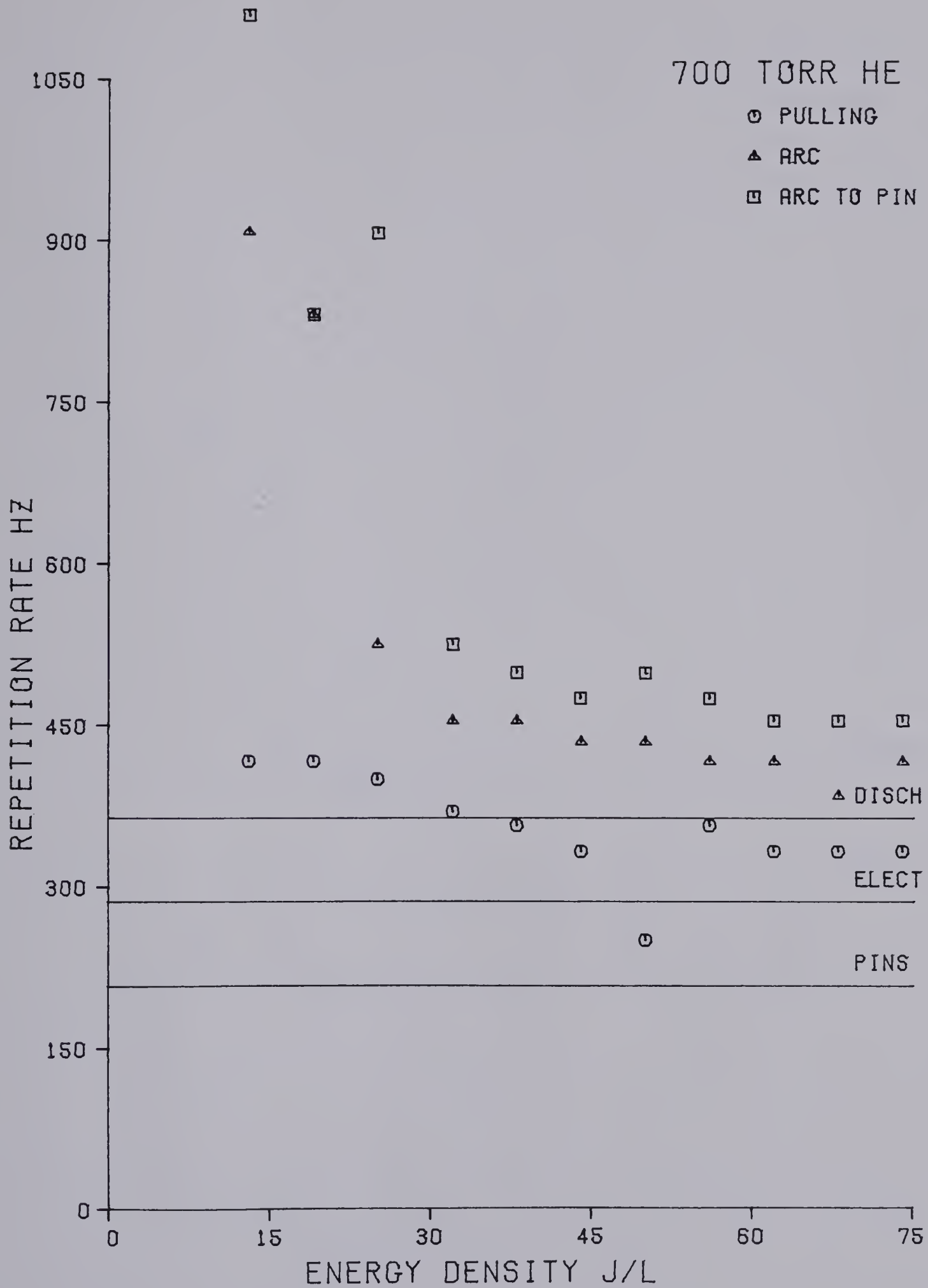


Fig. 6.50 Repetition Rate Induced Instabilities as a Function of Energy Density in 700 Torr He for a Gas Flow Velocity of 24 m/sec.

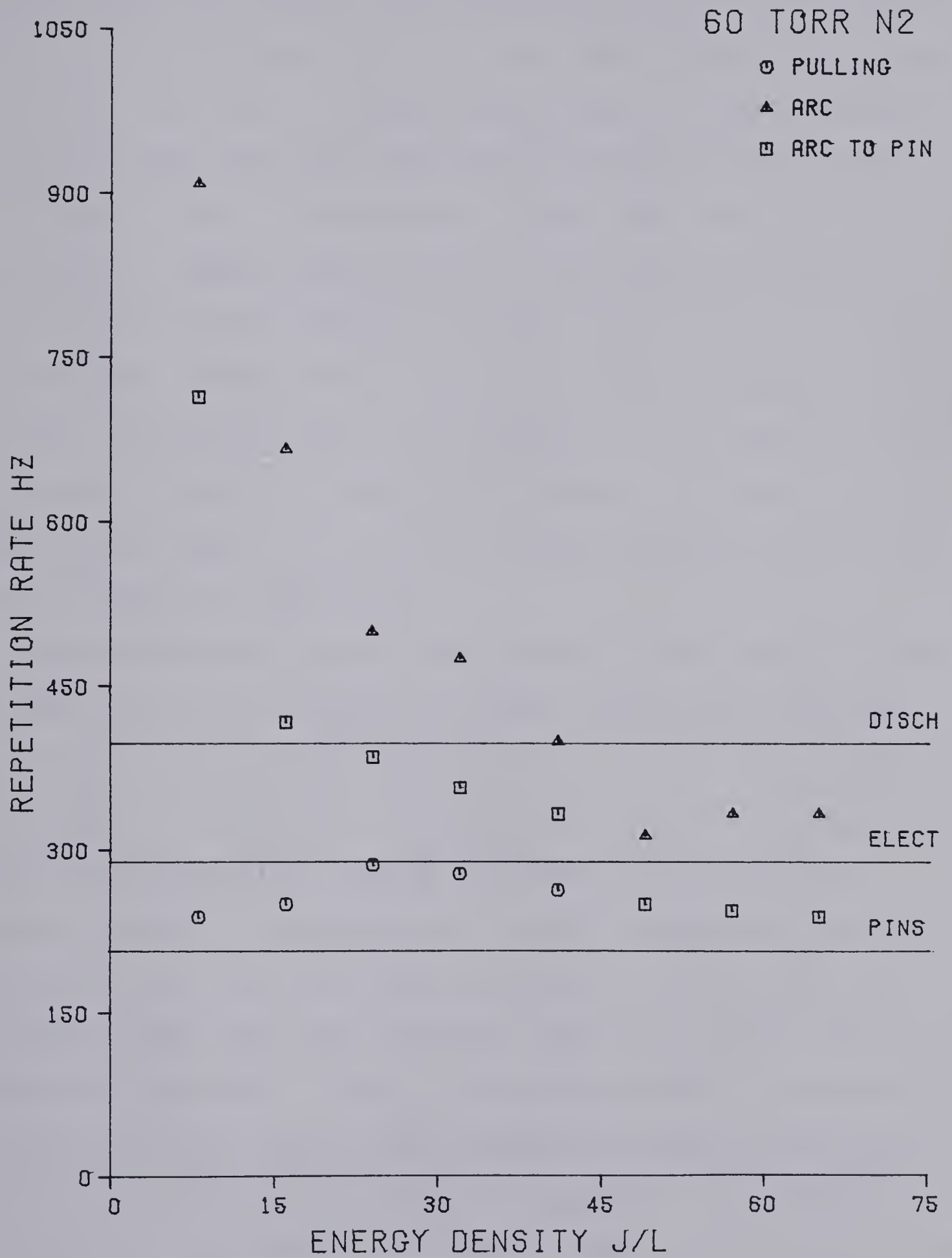


Fig. 6.51 Repetition Rate Induced Instabilities as a Function of Energy Density in 60 Torr N₂ for a Gas Flow Velocity of 19.5 m/sec.

repetition rate is increased arcing between the cathode and the spark pin sets in. For still higher repetition rates arcing between the electrodes also occurs. Note that for energy densities above 45 J/l pulling stops and arcing between the cathode and spark pin becomes the dominant mode.

Figures 6.52 to 6.56 show the basic arcing modes and extend the measurements to higher energy densities. The vertical bars map the regions in which energy induced instabilities occur ranging from no energy induced arcing, through sporadic arcing, to a completely unstable discharge. Note that in 80 torr CO₂ there is a transition in arcing modes from arcing between the electrodes to arcing from the cathode to the spark pin in the energy density range of 30 to 40 J/l. The same transition occurs in the 400 torr laser mix at about 65 J/l.

The repetition rate instabilities observed and the repetition rates for which they occur are consistent with gas convection not having had enough time to sweep the discharge products out of the regions between the electrodes or the spark pins. In particular the transition in arcing modes in CO₂ and in the 400 torr laser mixture seems to support this view because it occurs at a repetition rate for which the gas has cleared the electrodes but not the space between the electrodes and the spark pins. Hence arcing jumps from being between the electrodes to being between the cathode and a spark pin. In CO₂ at higher energy densities the repetition rate drops below that predicted from the convection time for clearing the spark pins. But this can be explained by expansion of the discharge gases which will increase the time needed to clear the spark pins to somewhat longer than predicted from the convection time.

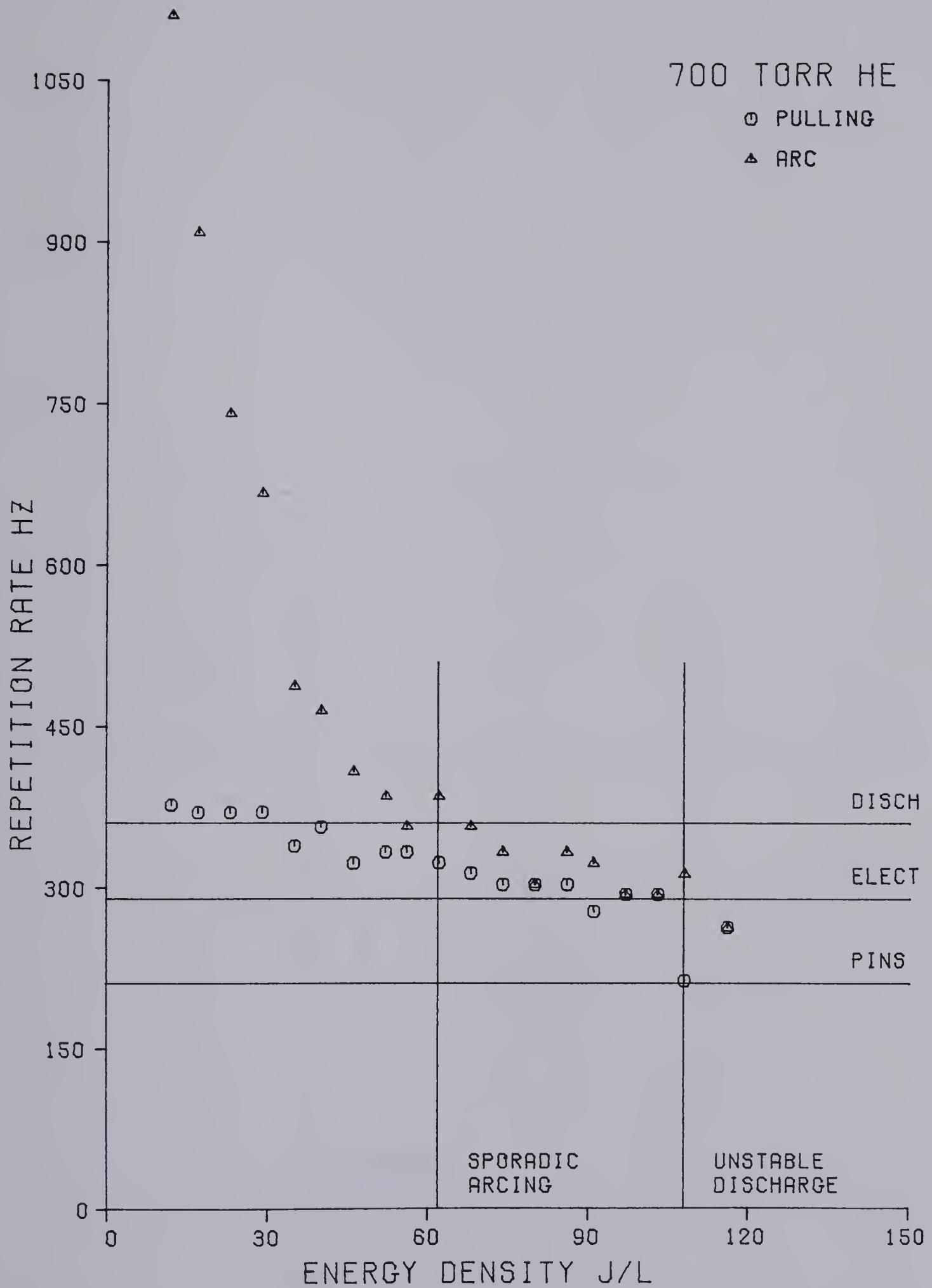


Fig. 6.52 Onset of Arcing Modes as a Function of Energy Density in
700 Torr He for a Gas Flow Velocity of 24.7 m/sec.

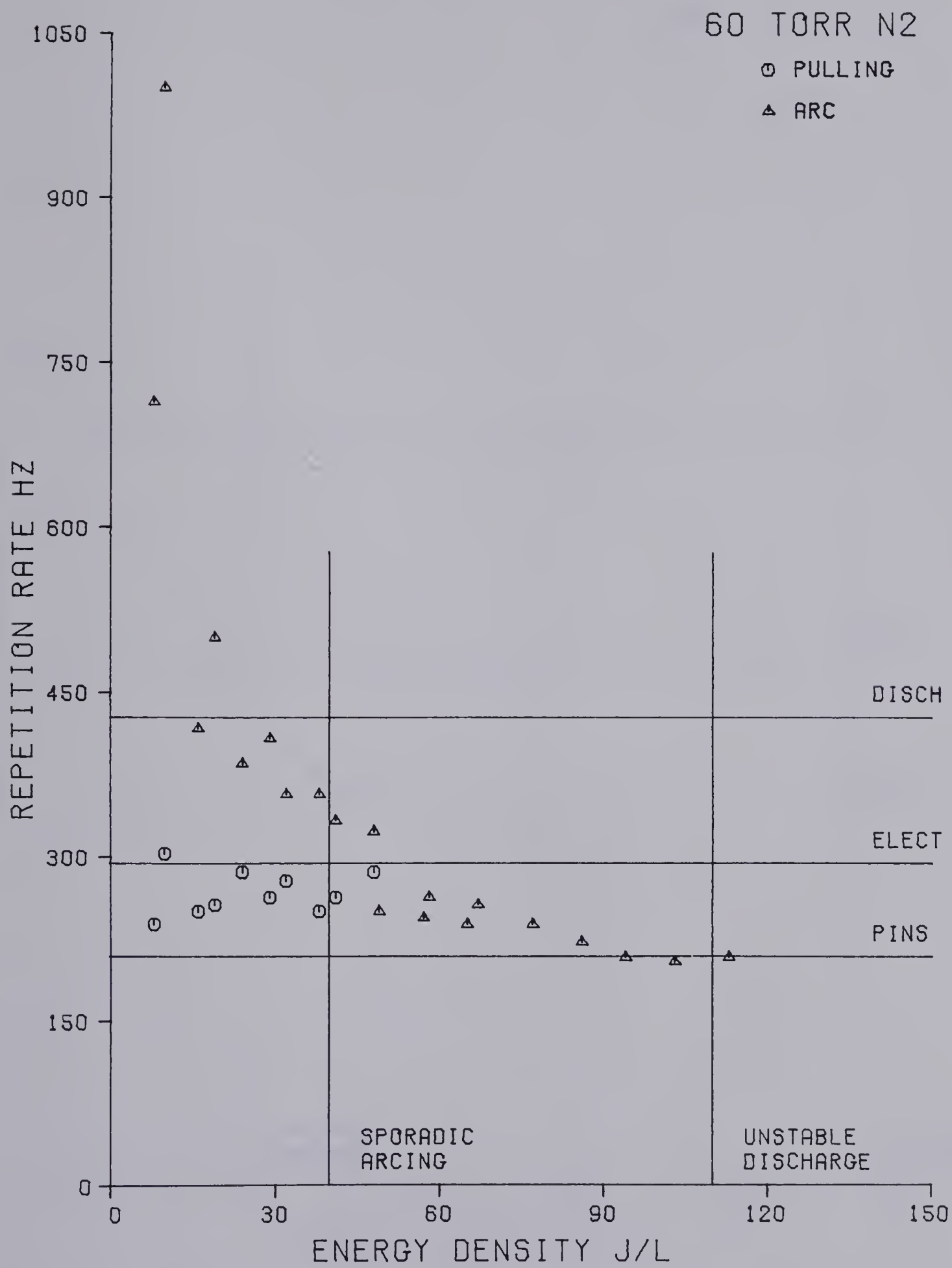


Fig. 6.53 Onset of Arcing Modes as a Function of Energy Density in 60 Torr N₂ for a Gas Flow Velocity of 19.5 m/sec.

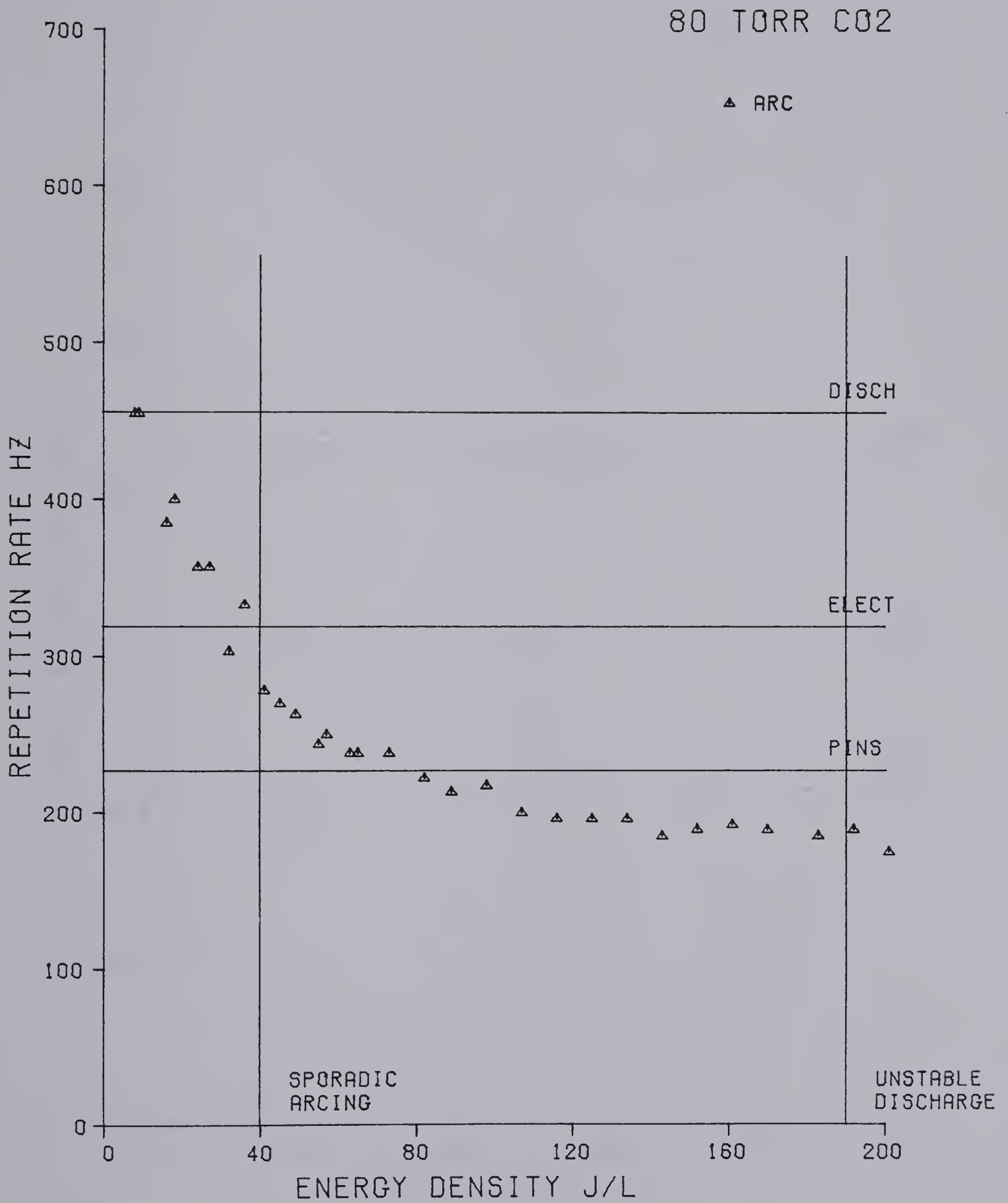


Fig. 6.54 Onset of Arcing as a Function of Energy Density in 80 Torr CO₂ for a Gas Flow Velocity of 21.7 m/sec.

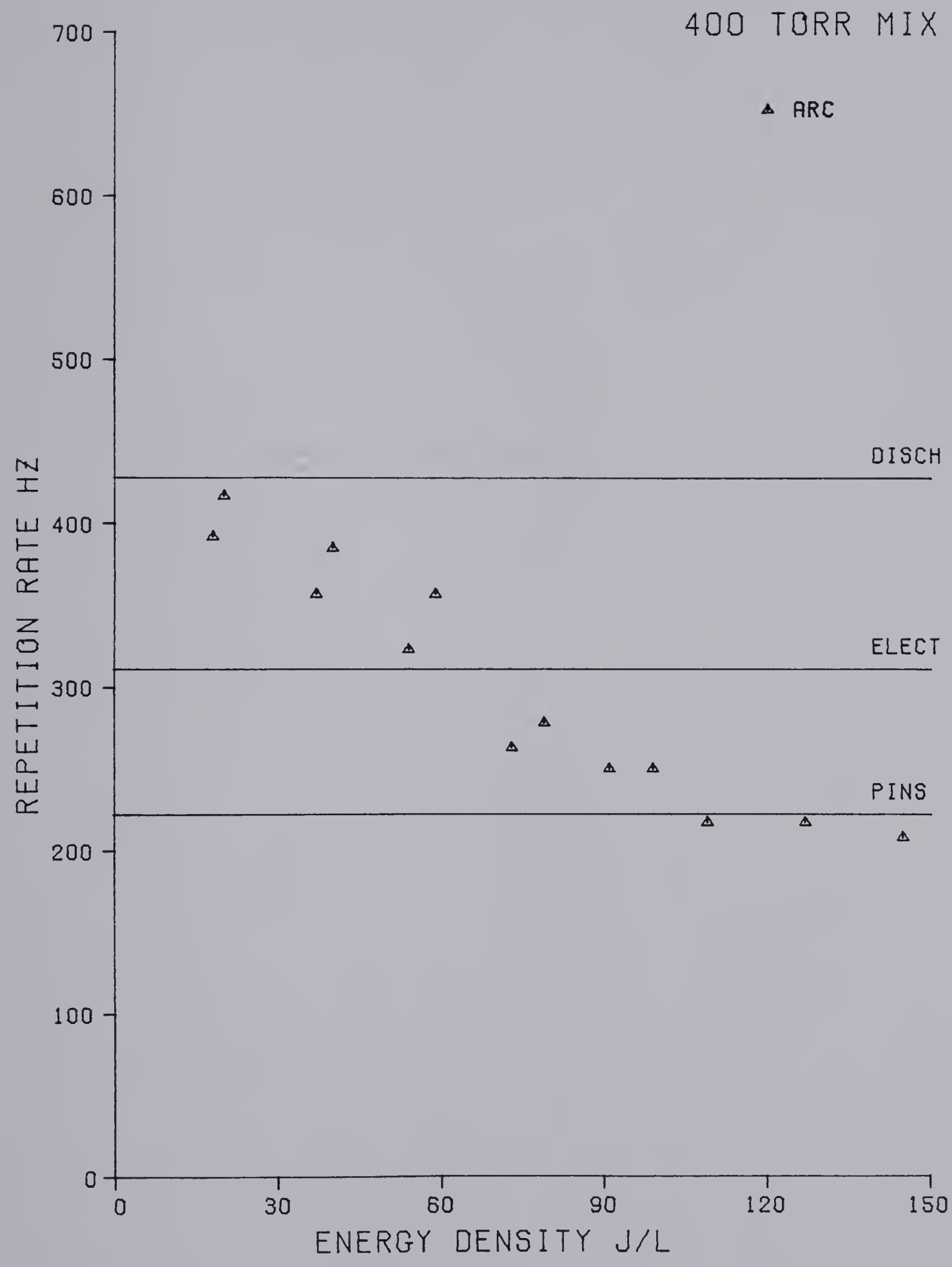


Fig. 6.55 Onset of Arcing as a Function of Energy Density in 400 Torr
of 1:1:8 CO₂:N₂:He Laser Mix.
Gas flow velocity is 24.8 m/sec.

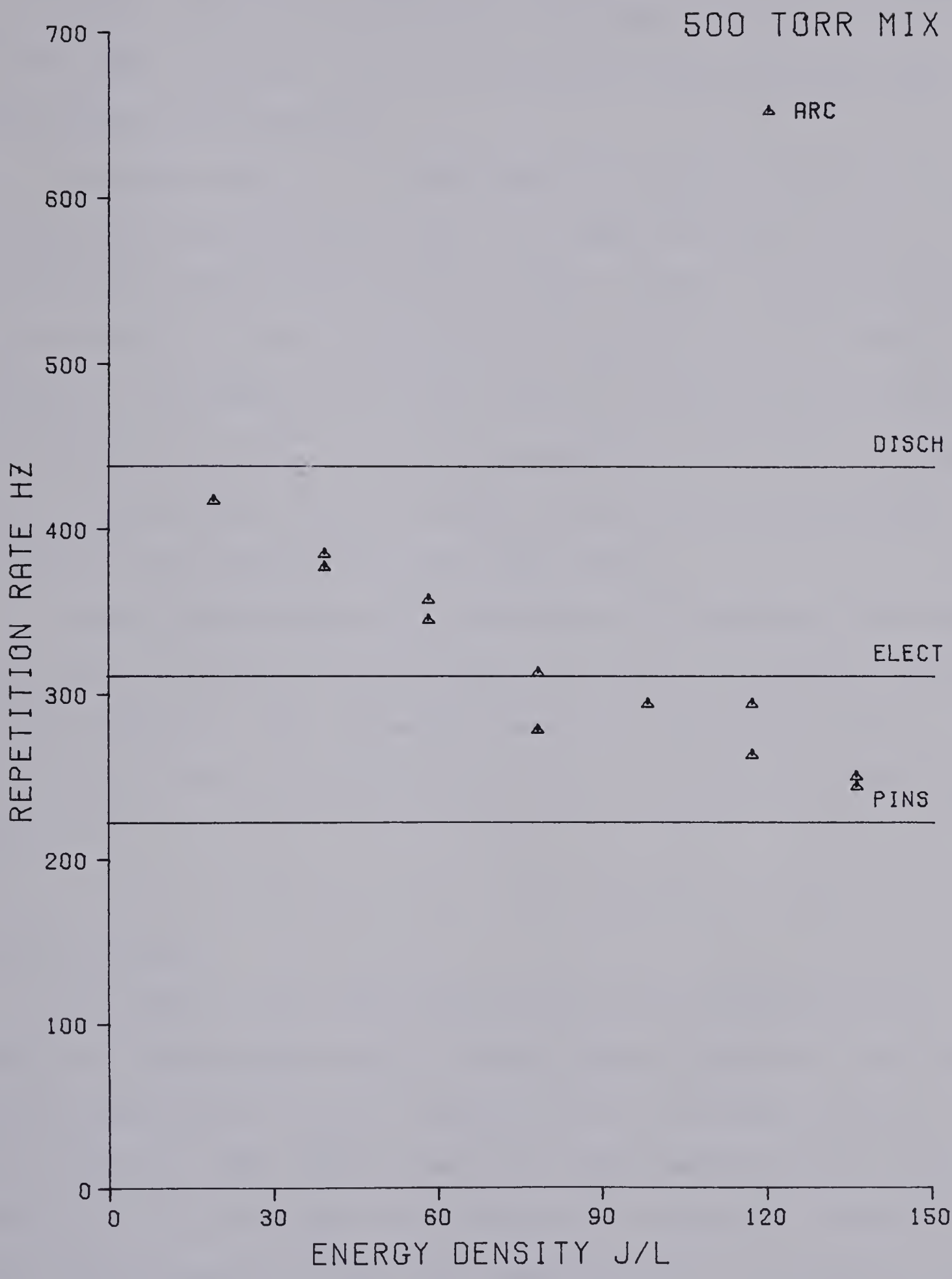


Fig. 6.56 Onset of Arcing as a Function of Energy Density in
500 Torr of 1:1:8 CO₂:N₂:He Laser Mix.
Gas flow velocity is 24.5 m/sec.

6.11 GAS POISONING

Besides repetition rate effects an additional problem was observed in the laser gas mixture that was not apparent in the individual gases. The problem is gas poisoning.

A discharge was run in a 1:1:8 mixture of $N_2:CO_2:He$ at 400 torr pressure and 100 Hz repetition rate. The energy per pulse was 4.6 J. Although the discharge was initially uniform, sporadic arcing occurred after about four minutes. A similar result was observed for a 500 torr mixture. The poisoning of the laser mixture is almost certainly due to the dissociation of CO_2 into CO and O_2 as demonstrated by Pace and Lacombe (22). This poisoning was also probably an important but unrecognized problem in the high repetition rate laser system.

Although dissociation of CO_2 was observed for discharges in 80 torr CO_2 in the flowing gas discharge system, the effect on discharge uniformity seemed negligible. This was probably because the CO_2 discharge was running at a fairly low pressure and so was less likely to collapse into an arc.

6.12 CONCLUSIONS

The results of this study show that the maximum repetition rate limit for a uniform discharge in a flowing gas high repetition rate system is due essentially to the time needed to clear the discharge region by gas convection. The clearing time can be complicated by several things. Expansion of the discharge products reduces the attainable repetition rate. Also system geometry can reduce the repetition rate. For example in the flowing gas discharge system (and the high repetition rate laser), when the energy density gets large enough the discharge products must clear

not only the electrodes but the spark pins as well resulting in a large decrease in attainable repetition rate.

In this experiment the effect of convective clearing of discharge products on repetition rate is somewhat obscured by the transitions in arcing mode with a change in energy density and by the presence of energy density induced instability.

Besides convective limits on repetition rate another important limit that was observed was the occurrence of gas poisoning.

CHAPTER 7

COMPARISON OF SPARK PREIONIZED SYSTEM AND DIELECTRIC DISCHARGE PREIONIZED SYSTEM

One of the problems encountered in the experiments with the high repetition rate discharge was that of arcing from the cathode to the preionizing spark pins. This problem caused a significant decrease in repetition rate capability since it meant that not only the electrodes but the spark pins as well had to be cleared of discharge products resulting in a much longer clearing time. It seemed that this problem could be easily eliminated by removing the spark pin and going to another preionization scheme. The other popular preionization technique is to preionize from behind a screen electrode either using spark sources or a dielectric discharge. The dielectric discharge technique was chosen for a comparison experiment because it was easy to construct and looked like it would produce very uniform preionization. In addition Pace and Lacombe (22) indicated that it should result in reduced gas poisoning compared to spark preionization.

7.1 CONSTRUCTION

The flowing gas discharge system was modified by replacing the pin preionized electrode configuration (Figure 4.7) with a double discharge configuration (Figure 7.1). In the double discharge configuration one of the copper Rogowski electrodes was left as it was before. The other electrode was replaced with a flat copper screen electrode that had a dielectric coated electrode placed behind it. This resulted in a slight increase in electrode separation from 24 mm to 27 mm.

The dielectric electrode (Figure 7.2) was formed by encasing a copper

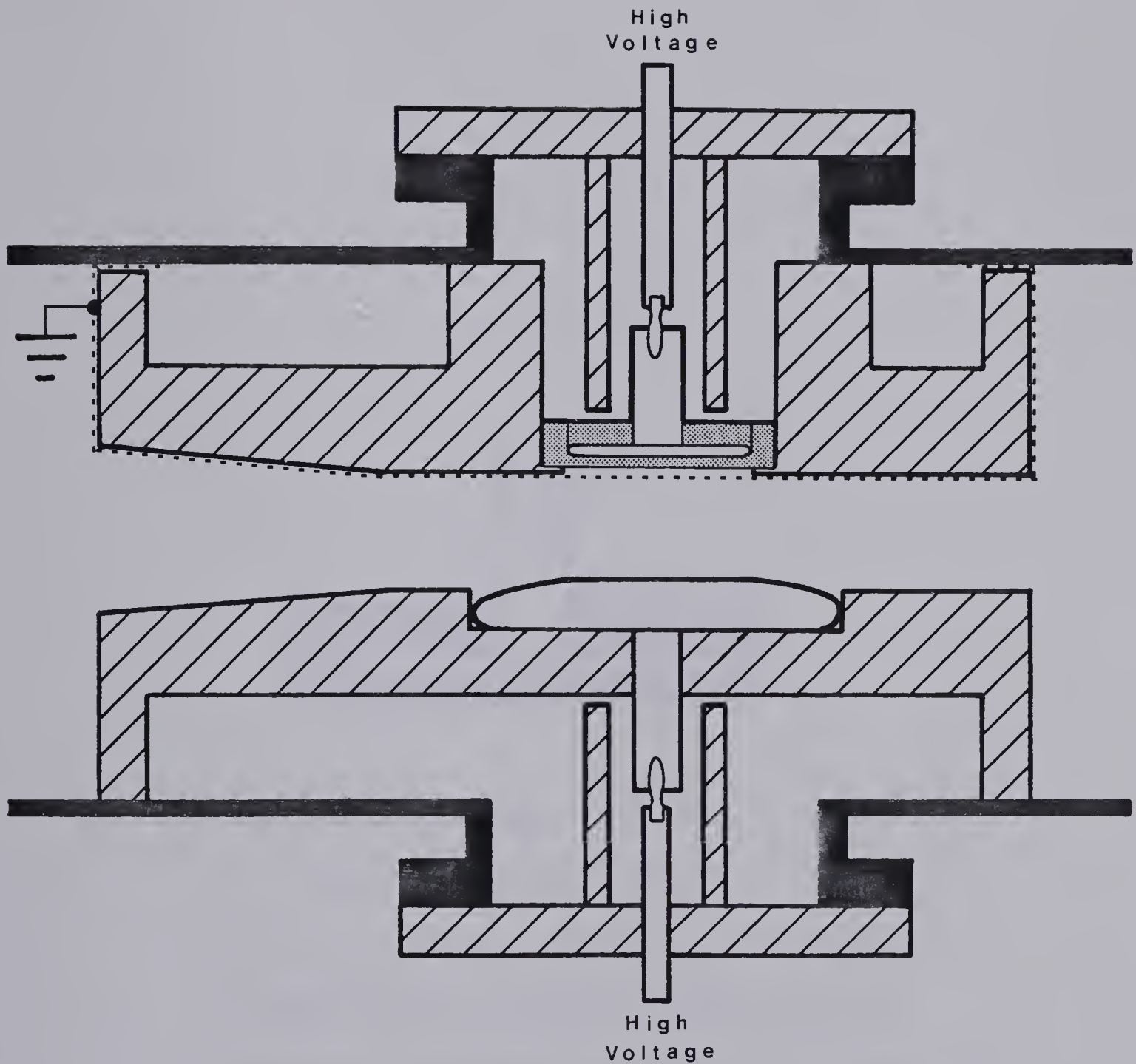


Figure 7.1 Dielectric Discharge Configuration. The Discharge is Formed Between a Copper Rogowski Profiled Electrode and a Copper Screen. Preionization is provided by a smaller discharge between a dielectric coated electrode and the screen.

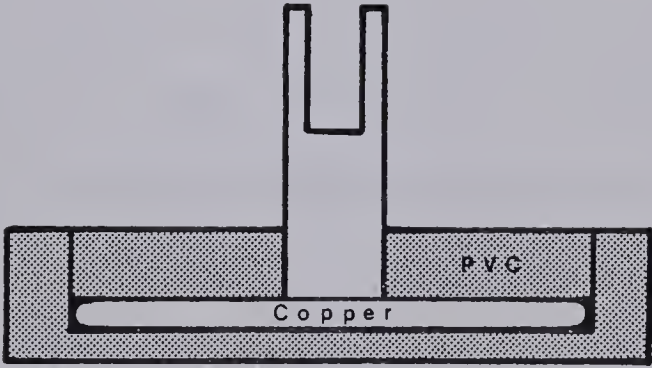


Fig. 7.2 Dielectric Electrode.

A copper disc 1/8" thick and 2" in diameter is encased in PVC. The PVC on the front surface is 1/8" thick. The post in the back is an electrical connection and mates with a banana plug.

plate in PVC. The edges of the copper plate were rounded to reduce electric field concentration and the plate was bonded to the PVC using epoxy. The PVC on the front of the plate was 1/8" thick and the gap between the back of the screen and the dielectric was 1 mm.

Except for replacing the spark pin with the dielectric electrode the circuit remains unchanged (Figure 7.3). Note that the voltage to the dielectric discharge is reduced by using the peaking capacitor as a capacitive voltage divider. The peaking capacitor corresponds to the spark pin coupling capacitor in the spark pin preionized system and has the same value of capacitance. Typical discharge voltages and current waveforms are shown in Figure 7.4. They are similar to the waveforms for the pin preionized system, the main difference being that there is a smaller initial current spike.

7.2 GAS FLOW CALIBRATION

The new electrode configuration altered the flow duct spacing so it was necessary to recalibrate the gas flow velocity as a function of fan speed. As a result of the new configuration flow velocity increased slightly. For example, in 60 torr N_2 , at 3600 rpm the flow velocity rose from 22 to 25 m/sec. The new coefficients for the calibration curves are given in Table 7.1.

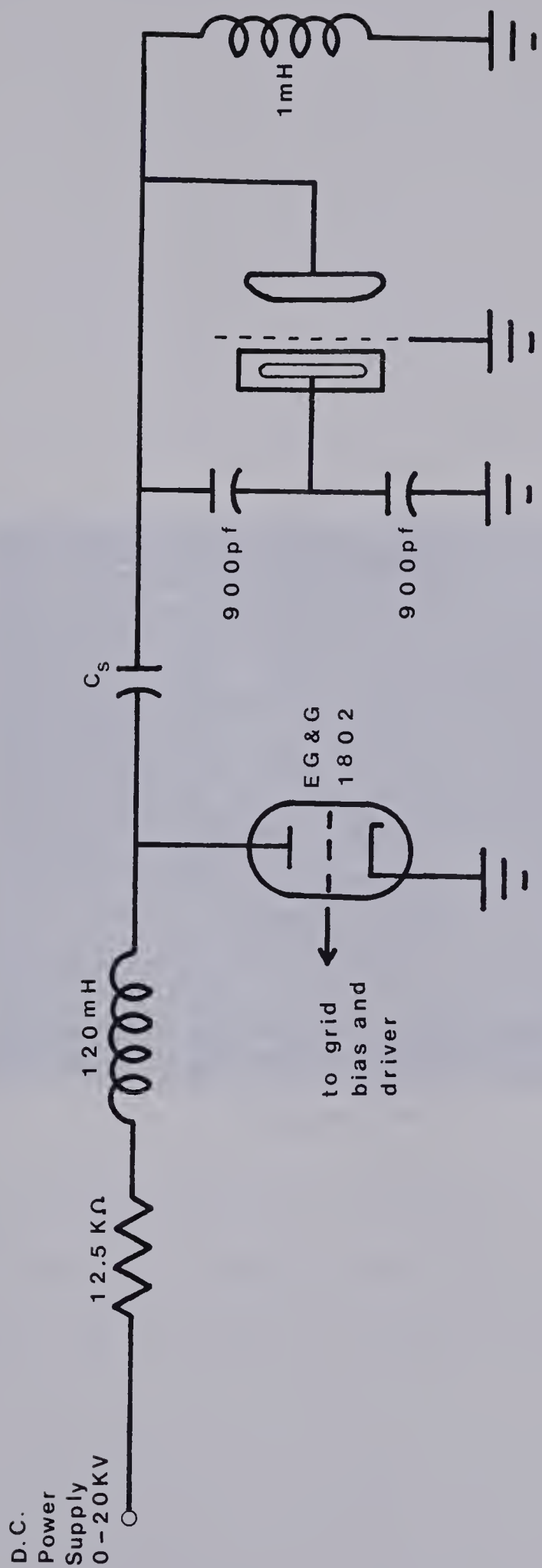


Fig. 7.3 Dielectric Discharge Preionization Discharge Circuit.

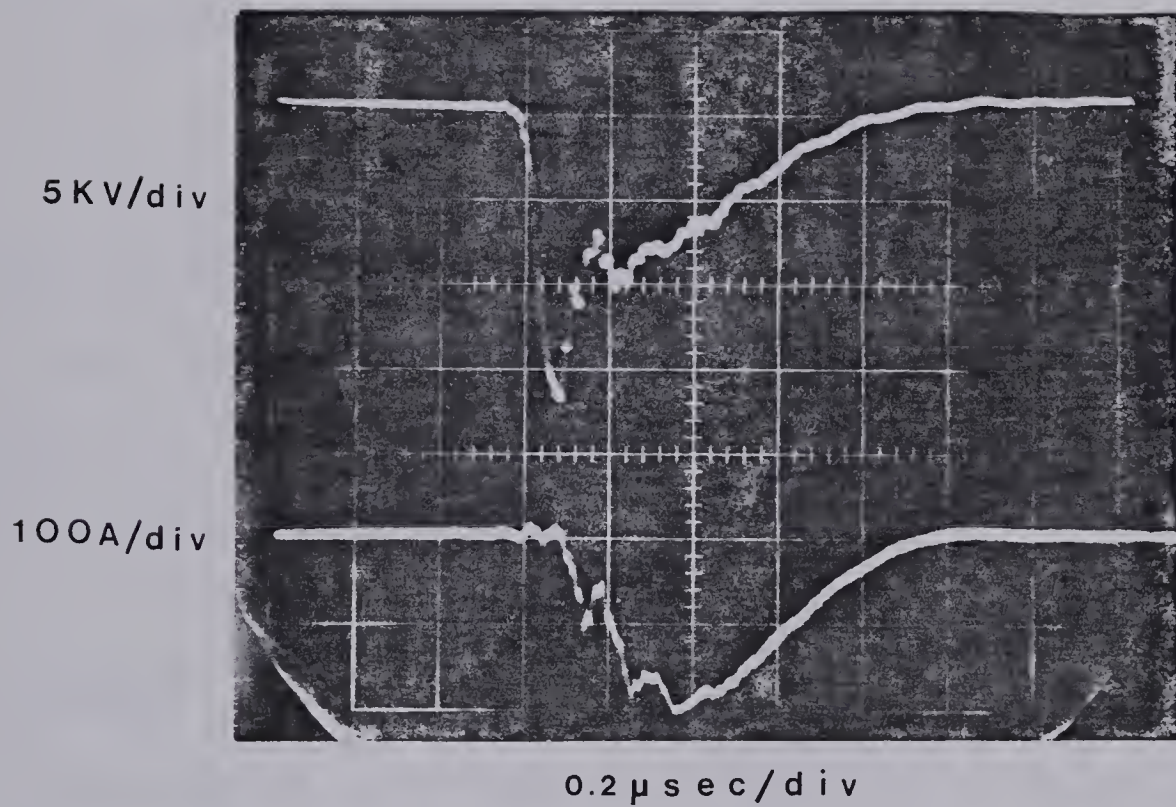


Figure 7.4 Typical Voltage and Current Waveforms for a 60 Torr N_2 Discharge in the Dielectric Discharge Preionized System. The discharge capacitor was 10 nf and the charging voltage was 10 KV.

$$y = A + Bx + Cx^2 + Dx^2$$

gas	A	B	C	D
60 torr N ₂	0.138677x10 ⁻¹	0.275098x10 ⁻²	0.198219x10 ⁻⁵	-0.220352x10 ⁻⁹
80 torr CO ₂	-0.492731x10 ⁻¹	0.549936x10 ⁻²	0.145971x10 ⁻⁵	-0.179170x10 ⁻⁹
700 torr He	-0.668171x10 ⁻¹	0.386930x10 ⁻²	0.164515x10 ⁻⁵	-0.171502x10 ⁻⁹
400 torr Mix	-0.761284x10 ⁻¹	0.510157x10 ⁻²	0.134211x10 ⁻⁵	-0.127824x10 ⁻⁹
699 torr Air	-0.347010x10 ⁻¹	0.597285x10 ⁻²	0.236838x10 ⁻⁵	-0.453158x10 ⁻⁹

Table 7.1 Calibration curve coefficients for dielectric discharge preionized system.

An interesting result was also obtained by recording a velocity profile between the cathode and anode (screen). It shows an asymmetric flow with the screen having a much thicker boundary layer than the smooth electrode (Figure 7.5). This is not surprising because the screen is a much rougher surface than the solid electrode.

7.3 RESULTS

Two parameters were measured in the dielectric discharge preionized system for comparison with the spark pin preionized system. They were maximum repetition rate as a function of energy density and maximum repetition rate as a function of gas flow velocity. Maximum repetition rate in this case is the repetition rate at which a discharge instability appears to become continuous, which is how it was defined in section 6.10. In addition discharge intensity profiles were monitored with the photo-multiplier for the purpose of establishing representative diameters to use for calculating energy density, and also to monitor discharge uniformity.

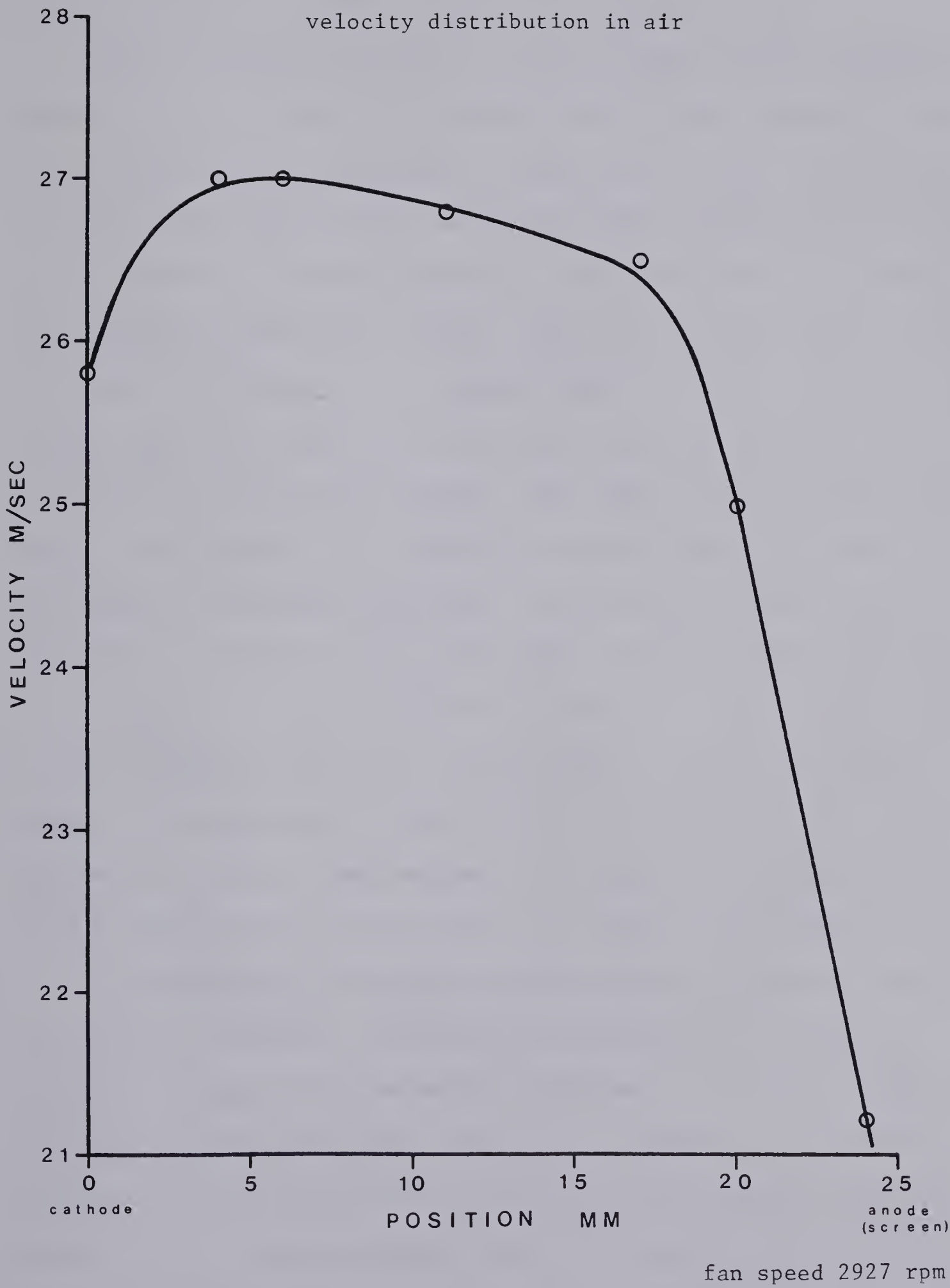


Fig. 7.5 Velocity Profile Between the Electrodes.

As before the discharge diameter is taken to be at 10% of the peak of the intensity profile. Typical intensity profiles are shown in Figures 7.6 to 7.8 and the discharge diameter was typically 70 mm.

Plots of maximum repetition rate versus energy density are shown in Figures 7.9 to 7.13 and can be compared with the same results for the pin preionized system summarized in Figures 6.52 to 6.56. The maximum repetition rate drops off with increasing energy density much more rapidly for the dielectric discharge preionized system than does the repetition rate for the pin preionized system. There are two likely causes for this reduction in performance of the screen electrode system. One is that the screen, being less uniform than the solid electrode, probably causes arcing to set in at a lower energy density. The other is that discharge products probably get trapped in the stagnant gas region behind the screen and contribute to discharge instability. An observation supporting this hypothesis is the fact that for the screen electrode system repetition rate induced arcs tended to take 6 or 7 seconds to build up in 60 torr N_2 and a similarly long time to die out when the repetition rate was reduced. Although this long time for arcs to build up and die out was observed in N_2 only, it does suggest that trapping of discharge products in the stagnant gas behind the screen is a mechanism affecting arcing.

In the dielectric discharge preionized system, as was the case in the spark pin preionized system, maximum repetition rate generally increases linearly with flow velocity (Figures 7.14 to 7.17). There was however one notable exception. For 45 J/l in 60 torr N_2 the repetition rate stayed almost constant at a low value as flow velocity increased (Figure 7.15). This also suggests that the repetition rate in this case is being limited by the time needed to clear discharge products out from behind the screen rather than by the convection of gas between the

60 TORR N₂
81.2 NF

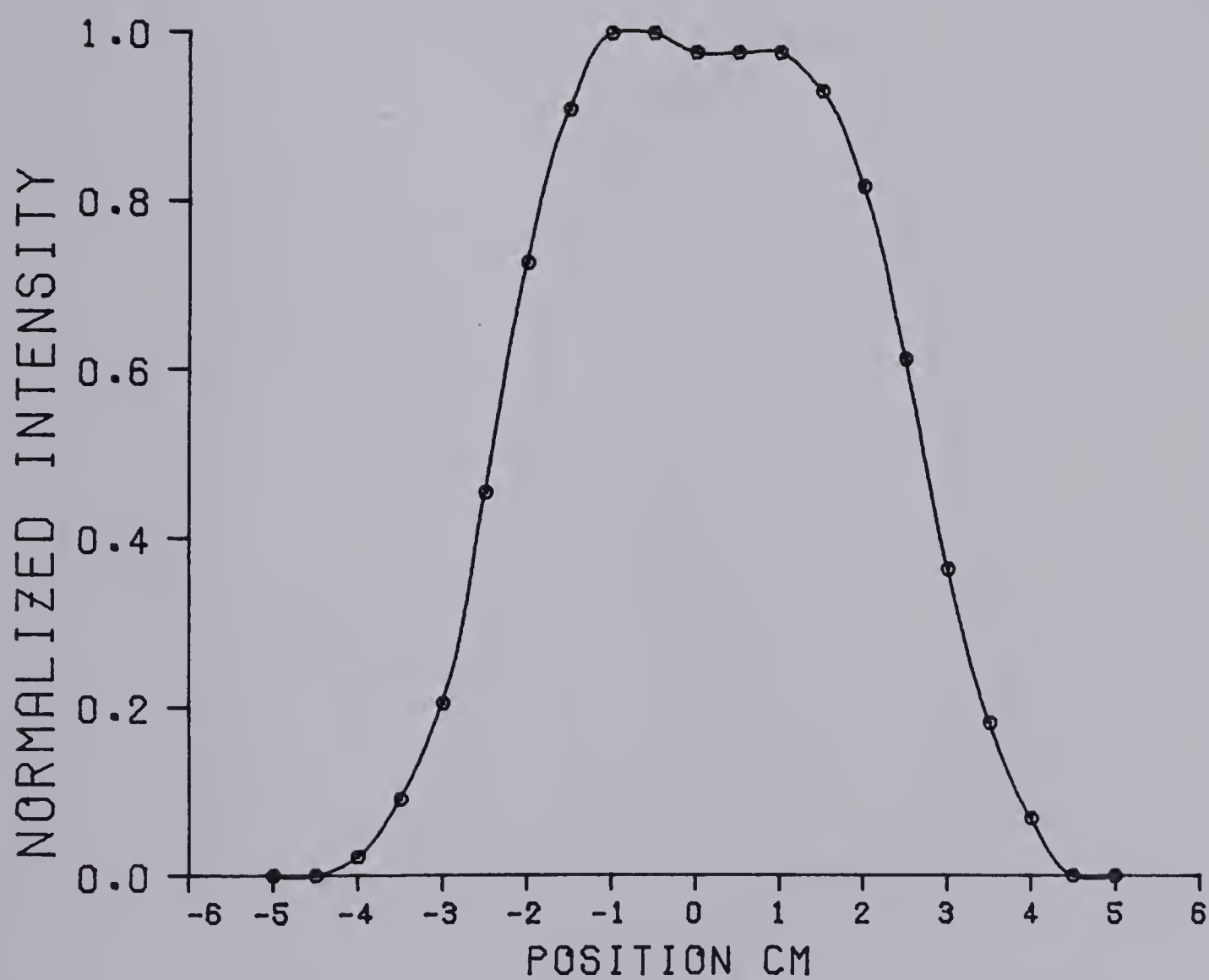


Fig. 7.6 Intensity Profile for Screen Electrode System.

Discharge in 60 torr N₂ with an 81.2nf capacitor.

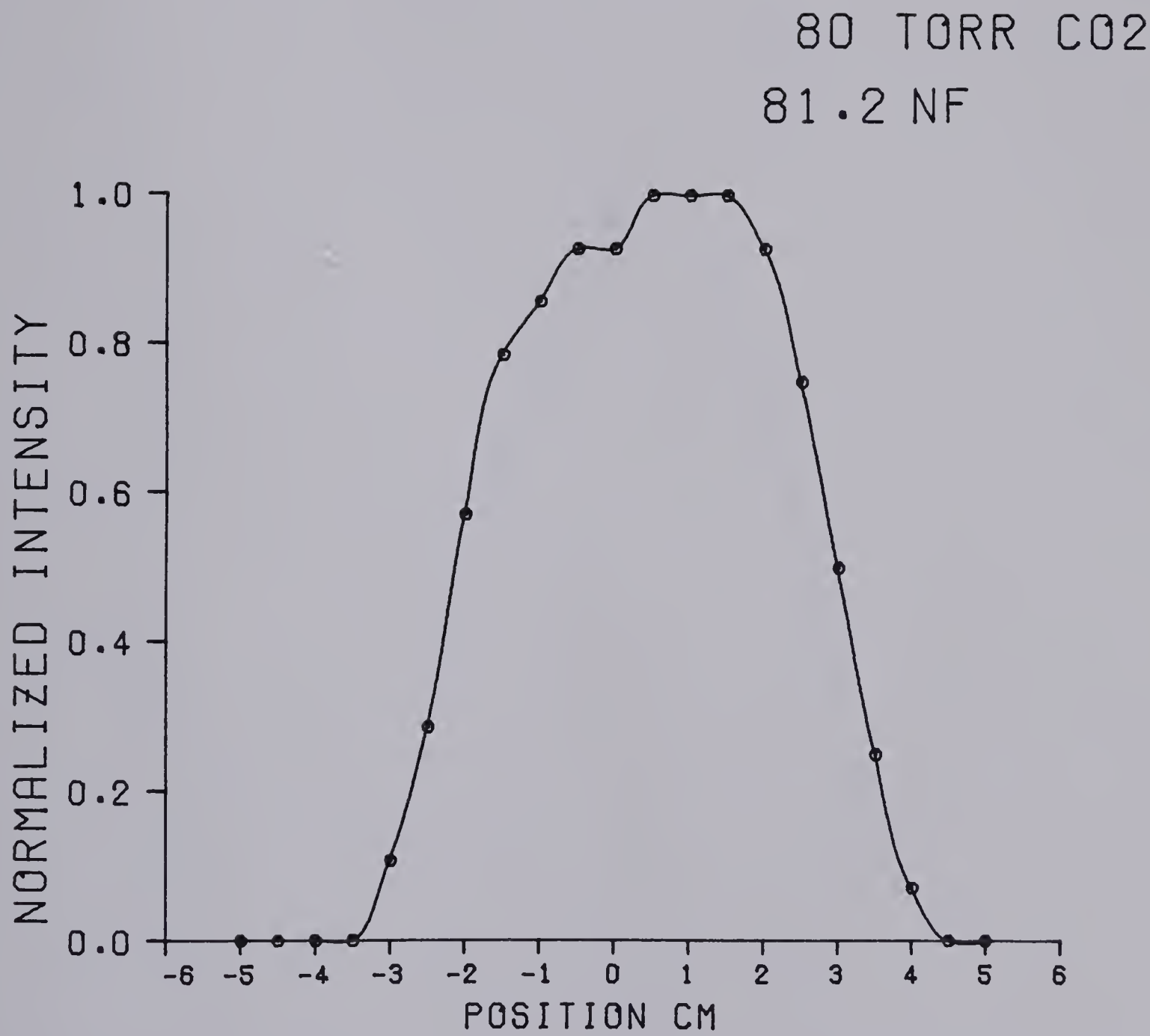


Fig. 7.7 Intensity Profile for Screen Electrode System.

Discharge in 80 torr CO₂ with an 81.2 nf capacitor.

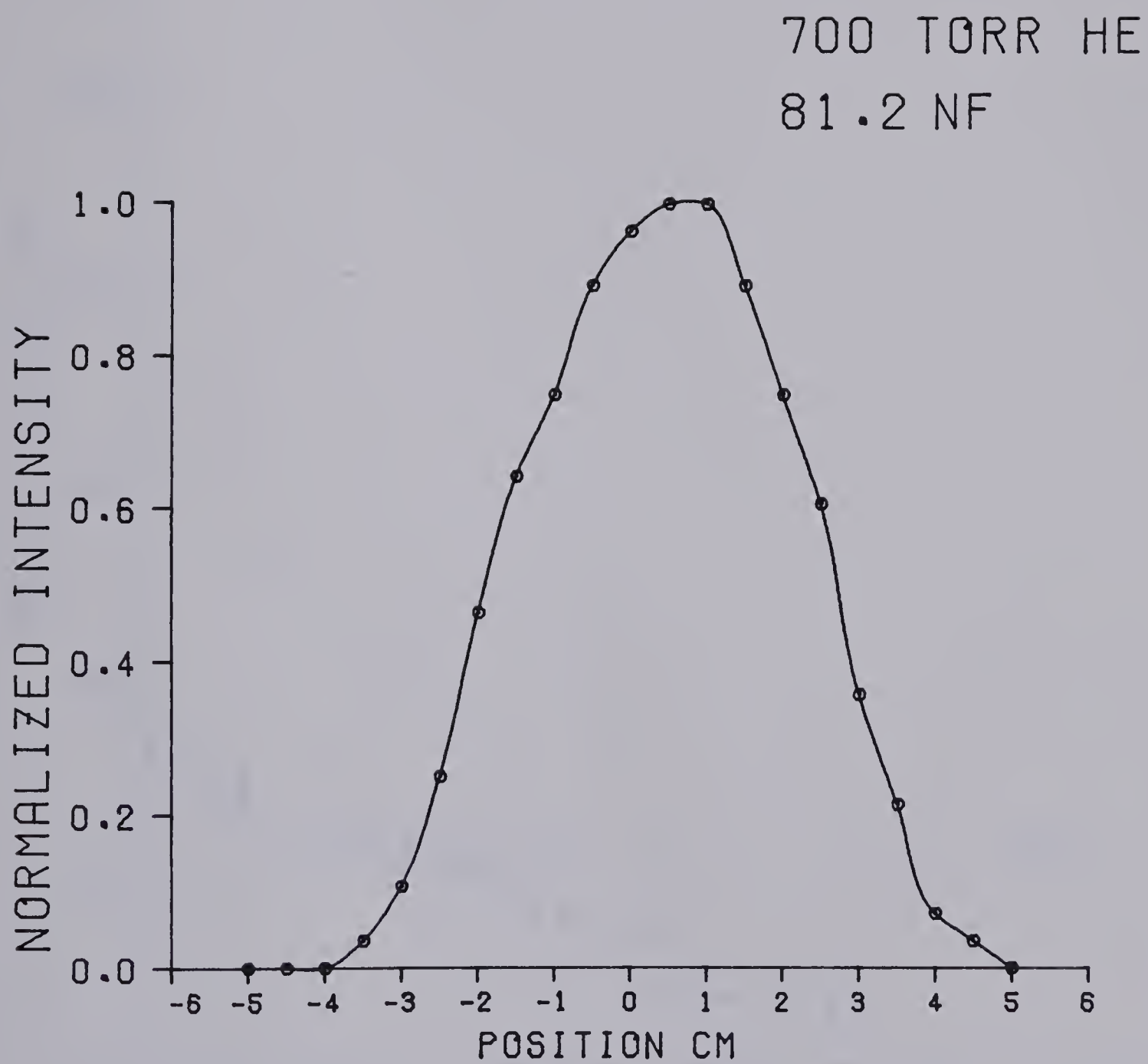


Fig. 7.8 Intensity Profile for Screen Electrode System.

Discharge in 700 torr He with an 81.2 nf capacitor.

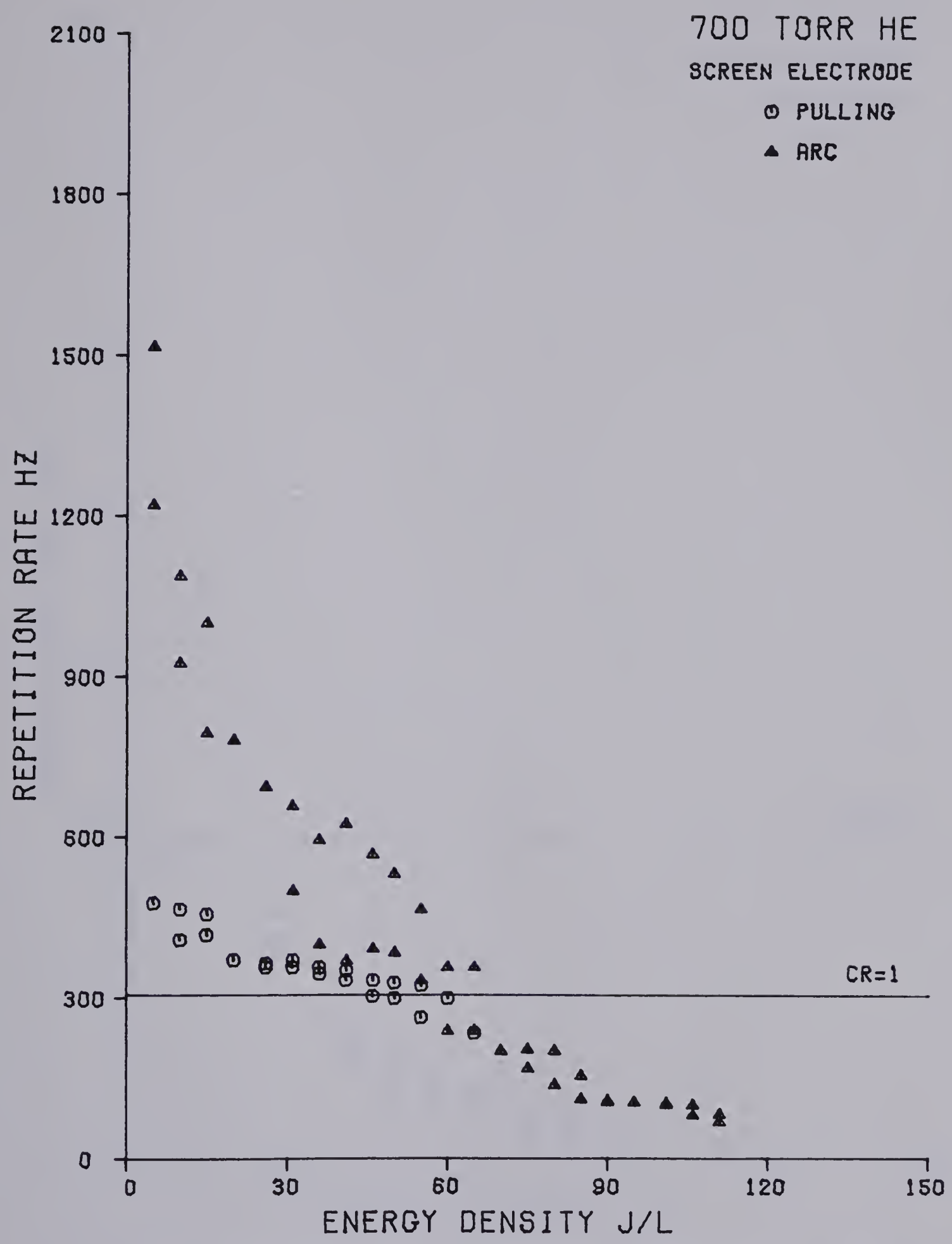


Fig. 7.9 Maximum Repetition Rate as a Function of Energy Density for the Screen Electrode System. Data for 700 torr He and a flow velocity of 26 m/sec. CR=1 is the repetition rate corresponding to a clearing ratio of 1.

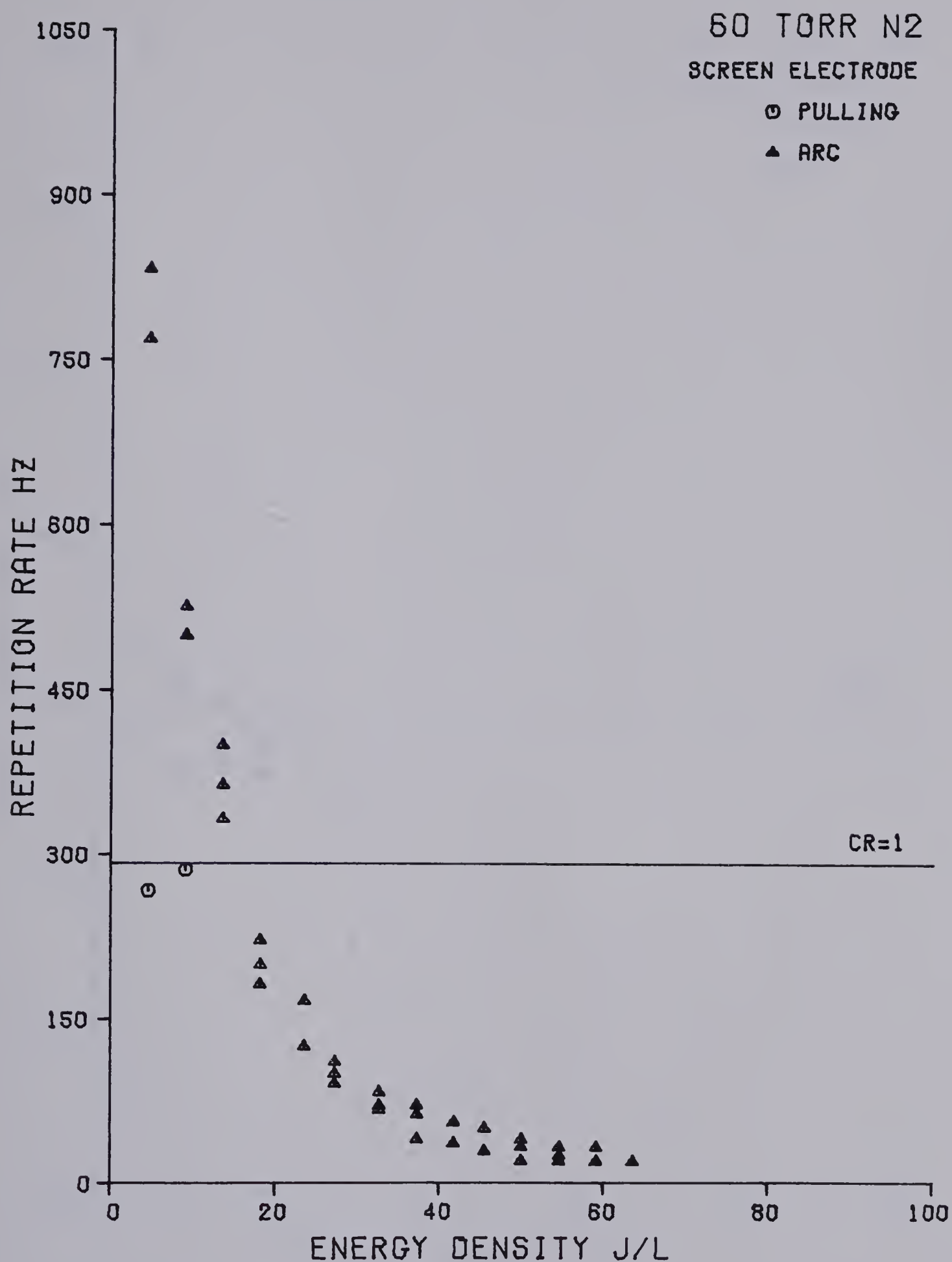


Fig. 7.10 Maximum Repetition Rate as a Function of Energy Density for the Screen Electrode System. Data for 60 torr N₂ and a flow velocity of 25 m/sec. CR=1 is the repetition rate corresponding to a clearing ratio of 1.

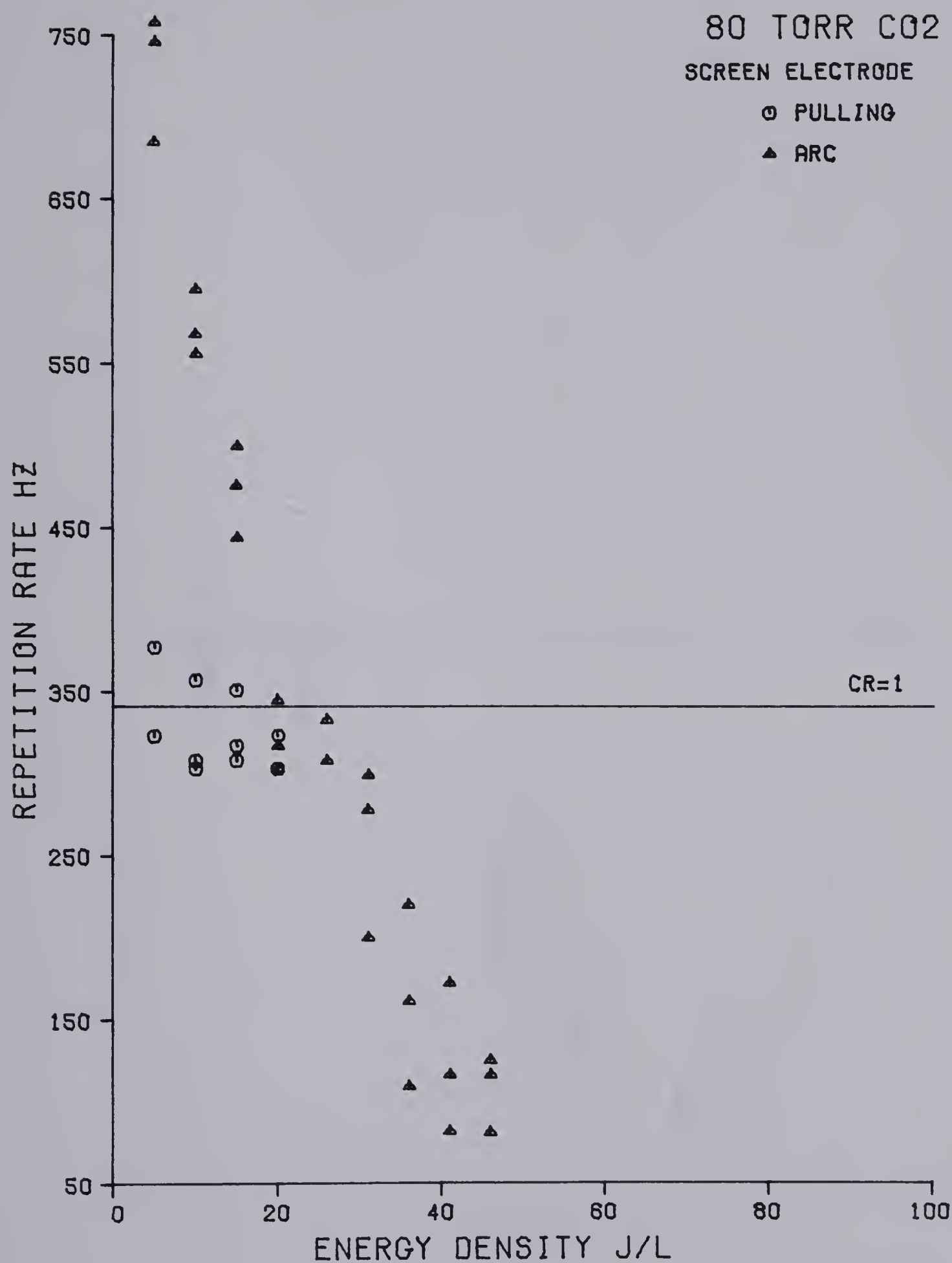


Fig. 7.11 Maximum Repetition Rate as a Function of Energy Density for the Screen Electrode System. Data for 80 torr CO₂ and a Flow velocity of 29 m/sec. CR=1 is the repetition rate corresponding to a clearing ratio of 1.

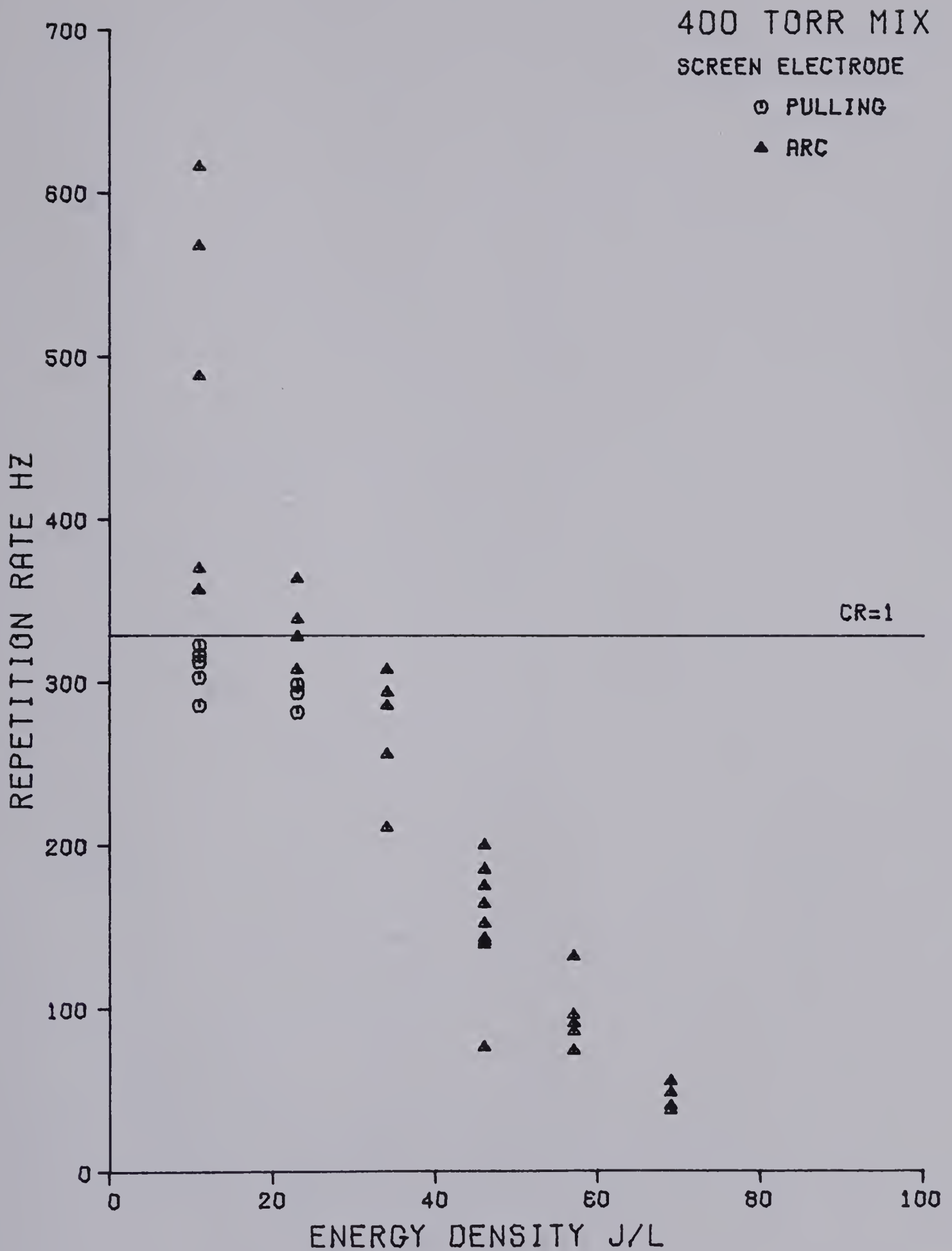


Fig. 7.12 Maximum Repetition Rate as a Function of Energy Density for the Screen Electrode System. Data for a 400 torr 1:1:8 laser mix and a flow velocity of 28 m/sec. CR=1 is the repetition rate corresponding to a clearing ratio of 1.

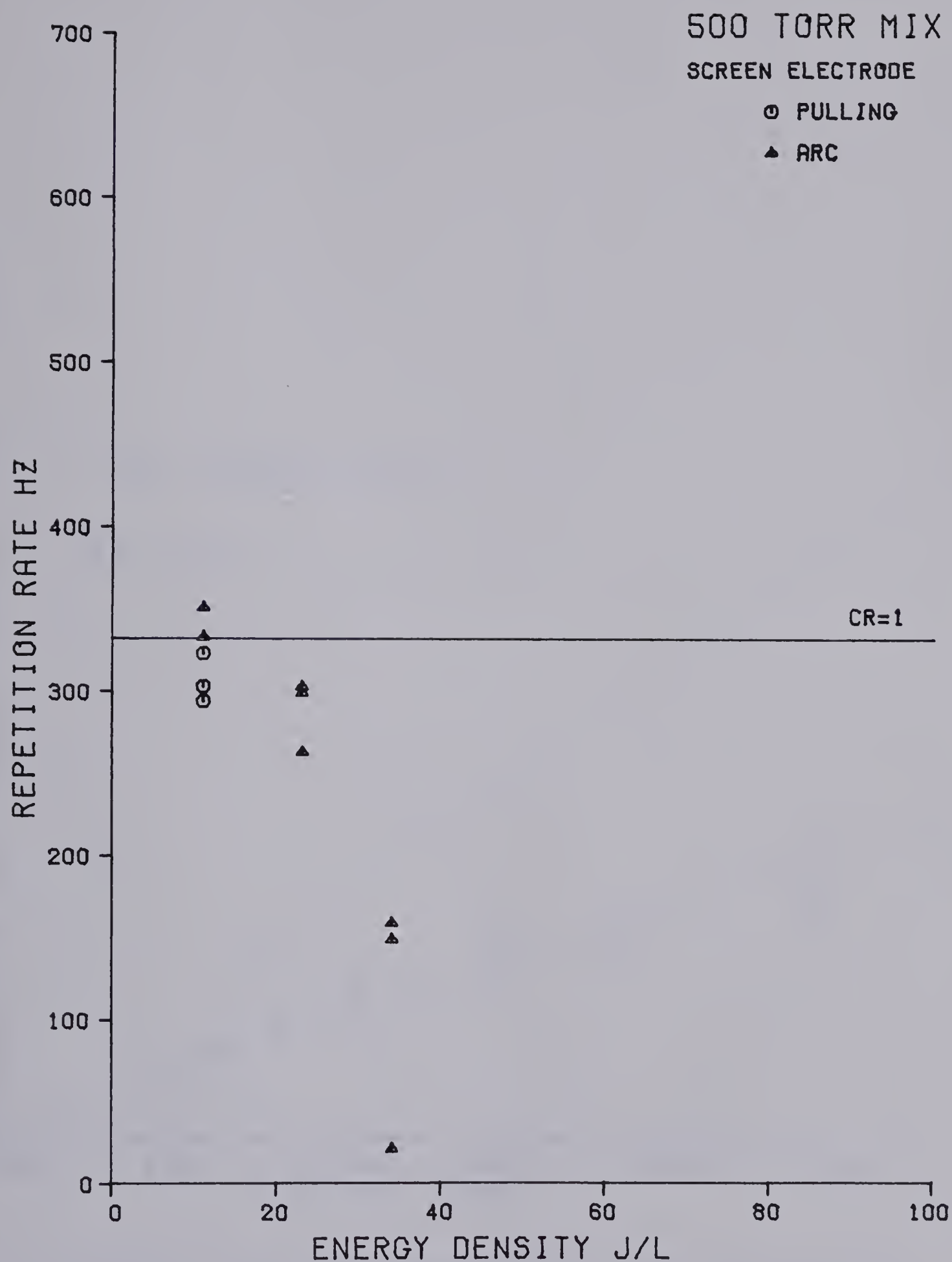


Fig. 7.13 Maximum Repetition Rate as a Function of Energy Density for the Screen Electrode System. Data for a 500 torr 1:1:8 laser mix and a flow velocity of 28 m/sec.

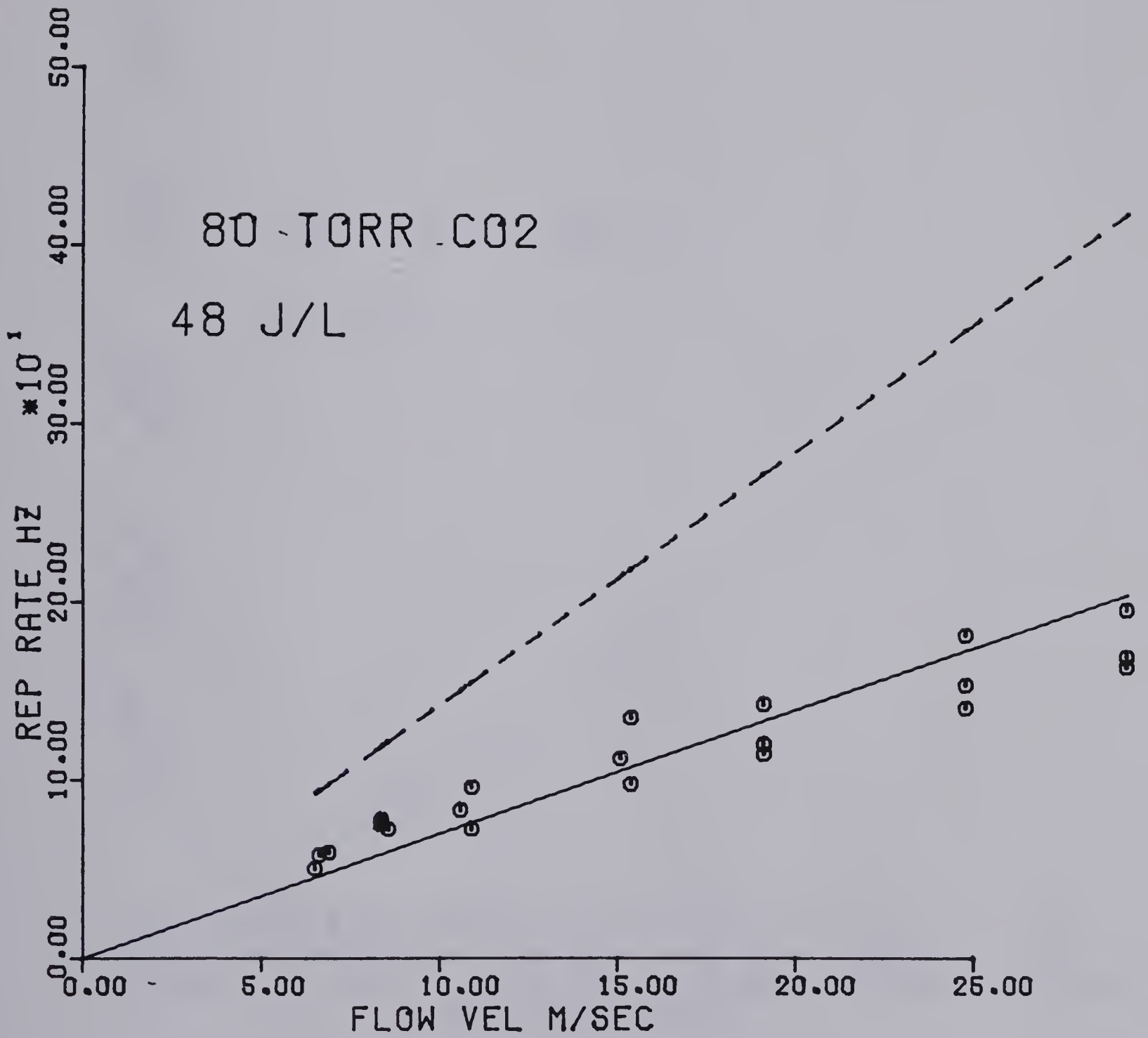


Fig. 7.14 Repetition Rate Versus Gas Flow Velocity for Screen Electrode System. Data for 80 torr CO₂ and 48 J/l energy density.

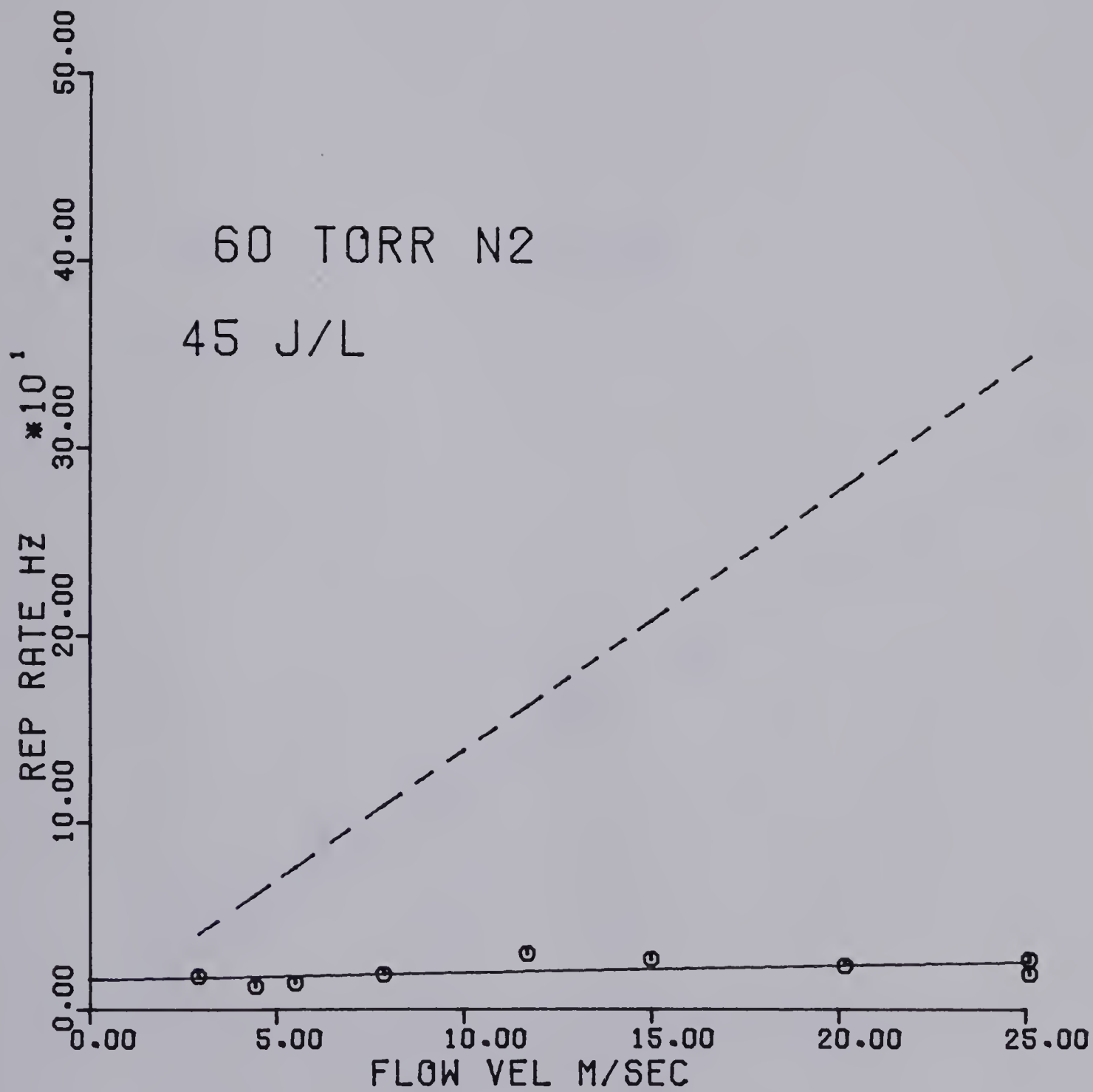


Fig. 7.15 Repetition Rate Versus Gas Flow Velocity for Screen Electrode System. Data for 60 torr N₂ and 45 J/l energy density.

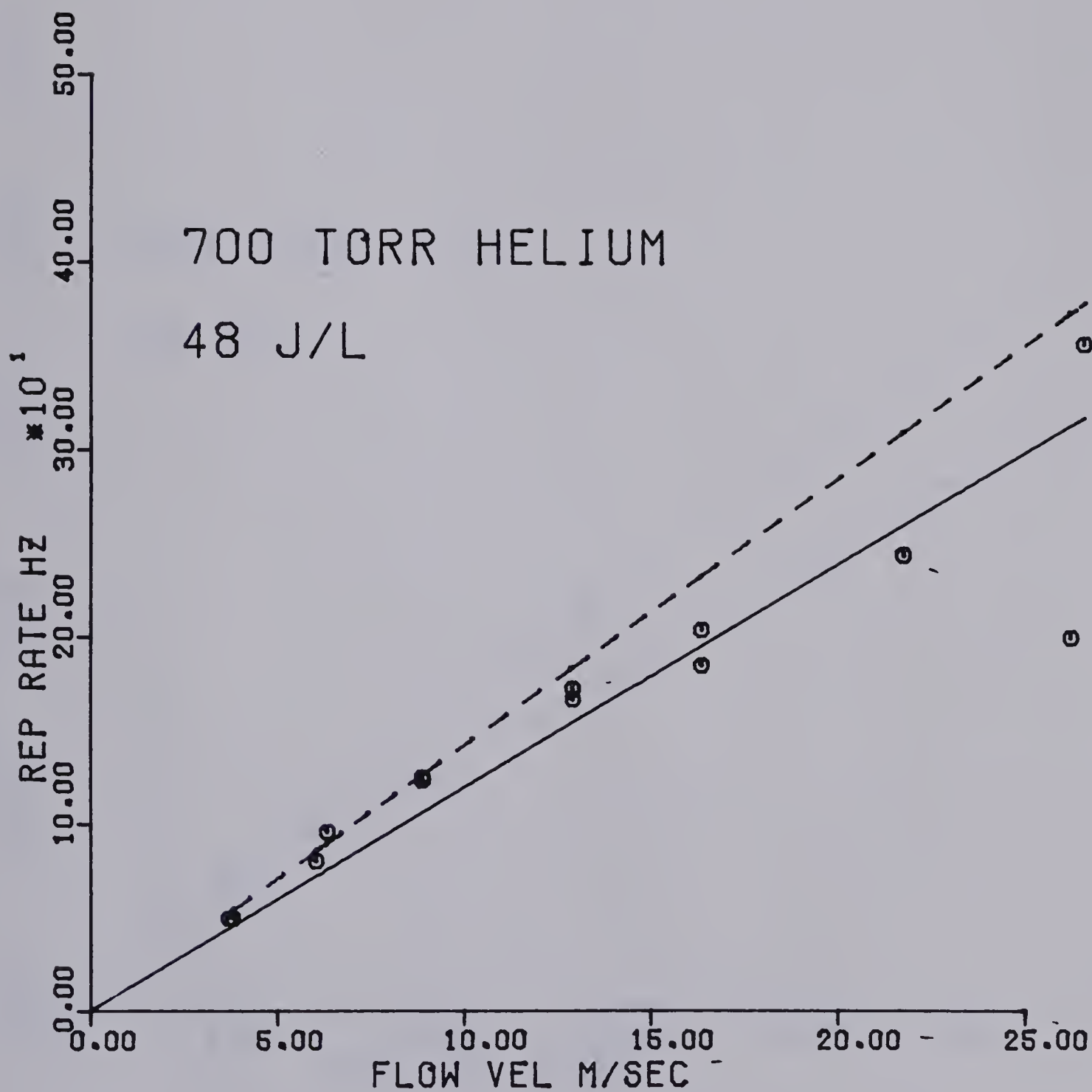


Fig. 7.16 Repetition Rate Versus Gas Flow Velocity for Screen Electrode System. Data for 700 torr He and 48 J/l energy density.

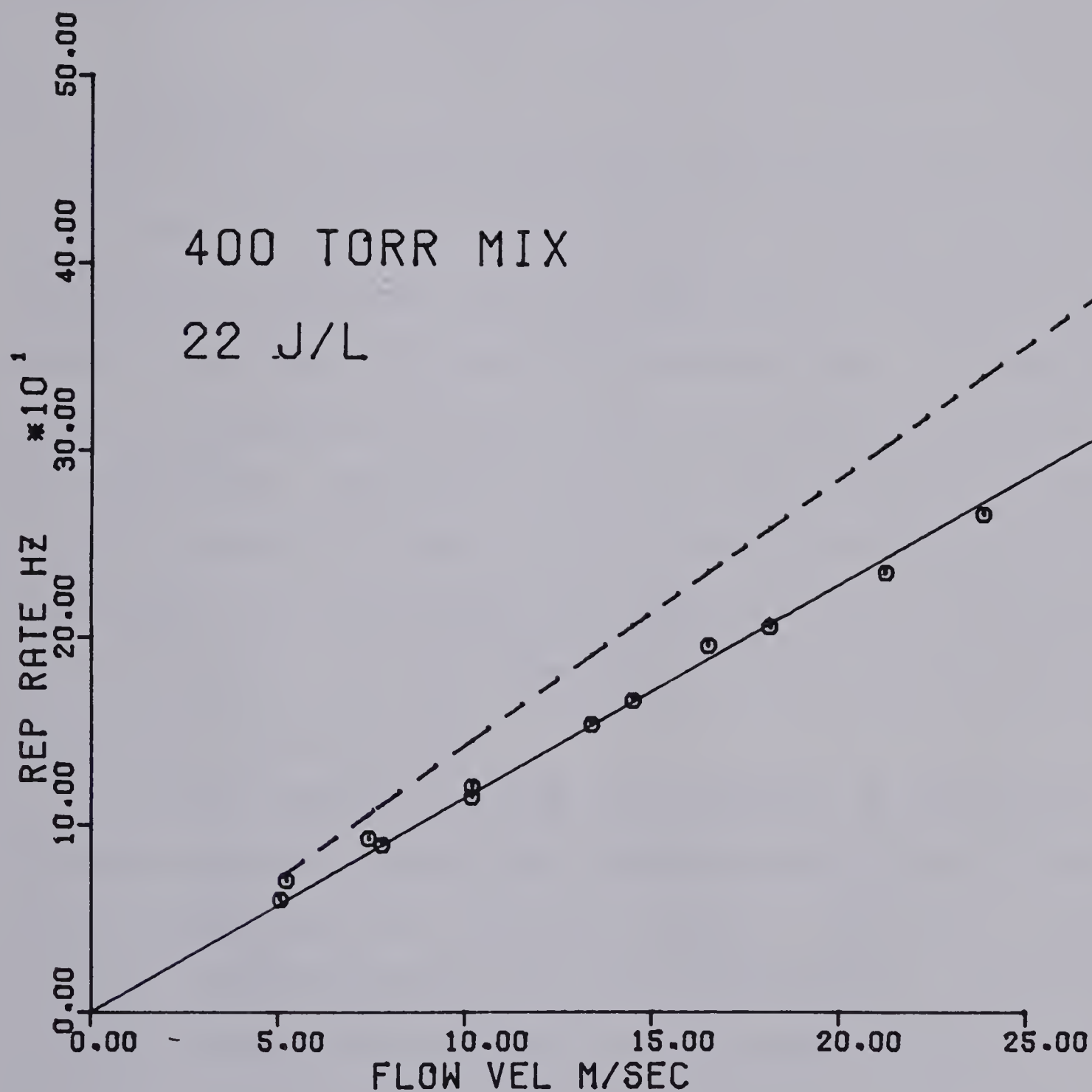


Fig. 7.17 Repetition Rate Versus Gas Flow Velocity for Screen Electrode System. Data for 400 torr of 1:1:8 CO₂:N₂:He laser mix and 22 J/l energy density.

electrodes.

For the dielectric discharge preionized system gas poisoning was also observed to occur in the laser mixture. Typically poisoning took about four minutes in the 400 torr laser mixture using a 40 nf storage capacitor. This system seems to provide no improvement over the spark pin preionized system with regards to poisoning time.

7.4 CONCLUSIONS

The dielectric discharge preionized system did not operate as well as the spark pin preionized discharge system. The maximum repetition rate dropped off much more rapidly as energy density increased, and the maximum energy density that could be obtained was lower. No significant change was observed in the time that the system took to poison due to CO_2 dissociation. The spark pin preionized system, therefore, appears to be the superior of the two. This is somewhat surprising because Pace and Lacombe (22) claim that their work showed the dielectric discharge preionized system to be better than spark preionized systems, particularly with respect to gas poisoning.

A possible explanation for the poor performance of the dielectric discharge preionized system is that discharge products can get trapped in the stagnant gas behind the screen electrode. This could be tested by arranging for gas flow behind the screen and rerunning the experiment to see if it results in an improvement in maximum repetition rate.

CHAPTER 8

FLOWING GAS DISCHARGE SYSTEM STREAK CAMERA OBSERVATIONS

INTRODUCTION

This chapter describes some observations that were made using a streak camera to study discharges in 60 torr N_2 . The experiment had two main goals. The first was to measure the gas expansion that had been predicted. Since N_2 had a luminous afterglow it was hoped that the expansion of the afterglow would be visible. The other goal was to produce some streak photographs which showed typical examples of the discharge instabilities that occurred in this system.

8.1 APPARATUS

These observations were made using a TRW model 1D image converter camera with a model 5B wide range plug-in. Writing rates for the plug-in are 100, 50, 25, 10 and 5 mm/ μ sec. A model 46A trigger delay generator was used to trigger the camera. These units were borrowed from the Plasma Laboratory.

A block diagram of the circuit arrangement is shown in Figure 8.1. A master trigger generator synchronized the experiment by triggering the discharge and the scope. The scope triggered the trigger delay generator which in turn triggered the camera. Both the scope and the trigger delay generator could be used for adjusting the delay before the camera was triggered but only the trigger delay generator was used for this function. Electrical noise was a problem with this experiment and initially caused the camera to trigger spuriously, and to terminate streaks prematurely. Both radiated noise and noise conducted along the cables contributed to the problem. By keeping the cables short and

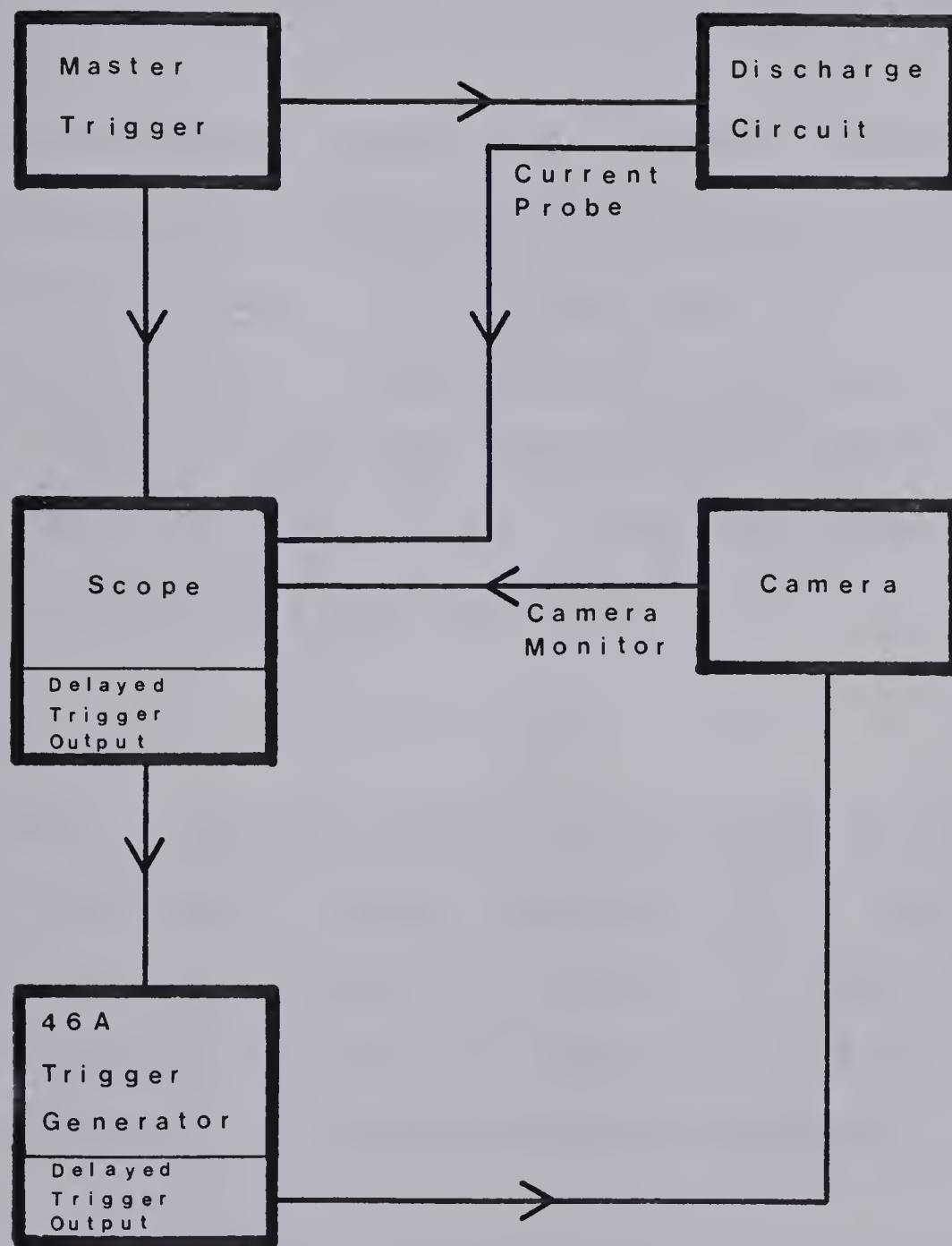


Fig. 8.1 Block Diagram of Streak Camera Experiment Showing Triggering Chain of Command and Signal Paths. The current probe and camera monitor paths are signal paths. All others are trigger paths.

shielding them with copper pipe the effect of radiated noise was reduced to the point where reasonably reliable results could be obtained. More work was needed however. Better reliability could be achieved by shielding the camera with a copper mesh cage or a metal box, and some of the cables should have been isolated using opto-isolators. However since the camera was available on a short term loan there was not time to take these additional steps.

Measurements were made in 60 torr N_2 . Charging voltage for the discharge was typically 10 KV and the storage capacitors were 40 nf and 80 nf. Because the spark pin preionized discharge system proved superior to the dielectric discharge preionized system it was used for these experiments. Figure 8.2 shows the orientation of the streak camera slit with respect to the discharge. This slit orientation allows monitoring the discharge diameter as a function of time.

8.2 RESULTS

The attempt to record gas expansion by monitoring the afterglow diameter was unsuccessful. The main reason was that the camera had insufficient sensitivity to record the afterglow for longer than about 20 μ sec after the discharge. Also the image was reduced from the original discharge by a factor of four which decreased the sensitivity of the measurement.

An estimate of expected expansion was calculated for an energy density of 60 J/l, the energy density produced by an 80 nf capacitor charged to 10 KV. The afterglow diameter should expand from 60 mm to 96 mm, or a total expansion of 36 mm. Using shock theory the particle flow velocity was estimated to be .34 mm/ μ sec, so the diameter would expand

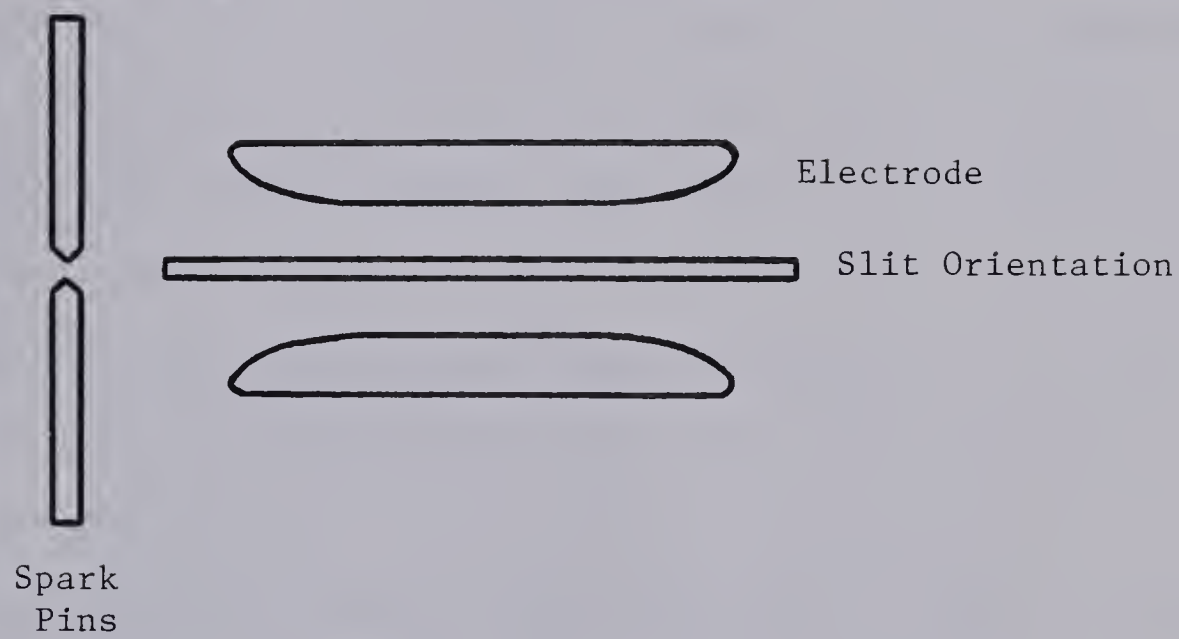


Fig. 8.2 Orientation of Streak Camera Slit with Respect to the Discharge Electrodes.

at twice that rate or $.68 \text{ mm}/\mu\text{sec}$. About $53 \mu\text{sec}$ would be required for the entire expansion. The longest streak available was $5 \mu\text{sec}$ streak, since the expansion is reduced by a factor of four on the image, the image diameter would change by only $.86 \text{ mm}$ which is too small to judge accurately due to the fuzzy edges of the image. By using delay the afterglow could be examined for up to $20 \mu\text{sec}$ after the discharge. Over $20 \mu\text{sec}$ the estimated change in image diameter is roughly 3 mm which should be visible. However the results are ambiguous because a variation in light intensity due to a change in exposure can result in a diameter variation of this much. For example, the image diameter at $20 \mu\text{sec}$ is 14 mm and required multiple exposures to be visible. Multiple exposures may result in a widening of the streak due to image jitter from shot to shot. However the initial discharge image diameter was between 11 and 15 mm depending on which exposure is used. If it was 11 mm then roughly the correct amount of expansion seems to have occurred in $20 \mu\text{sec}$, but if it was 15 mm then no expansion occurred. As a result no definite conclusion about gas expansion can be drawn from these pictures.

The streak camera measurements produced pictures of typical discharge instabilities. Figure 8.3 shows the discharge current waveform for a uniform discharge, with the streak camera monitor pulse, and the synchronization between the two. A streak of the uniform discharge is shown in Figure 8.4a. The afterglow appears, faintly, following the discharge. An energy induced glow to arc transition is shown in Figure 8.4b and a repetition rate induced glow to arc transition in Figure 8.4c. It can be seen that the glow to arc transitions are characterized by a collapse in the discharge diameter. Also that the two types of collapse occur at different positions, with the repetition rate induced glow to arc occurring on the downstream edge of the discharge. The

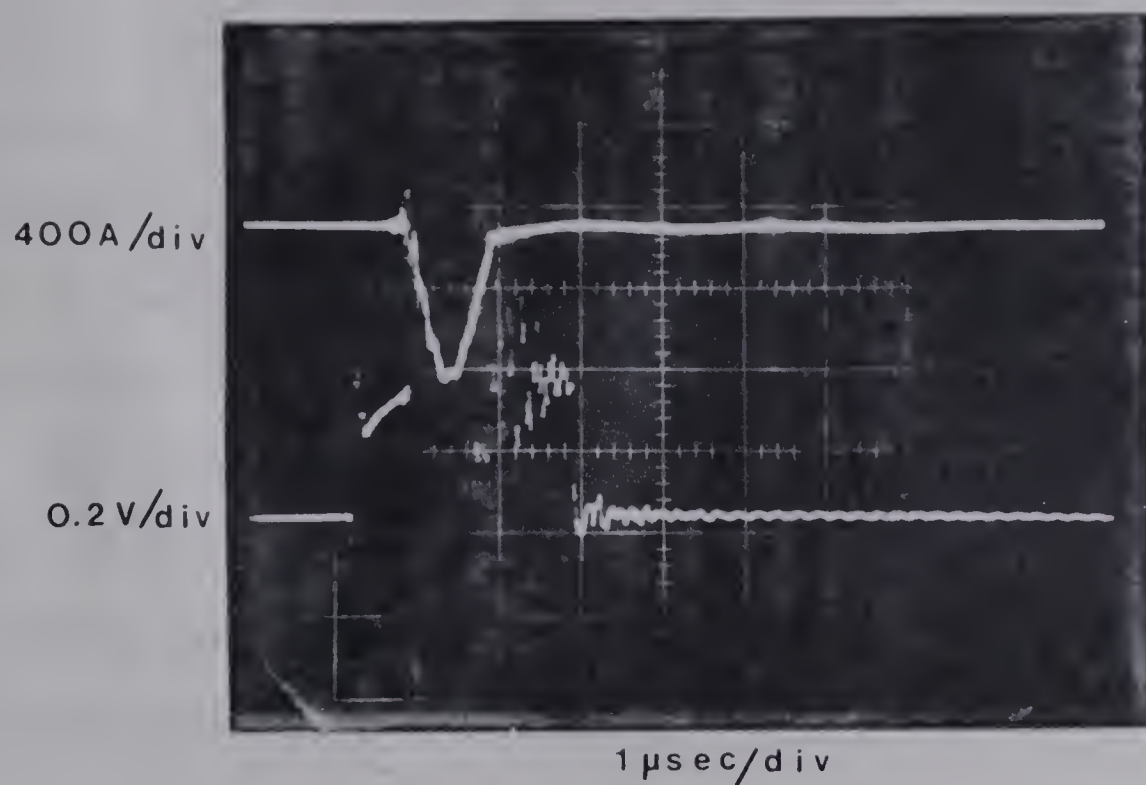


Fig. 8.3 Synchronization Between Discharge Current Pulse (Upper Trace) and Streak Camera Monitor Pulse (Lower Trace). The streak duration is 2.6 μsec.

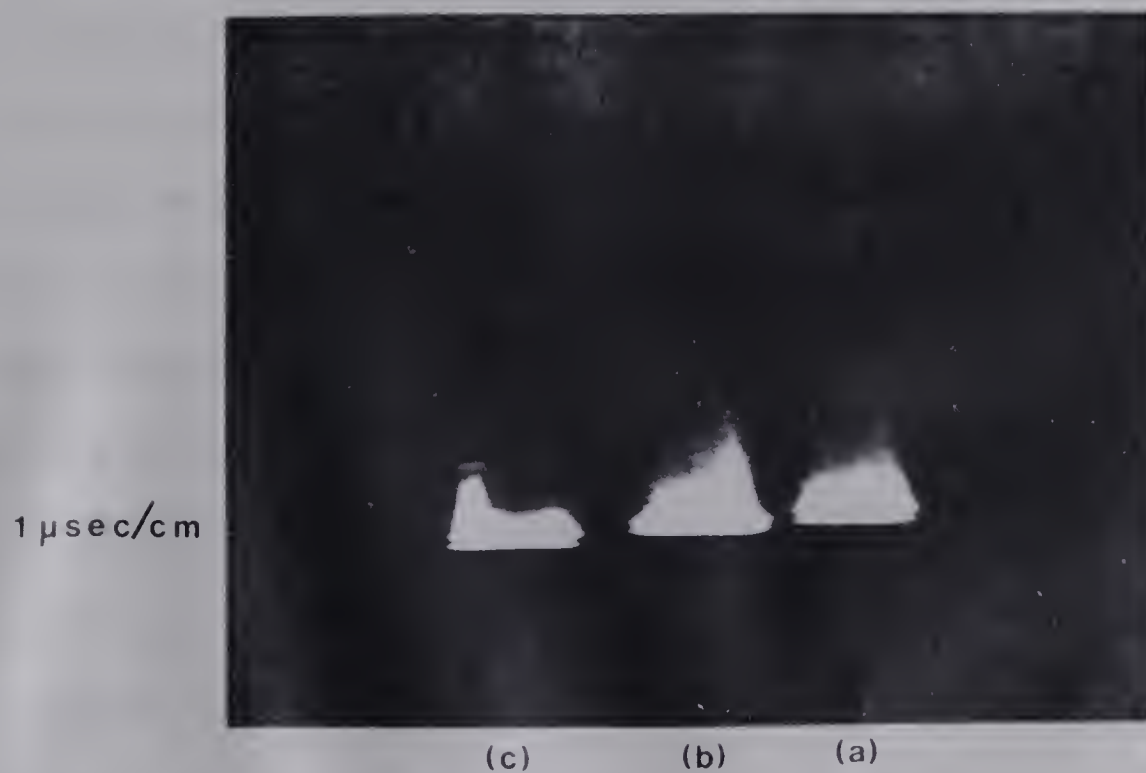


Fig. 8.4 Streak Camera Pictures of (a) A Uniform Discharge, (b) An Energy Induced Glow to Arc Transition and (c) A Repetition Rate Induced Glow to Arc Transition. The streak duration is 2.6 μsec.

results in Figure 8.4 are for a 40 nf storage capacitor charged to 10 KV. In Figure 8.5 a higher charging voltage, 18 KV, is used to produce some examples of severe energy induced glow to arc transitions. The discharge current lasts about 1 μ sec and the streak lasts approximately 5 μ sec., so the arc channel stays luminous well into the afterglow region. If the repetition rate is very high an arc may result instead of a glow to arc. Figure 8.6a shows a uniform discharge and Figure 8.6b shows a repetition rate induced arc.

Similar results were obtained for discharges in 60 torr N₂ using an 80 nf storage capacitor.

8.3 CONCLUSIONS

The streak camera measurements failed to show whether or not gas expansion occurred. With respect to discharge arcing they showed the kinds of arcing that could be encountered. The energy induced instability is a glow to arc transition. Repetition rate induced instabilities can occur either as glow to arc transitions or as arcs. The two types of repetition rate instability would be indistinguishable visually without the streak camera because the eye would superimpose the arc on following glow pulses so both effects would visually appear as a glow to arc. These pictures do show that repetition rate induced arcs and energy induced arcs can be readily distinguished from their positions in the discharge. Energy induced arcing occurs on the upstream edge or, more often, toward the center of the electrodes. Repetition rate induced arcing always occurs on the downstream edge of the electrodes. The fact that repetition rate induced arcing occurs on the downstream side of the discharge supports the conclusion that it is a convective effect and is due to gas convection



Fig. 8.5 Examples of Energy Induced Glow to Arc Transitions. The streak duration is 4.7 μ sec.

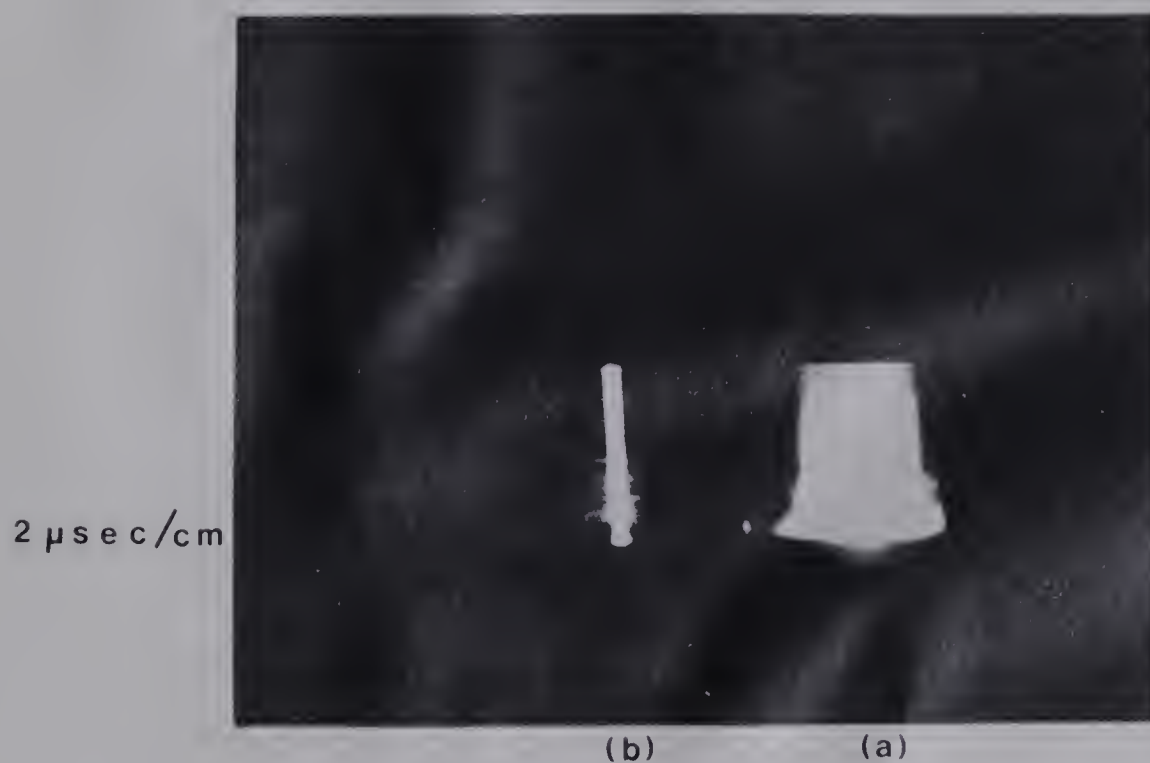


Fig. 8.6 (a) Shows a Uniform Glow and (b) Shows a Repetition Rate Induced Arc. The streak duration is 4.7 μ sec.

not having enough time to clear discharge products from the discharge region between pulses.

CHAPTER 9

CONCLUSIONS AND RECOMMENDATIONS FOR FURTHER STUDY

9.1 LASER SYSTEM RESULTS

These experiments showed that a high repetition rate closed cycle CO_2 TEA laser is feasible to construct and operate. This laser was pumped by a 10 stage Marx generator. Gas flow through the discharge region was approximately 100 m/sec, giving an expected repetition rate of about 2 KHz. A typical discharge pulse length was 1 μsec . Although pulse stretching was attempted it was not very successful, with maximum practical pulse lengths being in the 6 to 7 μsec range. Maximum repetition rates for reliable operation were in the 200 to 300 Hz range. The best optical efficiency was 6% with 16 J per pulse energy input and 1 J per pulse optical output. This was achieved by using an unstable resonator with a square skimmer. Other resonators were tested but found to be less efficient. The maximum average power output was about 200 W (1 J/pulse at 200 pulses per second). The optical system design still needed improvement as vibration caused a large pulse to pulse variation in the optical energy output.

Two major problems existed with this laser however. The first was the reduction in achieved repetition rate from the original estimate by an order of magnitude - from 2 KHz to 200 Hz. The second was the suspected poisoning of the laser system after a short time due to dissociation of CO_2 into CO and O_2 . The discharge experiments which followed were to identify the causes of discharge arcing and to confirm the presence of gas poisoning.

9.2 SHOCK WAVE MEASUREMENTS

One explanation considered for the reduction in repetition rate was

that possibly discharge generated shock waves were producing a nonuniform gas density and so causing discharge arcing. By monitoring the deflection of a probe laser beam that traversed the discharge region shock waves could be studied. They were observed both in static and flowing gas.

In static gas a large thermal gradient was observed after the discharge but it was absent in flowing gas. This is because the hot gases had to dissipate by diffusion in the static gas whereas in the flowing gas they were swept away very quickly by convection.

In both static and flowing gas shock waves were observed that originated from gas heating in the cathode fall region of the discharge. These shock waves were followed by an oscillation which seemed to originate from the Marx spark pins. The shock waves from the cathode and from the spark pins died out in approximately 0.5 msec so they would not contribute to discharge arcing for repetition rates less than 2 KHz. As a result it can be concluded that shock waves were not a source of discharge arcing in this laser system.

9.3 FLOWING GAS DISCHARGE SYSTEM MEASUREMENTS

The tests in the flowing gas discharge system showed that several factors affected the repetition rate induced arcing limit in the high repetition rate laser. The repetition rate was linearly proportional to flow velocity which indicates that repetition rate induced arcing is a convective effect. The types of instabilities which occurred, and which are shown in Fig. 6.49, also suggest that it is a convective effect because the repetition rate induced instabilities always occur on the downstream side of the discharge.

The repetition rate at which repetition rate induced arcing occurred was independent of pulse length but decreased with increasing energy density. Dzakowic and Wutzke have proposed that this decrease is due to

expansion of the discharge products so that more time is required to convect them out of the discharge region. However repetition rate decreased more rapidly with increasing energy density than predicted by their theory. The afterglow measurements supported the concept of discharge product expansion because the afterglow plug diameter increased with increasing energy density. The data fit the expansion theory well for N_2 but not as well for CO_2 (Figs. 6.34 and 6.35). However there was some ambiguity because the afterglow plug diameter seemed to be smaller than the discharge diameter as defined by the discharge intensity profile measurements. The afterglow measurements also supported the conclusion that the repetition rate is essentially limited by the time needed for convective clearing, since fractional frequencies based on the time needed to clear the afterglow products past the spark pins in N_2 agreed well with observed fractional frequencies (Fig. 6.38).

The streak camera measurements were intended to observe the afterglow expansion predicted by Dzakowic and Wutzke but were inconclusive on this point. They did however give useable pictures of the various arcing modes.

The experiments in the flowing gas discharge system showed that geometry is an important factor in limiting the maximum repetition rate. Upstream spark pins were shown to be detrimental to system performance. In the case of a downstream spark pin the repetition rate at high energy densities is limited by having to clear the discharge products not only from the electrodes but past the spark pins as well. Otherwise arcing would occur from the electrodes to the spark pins. Removing the downstream spark pins and preionizing from behind a screen electrode does not necessarily solve the problem either. The solid electrodes

with the downstream preionizing spark pins performed better than the system with preionization from a dielectric discharge behind a screen electrode. This was probably because discharge products got trapped in the stagnant gas behind the screen.

Geometry was the most important factor in reducing repetition rate as energy density increased in the flowing gas discharge system. Consider first the case of the spark pin preionized system. As the discharge energy density increased so did the density of discharge products left over after the pulse. At low energy densities it was sufficient to clear them out from between the electrodes in order to produce a stable discharge. But as the density of discharge products increased a point was reached where they could form a conductive bridge from the electrodes to the spark pins. When this point was reached it became necessary to clear the discharge products past the spark pins in order to prevent arcing to the spark pins from occurring. This results in a greater decrease in repetition rate than expansion of the discharge products does. In the case of the screen electrode with the dielectric discharge for preionization discharge products trapped in the stagnant gas behind the screen appeared to be the main factor limiting repetition rate, so once again the system geometry was important.

Gas poisoning was also observed in the flowing gas discharge system and is believed to be due to the dissociation of CO_2 into CO and O_2 in the discharge. As a result of poisoning the sealed off lifetime of the system at 100 Hz repetition rate is roughly 4 minutes.

9.4 CONSIDERATIONS FOR HIGH REPETITION RATE CO_2 TEA LASER DESIGN

Several important considerations have arisen from this study which would be useful in future high repetition rate CO_2 TEA laser designs.

A Marx generator switched system in which the Marx switches provide preionization appears to be feasible. However the Marx pins must be downstream from the discharge in order to avoid adversely affecting the discharge. In addition the repetition rate will be limited by the time needed to clear discharge products from between the electrodes and past the spark pins rather than just from between the electrodes. Using a peaking capacitor in connection with the Marx generator improves the discharge stability.

Gas poisoning was shown to be a problem in a sealed system and dissociation of CO_2 into CO and O_2 is the suspected cause. Therefore future high repetition rate systems would either have to be run with a make-up gas flow or with some catalyst system to recombine the CO and O_2 . Work is being done by other researchers on such catalyst systems (ref. 23).

The conversion efficiency of electrical energy to optical output was low for a CO_2 laser, being about 6%. However the gain was low and the gain path length of 60 cm was fairly short for a low gain system. In future lasers of this type the optical efficiency could probably be improved by using a longer discharge.

9.5 SUGGESTIONS FOR FURTHER WORK

Several possibilities for future work arise out of this project. One experiment would be to arrange for gas flow behind the screen in the dielectric discharge preionized system then compare its performance with the solid electrode system. It is possible that with this change the dielectric discharge preionized system may prove to be superior. Work can also be done on a means of controlling gas poisoning using a catalyst. Extension of high repetition rate TEA laser techniques to

other gases is another possible project. Olson et al. (21) have done this for He-Xe and several other rare gas mixtures.

The photomultiplier monitoring could be expanded as well. The intensity profile monitoring could be expanded into a tool for measuring discharge uniformity. Also, the photomultiplier could be shuttered to protect it from the initial discharge flash when doing afterglow monitoring in N_2 and CO_2 . This might permit observing the afterglow between the electrodes and resolve why the afterglow plug diameter appears to be smaller than the discharge diameter.

The streak camera results could also use more work. The camera triggering reliability at high repetition rates should be improved. Also the camera could be used to take high speed framing photographs which would better illustrate the spatial development of the discharge and arcs than the streak photographs.

REFERENCES

1. C.K.N. Patel, "Interpretation of CO_2 optical maser experiments", Phys. Rev. Lett. Vol. 12, pp. 588-590. May 25, 1964.
2. C.K.N. Patel, "Continuous-wave laser action on vibrational-rotational transitions of CO_2 ", Phys. Rev. Vol. 336A, pp. 1187-1193, Nov. 30, 1964.
3. F. Legay and N. Legay-Sommaire, "Sur les possibilités de réalisation d'un maser optique utilisant l'énergie de vibration des gaz excités par l'azote actif", C.R. Acad. Sci. Vol. 259, pp. 99-102, July 6, 1964.
4. C.K.N. Patel, "Selective excitation through vibrational energy transfer and optical maser action in $\text{N}_2\text{-CO}_2$ ", Phys. Rev. Lett. Vol. 13, pp. 617-619, Nov. 23, 1964.
5. G. Moeller and J.D. Rigden, "High-power laser action in $\text{CO}_2\text{-He}$ mixtures", Appl. Phys. Lett. Vol. 7, pp. 274-279, Nov. 1965.
6. C.K.N. Patel, P.K. Tien, and J.H. McFee, "CW high-power $\text{CO}_2\text{-N}_2\text{-He}$ laser", Appl. Phys. Lett. Vol. 7, pp. 290-292, Dec. 1965.
7. A.E. Hill, "Roll of thermal effects and fast flow power scaling techniques in $\text{CO}_2\text{-He-N}_2$ lasers", Appl. Phys. Lett. Vol. 16, pp. 423-426, June 1970.
8. T.F. Deutsch, F.A. Horrigan, and R.I. Rudko, "CW operation of high-pressure flow CO_2 lasers", Appl. Phys. Lett. Vol. 15, pp. 88-91, Aug. 1969.
9. W.B. Tiffany, R. Targ, and J.D. Foster, "Kilowatt CO_2 gas transport laser", Appl. Phys. Lett. Vol. 15, pp. 91-93, Aug. 1969.

10. R. Dumanchin and J. Rocca-Serra, "Augmentation de l'energie et de la puissance fournie par unite de volume dans un laser a CO_2 en regime pulse", C.R. Acad. Sci. Vol. 269, pp. 916-917, Nov. 1970.
11. A.J. Beaulieu, "Transversely excited atmospheric pressure CO_2 lasers", Appl. Phys. Lett. Vol. 16, pp. 504-506, June 1970.
12. A.K. LaFlamme, "Double discharge excitation for atmospheric pressure CO_2 lasers", Rev. Sci. Instrum. Vol. 41, pp. 1578-1581, Nov. 1970.
13. H. Seguin and J. Tulip, "Photoinitiated and photosustained lasers", Appl. Phys. Lett. Vol. 21, pp. 414-415, Nov. 1972.
14. D. Yu. Zaroslov et al., "Plasma jet CO_2 lasers", JETP-Lett. Vol. 15, pp. 470-472, June 1972.
15. C.A. Fenstermacher, M.J. Nutter, W.T. Leland, and K. Boyer, "Electron-beam controlled electrical discharges as a method of pumping large volumes of CO_2 laser media at high pressure ", Appl. Phys. Lett. Vol. 20, pp. 56-60, Jan. 1972.
16. T. Ganley, J.T. Verdeyan, and G.H. Miley, "Enhancement of CO_2 laser power and efficiency by neutron irradiation", Appl. Phys. Lett., Vol. 18, pp. 568-569, June 1971.
17. R.L. Schrieffer, "Uniform direct-current discharges in atmospheric pressure $\text{He}/\text{N}_2/\text{CO}_2$ mixtures using gas additives", Appl. Phys. Lett., Vol. 20, pp. 354-356, May 1972.
18. G.S. Dzakowic and S.A. Wutzke, "High-pulse-rate glow-discharge stabilization by gas flow", J. Appl. Phys. Vol. 44, No. 11, pp. 5061-5063, Nov. 1973.
19. R.T. Brown, "High repetition-rate effects in TEA lasers", IEEE Journal of Quantum Electronics, pp. 1120-1122, Nov. 1973.

20. J. Tulip, H.J. Seguin and W. Faszer, "High-repetition-rate TEA-laser discharge using integrated preionization and switching", IEEE Journal of Quantum Electronics, Vol. QE-12, No. 2, pp. 155-159, Feb. 1976.
21. R.A. Olson, D. Grosjean, and B. Sarka, Jr., "High-repetition-rate closed-cycle rare gas electrical discharge laser", Rev. Sci. Instrum., Vol. 47, No. 6, pp. 677-683, June 1976.
22. P.W. Pace and M. Lacombe, "A sealed high-repetition-rate TEA CO₂ laser", IEEE Journal of Quantum Electronics, Vol. QE-14, No. 4, pp. 263-274, April 1978.
23. R.B. Gibson and A. Javan, "Sealed multiatmosphere CO₂ TEA laser: Seed-gas compatible system using unheated oxide catalyst", Appl. Phys. Lett. 32 (11), pp. 726-727, June 1, 1978.
24. A. Pope, "Wind-Tunnel Testing", John Wiley & Sons Inc., New York, 1954, Chapter 2.
25. R.C. Pankhurst and D.W. Holder, "Wind-Tunnel Technique", Sir Isaac Pitman and Sons Ltd., London, 1965, Chapter 2.
26. "Trane Air Conditioning Manual", The Trane Co., La Crosse, Wisconsin, Chapter 9.
27. "Handbook of Fundamentals", American Society of Heating, Refrigerating and Air-Conditioning Engineers, 1972, Chapter 25.
28. O.G. Feil, "Vane systems for very-wide-angle subsonic diffusers", Transactions of the ASME Journal of Basic Engineering, pp. 759-764, Dec. 1964.
29. G.N. Glasoe and J.V. Lebacqz, "Pulse Generators", 1948, McGraw-Hill, Section 11-8.

30. R.W. Morrison and A.M. Smith, "Overvoltage and Breakdown Patterns of Fast High-Voltage Marx Pulse Generators for Streamer Chambers", Dept. of Physics, Carleton University, Ottawa, Canada.
31. E.C. Levy, A New Table of Laplace Transform Pairs, The Book Page 6600 Sunset Blvd. Los Angeles 28, Calif. 90028, Nov. 1963.
32. A.E. Siegman, "Stabilizing Output with Unstable Resonators", Laser Focus, May 1971, pp. 42-47.
33. A.A. Offenberger, P.R. Smy, N.H. Burnett, "High Power CO₂ Laser Energy Detector", Rev. Sci. Instrum. Vol. 46, No. 3, pp. 317-321, March 1975.
34. J.K. Wright, Shock Tubes, Chapter 4, Methuen & Co., Ltd., 1961.
35. L.E. Kline and L.J. Denes, "Investigation of Glow Discharge Formation with Volume Preionization", Journal of Applied Physics, Vol. 46, No. 4, pp. 1567-1574, April 1975.
36. W.M. Clarke, Jr., "Optical Homogeneity of a Ultraviolet-Preionized CO₂ Laser Discharge", Applied Optics, Vol. 13, No. 9, pp. 1995-1997, Sept. 1974.
37. A. Parrish, Editor, Mechanical Engineer's Reference Book, 11th Edition, 1973 Butterworth & Co. Ltd. pp. 7-51.
38. J. Tulip, "Long Lived Ionization in a N₂ Afterglow," Phys. Lett. A., Vol. 58, No. 3, pp. 173-174, 1976.
39. A.J. Palmer, "Physical Model on Initiation of Atmospheric-Pressure Glow Discharges," Appl. Phys. Lett., Vol. 25, No. 3, pp. 138-140, 1 Aug. 1974.
40. L.J. Denes and J.J. Lowke, "V-I Characteristics of Pulsed CO₂-Laser Discharges," Appl. Phys. Lett., Vol. 23, No. 3, pp. 130-132, 1 Aug. 1973.
41. E. Nasser, Fundamentals of Gaseous Ionization and Plasma Electronics, J. Wiley & Sons, 1971.

Appendix

Listing of Computer Routines used in these experiments.

The APL functions were used for the circuit model of section 3.3.

A sample output is included with the listings. The function CUQULI was written by Hugh Woods and the function PLOT is from the University's APL Computing Library.


```

)FNS
CUQUULI DISCH DRIVER PLOT IBE
  ▽ DRIVER[C] ▽
  ▽ NB DRIVER V;N
[1] N+NB[2],NB[3]
[2] OUT+N DISCH V
[3] +(NB[1]=0)/AB
[4] D+OUT
[5] AB: 50 120 PLOT OUT
  ▽

  ▽ DISCH[C] ▽
  ▽ RR+N DISCH V;A;AL;AN2;AN3;A0;A1;A2;B;RE;C;C1;C2;DE;GA;I;L;ON;P;PSI;Q;R;RT;TB;TW;VB;UR;V0;W;TI;VC2;T;Z;FLAG
  ▽ WRITTEN OCTOBER 7, 1975 LAST UPDATE OCT. 16, 1975
  VR+11-I+1
  FLAG+1
[4] W+(÷(L+V[3]))x C1xC2÷(C1+V[1])+C2+V[2])*0.5
[5] (V'UB = '),V[5]
[6] (V'TB = '),V[5]÷W)x(-2)01-(VB+V[5])÷(V0+V[6])x C1÷C1+C2
[7] TI+(0 1 2 3 4)x(TB÷4)
[8] VC2+(V0xC1÷(C1+C2))x(1-20(WxTI))
[9] (V'VC1TB = '),V[5]÷(V0÷C1+C2)x C1+C2x20WxTB
[10] (V'ILTB = '),V[5]÷(V0÷WxL)x10WxTB
[11] A0+(÷(C2xVB)+C1xP)÷LxC1xC2xR+V[4]
[12] A1+Q÷C2xR
[13] A2+VB÷R
[14] D+RT+(-CUQUULI D+(-RXLxC1xC2),(W*2),(-RxC2)),1
[15] DE+((AL+RT[1;2])-GA+RT[1;1])*2+(BE+RT[2;3])*2
[16] AN2+((A0+A2xGA*2)-A1xGA)÷DE
[17] ON+(A0+A2x(AL*2)-BE*2)-A1xAL
[18] TW+BEXA1-2xA2xAL
[19] PSI+((-3)0ON÷TW)+(-3)0BE÷GA-AL
[20] AN3+(÷BE)x((ON*2)+TW*2)÷DE)*0.5)
[21] Z+((÷AL)Γ(÷GA)Γ(2x(01)÷BE)
[22] T+Zx(1+11+N[1]xN[2])÷NC2]
[23] SF:A+AN2x*-GAXT[I]
[24] B+AN3x(*-ALxT[I])x20(BEXT[I])-PSI
[25] C+A+B
[26] +I*1)/SG
[27] +((CXR)=VB)/SG
[28] +(FLAG>1)/SH
[29] PSI+PSI+(0x1)
[30] FLAG+FLAG+1
[31] +SF
[32] SH:'UNEQUAL VALUES AT TB FLAGGED'
[33] SG:VR+VR,CxR
[34] +((1+PT)>I+I+1)/SF
[35] (V'AN2),(V'EA(-'),(V'GA),(V'T) + '),((V'AN3),(V'EA(-'),(V'AL),(V'T)COS('),(V'BE),(V'XT -'),(V'PSI),V')'
[36] 'AN2E*(-GAXT) + AN3(EA(-AL))COS(BEXT - PSI)'
[37] T+T+TB
[38] RR+ 2 1 Q(2,(PTI)+(PT))PTI,T,VC2,VR
  ▽

```



```

[1]  CUQUULI[0]
[2]  RR+CUQUULI B;D;Q;R;S;T;V;TH;A1;A2;A3;X1
[3]  A ENTERED ON 25 SEPTEMBER, 1975. BASED ON CUB2.
[4]  +(0=(B+0B)[1])/LA
[5]  Q+((A2+B[3])÷B[1])÷3)-((A1+B[2])÷B[1])×A2)÷9
[6]  R+(A1×A2÷6)-((A3+B[4])÷B[1])÷2)+(A1×A3)÷27
[7]  D+(Q×A3)+R×A2
[8]  +(D>0)/SF
[9]  RR+-(A1÷3)+2×((-Q)×0.5)×(20TH÷3), (20(TH+2×01)÷3), 20((TH+(-2)0-R÷(-Q)×3÷2)+4×01)÷3
[10]  +0
[11]  SF:S+(R+D×0.5)×÷3
[12]  T+(R-D×0.5)×÷3
[13]  RR+ 2 3 PX1,(2P(X1+S+T-A1÷3)-1.5×S+T),0,V,-V+(S-T)×(3×0.5)÷2
[14]  +0
[15]  LA:+(0=B[2])/TI
[16]  S+(B[3]×A2)-4×B[2]×B[4]
[17]  +(S×0)/SD
[18]  RR+(((S×0.5)-B[3]),-(S×0.5)+B[3])÷2×B[2]
[19]  +0
[20]  SD:RR+ 2 2 P((2P-B[3]),((-S)×0.5),-((-S)×0.5)÷2×B[2]
[21]  TI:RR+-(B[4])÷B[3]
[22]  +

```



```

[1]  VPLOT[0]
[2]  A PLOT B;C;D;F;G;H;I;J;L;T;Y;HZ;NB;VT;PT;ST;ISV;U
[3]  RC+ '0A' + 'A0',
[4]  HS+0
[5]  SI+ 1 2 5
[6]  SM+ 5 10
[7]  +((0=x/(2PA),PB), 3 2 1 <PPB)/0,PL7,PL1,PL2
[8]  +PL2,PB+M(2,D)P(1D+P,B),B
[9]  PL1:B+B[1];
[10] PL2:Y+1+(PB)[2]-1
[11] C+((F/B[;Y])-L/L/B[;Y]),(F/B[;1])-L/B[;1]
[12] F+I(2PA)/C+(C=0)*B[1; 2 1]+B[1; 2 1]=0
[13] F+(SI+/(L0.0001+FX10A-G)*.≥SI])x10AG+L10MF
[14] G+(SM÷F)xL((L/L/B[;Y]),L/B[;1])xF÷SM+16LSM 1 4
[15] B[;1]+L0.5+FC[2]x[B[;1]-G[2]
[16] B[;Y]+L0.5+FC[1]x[B[;Y]-G[1]
[17] H+SMxL((F/B[;Y]),F/B[;1])÷SM
[18] NB+G[1]+(SM[1]÷F[1])x0,HC[1]÷SM[1]
[19] HZ+G[2]+(SM[2]÷F[2])x0,HC[2]÷SM[2]
[20] OPST+6P~ISV+1+U+9
[21] PL3:VT+V/O>NB+NBx10AU-ST[6-ISV]+I+1+L10M1(NB≠0)/NB
[22] PT+L1+10IPT-1IPT+0.00001+(INB)*.÷10A-1+ΦIU
[23] L+U+1-(Φ((C+PNB)P1)A.=FT)10
[24] +(U>T+VT+L/I,(L+L=I),(I≠0)x2+L-I),ST[2-ISV]+ST[2-ISV]÷L≥U-VT+L>I)/ 3 2 +IBE 26
[25] +(-1+IBE 26),PST[4-ISV]+I+1
[26] +PL3,PNB+SM[1+~ISV]x-1+IC
[27] PT+(-VT+0F1-I)ΦPT
[28] PT+(-FT)xJ+Φ(ΦPT)P(,Φ(1≠PT)∨.^(IU)*.≠\VT(I-1),(CxU+1-I+VT+IFI≤0)P1
[29] +(~VT)/2+IBE 26
[30] PTC(U+/(C,U)PJ)+Ux-1+IC]+11xNB<0
[31] PT+~(IU+J)ε(I+J),1-1+J+U-T)\(1 0 +C,U)PFT,UPO
[32] PTC(I+J)+12
[33] PT+ ' 0123456789' . 'L1+PTC;IU-1]]
[34] +(~ISV)/PL6
[35] L+1,HC[2]POXC+HC[1]
[36] PL4:L+(LxHSC≠0)F1,HC[2]PO
[37] L[1]+(D≠0)/B[;1]÷(D≠0)/D+(C=B[;Y])F.xY
[38] + (C≠0)/PL5
[39] L+LFO=(SM[2]÷2)10,HC[2]
[40] PL5:PTC((PPT)I],1+C÷SM[1])[1+0=SM[1]IC];(' 1',(PY)PEC)[1+L]
[41] + (0≤C+C-1)/PL4
[42] + (U=U+SM[2]-~ISV+~PPNB+HZ)/PL3
[43] PL6:(SM[2]-9)Φ(,0 0 ,(U-1)P1)\PT),' '
[44] + (ST[1 3 2 4J+1]/ 1 3 5 7 10 +IBE 26
[45] (V'ORIGIN AND SCALE FACTOR FOR ORIGINATE: '),VG[1],÷F[1]
[46] + (0=ST[3])/2+IBE 26
[47] (V'SCALE FACTOR FOR ORIGINATE: '),V10*ST[5]-1
[48] + (0=ST[2])/2+IBE 26
[49] (V'ORIGIN AND SCALE FACTOR FOR ABSCISSA: '),VG[2],÷F[2]
[50] + (0=ST[4])/0
[51] (V'SCALE FACTOR FOR ABSCISSA: '),V10*ST[6]-1
[52] +0
[53] PL7:'THE RIGHT ARGUMENT OF PLOT MUST HAVE RANK ≠ 3.'

```

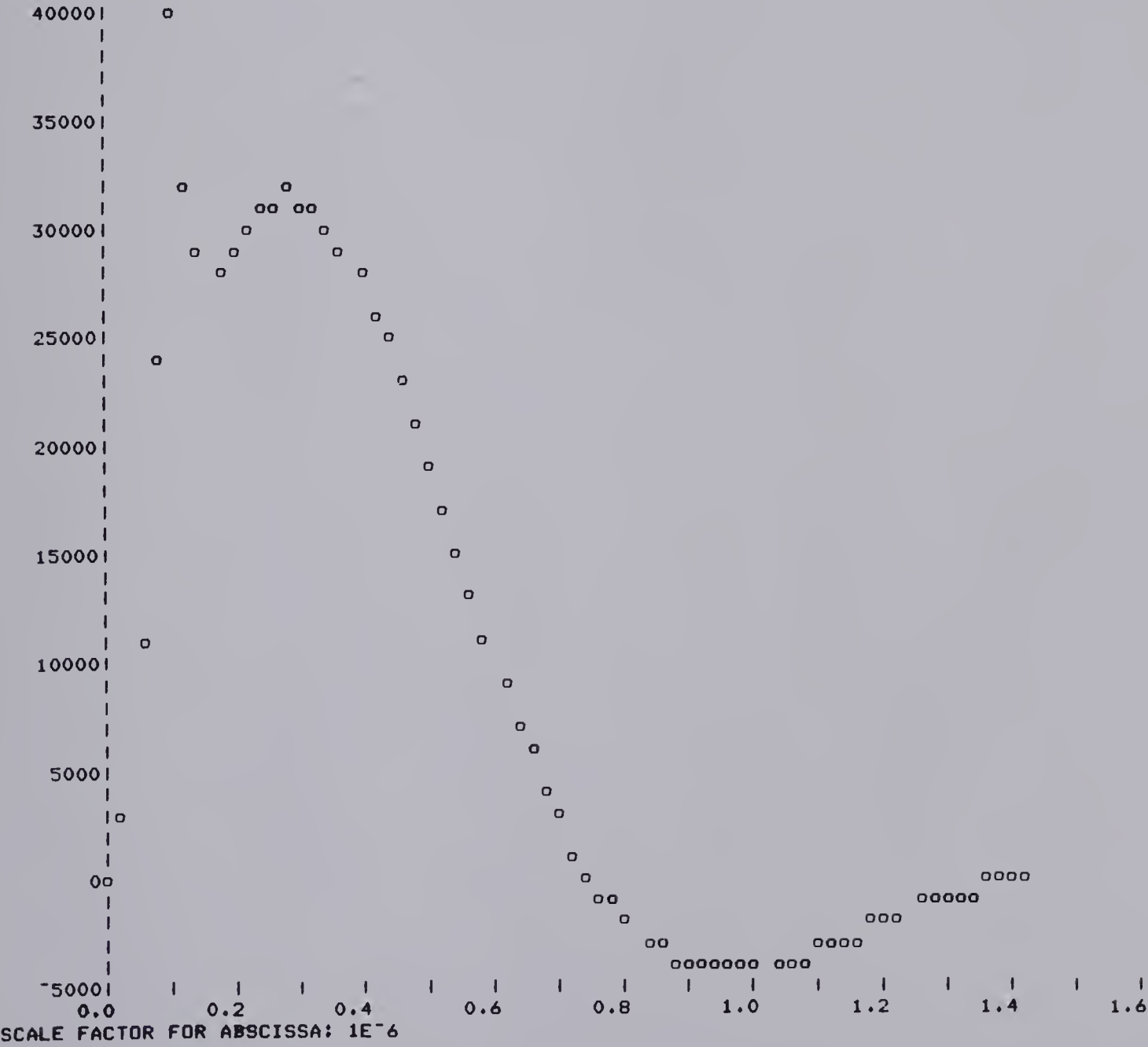


```

      NB
1 1 60
      VV
1E-8 1.75E-9 4E-6 20 40000 60000
      NB DRIVER VV
VB =40000
TB = 1.043841304E-7
VC1TB = 53000
ILTB = 1130.265456
7.142857143E20 1.678571429E14 28571428.57 1
      22527764.73      3021831.919      3021831.919
      0      -4751361.663      4751361.663
1776.612791E*(-22527764.73T) + 3343.061996E*(-3021831.919T)COS(4751361.663xT -1.503925361)
AN2E*(-GAXT) + AN3(E*(-AL))COS(BEXT - PSI)
0.000000000E0      0.000000000E0
2.609603261E-8      2.890887418E3
5.219206522E-8      1.123622483E4
7.828809783E-8      2.409109952E4
1.043841304E-7      4.000000000E4
1.043841304E-7      4.000000000E4
1.264240766E-7      3.230769781E4
1.484640227E-7      2.912862630E4
1.705039688E-7      2.837280698E4
1.925439150E-7      2.879156434E4
2.145838611E-7      2.964969071E4
2.366238072E-7      3.052537640E4
2.586637534E-7      3.118795814E4
2.807036995E-7      3.152308559E4
3.027436456E-7      3.148680242E4
3.247835918E-7      3.107727825E4
3.468235379E-7      3.031733414E4
3.688634840E-7      2.924358518E4
3.909034302E-7      2.789965584E4
4.129433763E-7      2.633191604E4
4.349833224E-7      2.458679014E4
4.570232686E-7      2.270905856E4
4.790632147E-7      2.074079523E4
5.011031608E-7      1.872072020E4
5.231431070E-7      1.668382957E4
5.451830531E-7      1.466121558E4
5.672229993E-7      1.268002017E4
5.892629454E-7      1.076348477E4
6.113028915E-7      8.931070325E3
6.333428377E-7      7.198629272E3
6.553827838E-7      5.578615506E3
6.774227299E-7      4.080321732E3
6.994626761E-7      2.710135525E3
7.215026222E-7      1.471806999E3
7.435425683E-7      3.667221093E2
7.655825145E-7      -6.058234444E2
7.876224606E-7      -1.448353995E3
8.096624067E-7      -2.164950937E3
8.317023529E-7      -2.760999982E3
8.537422990E-7      -3.242951068E3
8.757822451E-7      -3.618092827E3
8.978221913E-7      -3.894343075E3
9.198621374E-7      -4.080056343E3
9.419020835E-7      -4.183849111E3
9.639420297E-7      -4.214443062E3
9.859819758E-7      -4.180526361E3
1.008021922E-6      -4.090632713E3
1.030061848E-6      -3.953037730E3
1.052101814E-6      -3.775671937E3
1.074141760E-6      -3.566049594E3
1.096181706E-6      -3.331212395E3

```


1.118221653E-6	-3.077686988E3
1.140261599E-6	-2.811455213E3
1.162301545E-6	-2.537935897E3
1.184341491E-6	-2.261977030E3
1.206381437E-6	-1.987857133E3
1.228421383E-6	-1.719294660E3
1.250461329E-6	-1.459464296E3
1.272501276E-6	-1.211019046E3
1.294541222E-6	-9.761170907E2
1.316581168E-6	-7.564524119E2
1.338621114E-6	-5.532882901E2
1.360661060E-6	-3.674928233E2
1.382701006E-6	-1.995757092E2
1.404740952E-6	-4.972560106E1
1.426780898E-6	8.215257077E1



The program REGRESS was used to generate the gas flow calibration curve coefficients shown in Tables 5.1 and 7.1.


```

1      DOUBLE PRECISION P(200),T(20)
2      INTEGER ID(4) /' ',' ',' ',' ' /
3      DIMENSION X(100),Y(100),X1(100),Y1(100)
4      DIMENSION C(8), S(8), A(5), B(5)
5      NAMELIST /DATA/ ID, X, Y, N
6      DO 5 I=1,100
7          X(I)=0.
8      5 Y(I)=0.
9          WRITE(6,100)
10     100 FORMAT ('ENTER DATA')
11         READ(5,DATA)
12         WRITE(6,105) ID
13     105 FORMAT ('CALIBRATION CURVE FITTING FOR'/' ',4A4)
14         WRITE(6,110) X,Y,N
15     110 FORMAT ('RPM=' /20(' ',5F10.1) /' VEL=' /20(' ',5F10.1) /' N=' ,I4)
16         RSQ=100
17         MD=1
18     15 CONTINUE
19         DO 6 I=1,8
20             S(I)=0.
21         6 C(I)=0.
22             DO 7 I=1,5
23                 B(I)=0.
24             7 A(I)=0.
25             DO 20 I=1,100
26                 X1(I)=X(I)
27             20 Y1(I)=Y(I)
28             CALL RLFOTH(X1,Y1,N,RSQ,MD,ID1,P,C,S,A,F,IER)
29     C      WRITE(6,120) X1,Y1
30     120 FORMAT('OX1=' /20(' ',5F10.6) /' Y1=' /20(' ',5F10.6) /)
31         WRITE(6,125) ID1
32     125 FORMAT('OID1=' ,I3)
33     C      WRITE(6,130) C
34     130 FORMAT('OC=' ,2(/' ',5G15.6) )
35         WRITE(6,135) S
36     135 FORMAT('OS=' ,2(/' ',5G15.6) )
37         ANUM=N-ID1-1
38         VAR=S(ID1+3)/ANUM
39         WRITE(6,137) VAR
40     137 FORMAT (' VARIANCE=' ,G15.6)
41     C      WRITE(6,140) A
42     C  140 FORMAT('OA=' ,2(/' ',5E15.6) )
43     C      WRITE(6,145) B
44     C  145 FORMAT('OB=' ,2(/' ',5E15.6) )
45         WRITE(6,150) IER
46     150 FORMAT('OIER=' ,I3)
47         CALL PLOPDC(X1,N,A,B,C,ID1,1,P,Y1,IER)
48         WRITE(6,160) Y1
49     160 FORMAT('OY1=' /20(' ',5F10.6) /)
50         CALL PLDOPM(C,ID1,A,B,T)
51         WRITE(6,130) C
52         MD=MD+1
53         IF(MD.LE.4) GOTO 15
54         STOP
55         END
56     C
57     C      SAMPLE DATA DECK FOLLOWS
58     C
59     &DATA ID='400 ','TORR',' HEL',' IUM ',
60     X=0.,750.,1034.,1463.,2000.,2400.,3000.,3571.,
61     Y=0.,2.4,4.1,6.5,10.1,13.2,17.6,22.2,
62     N=8 &END

```

END OF FILE

The program ANALYSE was used to do the fractional frequency analysis of repetition rate data. In addition to the sample output shown in the appendix this program also generates a repetition rate versus flow velocity plot. The plot corresponding to the sample output is Figure 6.16.


```

list analyse2
> 1 C PROGRAM WRITTEN OCT. 30, 1978
> 2 C LATEST REVISION NOVEMBER 10, 1978
> 3 C
> 4 DIMENSION CAL(4)
> 5 DIMENSION RPM(24), REPRAT(24), PREP(24)
> 6 INTEGER ID(4) '/' ' ' ' ' ' ' ' ' ' '
> 7 DIMENSION XLINE(26), YLINE(26)
> 8 DIMENSION FAN(24), DISCH(24), VEL(24), FPREP(24)
> 9 NAMELIST /DATA/ ID, CAP, VOLT, DIA, CAL, FAN, DISCH, N
> 10 DO 5 I=1,24
> 11 VEL(I)=0.
> 12 FAN(I)=0.
> 13 DISCH(I)=0.
> 14 RPM(I)=0.
> 15 REPRAT(I)=0.
> 16 FPREP(I)=0.
> 17 FPREP(I)=0.
> 18 XLINE(I)=0.
> 19 YLINE(I)=0.
> 20 5 CONTINUE
> 21 XLINE(25)=0.
> 22 YLINE(25)=0.
> 23 XLINE(26)=0.
> 24 YLINE(26)=0.
> 25 C
> 26 C INPUT DATA
> 27 C
> 28 WRITE(6,90)
> 29 90 FORMAT('ENTER DATA')
> 30 READ(5,DATA)
> 31 ENERGY=CAP*VOLT*VOLT/2.
> 32 C
> 33 C ELECTRODE SEPARATION IS 15/16 INCH=23.8125MM
> 34 C
> 35 RAD=DIA/2.0
> 36 VOL=3.141593*RAD*RAD*23.8125*1.E-6
> 37 EDNSTY=ENERGY/VOL
> 38 C
> 39 C CALCULATE RPM AND REPETITION RATE
> 40 C
> 41 DO 10 I=1,N
> 42 RPM(I)=60.*(1./(FAN(I)*.001))
> 43 10 REPRAT(I)=1./(DISCH(I)*.001)
> 44 C
> 45 C CALCULATE FLOW VELOCITIES CORRESPONDING TO OBSERVED RPM
> 46 C
> 47 DO 15 I=1,N
> 48 T1=CAL(2)*RPM(I)
> 49 T2=CAL(3)*RPM(I)*RPM(I)
> 50 T3=CAL(4)*RPM(I)*RPM(I)*RPM(I)
> 51 VEL(I)=CAL(1)+T1+T2+T3
> 52 15 CONTINUE
> 53 C
> 54 C CALCULATE IDEAL REP RATE CORRESPONDING TO OBSERVED
> 55 C REP RATES
> 56 C
> 57 DO 25 I=1,N
> 58 25 PREP(I)=1000.*VEL(I)/DIA
> 59 C
> 60 C OUTPUT DATA AND CALCULATED RESULTS
> 61 C
> 62 WRITE(6,130) ID
> 63 130 FORMAT('-REPETITION RATE ANALYSIS'/' ',4A4)
> 64 WRITE(6,132) CAP,VOLT,DIA,EDNSTY,N

```



```

> 65      132 FORMAT(' CAPACITANCE=',E8.3,' FARADS'// VOLTAGE=',E8.3,' VOLTS'//
> 66      1 ' DISCHARGE DIAMETER=',F8.2,'MM'// ENERGY DENSITY=',F8.2,
> 67      1 'J/L'// N=',I4)
> 68      WRITE(6,134) CAL
> 69      134 FORMAT('OCALIBRATION CURVE COEFFICIENTS'// ',4015.6)
> 70      WRITE(6,136)
> 71      136 FORMAT('OFAN PERIOD AND INTERPULSE PERIOD'// ',T7,'MSEC',T17,
> 72      1 'MSEC')
> 73      DO 30 I=1,N
> 74      WRITE(6,138) FAN(I),DISCH(I)
> 75      138 FORMAT(' ',2F10.3)
> 76      30 CONTINUE
> 77      WRITE(6,140)
> 78      140 FORMAT('OCALCULATED VALUES'// ',TB,'FAN SPEED',T24,'FLOW VEL',
> 79      1 T39,'REP RATE',T48,'IDEAL REP RATE'//
> 80      1 ' ',T14,'RPM',T27,'M/SEC',T45,'HZ',T60,'HZ')
> 81      DO 40 I=1,N
> 82      WRITE(6,142) RPM(I), VEL(I), REPRAT(I), PREP(I)
> 83      142 FORMAT(' ',4F15.1)
> 84      40 CONTINUE
> 85      C
> 86      C      LEAST SQUARES FIT OF REP RATE DATA TO COMPARE WITH
> 87      C      IDEAL REP RATE.  LEAST SQUARES FIT IS FOR REP RATE
> 88      C      VERSUS GAS FLOW VELOCITY
> 89      C      PLOTTED FIT ASSUMES A ZERO INTERCEPT.
> 90      C
> 91      X=0.
> 92      Y=0.
> 93      XY=0.
> 94      XX=0.
> 95      DO 45 I=1,N
> 96      XX=XX+VEL(I)*VEL(I)
> 97      XY=XY+VEL(I)*REPRAT(I)
> 98      X=X+VEL(I)
> 99      45 Y=Y+REPRAT(I)
> 100     C
> 101     C      A IS SLOPE OF LINE THROUGH ORIGIN
> 102     C
> 103     A=Y/X
> 104     C
> 105     C      AMS IS SLOPE OF LEAST SQUARES FIT
> 106     C      BMS IS INTERCEPT OF LEAST SQUARES FIT
> 107     C
> 108     DENOM=N*XX-X*X
> 109     ANUM=N*XY-X*Y
> 110     BNUM=Y*XX-X*XY
> 111     AMS=ANUM/DENOM
> 112     BMS=BNUM/DENOM
> 113     C
> 114     C      CALCULATE EXPERIMENTAL FRACTIONAL FREQ.
> 115     C
> 116     DO 50 I=1,N
> 117     50 FPREF(I)=REPRAT(I)/PREP(I)
> 118     C
> 119     C      CALCULATE MEAN FRACTIONAL FREQ AND STANDARD DEV
> 120     C
> 121     SUM=0.
> 122     DO 55 I=1,N
> 123     55 SUM=SUM+FPREF(I)
> 124     AN=N
> 125     AMEAN=SUM/AN
> 126     SUM2=0.
> 127     DO 60 I=1,N
> 128     DEV2=FPREF(I)-AMEAN
> 129     60 SUM2=SUM2+DEV2*DEV2
> 130     SIGMA=SQRT(SUM2/AN)

```



```

> 131      STER=SIGMA/SQRT(AN)
> 132      C
> 133      C      OUTPUT CALCULATED DATA
> 134      C
> 135      WRITE(6,143) AMS,BMS
> 136      143 FORMAT('OLEAST SQUARES FIT TO DATA IS'' Y=',G14.5,' X+ ',G14.5)
> 137      WRITE(6,144) A
> 138      144 FORMAT('OLEAST SQUARES FIT THROUGH ORIGIN IS'' Y=',
> 139      1 G14.5,'X')
> 140      WRITE(6,146)AMEAN,SIGMA
> 141      146 FORMAT(' MEAN FRACTIONAL FREQ=',G10.3,' STANDARD DEV=',G10.3)
> 142      WRITE (6,147) STER
> 143      147 FORMAT(' STANDARD ERROR=',G10.3)
> 144      C
> 145      C      PLOT OF DATA
> 146      C
> 147      C      INITIALIZE PLOTTING SYSTEM
> 148      C
> 149      CALL PLOTS
> 150      C
> 151      C      POSITION NEW ORIGIN
> 152      C
> 153      CALL PLOT(3.0,3.0,-3)
> 154      C
> 155      C      DRAW X AXIS
> 156      C
> 157      CALL AXIS(0.,0., 'FLOW VEL M/SEC',-14,5.,0.,0.,5.)
> 158      C
> 159      C      DRAW Y AXIS
> 160      C
> 161      CALL AXIS(0.0,0., 'REP RATE HZ',11,5.,90.,0.,100.)
> 162      C
> 163      C      DRAW EXPERIMENTAL DATA POINTS
> 164      C
> 165      DO 65 I=1,N
> 166      XLINE(I)=VEL(I)
> 167      65 YLINE(I)=REPRAT(I)
> 168      XLINE(N+1)=0.
> 169      YLINE(N+1)=0.
> 170      XLINE(N+2)=5.0
> 171      YLINE(N+2)=100.
> 172      CALL LINE(XLINE, YLINE, N,1,-1,1)
> 173      C
> 174      C      DRAW LEAST SQUARES FIT
> 175      C
> 176      CALL PLOT(0.,0.,3)
> 177      CALL PLOT(XLINE(N)/XLINE(N+2),A*XLINE(N)/YLINE(N+2),2)
> 178      C
> 179      C      DRAW IDEAL REP RATE
> 180      C
> 181      DO 70 I=1,N
> 182      70 YLINE(I)=PREP(I)
> 183      C
> 184      C      THIS PART OF THE PROGRAM THROWS OUT REDUNDANT POINTS AS THEY
> 185      C      CAUSE PROBLEMS WITH DASHLN.
> 186      C
> 187      J=N
> 188      K=N-1
> 189      DO 75 I=1,K
> 190      LM=N-I
> 191      C      WRITE (6,999)
> 192      C 999 FORMAT (' LOOP1')
> 193      72 IF(XLINE(LM).NE.XLINE(LM+1)) GO TO 75
> 194      DO 74 L=LM,25
> 195      XLINE(L)=XLINE(L+1)
> 196      74 YLINE(L)=YLINE(L+1)

```



```

> 197          J=J-1
> 198          C      WRITE (6,1000)
> 199          C1000 FORMAT (' LOOP2')
> 200          75 CONTINUE
> 201          CALL DASHLN(XLINE,YLINE,J,1)
> 202          C
> 203          C      ADD IDENTIFICATION
> 204          C
> 205          CALL SYMBOL(0.5,4.0,.2,ID,0.,16)
> 206          CALL NUMBER(0.5,3.5,.2,EDNSTY,0.0,-1)
> 207          CALL SYMBOL(1.,3.5,.2,'J/L',0.,3)
> 208          C
> 209          C      TERMINATE PLOT
> 210          C
> 211          CALL PLOT(0.,0.,999)
> 212          STOP
> 213          END
> 214          C
> 215          C      SAMPLE DATA DECK FOLLOWS
> 216          C
> 217          &DATA ID=' 80 ','TORR',' CO2',' ',
> 218          CAP=30.3E-9, VOLT=10000, DIA=48.26,
> 219          CAL=-0.189129,0.378319E-02,0.135675E-05,-0.183620E-09,
> 220          FAN=51.,49.,41.,40.,30.,30.,25.,25.,20.,20.,17.2,17.,
> 221          DISCH=12.4,12.2,9.5,9.1,6.,5.8,4.65,4.5,3.7,3.6,3.05,2.95,
> 222          N=12 &END
#END OF FILE
#

```


ENTER DATA

REPETITION RATE ANALYSIS

80 TORR CO₂
 CAPACITANCE=.303E-07 FARADS
 VOLTAGE=.100E+05 VOLTS
 DISCHARGE DIAMETER= 48.26MM
 ENERGY DENSITY= 34.78J/L
 N= 12

CALIBRATION CURVE COEFFICIENTS

-0.189129 0.378319E-02 0.135675E-05 -0.183620E-09

FAN PERIOD AND INTERPULSE PERIOD

MSEC	MSEC
51.000	12.400
49.000	12.200
41.000	9.500
40.000	9.100
30.000	6.000
30.000	5.800
25.000	4.650
25.000	4.500
20.000	3.700
20.000	3.600
17.200	3.050
17.000	2.950

CALCULATED VALUES

FAN SPEED	FLOW VEL	RFP RATE	IDEAL REP RATE
FPM	M/SEC	HZ	HZ
1176.5	5.8	80.6	121.0
1224.5	6.1	82.0	127.2
1463.4	7.7	105.3	159.1
1500.0	7.9	109.9	164.1
2000.0	11.3	166.7	234.9
2000.0	11.3	172.4	234.9
2400.0	14.2	215.1	293.6
2400.0	14.2	222.2	293.6
3000.0	18.4	270.3	381.5
3000.0	18.4	277.8	381.5
3488.4	21.7	327.9	450.1
3529.4	22.0	339.0	455.7

LEAST SQUARES FIT TO DATA IS

Y= 15.836 X+ -12.569

LEAST SQUARES FIT THROUGH ORIGIN IS

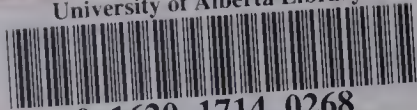
Y= 14.888 X

MEAN FRACTIONAL FREQ= 0.707

STANDARD DEV= 0.356E-01

STANDARD ERROR= 0.103E-01

University of Alberta Library



0 1620 1714 0268

B30275